Global and local anthropogenic effects on hydrodynamics of lakes - Applications to Lake Biel drinking water management

THÈSE Nº 7976 (2018)

PAR

Carl Love Mikael RÅMAN VINNÅ

ÉCOLE POLYTECHNIQUE
FÉDÉRALE DE LAUSANNE

Suisse
2018

Acknowledgements

And finally, to all of you:

Keep calm, learn cool stuff that counts and be good to the people that matters in your life, simple really. And remember, minds are like parachutes, they only function when open!

Abstract

In many countries water quality is a major concern for drinking water management authorities. Freshwater is a limited resource and the demand for good-quality water from natural aquatic systems is therefore high. Additional stress arises from anthropogenic emissions of nutrients, chemicals, pathogens, heat and hydrological alterations as well as from the ongoing global climate change. In this thesis the relevant recent past, present and future factors affecting water quality in the perialpine Lake Biel, used as a source for drinking water, was investigated. Through measurements in the field combined with hydrodynamic logical modelling in one and three dimensions, optimal locations for forthcoming lake water intakes was identified. Water quality properties considered were temperature, oxygen, suspended sediment concentration (SSC) and the risk of subaqueous mass movements.

The results identified the forthcoming changes expected in Lake Biel due to the upcoming decommission of the Mühleberg Nuclear Power Plant (MNPP) in 2019. This plant currently release ~700 MW of heat into the upstream Aare River in the form of cooling water. The removal of this anthropogenic thermal source will decrease future lake temperature by ~0.3 °C (volume average). Due to seasonal river discharge patterns, the main impact of the plant closure will occur during winter. Minor effects are expected in summer in the form of moderately weaker lake stratification. Furthermore, the current fate of thermal pollution emitted from MNPP was linked to the hydraulic residence time of Lake Biel.

While short-term anthropogenic thermal impacts in Lake Biel can be large, the system is additionally experiencing continuous warming up to ~0.1 °C per decade (volume average) by the ongoing climate change. The climate effect on Lake Biel and its primary tributary, the Aare River, was investigated as well as compared to the much larger Lake Geneva and Rhône River. Climate change causes seasonal river discharge shifts resulting in enhanced river warming in summer and diminished warming in winter, while at the same time SSC increases in winter and decreases in summer. Differences in temperature as well as warming rates between rivers and lakes in turn resulted in a discharge and hydraulic residence time-dependent decrease in climate warming of lakes. Furthermore, deep-water renewal in both lakes is predicted to increase in summer and decreases in winter, possibly influencing the replenishment of deep water oxygen.

Additionally, sedimentation patterns in Lake Biel were examined and linked to the historical diversion of the Aare River into the lake. The majority of sediment supplied to Lake Biel (~80 %) came from large SSC events in the Aare. These events resulted in a selective particle settling pattern, which concentrated sedimentation on the shallow shelf area North-East of the Aare delta. Both the large SSC events as well as this selective sedimentation pattern were connected to weather fronts coming in from the Atlantic Ocean.

Lake Biel bathymetry was found to steeply drop (slope > 10°) from shallow areas towards the lake interior, thereby increasing the likelihood of subaqueous mass movements. An area with enhanced historical occurrences of major subaqueous slides was identified to the North-East of the Aare estuary and linked to the passage of the river plume. Wind driven selective sedimentation is thereby likely to increase the occurrence rate and the severity of subaqueous mass movements.

The research performed here opens up for further promising interdisciplinary research between Meteorology, Climatology, Hydrology and Sedimentology. Inland water management would benefit through increased knowledge regarding the propagation of particles and/or anthropogenic heat, from river catchments into downstream lakes and sediments.

Key words

Drinking water, water quality, thermal pollution, climate change, discharge regime, residence time, hydrodynamic modeling, sedimentation, subaqueous mass movements, Lake Biel, Aare River.

Zusammenfassung

In vielen Ländern ist die Wasserqualität ein wichtiges Anliegen der Trinkwasserversorgungs-behörden. Süßwasser ist eine begrenzte Ressource und die Nachfrage für qualitativ gutes Wasser aus natürlichen Gewässern ist gross. Die Wasserqualität wird durch anthropogene Aktivitäten belastet. Dazu gehören Emissionen von Nährstoffen, Chemikalien, Krankheitserregern oder Wärme, sowie hydrologische Veränderungen und natürlich der anhaltenden Klimawandel. In dieser Arbeit wurden gegenwärtige und zukünftige Einflussfaktoren auf die Wasserqualität des perialpinen Bielersees untersucht, welcher als Quelle für Trinkwasser verwendet wird. Durch Feldmessungen und hydrodynamische Modelle in ein und drei Dimensionen wurden optimale Standorte für die zukünftige Trinkwasserversorgung identifiziert. Die untersuchten Wassereigenschaften waren Temperatur, Sauerstoff, suspendierte Sedimentkonzentration (englisch: *suspended sediment concentration*, SSC) und das Risiko von Unterwasserrutschungen.

Die Ergebnisse identifizierten die bevorstehenden Veränderungen im Bielersee aufgrund verminderter «thermischer Verschmutzung». Die bevorstehende Stilllegung des Kernkraftwerks Mühleberg (englisch: *Mühleberg Nuclear Power Plant*, MNPP) im Jahr 2019, welches im Augenblick ~700 MW Wärme in Form von Kühlwasser in den Zufluss Aare abgibt, wird die Seetemperatur um ~0,3 ° C senken. Aufgrund des saisonalen Regimes der Zuflüsse werden die Effekte der Stilllegung im Winter am stärksten sein, während sich im Sommer lediglich kleinere Effekte in Form einer moderat schwächeren Schichtung zeigen. Der heutige Effekt der thermischen Verschmutzung, die vom MNPP emittiert wird, ist stark mit der kurzen hydraulischen Verweilzeit des Sees verbunden.

Während kurzfristige anthropogene thermische Veränderungen im Bielersee relevant sind, wird das Gewässer zudem durch den Klimawandel kontinuierlich erwärmt (~0,1 °C pro Jahrzehnt). Sein Effekt auf den Bielersee und seinen primären Zufluss Aare wurde untersucht und mit dem größeren Genfersee verglichen. Der Klimawandel verursacht saisonale hydrologische Veränderungen der Zuflüsse und führt zu erhöhter Erwärmung im Sommer und geringerer Erwärmung im Winter, während SSC im Winter ansteigt und im Sommer sinkt. Der Unterschied zwischen der Temperatur der Zuflüsse und der Seen führte wiederum zu einer von der hydraulischen Aufenthaltszeit des Wassers abhängigen Abnahme der Erwärmung der Seen.

Darüber hinaus erhöht sich die Aufenthaltszeit in beiden Seen im Sommer und sinkt im Winter, was die Tiefenwassermischung beeinflusst.

Darüber hinaus wurde die Sedimentation im Bielersee untersucht und mit der Einmischung der Aare in den See verknüpft. Die meisten Feststoffe, die in den Bielersee eingetragen wurden (~80%), stammten aus großen SSC-Ereignissen in der Aare. Diese Ereignisse führten zu einer Präferenz der Sedimentation auf dem flachen Schelfgebiet im Nordosten des Aare-Deltas. Sowohl die großen SSC-Ereignisse als auch diese selektive Sedimentation wurden mit Wetterfronten aus dem Atlantischen Ozean in Verbindung gebracht.

Die Uferzonen um den gesamten Bielersee fallen steil ab (> 10°). Daher ereignen sich regelmässig Unterwasserrutschungen. Ein Bereich mit in der Vergangenheit verstärkt auftretenden Unterwasserrutschungen wurde im Nordosten des Aare-Zuflusses identifiziert, und mit dem Verlauf der Aare innerhalb des Sees in Verbindung gebracht. Windgetriebene selektive Sedimentation erhöht das Auftreten und die Schwere der Unterwasserrutschungen zusätzlich.

Die hier durchgeführte Forschung eröffnet eine vielversprechende interdisziplinäre Forschung zwischen Meteorologie, Klimatologie, Hydrologie und Sedimentologie. Die Binnenwasserwirtschaft würde von einem erhöhten Wissen über die Ausbreitung von Partikeln und/oder anthropogener Hitze, von Flusseinzugsgebieten zu nachgelagerten Seen und Sedimenten profitieren.

Schlagwörter

Trinkwasser, Wasserqualität, thermische Verschmutzung, Klimawandel, Verweilzeit, hydrodynamische Modellierung, Sedimentation, Unterwasserrutschungen, Bielersee, Genfersee, Aare, Rhône.

Contents

8

Chapter 1:

Introduction

1.1 Drinking water through time

The availability of clean water resources has been one of humanity's major concerns throughout the ages and will likely stay important as history progresses [*Gleick*, 1993]. As *Vuorinen et al.* [2007] so elegantly put it "*Water is life… our existence is dependent on water... one could say that our whole civilization is built on the use of water*". The selection criteria's for finding suitable water, commonly referred to as water quality, have developed throughout history. The Romans considered the taste, smell, appearance and temperature of water as well as the health of the users in order to find suitable water resources [*Vitruvius*, ca 10AD].

Freshwater on Earth is mainly found deep in the ground or bound as snow and ice. Free flowing freshwater in rivers and lakes is limited, but usually preferable as source due to ease of access. However, the setting of upstream events, such as emissions of heat or contaminants, are sooner or later transported downstream and stored in lakes/reservoirs. How these upstream events concur with downstream lake processes will affect water quality in the system.

Our ability to measure and understand water quality processes in lakes started with the birth of limnology at the end of the 19th century. Scientists have since the early days been interested in the interaction of rivers and lakes as well as quantitative water quality parameters such as temperature and oxygen [*Forel*, 1892]. Since then, the level of details to which we can describe and resolve processes affecting water quality has increased immensely. Some of the important aspects considered in the past include temperature, heavy metals, and nutrients with effects on oxygen as well as odour. These are still considered today with the addition of bacterial and viral pathogens, antibiotic resistance, hormones, chemicals, nanoparticles, radioactivity and the effects of climate change [*Schwarzenbach et al.*, 2010; *WHO*, 2017]. In Switzerland water quality and usage of water is regulated through the Waters Protection Act (WPA, 814.20). Overall, the aims of the WPA are to protect waters against harmful effects, preserve natural habitats with indigenous species, and guarantee future supply of drinking water. Of special importance for this dissertation is, that the WPA allows anthropogenic changes of watercourse temperature by ± 3 °C (± 1.5 °C in trout habitats) up to maximum 25 °C. In lakes anthropogenic influences should not change the natural temperature regime, or alter the distribution of nutrients, nor disrupt conditions for living and reproduction of organisms as well as keeping the minimum oxygen concentration above 4 mg L^{-1}.

The effects of most of the above mentioned parameters have affected people and water quality throughout history, however only recently, have we started studying them in detail. Consequently, the methods of measuring and understanding the processes affecting water

quality have evolved over time, yet we still consider the same issues as people have done for millennias while selecting resources of water. Where we once had to physically go and taste the water source, we can now use state of the art instrumentation and/or complex coupled model chains to determine the best location for obtaining present and future drinking water.

1.2 Factors affecting water quality in lakes

1.2.1 Temperature and stratification

Temperature is both a major water quality parameter due to taste, as well as affecting biological transformation processes with the potential to limit bacterial growth at cold temperature and thereby improving water quality [*LeChevallier et al.*, 1996]. Additionally, in the vertical direction, temperature is one of the most influential physical factor affecting processes in lakes. Since the salinity in freshwater lakes is low by definition, the dominant feature controlling density stratification and thereby stability is temperature, which sets up a vertical density gradient in summer as lakes heat up. This gradient is in turn counteracted by mixing (*turbulence*) which strives to smooth out the density difference, resulting in warmer water being mixed downward [*Schmidt*, 1928]. Yet, turbulence is seldom strong enough to completely homogenise a water body. The efficiency of turbulence to mix water is a complex function of local factors such as lake size, bathymetry, wind conditions and heat flux [*Rueda and Schladow*, 2009]. The ongoing competition between stabilizing heating and destabilizing turbulence divides lakes into three distinct vertical layers, the surface layer (*epilimnion*), an intermediate layer where temperature changes rapidly (*metalimnion*), and the deep layer (*hypolimnion*). As winter approaches, lakes cool down and convective turbulence deepens the epilimnion. Depending on the extent of cooling, the lakes can remain stratified (*meromictic*), can completely overturn (*monomictic*) or become stratified a second time (*dimictic*) as the water cools beyond the fresh water temperature of maximum density (4 °C).

1.2.2 Pollutants and water movements

Water quality in lakes can be affected by the introduction of potential harmful substances from rivers [*Laborde et al.*, 2010; *Schimmelpfennig et al.*, 2012; *Thevenon et al.*, 2013; *Hoyer et al.*, 2015], waste water treatment plants [*Bonvin et al.*, 2013; *Hoerger et al.*, 2013] or shore industrial facilities [*Thevenon et al.*, 2011]. The fate of pollutants in lakes, and thereby the temporal and spatial scale of negative impact on water quality, is dependent on both the

temporal and spatial scale of the emission as well as the residence time of the constituents. These scales are determined by water movements, transformation rates due to chemical as well as biological breakdown and binding to particles, sedimentation, resuspension and remineralisation of the pollutant. Water exchange between the epilimnion and the hypolimnion in freshwater systems is strongly repressed by the vertical temperature gradient, separating shallow and deep water. Horizontal advection of river plumes in lakes and oceans are affected by the local wind field [*García Berdeal*, 2002; *Choi and Wilkin*, 2007; *Schimmelpfennig et al.*, 2012] and the Coriolis effect [*Riccioli*, 1651; *Coriolis*, 1835; *Wright and Nydegger*, 1980]. Spatial distribution of water constituents and pollutants is thus directly linked to both stratification, as well as to horizontal circulation patterns which can transport water over considerable distances.

1.2.3 Particles and turbidity

Rivers are an important source of sediment to lakes. Processes affecting river plume propagation inside lakes are thus indirectly affecting sedimentation patterns [*Righetti et al.*, 2011]. High discharge events and floods are associated with high sediment content in rivers because of erosion in the catchment. However, sediment concentrations can be hard to predict due to the so-called hysteresis effect. A given river discharge can seldom be linked to a certain sediment concentration, owing to the nonlinearity between the amount of available sediment in the catchment and the river discharge [*Tananaev*, 2012].

The amount of sediment carried by rivers to lakes can be immensely increased through redirection of rivers into lakes [*Wirth et al.*, 2011], or diminished by construction of dams [*Loizeau and Dominik*, 2000]. The former, in combination with steep sloping bathymetry (10° to 30°), which are typical for alpine and perialpine lakes, have both been linked to increased risk for subaqueous mass movements [*Hampton and Homa*, 1996; *Schnellmann et al.*, 2006; *Lee et al.*, 2007; *Wirth et al.*, 2011]. These can damage lake-internal infrastructure, resuspend large amounts of sediment and give rise to tsunami waves with potential lethal impact on near-shore communities [*Girardclos et al.*, 2007; *Kremer et al.*, 2012, 2014]. Suspended particles from rivers, subaqueous slides and wave erosion can stay in the water column over long time and in turn affect water quality.

1.2.4 Nutrients and oxygen

Nutrients are the building blocks of life and essential for all primary producers. They are transported across aquatic systems just like pathogens and sediments [*Rueda et al.*, 2007], which can cause local alga blooms [*Vidal et al.*, 2012]. The lack of nutrients can create the equivalent of deserts in aquatic systems [*Irwin and Oliver*, 2009]. While increased nutrient levels can lead to extreme levels of growth (*eutrophication*) which can cause problems for water quality [*Correll*, 1998].

The problems of eutrophication are twofold: (i) increased nutrient levels can favour certain toxic primary producers (Cyanobacteria) which degrade water quality [*Hitzfeld et al.*, 2000] and (ii) alga blooms create large amounts of detritus which settle towards the bottom and subsequently decompose. The later process requires oxygen and can reduce oxygen concentration towards hypoxia (< 4 mg L^{-1}) or even anoxia (0 mg L^{-1}). Living organisms are negatively affected and start to migrate (if possible) from hypoxic zones, while at anoxia all forms of higher life perish. Of utmost concern for water quality during hypoxic and anoxic conditions are the release of reduced substances (CH_4, NH_4^+, Fe^{2+}, Mn^{2+} or H_2S) from the sediment, which can be poisonous or produce strong odour [*Schwarzenbach et al.*, 2010]. These substances become bound in particulate form as oxygen levels increase and thereby settle into the sediment.

Transport of oxygen to the hypolimnion from the atmosphere and primary producers in the epilimnion is strongly counteracted for most part of the year by the sharp density gradient in the metalimnion. The replenishment of oxygen in the hypolimnion mainly occurs as lakes overturn in winter enabling deep convective mixing to bring oxygen from the surface to deeper layers. The problem of low oxygen content is thus predominant in systems that (i) do not completely overturn each year; and (ii) in systems where primary production is high in the epilimnion and therefore oxygen consumption is substantial in the hypolimnion. Since the problem of eutrophication was first discovered, procedures have been put in place to limit the emission of nutrients into inland waters. The trophic level in many inland aquatic systems has thus improved from eutrophic to less productive mesotrophic or oligotrophic level. However, the positive effect predicted for oxygen have not followed expectations in all systems. Explanations include accumulation of organic matter in the sediment, which during hypoxia/anoxia continues supplying the water column with nutrients [*Müller et al.*, 2012].

1.2.5 Climate change and thermal pollution

The ongoing global warming has increased mean surface air temperature since the beginning of the century by ~0.85 °C (1880 to 2012). Inland waters are identified as risk-hotspots and proven especial sensitive to climate stress [*Pachauri et al.*, 2015]. Yet, thermal and hydrodynamic reactions amongst lakes to climate change varies considerably among global, regional and even local scales (surface water temperature change varies from -0.7 to +1.4 °C decade^{-1} [*O'Reilly et al.*, 2015]). Factors affecting heating include, but are not limited to, morphology, irradiance absorption and stratification [*Kirillin*, 2010; *Toffolon et al.*, 2014; *Piccolroaz et al.*, 2015]. Heating of lakes are generally concentrated to the shallow epilimnion rather than the deep hypolimnion [*Perroud and Goyette*, 2010]. This depth-dependent warming increase the stratification strength and prolongs the stratified period, with negative effects on renewal of deep oxygen content [*Peeters et al.*, 2002; *Golosov et al.*, 2012; *Schwefel et al.*, 2016]. Problems associated with eutrophication are thus likely to increase with climate change.

The increase of air temperature with associated shift in precipitation and flood frequencies [*Pachauri et al.*, 2015] likewise affects rivers. As temperature increase in both atmosphere and river water, the ice and snow melt cycles will shift, with consequently increasing river discharged in winter and opposite response in summer [*Birsan et al.*, 2005; *Isaak et al.*, 2012; *Van Vliet et al.*, 2013; *Addor et al.*, 2014]. This hydrological shift affects erosion rates and suspended sediment content in river waters [*Bennett et al.*, 2013a]. As water temperature and suspended sediment change, river water density will also be modified, affecting depths and occurrence rates of deep river intrusions in downstream lakes. Deep water renewal in lakes is consequently predicted to decrease in summer and increase in winter [*Fink et al.*, 2016; *Råman Vinnå et al.*, 2017b]. The net effects of climate change on re-oxygenation in the hypolimnion due to deep penetrating river intrusions is still under discussion. The introduction of river-borne terrestrial organic material into lakes can enhance mineralization rates of less available organic matter, and thus counteract the positive effects linked to deep-water renewal and riverine oxygen content [*Bouffard and Perga*, 2016].

Climate change warms aquatic systems over decades and centuries. Localized anthropogenic emission/uptake of heat (*thermal pollution*), usually by cooling water emission or hydropeaking, on the other hand can cause rapid local temperature fluctuations. The impact on the system is dependent on the size of the emission/uptake in relationship to the affected volume [*Fink et al.*, 2014b]. Thermal pollution can affect species composition and the metabolism of organism [*Cairns*, 1971; *Koschel et al.*, 2002], a phenomenon which recently

14

has been linked to climate change [*Dijkstra et al.*, 2011]. Depending on local factors such as trophic state and stratification, this can have an impact on the flux/decomposition of organic material and thereby water quality. Of more direct pressing concern, is the similarity between the effects of climate change and thermal pollution on stratification as well as river intrusions and thereby oxygen conditions in the hypolimnion [*Kirillin et al.*, 2013; *Råman Vinnå et al.*, 2017a]. Consequently, when considering water resources for present and future use, managing authorities should consider both global and local phenomena for water quality influences.

1.3 Dissertation context and motivation

This project was born due to a rare turbidity event forcing the Ipsach Drinking Water Plant, the main supplier for the City of Biel in Switzerland, to cease production for the first time since the plant was commissioned in the early 1970s. Early morning (06:00 am) on 31st of December 2009, the turbidity sensor in the raw intake water went off-scale (> 20 FNU) and the sediment filters became clogged. The only notable external forcing at this time was an earlier strong rainfall event in the catchment area of Lake Biel. However, no abnormal discharge nor turbidity levels were detected in the Aare or Schüss rivers which supply Lake Biel with freshwater and sediment. The analysis of the lake water level revealed an oscillating signal with a period of 30 min starting before 04.00 and lasting past 06.00 (Fig. 1.1).

This type of signal is extremely rare, within the spatial and temporal resolution of the instrument (1 mm and 10 min), but still resolvable despite the built-in wave damping. The signal was most likely caused by a small-scale (2 mm) shallow water wave (tsunami). Worth mentioning is that the travel time from the raw water intake in Lake Biel to the turbidity sensor and filters of the plant was ~2 hours for the treatment operation at this time. Thereby it was possible to link the measured surface oscillation directly to the turbidity signal measured inside the plant. Plans to renovate the Ipsach Drinking Water Plant are currently being made, including the possibility of renewing the lake water intake (as further explained in section 1.5).
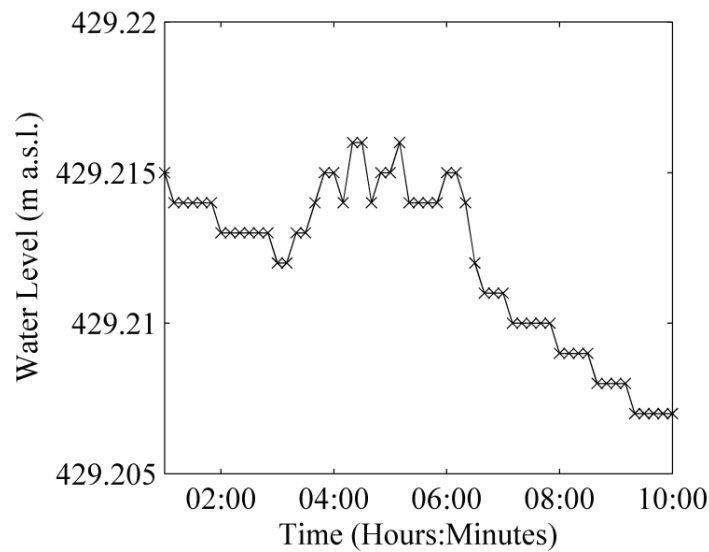
Figure 1.1. Lake Biel water level during the turbidity events at the Ipsach Drinking Water Plant on 31st of December 2009. Data from station Twann (47°5'N 7°9'E), data available at http://www.bafu.admin.ch/umwelt/index.html?lang=en.

1.4 Lake Biel

The perialpine Lake Biel is located 429 m above sea level in the North-Western part of Switzerland (7°10' E, 47°5' N, Fig. 1.2). The lake is boxed in with steep topography by the Jura Mountains to North-West and extensive hills to the South-East. It has a maximum depth of 74 m (mean depth 30 m), a surface area of 39.3 km^2 and a volume of 1.18 km^3. To the North-East, located at a depth of 47 m, is the present raw water intake structure, with the orifice at 38 m depth, for the Ipsach Drinking Water Plant.

Three rivers supply water and sediments (Fig. 1.2). The major tributary (providing ~61 % of the water) as well as the main outflow is the Aare River. This river originates in the Alps and on its way to Lake Biel it passes multiple lakes and dams, which enable the river water to heat up and particles to settle. This river has experienced a ~0.34 °C decade^{-1} water temperature increase, from 1978 to 2002, due to the warming climate [*Hari et al.*, 2006]. Other tributaries include the Schüss (La Suze) which brings water from the Jura Mountains as well as the Zihl Channel which connects Lake Biel to Lake Neuchâtel and thereby acts as both inflow and outflow. The water budget of Lake Biel, including precipitation in the drainage area not included in the tributaries above, are however not in balance. Less water (~2%) enters into the lake than leaves through the Aare outflow. The most likely missing source is groundwater

intrusion. The porous karstic rock north of Lake Biel has been linked to ground water intrusion through giant pockmarks (~100 m in diameter) in the nearby Lake Neuchâtel [*Reusch et al.*, 2015], which locally can affect sedimentation patterns. Smaller-sized pockmarks (~40 m in diameter) have been found close to the central peninsula in Lake Biel [*Dubois et al.*, 2017], suggesting that groundwater intrusions takes place in this lake (details in Appendix).

The Aare River has not always been part of Lake Biel's catchment. This alpine river was redirected into Lake Biel between 1868 and 1891 as part of the extensive First Jura Waters Corrections project, with the goal to limit flooding of the surrounding area and downstream Aare. This drastically changed the annual sedimentation rate in Lake Biel from 0.1 cm year^{-1} to 1.1 cm year^{-1} [*Nast*, 2006; *Jeannet et al.*, 2013; *Thevenon et al.*, 2013; *Dubois et al.*, 2017], the additional volume inflow reduced the hydraulic residence time of the lake from 253 to 58 days [*Liechti*, 1994].
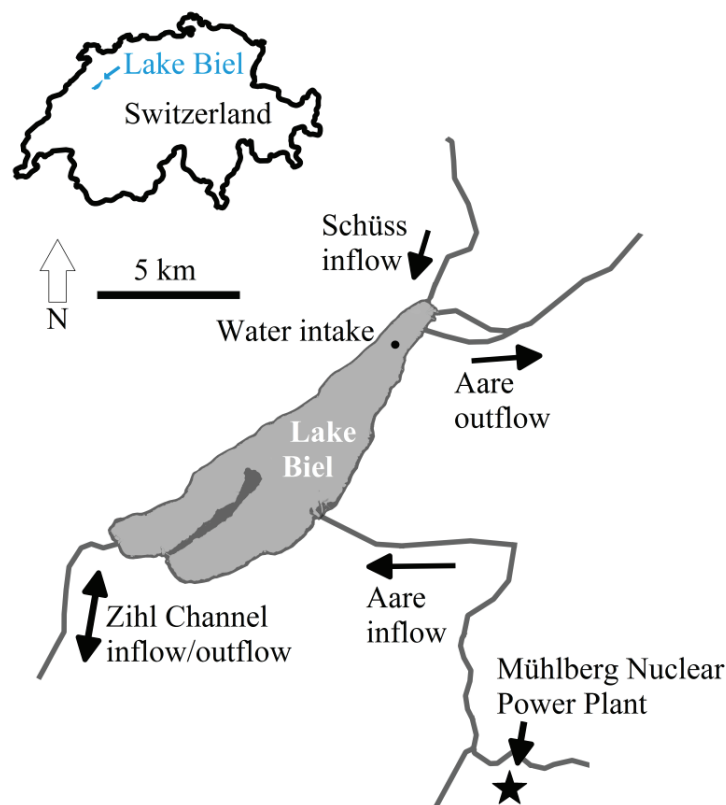
Figure 1.2. Map of Lake Biel (light grey), Aare River in- and outflow, Zihl Channel inflow/outflow, River Schüss inflow, Mühleberg Nuclear Power Plant and the water intake for Ipsach Drinking Water Plant.

Additionally, on the banks of the Aare River, ~19 km upstream from Lake Biel resides the Mühleberg Nuclear Power Plant, from which cooling water with an excess heat of ~700 MW is released into the river [*Meier et al.*, 1997]. The plant has an emission history of releasing radioactive ^{137}Cs into the Aare River which later sediment in the downstream Lake Biel [*Albrecht et al.*, 1998; *Thevenon et al.*, 2013]. The plant approaches the end of its lifetime and is consequently planned for decommission in 2019. Once the cooling water emission is withdrawn from the Aare River, the water temperature in the river will drop, as a consequence the temperature in Lake Biel will be lowered by ~0.3 °C [*Råman Vinnå et al.*, 2017a].

The nutrient load to Lake Biel has decreased since the 1970s when the lake was classified as eutrophic with a high biological productivity. The lake is now considered to be meso- to eutrophic [*Thevenon et al.*, 2013]. Yet, each year oxygen content in the deep layers is reduced to less than 4 mg L^{-1}, bringing large volumes of deep water into hypoxic state. Fortunately, Lake Biel is a warm monomictic lake and thus each winter deep complete convective mixing takes place [*Thevenon et al.*, 2013]. As the water column is homogenized deep water oxygen levels are replenished, hypoxic conditions are thus only problematic between September and December [*Albrecht et al.*, 1999].

The surrounding topography in combination with weather systems over central Europe and the Mediterranean sets up two dominant directions for the wind over Lake Biel. The *Vent* from South-West and the *Bise* from North-East (Fig. 1.3). As for other inland lakes the wind speed over Lake Biel is typically slow (generally < 6 m s^{-1}). However, these slow wind speeds regardless set up either clockwise or counter-clockwise circulation patterns in Lake Biel [*Råman Vinnå et al.*, 2017a]. The circulation patterns in turn determine the progression of intruding river plumes and thereby sedimentation patterns inside the lake [*Wright and Nydegger*, 1980; *Albrecht et al.*, 1999; *Råman Vinnå et al.*, 2017c].
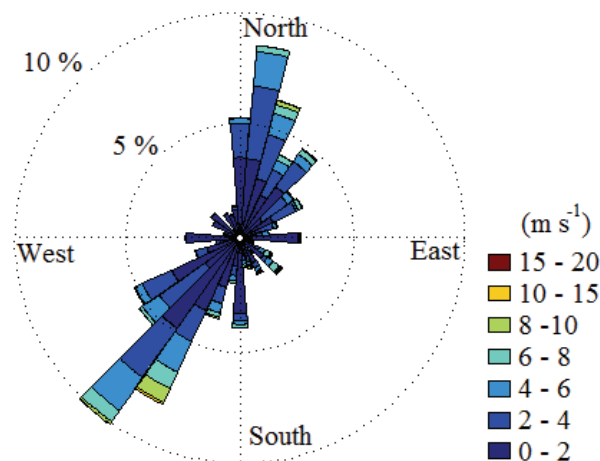
Figure 1.3. Wind rose visualizing the temporal occurrence frequency of wind strength and direction of origin close to Lake Biel from 2013 to 2014, data obtained from the meteorological station at Cressier (47°3'N 7°4'E; 1.4 km South-West of Lake Biel) data available at http://www.meteoswiss.admin.ch/home/services-and-publications/beratung-und-service/data-portal-for-teaching-and-research.html.

The steep topography surrounding Lake Biel continues below the surface of the lake, resulting in a steep sloping bottom topography (up to 30°) around the entirety of the lake. The steepness of the bottom in combination with high localized sediment load, enhances the local risk of submarine mass movements within Lake Biel [*Dubois et al.*, 2017; *Råman Vinnå et al.*, 2017c].

1.5 Research objectives and approaches

The objective of this dissertation is to provide guidance for future raw water extraction in Lake Biel. The goal is thus to answer the following questions;

(i)   What was the reason for the extreme turbidity event observed on December 31, 2009, and can such events reoccur in the future?

(ii)   What kind of changes can be expected as a result of the climatic development and the decommissioning of the upstream Mühleberg Nuclear Power Plant?

(iii)   What is the role of the two tributaries Aare and Schüss for the turbidity in Lake Biel?

(iv)   Which areas of Lake Biel are particularly critical with regard to risks for subaqueous mass movements?

(v)   Where are the ideal areas inside Lake Biel for future water intake of raw water taking into account water quality, particle distribution patterns, the Mühleberg Nuclear Power Plant and effects of a changing climate?

To answer these questions a two years long field campaign was conducted in combination with numerical modelling in one and three spatial dimensions. Temperature conditions, occurrence of particles with resulting sedimentation patterns and bathymetry as well as water velocities were measured continuously at three locations in the lake as well as in the four surrounding rivers. A wide variety of instruments were used including temperature loggers, Acoustic Doppler Current Profilers (ADCPs), optical turbidity sensors, multibeam and LIDAR bathymetric sensors and sediment traps/cores. The results from the measurement campaign was used as forcing and to validate the one-dimensional model SIMSTRAT [*Goudsmit et al.*, 2002] for long-term evaluations, as well as the three-dimensional model Delft3D (http://oss.deltares.nl/web/delft3D) for shorter term detailed investigations.

1.6 Structure of this dissertation

In this section I provide a short summary of each chapter and the current state of publication.

Chapter 2 - used the field measurements of temperature and currents to calibrate and validate both the one- and the three-dimensional models. These are thereafter used to predict changes in Lake Biel due to the upcoming decommission of Mühleberg Nuclear Power Plant in regard to water temperature, stratification and heat fluxes. A comparison between the models distinguish which processes can be resolved in which dimension. Overall changes could be resolved well in one dimension while local changes require three dimensions. The results indicate that point sources of anthropogenic heat can warm Lake Biel comparable to climate change.

This chapter has been published in its entirety in AGU Water Resources Research (and was featured for more than one month on the front page of the journal), cited as: Råman Vinnå, L., A. Wüest, and D. Bouffard, 2017, *Physical effects of thermal pollution in lakes*, *Water Resources Research* **53**(5): 3968–3987, doi: 10.1002/2016WR019686.

Chapter 3 - investigated the impact of climate change on lakes and surrounding rivers. The effects of warming in Lakes Biel and Geneva with the main tributaries Aare and Rhône, were examined using a one-way coupled model scheme. Special emphasis is put on how upcoming changes in river discharge, temperature and suspended sediment concentration affect the

reaction of downstream located lakes to climate warming. The results show that rivers, which are colder than downstream lakes, have a repressive effect on climate-related warming in lakes, inversely proportional to the hydraulic residence time of the system.

This chapter has been submitted in its entirety to Hydrology and Earth System Sciences (HESS) and is under review in HESS Discussions, it is currently cited as: Råman Vinnå, L., Wüest, A., Zappa, M., Fink, G., and Bouffard, D.: *Tributaries affect the thermal response of lakes to climate change, Hydrol. Earth Syst. Sci. Discuss.,* https://doi.org/10.5194/hess-2017-337, in review, 2017.

Chapter 4 - used the field campaign measurements of particles and sediments to visualize sedimentation patterns in Lake Biel. The special sedimentation conditions in this lake, with increased sedimentation localized to a certain geographical area, is linked to local weather patterns over the lake and upstream river catchments. The results clearly show that the majority of supplied sediment is associated with high turbidity events in surrounding tributaries, and thus enter the lake during a limited amount of time. The Jura Waters Corrections projects, performed in order to limit negative effects of floods, is hypothesised to create areas inside Lake Biel with enhanced risk for submarine mass movements.

This chapter is currently under preparation for submission to AGU *Water Resources Research* alternatively to *Sedimentology*.

Synthesis Chapter 5 - used the findings of chapter 2 to 4 and the Appendix as well as historic data to provide guidelines for future raw water extraction from Lake Biel. Water quality, sedimentation, closure of Mühleberg Nuclear Power Plant and future changes are considered.

The core part of this chapter, translated to German, is published in Aqua & Gas **97**(9) cited as: Råman Vinnå L., D. Bouffard, N. Dubois, M. Hilbe, R. Käser und A. Wüest, 2017, *Seewasserentnahme im Bielersee - Gibt es eine ideale Position? Aqua & Gas - Fachzeitschrift für Gas, Wasser und Abwasser* **97**(9): 14 - 20.

Chapter 6 - provides conclusions from all chapters in this dissertation as well as an outlook for future research.

Appendix - investigates the geomorphology of Lake Biel using high resolved multibeam and LIDAR bathymetry measurements in combination with sediment cores. Areas of subaquatic mass movements, ground water intrusion and anthropogenic activities were identified. A very recent singular subaqueous slide event is determined to be the cause behind the major turbidity event on 31st December 2009 causing a four days long production stop at the Ipsach Drinking Water Plant.

This chapter is currently under preparation for submission to *Sedimentology.*

Chapter 2:

Physical effects of thermal pollution in lakes

Love Råman Vinnå[1], Alfred Wüest[1,2], Damien Bouffard[1,2]

[1]Aquatic Systems Laboratory, Margaretha Kamprad Chair, École Polytechnique Fédérale de Lausanne, Institute of Environmental Engineering, Lausanne CH-1015, Switzerland.
[2]Eawag, Swiss Federal Institute of Aquatic Science and Technology, Surface Waters - Research and Management, Kastanienbaum, Switzerland.

Abstract

Anthropogenic heat emissions into inland waters influence water temperature and affect stratification, heat and nutrient fluxes, deep-water renewal and biota. Given the increased thermal stress on these systems by growing cooling demands of riparian/costal infrastructures in combination with climate warming, the question arises on how to best monitor and manage these systems. In this study, we investigate local and system-wide physical effects on the medium-sized perialpine Lake Biel (Switzerland), influenced by point-source cooling-water emission from an upstream nuclear power plant (heat emission ~700 MW, ~18 W m^{-2} lake-wide). We use one-dimensional (SIMSTRAT) and three-dimensional (Delft3D-Flow) hydrodynamic numerical simulations and provide model resolution guidelines for future studies of thermal pollution. The effects on Lake Biel by the emitted excess heat are summarized as: (i) clear seasonal trend in temperature increase, locally up to 3.4 °C and system-wide volume-mean ~0.3 °C, which corresponds to one decade of regional surface water climate warming, (ii) the majority of supplied thermal pollution (~60%) leaves this short residence time (~58 days) system via the main outlet, whereas the remaining heat exits to the atmosphere, (iii) increased length of stratified period due to the stabilizing effects of additional heat, (iv) system-wide effects such as warmer temperature, prolonged stratified period and river-caused epilimnion flushing are resolved by both models whereas local raised temperature and short-circuiting was only identifiable with the three-dimensional model approach. This model-based method provides an ideal tool to assess man-made impacts on lakes and their downstream outflows.

2.1 Introduction

Anthropogenic excess heat, discharged as cooling water from power plants, has been recognized as a form of pollution in lakes, reservoirs and rivers since the middle of the 20th century [*Davidson and Bradshaw*, 1967; *Dracup and Fogabty*, 1974; *Scherer*, 1975]. These emissions of heat, commonly known as "thermal pollution", affects water temperature and therefore water quality and biota. In lakes effects can be seen both locally and on system-wide scales, include mixing regime shifts from dimictic to warm monomictic [*Kirillin et al.*, 2013], modification of nutrient cycling [*Chen et al.*, 2000] or reduction of ice cover [*Dingman et al.*, 1968]. In rivers introduced excess heat can be traced for long distances ($\sim10^2$ to $\sim10^3$ km) downstream from the point of input [*Prats et al.*, 2012]. Physical effects of thermal pollution in lakes and rivers affects the entire aquatic food web from benthic organisms [*Barnett*, 1971] to plankton [*Cairns*, 1971; *Vandysh*, 2009] and fish [*Sylvester*, 1972; *Luksiene et al.*, 2000].

The horizontal dispersion of thermal plumes is mainly driven by wind-induced currents [*He et al.*, 2006; *Choi and Wilkin*, 2007; *Cardoso-Mohedano et al.*, 2015]. Near shore regions close to the emitting source are therefore especially sensitive to thermal pollution since heat plumes can be trapped by coastal currents without being dispersed across the water body [*Raithby et al.*, 1988; *Salgueiro et al.*, 2015].

Future thermal stress on aquatic systems is likely to increase due to intensified use of water bodies as sources and sinks of anthropogenic heat [*Fink et al.,* 2014] as well as due to ongoing climate warming [*Mulhollem et al.*, 2016]. Many water management authorities have enforced three kinds of limitations to heat use: (i) a maximum temperature of water used for cooling, (ii) a maximum temperature increase in the natural waters receiving the thermal effluents, and (iii) a maximum temperature in the receiving waters. The latter condition will restrict the suitability of various waters as heat recipient under the perspective of climate change, due to the expected increase of water temperature as well as changes in discharge/rain patterns [*Van Vliet et al.*, 2012; *Quijano et al.*, 2016]. Hence, it is of utmost importance to thoroughly assess how aquatic systems are affected by thermal pollution in order to improve management and mitigate harmful effects on water quality and biota. Previous studies have mainly focused on large lakes where system-wide effects are limited [*Reutter and Herdendorf*, 1976] or on small lakes with severe implications to the ecosystem [*Koschel et al.*, 2002].

Inland waters are often a complex web of rivers, streams, lakes and reservoirs. In such systems, studies of thermal pollution should include inter/intra system transport of heat to

comprehensively assess the spatial extent of negative effects. In the present study we investigate the impact of thermal pollution emitted from a nuclear power plant into a medium-sized lake with short hydraulic residence time. We focus on the influence of thermal pollution on water temperature and the subsequent effects on stratification and heat fluxes in the lake as well as the change of temperature in the downstream outflow. The physical processes responsible for flushing heat out of the lake ultimately determine how extensive the effects are in the lake versus at the outflow.

Prats et al. [2012] highlighted the importance of using sufficient spatial model resolution in order to correctly assess the downstream development of thermal pollution in rivers. We build on this work to further examine the capabilities of different spatial model resolutions, in one (1D) and three (3D) dimensions, to follow the propagation of thermal pollution across the lake towards the main outflow. Our goal is to provide guidelines specifying which of these modelling strategies are appropriate for reconstructing the effects of thermal pollution. We furthermore compare the importance of thermal pollution to the ongoing climate change. This analysis is based on the thermal response of Lake Biel (LB) to the future planned decommission of the Mühleberg Nuclear Power Plant (MNPP), located upstream alongside the Aare River.

2.2 Methods

2.2.1 Site Description and Thermal Pollution

LB is a meso-eutrophic warm monomictic perialpine lake located in the north-western part of Switzerland (7°10' E, 47°5' N, Fig. 2.1) at 429 m above sea level. It has a maximum depth of 74 m (mean depth 30 m), surface area of 39.3 km^2 and a volume of 1.18 km^3. Three tributaries enter the lake (Table 2.1). The Aare River, originating in the Alps, is both the main inflow (station 2085) and the only outflow (station 2029). It was redirected into LB during the Jura Correction in 1878 effectively reducing the average hydraulic residence time in LB from 253 to 58 days [*Liechti*, 1994]. Other tributaries include the Schüss (station 2307), originating in the Jura Mountains, and the Zihlkanal (station 2446) connecting LB to Lake Neuchâtel (Fig. 2.1a).
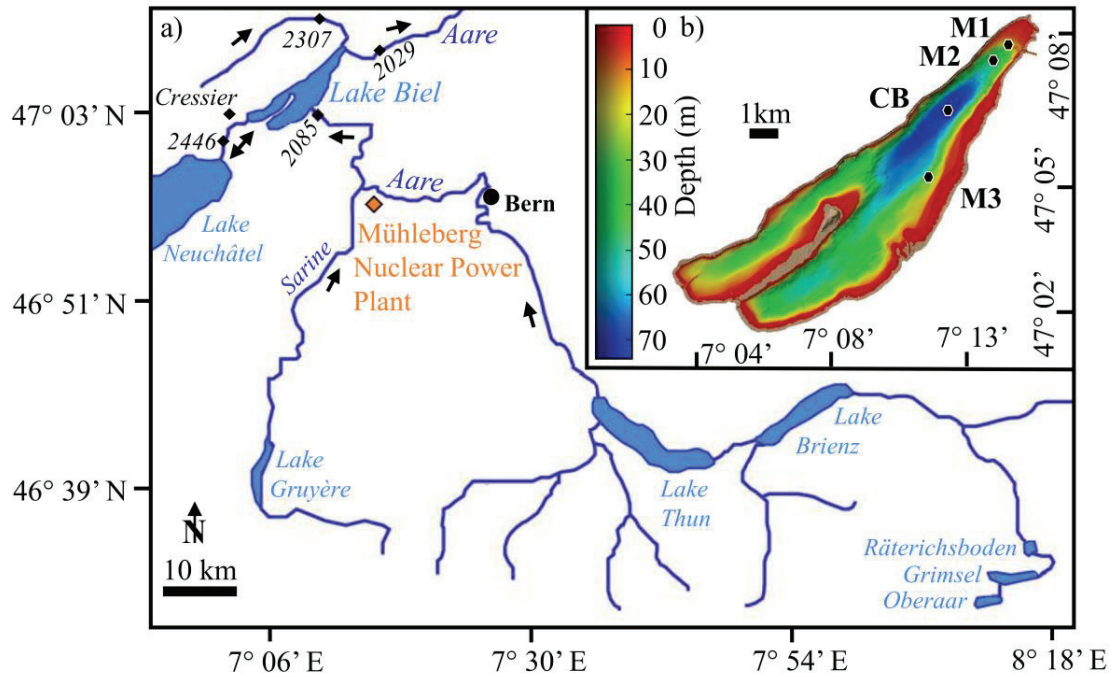
Figure 2.1. Area of investigation: (a) Lake Biel (LB) with watershed and monitoring stations (black diamonds), arrows indicate river flow direction (map modified from *Thevenon et al.* [2013]), (b) LB Multibeam/LIDAR bathymetry [*Hilbe* 2015] with locations for field sampling points (M1, M2, M3, CB).

Table 2.1. River Stations

Station Name (ID number)[a]	Drainage area (km^2)	Discharge (m^3 s^{-1})[b]	Station Feature
Hagneck (2085)	5104	175	Aare main inflow
Zihlkanal (2446)	2672	55	In- and outflow[c]
Schüss (2307)	150	5	Inflow
Aegerten (2029)	8293	240	Aare outflow

[a] Location indicated in Fig. 2.1a.

[b] Yearly mean from 1985 to 2014.

[c] In 3D model depending on the water level of LB relative to other tributaries/outflow.

MNPP is situated on the banks of the Aare River (7°16' E, 46°59' N, Fig. 2.1a) ~19 km upstream of LB. The plant, with a net electricity production of 373 MW, was commissioned in 1972 and is planned for decommission in 2019 (http://www.bkw.ch/ueber-bkw/unsere-infrastruktur/kernkraftwerk-muehleberg/#c1925). The plant discharges cooling water with an excess heat of ~700 MW (Fig. 2.2a) into the Aare River [*Meier et al.*, 1997] corresponding to ~18 W m^{-2} for LB. This emission has been shown to increase the temperature at station 2085 by ~2.4 °C in January and ~0.7 °C in June [*Hanafiah*, 2013]. In order to investigate the effect on LB by the upcoming plant decommission we calculate the change in river temperature ΔT_R (Fig. 2.2b and 2.2c) at station 2085 due to the removal of the heat supplied by MNPP. The discharge-dependent (Fig. 2.2d) loss of heat to the atmosphere between the point of cooling water input and LB is calculated as described in Supporting Information 2.S1. The grey area in Fig. 2.2 (and in subsequent Figures) marks the time when MNPP undergoes routine maintenance, during which only a small amount of standby-cooling is emitted. Upstream of LB, the Aare River and its tributary Sarine (responsible for much of the temperature and discharge variability at station 2085) are influenced extensively by hydropower electricity production (closest facility ~400 m upstream from LB). This anthropogenic river discharge control (Fig. 2.2d) causes thermo-peaking events with daily temperature fluctuations of ~2 °C (Figs. 2.2b and 2.2c).

2.2.2 Model Descriptions

2.2.2.1 One-Dimensional Model

We applied the 1D SIMSTRAT model, which is described in detail by *Goudsmit et al.* [2002]. The model is used to quantify the long-term impact of MNPP on LB as well as to investigate which system-wide thermal pollution effects can be resolved in 1D. It simulates the heat fluxes across the air-water interface and the kinetic energy uptake and dissipation using a k-ε turbulence closure scheme. It has previously been adapted and validated for multiple lakes including Lake Zürich [*Peeters et al.*, 2002], Lake Geneva [*Perroud and Goyette*, 2010; *Schwefel et al.*, 2016] and Lake Constance [*Fink et al.*, 2014b; *Wahl and Peeters*, 2014]. The hydraulic residence times for these lakes are in the order of a few years – compared to two months for LB – and river inflows are usually neglected.
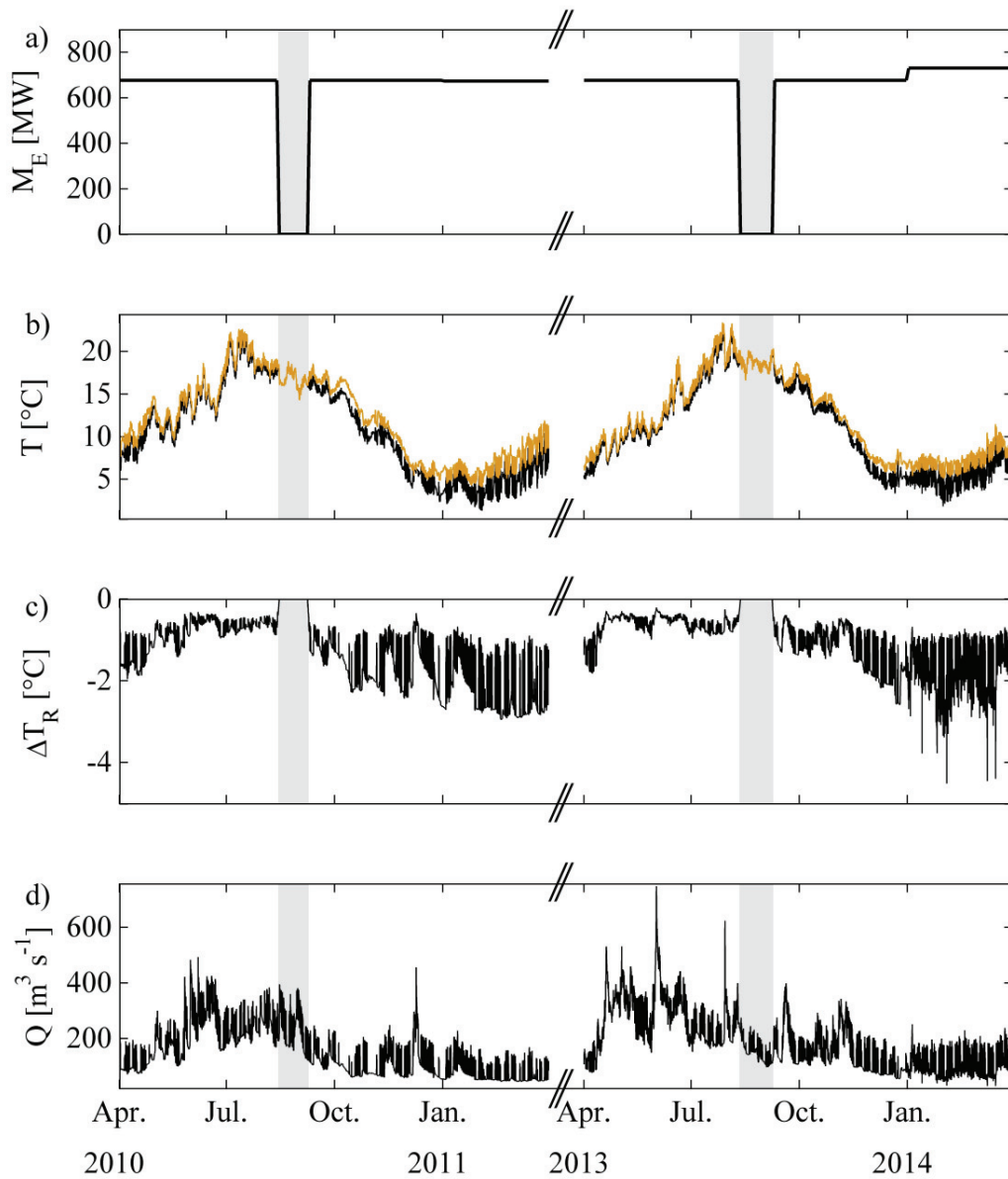
Figure 2.2. Aare River data for the cold (2010/2011) and warm period (2013/2014): (a) Thermal pollution heat input to Aare by MNPP, the rapid change on 1st January 2014 is an artifact due to annual-averaged data, (b) temperature T at station 2085 (Fig. 2.1) with (orange) and without (black) thermal pollution, (c) resulting temperature change ΔT_R due to removal of thermal pollution and (d) Aare River flow Q into LB. Grey bars denotes periods of MNPP maintenance, when no heat is emitted into the Aare River.

In this work, we included the influence of the surrounding watershed on LB by adding a simple (without entrainment) river intrusion scheme to SIMSTRAT which provides a lower limit of the river intrusion depth by locating the level of equal density between river and lake water. Due to model limitations the volume leaving the lake was set equal to the volume entering the lake. The intrusion scheme was applied to the three rivers entering into LB given in Table 2.1 (Fig. 2.1a). Following *Schwefel et al.* [2016] we seasonally varied the parameter α for kinetic energy transfer from wind to basin-scale internal waves: α_S for the summer (April to September) and α_W for winter (October to March), with $\alpha_S > \alpha_W$ (see Section 2.2.4 below).

2.2.2.2 Three-Dimensional Model

To investigate local effects of MNPP on LB, we used the 3D open source hydrodynamic model Delft3D-Flow version 4.001 (http://oss.deltares.nl/web/delft3D). The model has successfully been applied to simulate circulation patterns, water quality and climate impact in multiple Lake systems [*Zhu et al.*, 2009; *Razmi et al.*, 2013; *Wahl and Peeters*, 2014]. From the different options of turbulence closure schemes, we use the k-ε method as implemented in the 1D model. We apply the *Horizontal Large Eddy Simulation* for sub-grid processes and the *Ocean Heat Flux Model* [*Gill*, 1982; *Lane*, 1989] for heat transfer across the lake surface.

Rivers are entering the model domain through open boundaries. Propagation of river plumes was modeled by the advection-diffusion equation used for system-wide water movements. The intrusion of the Aare River into LB was tracked by a decaying tracer (half lifetime 7.0 days). The tracer decay and the fact that the pathway of the river water in LB is not constant in time and space enables us to monitor the temporally varying maximum intrusion depth of the river plume.

2.2.3 Data

Both models required air temperature, vapor pressure, wind speed/direction, solar radiation and cloud cover as atmospheric forcing. Here we used two different meteorological forcing datasets. One weather station-based data set (available since 1989) for long-term 1D simulations and one weather model-based data set (available since 2008) for short-term 3D simulations.

Hourly resolved atmospheric forcing data for 1D was obtained from multiple weather stations surrounding LB. These were Cressier (Fig. 2.1a, 7° 03' E, 47° 03' N), Grenchen (7° 25' E, 47° 11' N), Biel (7° 15' E, 47° 07' N), Neuchâtel (6° 57' E, 47° 00' N) and Chasseral (7° 03' E, 47° 08' N). Cressier was our main station in regard to air temperature, solar radiation, wind and vapor pressure. As cloud cover was not available at Cressier we used Biel as our main station for this parameter. Data gaps at the main stations given above were filled with data from the closest available station. Replacement data was scaled in order to match the variable specific amplitude of daily fluctuations observed at the main stations. The amount and origin of added data is indicated in Table 2.2.

Table 2.2. Percentage of Replaced Atmospheric Forcing Data at Main Station

Main Station	Cressier				Biel
Replacement Data Station	Air Temperature	Solar Radiation	Wind	Vapor Pressure	Cloud Cover
Grenchen	1.1	0	0.7	0	0
Neuchâtel	0.1	79.6	0	0	14.4
Chasseral	0	0	0	49.4	0

To correctly include spatial variability in 3D we used hourly resolved atmospheric forcing data from the highly resolved (2.2 x 2.2 km^2) meteorological COSMO-2 model (http://www.cosmo-model.org). This model has been validated for the region surrounding LB [*Hug et al.*, 2010; *Weusthoff et al.*, 2010]. Here we compare the two forcing datasets in regard to air temperature and wind speed at Cressier station from May 2013 to April 2014. The COSMO-2 model and observations match excellently in regard to air temperature with a root-mean-square-deviation (*RMSD*) of 0.02 °C. Wind speed deviation between the two datasets are still reasonably small with a *RMSD* of 0.40 m s^{-1}.

River forcing data was obtained from the stations given in Table 2.1, with positions indicated in Fig. 2.1a. Measured inflows (including rain) very closely match (by 96 %) the measured outflow for the period 2010 to 2014. Ground water intrusions, as well as discharge measurement errors (~1 % range), could explain the 4 % mismatch. Although ground water intrusions at pockmarks have indeed been reported in the nearby Lake Neuchâtel (Fig. 2.1) [*Reusch et al.*, 2015]. This lake is surrounded by similar bedrock as LB. However, the small

number of minor pockmarks observed in LB [*Hilbe*, 2015] do not indicate relevant groundwater inflows. Nevertheless, to obtain a water budget in balance for the 3D model we adjusted the discharge at station 2446 (mean volume change < 1%) by scaling the discharge to keep the modelled water level in line with observations at Ligerz (7° 09' E, 47° 06' N). No adjustment is made to the 1D forcing since the model version used here lacks adequate representation of water level fluctuations. Furthermore, in the 3D model the Aare outflow from LB is directed through two channels, Zihl and Nidau. Measurements at station 2029 were conducted ~4 km downstream from LB (Fig. 2.1). At this point the two channels have converged. Therefore, based on the channels cross-section area relationship we assume that 10% of the outflowing volume leaves the lake through Zihl and 90% through Nidau.

For 1D model hypsometry and 3D model bathymetry we used the Swisstopo digital height model DHM25 (https://shop.swisstopo.admin.ch/en/products/height_models/dhm25). Furthermore, the 1D model requires Secchi depth (measured on a monthly basis at CB station) while this parameter is provided as a constant in the 3D model.

Initial conditions for both models were based on monthly temperature (accuracy: 0.002 °C) profiles from station CB (Fig. 2.1). These profiles were furthermore used for 1D model evaluation and inter-model performance comparison. For evaluation of the 3D model we performed a 2.4-year long field campaign (May 2013 to September 2015) using three moorings M1, M2 and M3 (Fig. 2.1b). Temperature measurements were obtained with two types of loggers, Vemco Minilog II-T (accuracy 0.1 °C, response time 2 min) and Richard Brancker Research TR-1060 (accuracy 0.002 °C, response time 4 s). Current measurements were conducted with Teledyne RD Instruments Workhorse Sentinel Acoustic Doppler Current Profilers (ADCPs) in the 300, 600 and 1200 kHz frequency range (accuracy 0.3% to 0.5% of water velocity). The ADCPs were moored on the bottom facing upwards within a distance of 50 m from the temperature moorings. Due to LBs variable water level the depth of the temperature loggers had to be adjusted. For this purpose we used high resolved RBR temperature and pressure sensors. One RBRduo T.D (temperature and depth, accuracy 0.002 °C and 0.05% of pressure range) sensor at M1 and one RBRconcerto T.D.Fl.Tu (temperature, depth, fluorescence and turbidity, accuracy 0.002 °C and 0.05% of pressure range) at M2. Instrumentation setup details are shown in Supporting Information Table 2.S1.

2.2.4 Model Setup, Calibration, Validation and Sensitivity

Calibration and validation was performed by minimizing *RMSD* between temperature measurements at station CB for both models and stations M1, M2 and M3 for 3D (Fig. 2.1b). Using the Fourier Norm (*FN*) we furthermore calibrated/validated the 3D model towards measurements of current speed and direction at M1, M2 and M3. We follow the method described in *Paturi et al.* [2015] and define *FN* as:

$$FN = \sqrt{\frac{1}{n}\sum_n |\mathbf{M} - \mathbf{R}|^2} \Big/ \sqrt{\frac{1}{n}\sum_n |\mathbf{R}|^2} \tag{2.1}$$

Where $\mathbf{M}$ represents model current vector, $\mathbf{R}$ is measured current vector and n is the number of samples. A good model is considered to have a *FN* ratio between 0 and 1.

The ability of the models to reproduce temperature in the epilimnion, metalimnion and hypolimnion is demonstrated in Fig. 2.3. The water column stability $N^2 = -(g/\rho)\,d\rho/dz$, where $g = 9.81$ m s^{-2} is gravity, ρ density of water and N Brunt-Väisälä frequency, was used to determine the extent of the epilimnion, metalimnion and hypolimnion. During stratified conditions ($N^2 > 2 \times 10^{-4}$ s^{-2}) we defined the metalimnion as the region containing N^2 values greater than 0.4 times the temporally-varying maximal observed N^2. The epilimnion and hypolimnion is consequently the water body above and below the metalimnion.

Suspended particles contribute to the density of water and influence the river intrusion depth [*Fink et al.*, 2016]. For the Aare River, which flows through several upstream sediment-trapping dams and lakes, high suspended particles concentration is only a concern at the onset of high discharge events mostly related to flash-rainfalls occurring in summer. At this time of year the effect of MNPP on LB is at its lowest (Section 2.2.3). We therefore regard suspended particles as outside the scope of this study and omit their impact on river intrusion depth. The impact of salinity on river intrusion depth was tested for both models but was not implemented due to its negligible role (< 2 m during 90 % of the time).
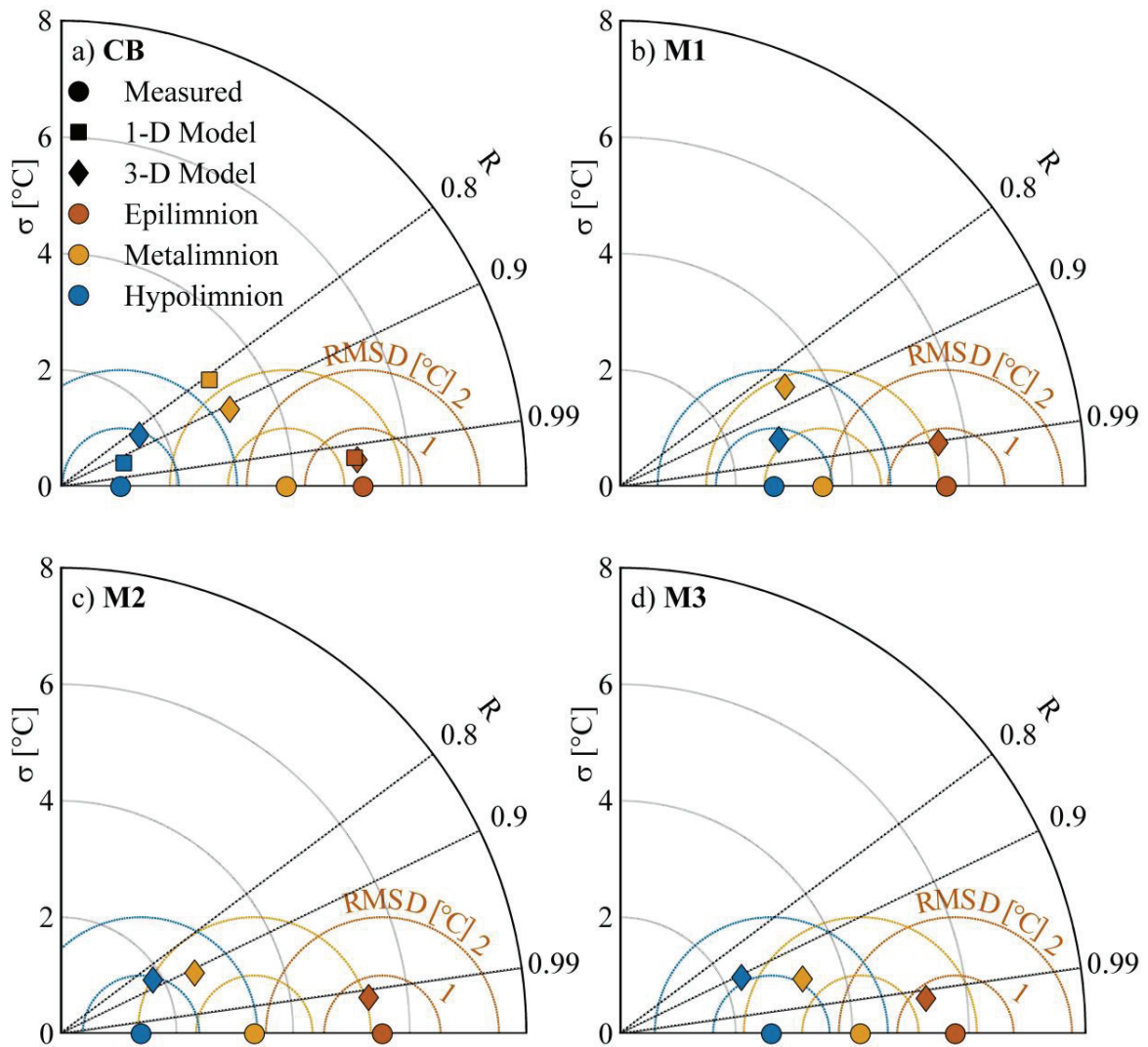
Figure 2.3. Taylor diagram for model performance showing the part of root-mean-square-difference *RMSD* that is attributable to variance or pattern correlation [*Taylor*, 2001]. The radial distance from origo specify the standard deviation σ. *RMSD* is the radial separation from measurement to model values. The Pearson product-moment correlation coefficient R is given by the azimuthal position. 1D (square) and 3D (diamond) models compared to temperature measurements (circle) at station CB (a), M1 (b), M2 (c) and M3 (d) from May 2013 to April 2014. Evaluation was performed in the epilimnion (red), metalimnion (orange) and hypolimnion (blue).

2.2.4.1 One-Dimensional Model

Tunable model parameters for the heat flux includes p_1, p_2 and K. While kinetic energy was tuned by the seasonal varying α_S / α_W, the empirical parameter q, the wind drag coefficient C_{10} and the bottom friction coefficient C_{Bot}. The calibration was preformed using a $6^{7\text{-}3}$ fractional factorial design setup (total 1296 runs; 7 is the number of variables and 3 is the number of generators) in order to incorporate the intra parameter dependency. The model time step was varied from 1 h to 5 min. We found that a time step of 10 min was sufficient to resolve the vertical temperature structure. No significant improvement was achieved past this point. A similar sensitivity analysis was conducted for the spatial resolution. The vertical model resolution was varied from 1 m to 10 cm. We found that no significant improvement occurred past 25 cm (*RMSD* improvement < 0.1 °C), which we used for the vertical resolution. A model spin-up period of one year (1994 to 1995) was adopted in order to remove any transient effects caused by initial conditions.

The impact of different forcing data sets as well as the effect of the intruding rivers were investigated by performing the calibration of the model four times. Three times with river intrusion active in combination with atmospheric forcing from weather stations (long-term 1995 - 2004 and short-term 2008 - 2015) as well as with COSMO-2 model data (2008 - 2015). The fourth time we turned off the river intrusion and used weather station data from 1995 - 2004. The results are shown in Table 2.3 and justify both the use of the river intrusion scheme as well the use of meteorological forcing data from weather stations surrounding LB rather than COSMO-2. The best fit parameter setup (Table 2.4) was obtained with weather station forcing data from 1995 - 2004 and river intrusion scheme active. The setup was validated from 2005 - 2014 (Table 2.3). As seen in Fig. 2.3a, model performance is equally good (*RMSD* between 0.4 to 1.1 °C) in both the epilimnion and the hypolimnion. The deviations are as expected largest in the metalimnion since baroclinic (vertical) movements are intrinsically unresolved in the 1D model.

Table 2.3. Model Performance and Best Fit Shown by Bold Numbers

Station	1D Model *CB*	3D Model *CB*	*M1*	*M2*	*M3*
Depth (m)	74	74	20	47	30
Calibration					
Cressier Wind Forcing					
RMSD (°C)	**0.73**[a] / 0.67[c]	1.35[b]	1.8[b]	1.25[b]	1.35[b]
FN (-)			0.92[b]	0.88[b]	0.96[b]
COSMO-2 Wind Forcing					
RMSD (°C)	0.88[c]	**1.03**[b]	**1.06**[b]	**0.98**[b]	**1.05**[b]
FN (-)			**0.91**[b]	**0.88**[b]	**0.99**[b]
Without River Intrusion					
RMSD (°C)	0.96[a]	1.14[b]	1.59[b]	1.18[b]	1.55[b]
FN (-)			1.08[b]	1.00[b]	1.01[b]
Validation					
RMSD (°C)	**0.68**[d]	**0.86**[e]	1.17[e]	1.31[e]	1.09[e]
FN (-)			**1.07**[e]	**0.99**[e]	**1.03**[e]

[a] January 1995 to December 2004.

[b] May 2013 to April 2014.

[c] January 2008 to December 2015.

[d] January 2005 to December 2015.

[e] May 2014 to April 2015.

Table 2.4. Tunable Model Parameters[a] Used in Present Simulations

1D Model							
p_1	p_2	K	q	C_{Bot}	C_{10}	α_S	α_W
1.30	1.20	0.70	1.30	5.0×10^{-3}	1.60×10^{-3}	6.0×10^{-3}	4.0×10^{-3}

3D Model									
W_{10}[b]	C_{10}	v_H[c]	v_V[c]	D_H[c]	D_V[c]	z_{Sec}[d]	k_S	c_H	c_e
0.008	1.60×10^{-2}	1.0	1.0×10^{-3}	1.0	5.0×10^{-6}	3.00	3.0×10^{-2}	5.0×10^{-3}	2.0×10^{-3}
4.00	1.18×10^{-3}								
50.00	4.10×10^{-3}								

[a] All 1D model parameters as well as C_{10}, k_S, c_H and c_e are non-dimensional.

[b] Wind speed references (m s^{-1}) at 10 m height for identifying C_{10}.

[c] Units: m^2 s^{-1}.

[d] Unit: m.

2.2.4.2 Three-Dimensional Model

In the horizontal direction we adapted a curvilinear grid enclosed by the LB shoreline. We evaluated several different horizontal resolutions ranging from 500 to 25 m sized cells, where 200 to 50 m proved to be optimal. Grid refinement past this point did not improve model results substantially (*RMSD* improvement at M2 < 0.1 °C). A vertical bottom boundary-fitted Sigma coordinate grid was tried but produced unacceptable artificial mixing due to the steep bathymetry of the lake. This is in accordance with previous observations made by *Stelling and Van Kester* [1994]. A Cartesian coordinate (Z-layer) grid was therefore adapted in order to minimize numerical mixing. We evaluated vertical resolutions with grid cell sizes between 0.2 to 5 m. Best results was obtained with a vertical resolution ranging from 0.2 to 1.5 m. In order to obtain ideal conditions for heat transfer and to incorporate the annual water level fluctuations of ~1 m we kept the topmost meter in the model domain at a constant vertical resolution of 0.2 m. Below the vertical grid was exponentially increased up to 1.5 m at the deepest point, resulting in a total of 100 vertical spaced layers. To maintain developed flows as the rivers enter LB we extended the grid into the surrounding tributaries (~200 m), while keeping the river cross-sectional area in line with river mouth bathymetry. Final resolution settings in the horizontal and the vertical direction resulted in a total of 115,778 grid cells. Multiple different model time steps were tried ranging from 10 min to 10 s, where 30 s proved to be optimal.

Tunable model parameters (Table 2.4) include the minimum background level for the horizontal eddy viscosity v_H, eddy diffusivity D_H, vertical eddy viscosity v_V and diffusivity D_V as well as the Secchi depth z_{Sec}, Stanton number c_H, Dalton number c_e and wind speed-dependent wind drag coefficient C_{10} (required at three different wind speeds in the model). For bottom roughness we apply a horizontal uniform White-Colebrook formulation with the tunable Nikuradse roughness length parameter k_S. C_{10} is dependent on both wave development and wind velocity [*Jones and Toba*, 2008]. Given the weak winds over LB (mean 2.5 m s⁻¹ at Cressier in 2013) with the expected difference in surface roughness from the ocean, we follow *Wüest and Lorke* [2003] for C_{10}. For wind speeds < 4 m s⁻¹ we apply:

$$C_{10} = 0.0044 \, W_{10}^{-1.15} \tag{2.2}$$

and for wind speed exceeding 4 m s⁻¹ we use:

$$C_{10} = \left[k^{-1} \ln\left(\frac{10g}{C_{10}W_{10}^2} \right) + K \right]^{-2} \tag{2.3}$$

Where $k = 0.41$ (von Kármán's constant), $K = 11.3$ [*Yelland and Taylor*, 1996] and W_{10} is the wind speed at 10 m above the surface. Equations (2.2) and (2.3) were used as a base level for optimization of C_{10} during the calibration process.

3D model calibration (May 2013 to April 2014) was performed by varying the above mentioned parameters within reasonable limits (Table 2.3). Through the calibration process we found that model performance in regard to temperature could be improved by utilizing spatially-varying atmospheric forcing from the highly resolved meteorological COSMO-2 weather model (Table 2.3). Minor changes in performance regarding modelled current speed/direction was also achieved. However, the difference in wind speed between modeled (COSMO-2) and observed wind (compared here at Cressier in Fig. 2.4a) still leads to differences between measured and modeled currents (Figs. 2.4b and 2.4c) with occasionally slower (example 23rd to 27th June) or faster (example 2nd July) modeled surface currents. Nevertheless, the use of space-varying atmospheric forcing still resulted in a better representation of lake conditions (Table 2.3). We therefore forced the 3D model with COSMO-2 model-based data instead of weather station-based data. In total 86 calibration runs were performed resulting in the best parameter set in Table 2.4 which was validated from May 2014 to April 2015 (Table 2.3).

The best 3D model parameterization is a trade-off between satisfactory fits with temperature and currents. In such conditions, the model slightly overestimates vertical mixing which result in a slightly larger model error in the hypolimnion compared to the epilimnion at all stations (Fig. 2.3). Performance does not vary significantly between the four stations indicating that the model correctly reproduces spatial and temporal temperature fluctuations. The 3D model resolves vertical pycnocline movements and consequently perform better in the metalimnion compared to the 1D model (Fig. 2.3a, orange) as illustrated in Figs. 2.4d to 2.4f. The current velocity is satisfactorily reproduced by the 3D model as illustrated for the mixed layer (0 to 10 m) at station M2 in Figs. 2.4g and 2.4h.

As part of the model sensitivity analysis, the impact of rivers entering and exiting LB was analyzed by running the model without river intrusion while using the best parameter setup. This resulted in drastically decreased model performance in regard to both temperature and current compared to the case with river intrusion active (Table 2.3). This, in combination with similar findings made for the 1D model (Section 2.4.1), highlights the importance of the surrounding watershed for the hydrodynamics of LB.
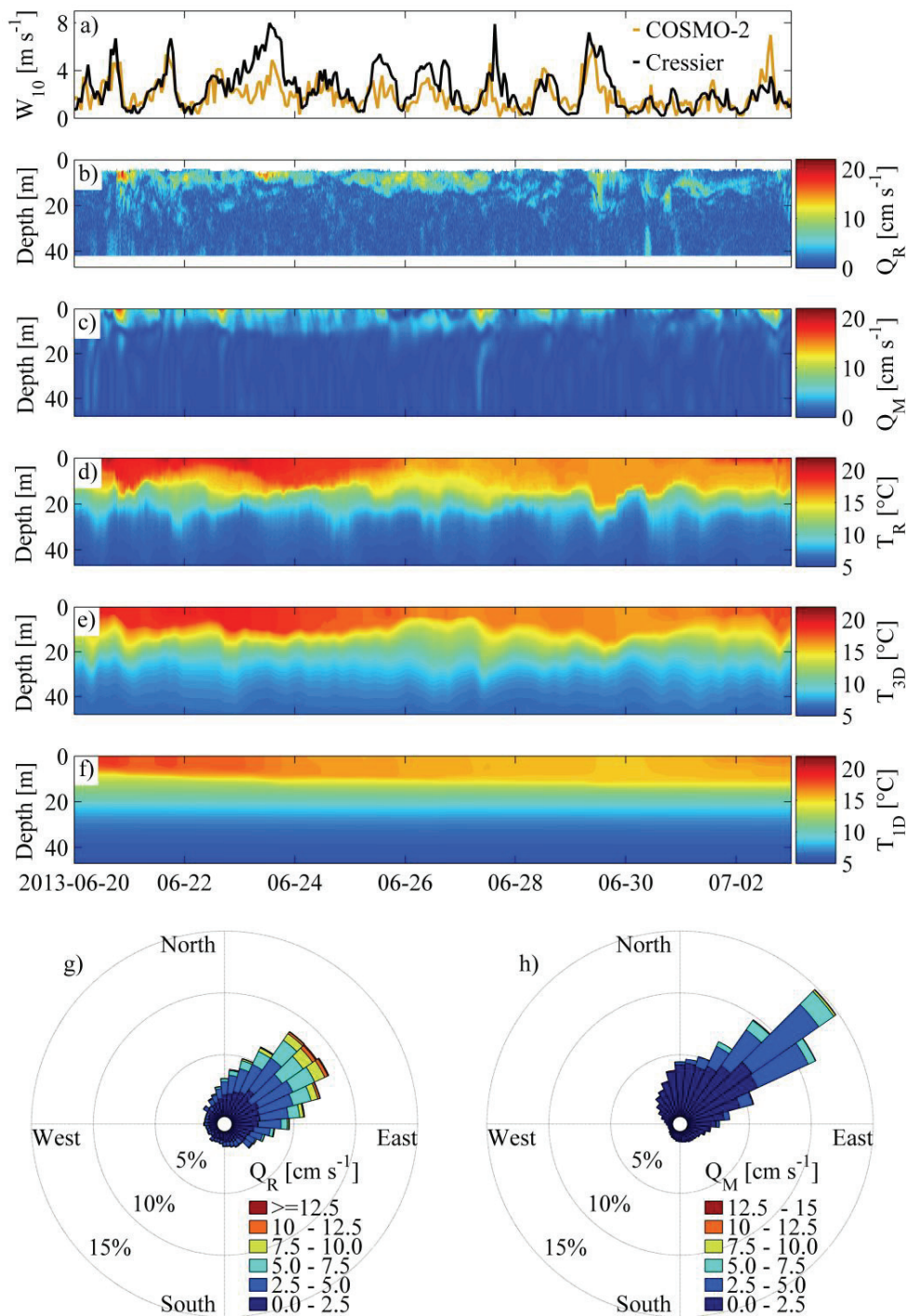
Figure 2.4. Modeled and measured wind, current and temperature. Wind 10 m above surface W_{10} (a) measurements (black) at Cressier (Fig. 2.1a) compared to the weather forecasting model COSMO-2 (orange). Temporal model performance at station M2 (Fig. 2.1b) for current speeds measured Q_R (b) and modeled Q_M in 3D (c) as well as temperature measured T_R (d), temperature modeled in 3D T_{3D} (e) and 1D T_{1D} (f). Percentage of occurrences for current velocities and direction (May 2013 to April 2014) between 0 and 10 m depth for measurements Q_R (g) and 3D model Q_M (h).

2.2.5 Model Scenario Classification

The impact of the upcoming decommission of MNPP on LB was investigated using eight model scenarios: four reference scenarios and four scenarios with modified river temperature. The scenarios are summarized in Table 2.5. Effects on LB were assessed in both 1D (1D-X-X) and 3D (3D-X-X). To accurately represent the range of different seasonal patterns that can be expected in LB we run the models during two twelve months periods (April to March). The periods were chosen to include a cooler and a warmer winter (October to March). April 2010 to March 2011 (X-2010-X) will be referred to as the "cold period". For this scenario the median and minimum winter air temperature at Cressier station (Fig. 2.1a) was 4.4 and -6.9 °C, respectively. The period April 2013 to March 2014 (X-2013-X) will be called the "warm period" with a median and minimum winter temperature at Cressier of 6.1 and -1.0 °C, respectively. For the reference scenarios (X-X-In) containing thermal pollution, we used the unmodified Aare River temperature measured at station 2085 (Fig. 2.2b). This is compared to the modified scenarios (X-X-Ex) where the MNPP heat release has been removed from the Aare River (Figs. 2.2b and 2.2c). This heat removal is explained in Supporting Information 2.S1. As an example, scenario 3D-2013-Ex represent the three dimensional model run from April 2013 to March 2014 without MNPP thermal pollution.

Table 2.5. Model Scenarios

Period	1D Model[a]	3D Model[b]	Thermal Pollution
April 2010 to March 2011[c]	1D-2010-In	3D-2010-In	included
April 2010 to March 2011[c]	1D-2010-Ex	3D-2010-Ex	excluded
April 2013 to March 2014[d]	1D-2013-In	3D-2013-In	included
April 2013 to March 2014[d]	1D-2013-Ex	3D-2013-Ex	excluded

[a] One-dimensional (1D) model.

[b] Three-dimensional (3D) model.

[c] cold (2010) period with (In) and without (Ex) thermal pollution.

[d] warm (2013) period with (In) and without (Ex) thermal pollution.

The impact of the upcoming decommission of MNPP on temperature, stratification and heat fluxes in LB is hereafter referred to as the change Δ in the respective variable. Δ was calculated by taking the change in the variable from scenarios including thermal pollution (X-X-In) to scenarios where thermal pollution has been removed (X-X-Ex), i.e. variable in X-X-Ex – variable in X-X-In. Long-term inter-annual variability of our results was tested using the 1D model (April 1995 to March 2014) with and without thermal pollution.

2.3 Results

2.3.1 Water Temperature

The removal of the thermal pollution supplied to LB by the MNPP results in significant changes in lake temperature ΔT. Interestingly, ΔT varies both spatially and temporally as shown in Fig. 2.5 and Table 2.6. The seasonal dependence is mainly driven by the magnitude of river volume (Fig. 2.2d) available for dilution of the thermal pollution (Supporting Information Equation 2.S3). The 1D and the 3D models both show a temperature decrease in the epilimnion throughout the year, while the hypolimnion is comparatively isolated from the Aare inflow during the stratified period. Consequently, the effects on ΔT in deeper layers is mostly observed during winter. The seasonal impact of MNPP on LB is summarized in Fig. 2.6, where the contributions to ΔT are scaled with volume, such that the histogram mean correspond to the volume-average. Fig. 2.6 furthermore demonstrates that the overall effect of thermal pollution is reproduced similarly by both models. However, as shown in Table 2.6, the range of extreme ΔT fluctuations are locally more pronounced in 3D (ΔT up to -3.4 °C) compared to 1D (ΔT up to -1.7 °C). On a system-wide and temporal scale the warm period (2013) is more affected than the cold period. However, during the cold period (2010) we observed the strongest local impacts. The seasonality of the impact is furthermore apparent in our long-term (1995 to 2014) 1D simulation (see Supporting Information Table 2.S2).
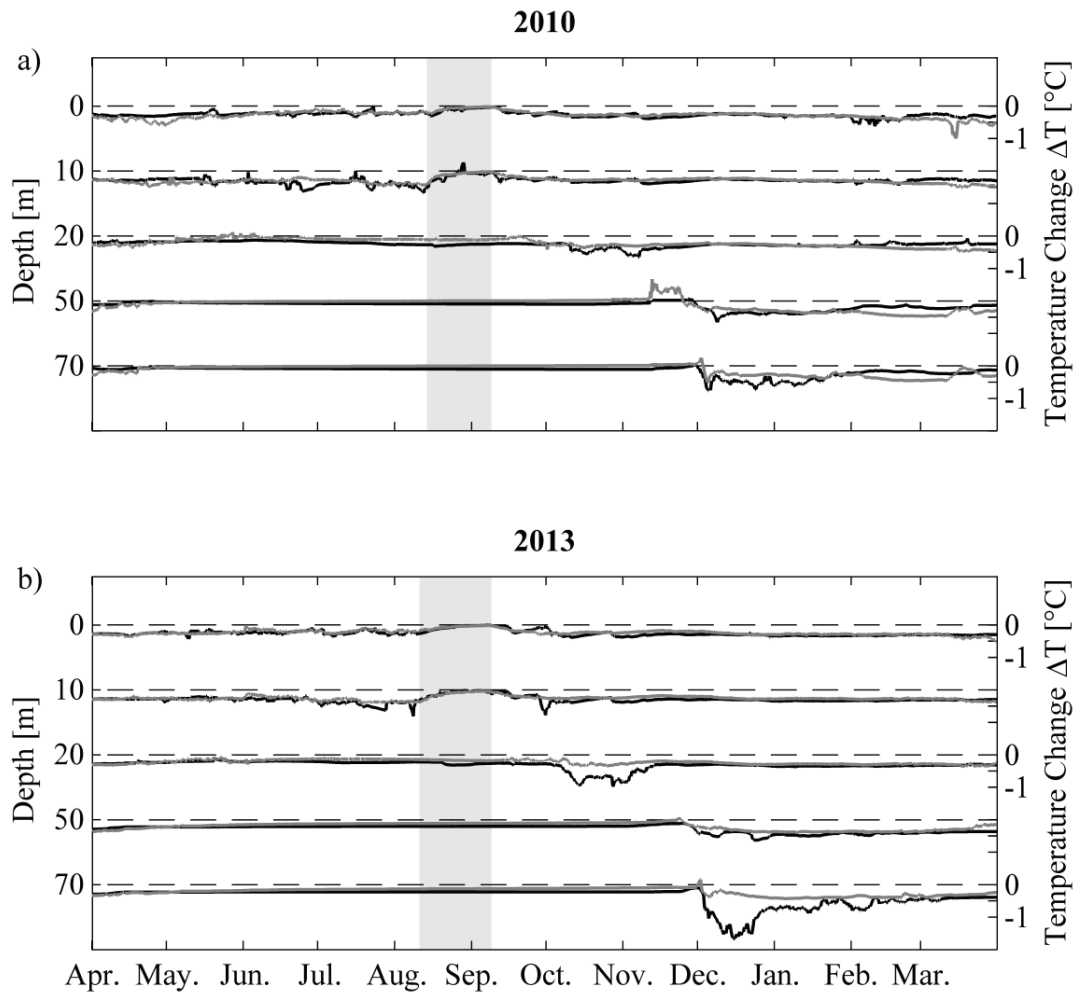
Figure 2.5. Water temperature change ΔT due to thermal pollution removal. 1D model (black) and horizontal volume-weighted mean temperature change in 3D model (grey) for the cold- (a) and the warm (b) period. Grey bars denotes MNPP maintenance with negligible heat emission into Aare River.

Table 2.6. Seasonal Change in Temperature ΔT

Depth (m)	Cold Period[a] Horizontal Volume-weighted Mean ΔT (°C) 1D Model Winter[c]	Cold Period[a] Horizontal Volume-weighted Mean ΔT (°C) 1D Model Summer[d]	Cold Period[a] Horizontal Volume-weighted Mean ΔT (°C) 3D Model Winter	Cold Period[a] Horizontal Volume-weighted Mean ΔT (°C) 3D Model Summer	Cold Period[a] Maximum ΔT (°C) 1D Model Winter	Cold Period[a] Maximum ΔT (°C) 1D Model Summer	Cold Period[a] Maximum ΔT (°C) 3D Model Winter	Cold Period[a] Maximum ΔT (°C) 3D Model Summer
1	-0.32	-0.24	-0.33	-0.26	-0.63	-0.36	-3.40	-2.71
10	-0.30	-0.33	-0.31	-0.31	-0.42	-0.68	-2.43	-2.07
20	-0.31	-0.20	-0.31	-0.12	-0.66	-0.32	-2.09	-2.09
30	-0.22	-0.08	-0.28	-0.06	-0.35	-0.20	-1.42	-1.42
40	-0.19	-0.04	-0.24	-0.04	-0.40	-0.15	-0.86	-0.61
50	-0.20	-0.07	-0.20	-0.04	-0.66	-0.12	-0.76	-0.52
60	-0.22	-0.08	-0.20	-0.04	-0.79	-0.11	-0.71	-0.44
70	-0.24	-0.08	-0.19	-0.04	-0.76	-0.11	-0.54	-0.30

Depth (m)	Warm Period[b] Horizontal Volume-weighted Mean ΔT (°C) 1D Model Winter[c]	Warm Period[b] Horizontal Volume-weighted Mean ΔT (°C) 1D Model Summer[d]	Warm Period[b] Horizontal Volume-weighted Mean ΔT (°C) 3D Model Winter	Warm Period[b] Horizontal Volume-weighted Mean ΔT (°C) 3D Model Summer	Warm Period[b] Maximum ΔT (°C) 1D Model Winter	Warm Period[b] Maximum ΔT (°C) 1D Model Summer	Warm Period[b] Maximum ΔT (°C) 3D Model Winter	Warm Period[b] Maximum ΔT (°C) 3D Model Summer
1	-0.32	-0.23	-0.28	-0.21	-0.39	-0.45	-3.18	-1.82
10	-0.33	-0.30	-0.26	-0.27	-0.61	-0.82	-1.06	-1.90
20	-0.39	-0.23	-0.27	-0.18	-0.99	-0.32	-1.86	-2.03
30	-0.31	-0.17	-0.25	-0.14	-0.67	-0.29	-1.31	-1.06
40	-0.31	-0.19	-0.24	-0.16	-0.48	-0.29	-1.11	-0.53
50	-0.34	-0.22	-0.24	-0.17	-0.63	-0.29	-0.56	-0.46
60	-0.44	-0.22	-0.25	-0.17	-1.29	-0.29	-0.48	-0.38
70	-0.52	-0.23	-0.26	-0.18	-1.65	-0.29	-0.43	-0.37

[a] April 2010 to March 2011.

[b] April 2013 to March 2014.

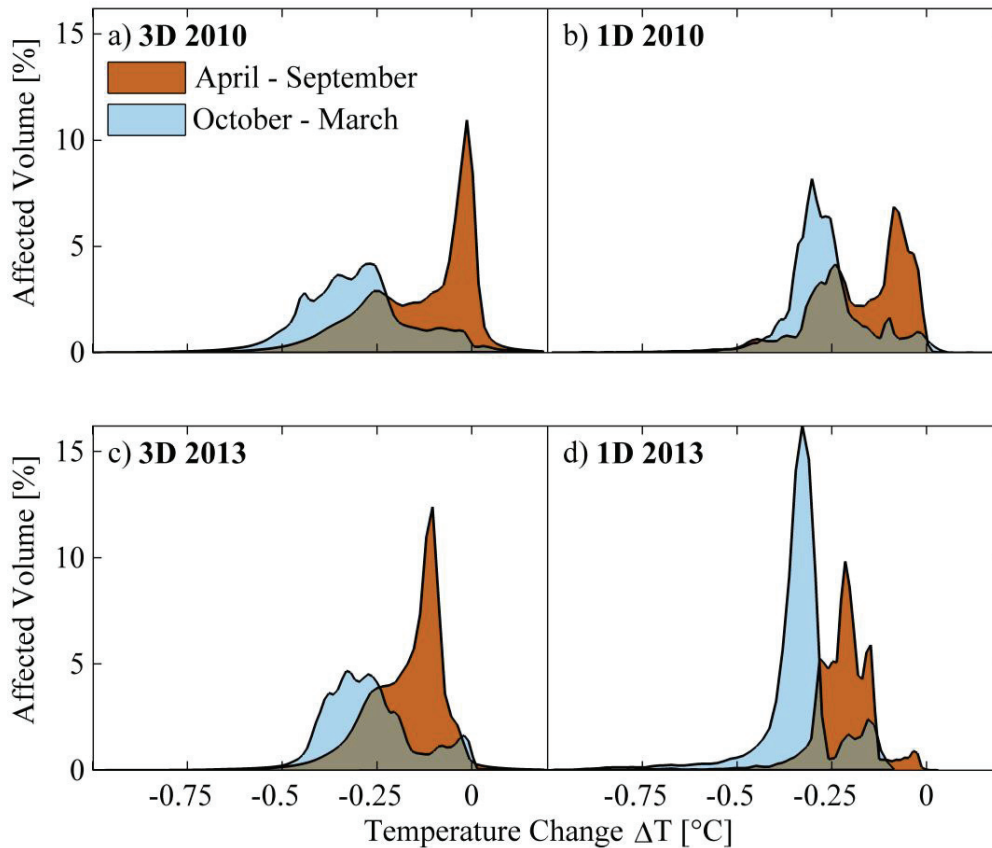[c] October to March.

[e] April to September.

Figure 2.6. Water temperature change ΔT due to thermal pollution removal relative to percentage of total volume affected. 3D model (a, c) and 1D model (b, d) during cold- (a, b) and warm periods (c, d).

The ability of the 3D model to resolve flow and temperature in horizontal directions enable us to follow the Aare River as it enters LB. Its plume has two dominant flow directions: north-west into the center of LB or north-east following the shallow eastern shore. The plume direction depend on the overall lake circulation in combination with the plume depth. During shallow intrusion events, the direction of the plume can be linked to the direction of the surface wind stress. Prevailing winds from the north-east (wind stress toward south-west) result in a clockwise gyre in the deep eastern basin which carries the Aare plume into the central parts of LB (Fig. 2.7a). Prevailing winds from south-west (wind stress toward north-east) set up a counter-clockwise rotation in the central parts of the lake. This circulation moves the plume towards the southern shoreline and conveys the river water towards the main outflow in the north-east (Fig. 2.7b).
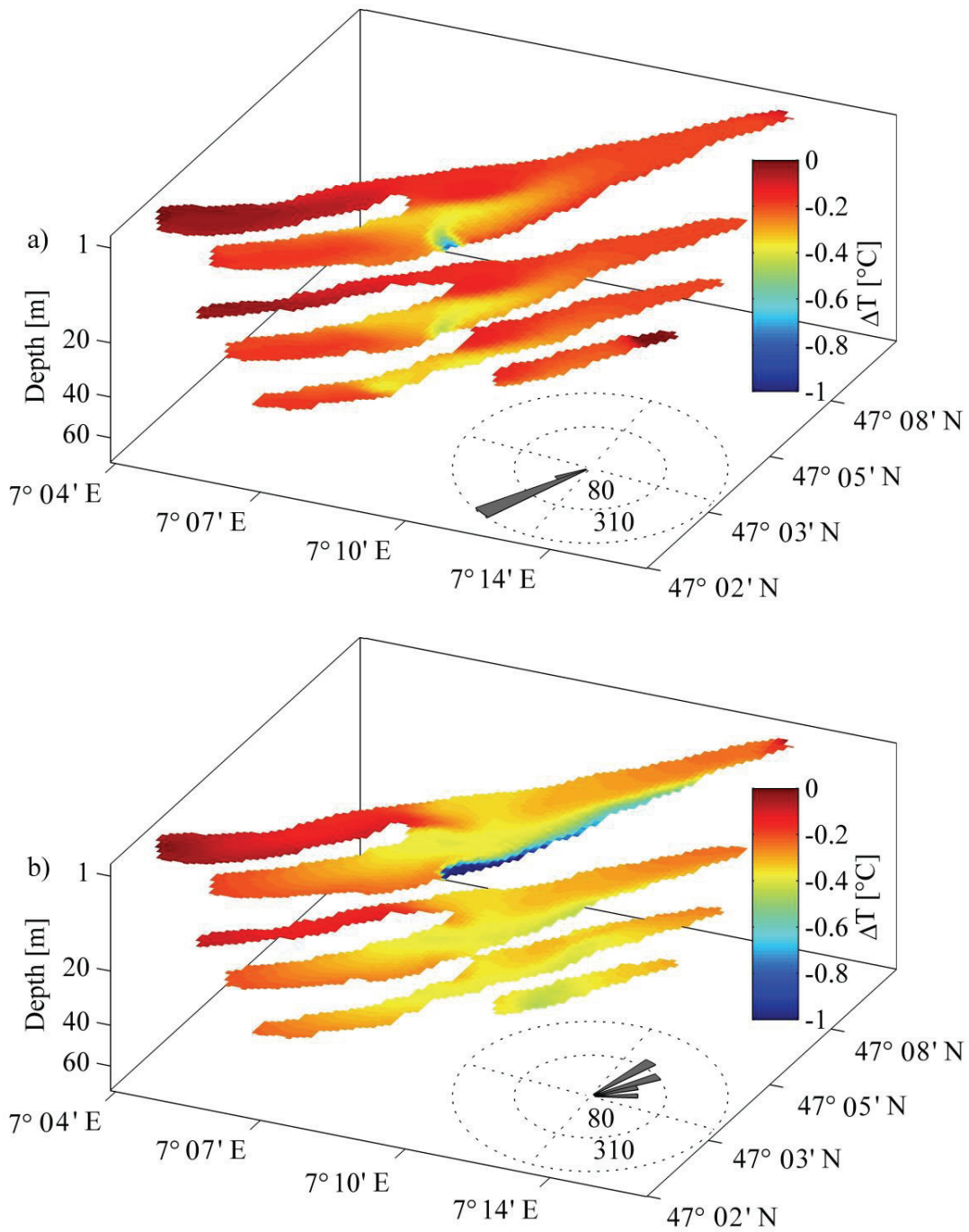
Figure 2.7. 3D modeled temperature change ΔT in LB at four depth levels (1, 20, 40 and 60 m) caused by removal of the thermal pollution on (a) midday 2ⁿᵈ December 2013 and (b) midday 23ʳᵈ December 2013. Rose diagrams represent the wind drag τ (mN m⁻²) supplied to the model during a 6 hours span prior to the displayed scene.

2.3.2 Stratification

Here we assess the impact of the upcoming closure of MNPP on stratification during the summer period in LB. For quantifying stratification strength we applied the Schmidt stability S [*Schmidt*, 1928]. For length of the stratified period we used the method proposed by *Foley et al.* [2012]. We consider the lake to be stratified if the surface (2 m) and deep-water (70 m) temperature differ more than 0.5 °C. As part of a sensitivity analysis for both models, three additional criteria for stratification length were tested (Supporting Information Text 2.S2 and Table 2.S3).
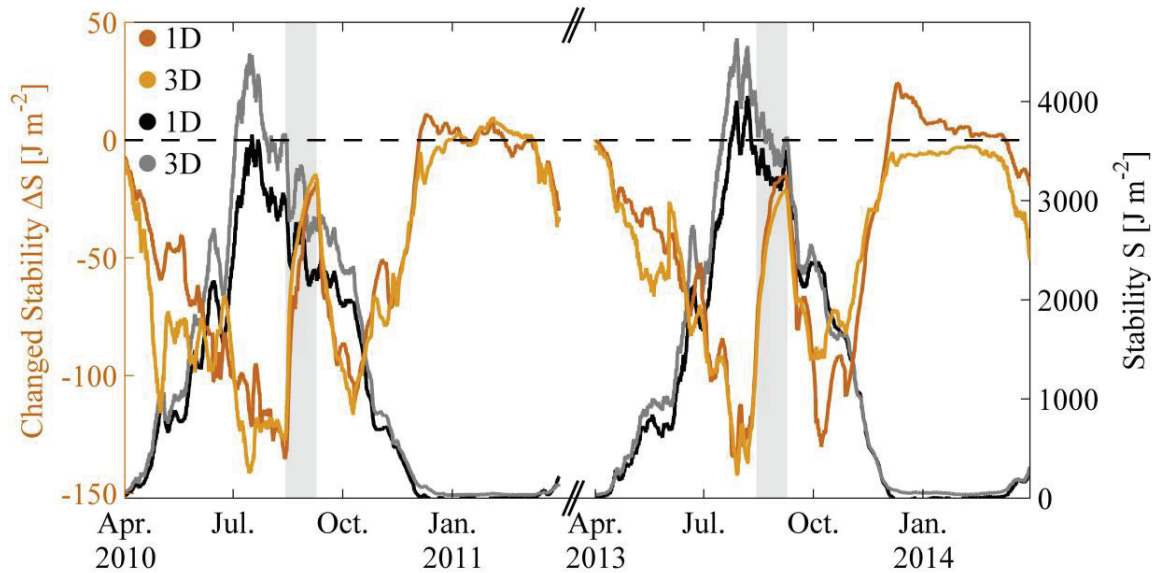

Figure 2.8. Modeled water column Schmidt stability S (right scale) with thermal pollution present in 1D (black) and 3D (grey) calculated using horizontal volume-weighted mean temperature [*Schmidt*, 1928; *Foley et al.*, 2012]. The change in stability ΔS (left scale) resulting from the removal of thermal pollution in 1D (red) and 3D (orange). Grey bars denotes MNPP maintenance with negligible heat emission into the Aare River.

Absolute values of S as well as changes in stratification strength ΔS are shown in Fig. 2.8. During the stratified period (April to November) S decreases by ~5 % as MNPP heat is removed. For the weakly-stratified winter period (December to March) we observe an increase in the water column stability, except in 3D-2013-X. The effect is largest in 1D with a mean increase of $\Delta S = 6.6$ (max 24) J m^{-2} and smallest in 3D with a mean increase for 3D-2010-X of $\Delta S = 3.4$ (max 10) J m^{-2}. The increase of ΔS in winter is due to the weak stratification combined with the intrusion of Aare water colder than 4 °C.

The removal of thermal pollution generally shortens the length of the stratified period. For the cold scenarios (comparisons X-2010-X) we observe a decrease of only -1 day in 1D and -4 days in 3D. Likewise the corresponding change during the warm scenarios (X-2013-X) was only -2 days in 1D and -1 day in 3D.

From Fig. 2.8 we estimate the response time of LB to thermal pollution from MNPP. The response time was defined as the time required for ΔS to decay past a threshold value (1%) during the plants maintenance period. For all scenarios, this was accomplished by fitting an exponential function to ΔS during both maintenance periods shown in Fig. 2.8 (grey areas). From these four curves the mean response time was calculated to ~40 days. Which is roughly 70% of the hydraulic residence time of LB (~58 days) and consistent with the two residence times defined by the hydraulic and the thermal throughflows (section 2.3.3).

2.3.3 Heat Fluxes

The removal of the MNPP thermal pollution will only affect the heat flux terms which are dependent on lake temperature. The change in the heat flux terms for shortwave and longwave absorption are thus equal to zero. The total change in heat flux ΔH_{Net} is therefore only determined by the change in longwave emission ΔH_W, evaporation/condensation ΔH_E, heat convection ΔH_C and throughflow ΔH_F:

$$\Delta H_{Net} \;=\; \Delta H_W + \Delta H_E + \Delta H_C + \Delta H_F \tag{2.4}$$

For both models the changes in each flux term in equation (2.4) were calculated using the method described in *Livingstone and Imboden* [1989] and *Fink et al*. [2014]. For H_W, H_E, and H_C we used the modeled surface temperature in each grid cell. H_F was obtained using the inflows and outflow river discharges and temperatures. The saturated vapor pressure e_s used for calculations of H_E was approximated by the Magnus formula [*WMO*, 2008], where T_W is the water surface temperature:

$$e_s \;=\; 6.112\exp\left[\left(17.62 T_W\right) \times \left(243.12 + T_W\right)^{-1}\right] \tag{2.5}$$

The median seasonal change of the considered heat flux terms in equation (2.4), with corresponding 25th and 75th percentiles, are presented in Fig. 2.9. In Supporting Information Table 2.S4 we provide the seasonal changes in mean heat fluxes and relate these to the present-

day fluxes. Heat flux changes in the 3D model shows a larger variability compared to the 1D model (Fig. 2.9). The range of extreme values is four to six times larger in 3D compared to 1D. The total change in heat flux ΔH_{Net} amounts for both models to ~17 W m^{-2}, which is in excellent agreement to the MNPP input of 18 W m^{-2}.
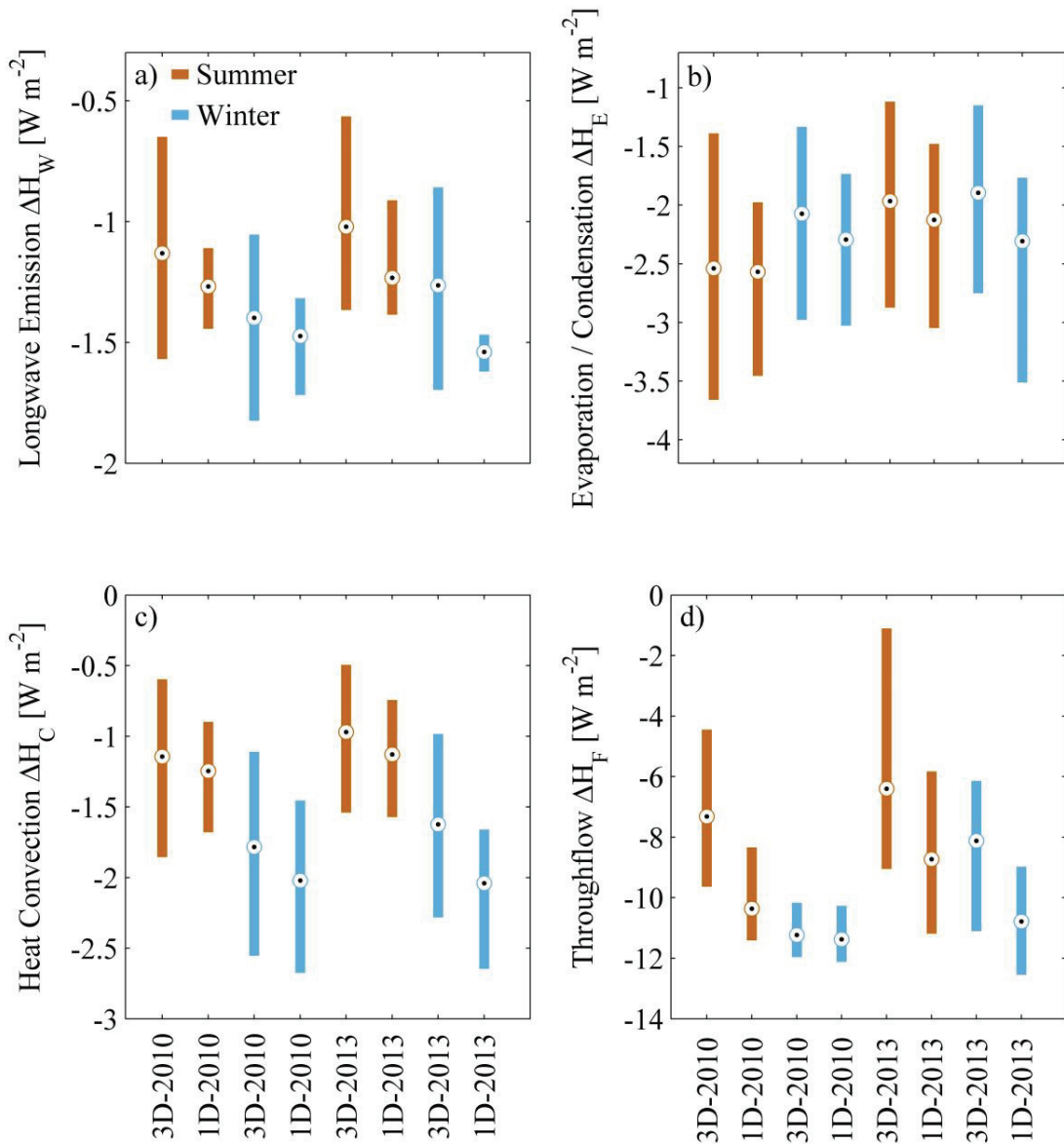

Figure 2.9. Modeled heat flux changes due to removal of thermal pollution during the cold- (X-2010) and warm (X-2013) periods in 3D (3D-X) and 1D (1D-X) during summer (April to September) in red and winter (October to March) in blue. The central black dots denote the median and the box extents the first (Q_1) and third (Q_3) quartile. Heat flux terms include longwave emission H_W (a), evaporation and condensation H_E (b), heat convection H_C (c) and throughflow H_F (d).

The majority of the change (~60% of ΔH_{Net}) is concentrated in ΔH_F. Most of the thermal pollution is thus transported through the system and transferred to downstream Aare River. This corresponds to the observed relationship between the thermal response time (section 2.3.2) and the hydraulic residence time of LB (60% ≈ 40 days / 58 days). In order to evaluate how far heat can reach downstream of LB, we apply the method described in Supporting Information 2.S1. The adjustment distance, where 37% of the heat remains, was calculated to ~350 km under the assumption that river properties do not change downstream. The remaining heat (~40% of ΔH_{Net}) leaves LB through the lake surface. H_E and H_C are only marginally affected while H_W is the least affected of all heat flux terms (Supporting Information Table 2.S4).
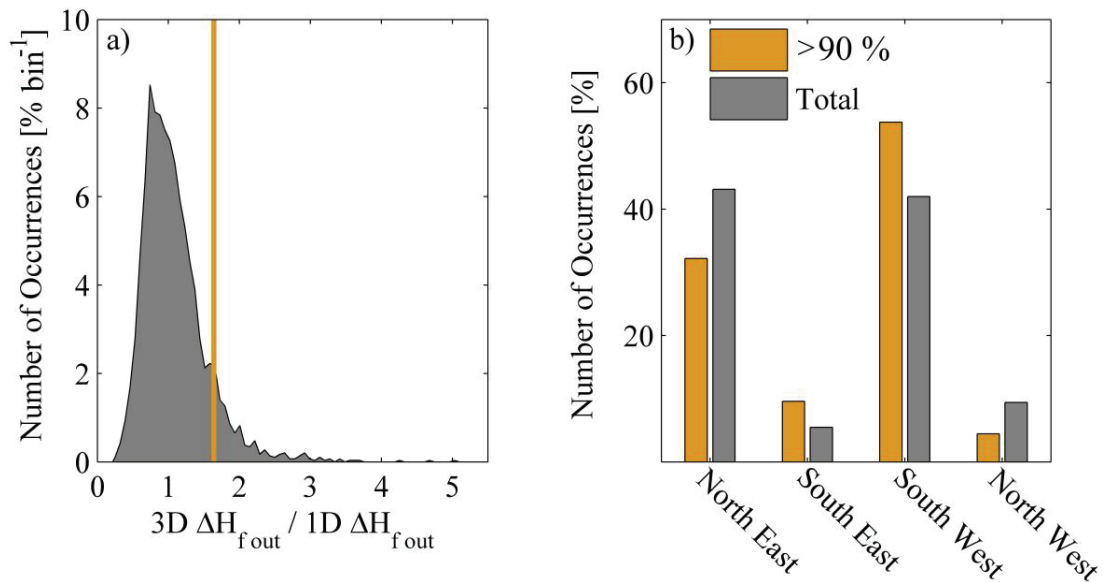

Figure 2.10. Inter-model difference of outflowing heat and wind direction for the cold and the warm scenarios combined (April 2010 to March 2011 and April 2013 to March 2014). (a) Distribution (x bin resolution 0.07) of 3D and 1D model ratios of the change in heat outflow $\Delta H_{f\,out}$ due to decommission of MNPP. The orange line marks the 90th percentile of the distribution. (b) Dominant wind direction (origin of the wind; COSMO-2 data) in % of occurrences within a six hours period prior to $\Delta H_{f\,out}$ output in (a). Grey bars in (b) represent wind direction during the complete period. Orange bars in (b) denotes the dominant wind direction corresponding to the instances to the right side of the 90% orange line in (a), i.e. to instances where the heat outflow from the 3D model is at least 65 % larger than in the 1D model.

50

The models differ regarding how the thermal pollution is transported from the Aare inflow (station 2085) to the outflow (station 2029). Therefore, the change in 1D and 3D modelled heat flux at the outflow $\Delta H_{F\,out}$ will be affected differently by the closure of MNPP. The deviation between 3D and 1D modeled heat leaving LB (3D $\Delta H_{F\,out}$ / 1D $\Delta H_{F\,out}$) is presented in Fig. 2.10a. Surprisingly the removal of thermal pollution leads to larger changes for $H_{F\,out}$ in 3D compared to 1D. This is shown in Fig. 2.10a by the long tail of the distribution towards higher values (topmost 10 %, to the right of the solid orange line). As shown in section 2.3.1, the circulation in the lake and the spatial extent of the Aare inflow plume is governed by the local wind field. We note that the tail of the distribution coincides mainly with winds from the south-west as indicated by the orange bars in Fig. 2.10b. We thereby conclude that the pathway of the Aare plume, resolved in 3D but not in 1D, determines how much of the MNPP heat is removed to the downstream Aare.

2.3.4 Intrusion Depth

The Aare inflow intrudes into the metalimnion during the stratified period (March to November). The intrusion depth is generally deeper in 1D compared to 3D. By removing the thermal pollution from the Aare River the water density generally increases. This deepens the river intrusion in both models. The magnitude of intrusion depth increase varies with the seasons and is strongest during winter. At this time a removal of thermal pollution increases the mean intrusion depth by 8.3 m in 1D and 3.2 m in 3D. The effect is much less pronounced in summer with 0.8 m (1D) and 1.1 m (3D) average deeper intrusions. The observed seasonality of the intrusion depth change is due to both the seasonal varying impact of thermal pollution on Aare water (largest in winter), and the strong lake stratification during summer.

Hydropower-induced thermo-peaking results in large sub-daily temperature fluctuations in the Aare inflow. This rapidly changing density of the river water leads to oscillations in intrusion depth. The effect is stronger in the 1D model (no entrainment) compared to the 3D model (including entrainment). Entrainment of ambient lake water into the river plume buffers rapidly changing densities in the inflow and thereby limits the effect of thermo-peaking on intrusion depth in 3D.

2.4 Discussion

2.4.1 Temperature Change

The MNPP thermal pollution enters LB via the Aare River inflow. Dispersion of the river water across the lake determines the heat distribution. Our results indicate that the upcoming decommission of MNPP will decrease the temperature in LB as a function of season, with the largest impact in winter which is in accordance with previous results published by *Mulhollem et al.* [2016]. At this time of year the available inflow from the Aare River is at its lowest level, resulting in considerable temperature fluctuations in LB of up to ~3.4 °C. This discharge-dependent sensitivity to thermal pollution is in line with previous findings made by *Prats et al.* [2012]. On a system-wide scale the effect is smaller and we find that LB volume-weighted mean temperature is likely to drop by ~0.3 °C (Fig. 2.6) between October and March. This is in the same order of magnitude as the observed global decadal increase (between 1985 and 2009) of summer lake surface temperature due to climate change [*O'Reilly et al.*, 2015]. Consequently, for a limited period of time, point sources of anthropogenic heat can have an equal impact as climate change as previously suggested by *Fink et al.* [2014]. The MNPP decommission could therefore affect the reaction of LB to the ongoing climate change.

Our results furthermore show that the upcoming plant decommission will have a smaller impact (mean volume-weighted temperature drop ~0.1 °C) during summer when the lake is strongly stratified. At this time of year the river discharge peaks, resulting in the thermal pollution being dispersed across a larger water volume and hence limiting local effects. Furthermore the strong summer stratification captures the intruding river water in the metalimnion. The intruding Aare water lifts the epilimnion towards the surface and out of the lake. Here we refer to this phenomenon as "flushing". The flushing effect is strengthened by the short hydraulic residence time of LB. It is thus expected to be present in similar aquatic systems which have small volume to inflow ratios.

The residence time of the MNPP heat in LB can be further shortened if the river plume is advected by lake-wide circulation along the eastern shore towards the outflow, potentially reducing the effect of mixing the thermal pollution across the lake. We refer to this process as "short-circuiting", which generally occurs during shallow intrusion events in combination with winds from south-west (Fig. 2.7b). This follows results by *Schimmelpfennig et al.* [2012] who linked river water residence time in a small lake to wind-induced lake-wide circulation patterns.

The seasonal peak in river discharge volume and the removal of heat from the lake through the outflow thus limits the effects of MNPP thermal pollution during summer.

Flushing and short-circuiting were likewise present during winter but due to the smaller inflow and in general deeper intrusion of the Aare inflow, the effects were much smaller. However, for river temperatures < 4 °C the effect of short-circuiting can be substantial, as the inflow floats at the lakes surface. Flushing was present in both models, while short-circuiting only takes place in the 3D model.

Our results can be compared to findings made by *Hanafiah* [2013], who modelled the signature of the MNPP thermal pollution downstream of LB. By resolving LB using shallow riverine segments, she found that heat remaining from MNPP at the outflow station 2085 would raise the river temperature by ~0.5 to ~0.8 °C. In our study we resolved the spatial and temporal processes taking place in LB to a considerable higher degree. Thus at the outflow station 2085 we found corresponding temperature increases of ~0.2 to ~0.4 °C. We conclude that the impact of MNPP thermal pollution on LB is seasonal and strongest during warm winters, when the lower temperature gradient between atmosphere and lake/river water is limiting the transfer of heat from the water to the atmosphere.

2.4.2 Water Column Stratification

Our study shows that thermal pollution entering LB prolongs the stratified summer period. The added heat strengthens the stratification and thus opposes vertical convection. Stronger stratification has been shown to decrease the concentration of dissolved oxygen in lakes [*Foley et al.*, 2012]. The impact of enhanced stratification combined with high primary productivity results in lower hypolimnion oxygen concentrations in LB. Between 2000 and 2016 the oxygen concentration in LB at 74 m depth annually drops to less than 3 mg L^{-1} in late autumn. We find that a removal of MNPP thermal pollution from the Aare inflow, would weaken the water column stability and decrease the duration of the stratified period in summer. This will slightly improve oxygen conditions in the hypolimnion.

Thermal pollution hinders the Aare River temperature to drop below 4 °C for most of the winters (Fig. 2.2b). We show that the upcoming decommission of MNPP will result in river temperatures colder than 4 °C. This can drive LB towards dimictic conditions with inverse stratification in winter (Fig. 2.8). Our findings are thus in line with observations made in

Stechlinsee [*Kirillin et al.*, 2013]. Increased stratification in winter generally limits deep-water re-oxygenation [*Golosov et al.*, 2007, 2012; *Schwefel et al.*, 2016]. However, for LB the effect is expected to be minor since the relative increase in stratification is small (Section 2.3.2). By using the mean wind speed over LB of 2.5 m s^{-1} and C_{10} from the 3D model we find that a stratification increase of ~20 J m^{-2} would be opposed by wind-induced mixing after ~3 weeks. Furthermore, the effect is larger in 1D (which lacks short-circuiting) compared to 3D.

2.4.3 Heat Budget and Heat Fluxes

Our findings indicate that the majority (~60%) of the thermal pollution leaves the lake via the main outflow (Fig. 2.9d). This is a substantial anthropogenic thermal contribution to the downstream Aare and Rhine Rivers which are extensively used for industrial cooling. As we remove the thermal pollution, the inflowing Aare water density increases. The river plume entering LB will therefore intrude deeper. River water that could previously quickly exit the lake via the outflow, may thus reach the hypolimnion and thereby limit the short-circuiting effect. For river water colder than 4 °C the likelihood of short-circuiting increases. The short-circuiting is thus the main cause behind the larger fluctuations in $\Delta H_{F\,out}$ observed in Fig. 2.10a for 3D compared to 1D model results.

The contribution of MNPP to H_E, the second most affected flux term, leads to an evaporation of ~0.1 mm day^{-1} (~4 cm year^{-1}). This evaporation remains negligible compared to the annual water level fluctuations in LB of ~1 m. *Kirillin et al.* [2013] showed that cooling water emitted from a nuclear power plant into a small lake mainly leaves the water body via H_E fluxes. Our results, however, suggests that the throughflow is the dominant sink of heat in short retention time system.

2.4.4 Model Divergences

The overall impact of the MNPP thermal pollution on LB temperature are well reproduced in both 1D and 3D as seen in Fig. 2.6. However the fine-scale processes such as local temperatures and short-circuiting are, as expected, better resolved in 3D, whereas extreme temperature fluctuations are smoothed out by the 1D approach. Therefore, harmful local effects on biota by extreme temperatures, up to ~3.4 °C in this study, cannot be investigated with a 1D model. As rapid changing temperature conditions have been shown to be destructive for biota [*Barnett*,

1971; *Sylvester*, 1972; *Reutter and Herdendorf*, 1976; *Vandysh*, 2009; *Bruno et al.*, 2013], it is important to consider 3D models when local heat emissions matter. This is particularly evident in lakes like LB, where the river plume often flows along shallow shores.

Surprisingly, we find that flushing compensates the lack of short-circuiting in 1D as seen by the overall good fit between 1D and 3D in the amount of heat leaving the lake via the outflow (Fig. 2.10a). We interpret this as the consequence of both the short residence time of the surface layer in LB, and the long distance (~8 km) between the Aare River in/outflow. We expect a larger influence of short-circuiting in aquatic systems where in/outlets are located closer together.

The two models reproduce the temperature equally well in the epilimnion (Fig. 2.3a) which is the most important zone for the heat fluxes. The 3D model includes baroclinic motions of the water column (Fig. 2.4e) and is therefore better suited for the metalimnion compared to the 1D model (Fig. 2.3a). In turn, the 1D model performs better in the hypolimnion compared to the 3D model (Fig. 2.3a). This is mainly due to the fact that the 3D model was optimized towards both temperature and current velocity at several locations. The 1D model, in contrast, was optimized only for temperature at the central station CB.

The temperature difference between both models and observations (*RMSD* from 0.4 to 2.3 °C; Fig. 2.3 and Table 2.3) were larger than the mean volume-weighted temperature change (~0.3 °C) induced by the MNPP closure. However, for the analyses concerning the effects of the MNPP closure, the modelled temperature divergences from measurements can be disregarded since identical biases are present in all model runs made with and without thermal pollution and with otherwise unchanged forcing. Furthermore, the excellent agreement between thermal pollution (18 W m^{-2}) in relation to modelled changes in heat fluxes (17 W m^{-2}) in both 1D and 3D, also proves the adequacy of the models. These arguments strengthens our confidence in the expected change of water temperature, heat flux and stratification after decommission of MNPP in 2019.

2.5 Conclusions

Aquatic ecosystems are often used as sinks for thermal pollution from anthropogenic activities. Here we studied the impact of heat emission (equivalent to 18 W m^{-2}) from a nuclear power plant on the perialpine Lake Biel, which has a short hydraulic residence time of ~58 days. We quantified the impact of thermal pollution on temperature, stratification and heat fluxes using both 1D and 3D models.

A clear seasonal trend was observed for the effect of thermal pollution on lake temperature, caused by seasonal varying discharge in the inflowing river. Maximal effects occurred in winter (lowest discharge) with up to 3.4 °C increase of local temperature. On system-wide scale, the mean volume-weighted lake temperature increased by ~0.3 °C. The effect was strongest during warm winters compared to cold winters. Anthropogenically increased temperature strengthened stratification and prolonged the stratified period by up to 4 days. Furthermore, the majority (~60%) of the emitted thermal pollution traversed the lake and was transported further downstream. The remaining heat (~40%) left the lake via the surface to the atmosphere mainly due to increased evaporation. The upcoming power plant decommission will thus shorten the stratified period as well as lower the temperature in the lake and in the downstream river.

The increase of volume-weighted lake temperature (~0.3 °C), is in the same range as the observed global increase of summer surface water temperature due to climate change [*O'Reilly et al.*, 2015]. We therefore recommend that local anthropogenic/natural sources and sinks of heat, should be included in studies evaluating the response of aquatic systems to climate change.

For future studies of thermal pollution in lakes and reservoirs we recommend the following model selection guidelines. The main processes only identifiable in 3D were spatial inhomogeneity of altered lake temperature caused by local wind patterns and distance to the thermal sources, resulting in short-circuiting between river inflow and outflow. Both 1D and 3D were sufficient to determine system-wide effects on lake temperature and stratification as well as tributary-induced epilimnion flushing.

Supporting Information Chapter 2:

Physical effects of thermal pollution in lakes

Love Råman Vinnå[1], Alfred Wüest[1,2],, Damien Bouffard[1,2]

[1]Aquatic Systems Laboratory, Margaretha Kamprad Chair, École Polytechnique Fédérale de Lausanne, Institute of Environmental Engineering, Lausanne CH-1015, Switzerland.
[2]Eawag, Swiss Federal Institute of Aquatic Science and Technology, Surface Waters - Research and Management, Kastanienbaum, Switzerland.

Supporting Information Introduction

In Text 2.S1 the thermal flux from river to the atmosphere is described. Stratified period duration calculations/results are described in Text 2.S2. Field campaign detailed setup is provided in Table 2.S1. One dimensional modelled long term change in water temperature due to a closure of MNPP are given in Table 2.S2. MNPP closure caused change in the length of the stratified period are shown in Table 2.S3. Seasonal one- and three dimensional modelled change in mean heat flux due to removal of MNPP heat is given in Table 2.S4.

Text 2.S1 River Borne Thermal Pollution Decay

Downstream of the point of thermal pollution input, the river will re-adjust towards temperature equilibrium with the surroundings and consequently loses heat. We use the method described by *Meier et al.* [1997] to quantify the level of thermal pollution decay in the river. The method assumes that atmospheric/river conditions remain similar throughout the spatial extent of the river. In brief, the method assumes a time dependent exponentially decay of the excess heat as a function of distance from the point of input. The rate of loss to the surroundings is determined by the river discharge Q, heat capacity c_p of water (4190 J kg^{-1} K^{-1}), water density ρ [*Chen and Millero*, 1986], the width of the river b set to 80 m and a heat exchange coefficient A_T. For A_T we use the height- and season-dependent approximation formula given by *Kuhn* [1977]. We parameterize A_T by a cosine function ranging from 16.4 W m^{-2} K^{-1} in January to 34.4 W m^{-2} K^{-1} in July. At distance X_A

$$X_A(t) = \frac{Q(t)\,\rho(T,t)\,c_p}{b\,A_T(t)} \tag{2.S1}$$

from the point of input 37% of the supplied heat remains in the river, We apply a first order exponential regression analysis on X_A to obtain coefficients c_1 and c_2 to express the fraction of thermal pollution E_R remaining after any downstream distance X_B.

$$E_R(t) = c_1(t)\exp\left(-c_2(t)\,X_B\right) \tag{2.S2}$$

The river temperature increase ΔT_R caused by thermal pollution from MNPP at any downstream location X_B can consequently be expressed as.

$$\Delta T_R(t) = \frac{M_E(t)\,E_R(t)}{c_p\,Q(t)\,\rho(t)} \tag{2.S3}$$

Here M_E represent the mean energy input into the river. ΔT_R is ultimately removed from the temperature at station 2085 (Figures 2b and 2c) before the Aare enters LB.

Text 2.S2 Stratification Length

To determine the length of the stratified period we use the four case method described by *Foley et al.* [2012]. In case 1 and 2 the lake is stratified if the temperature differ more than 0.5 °C (case 1) or 1.0 °C (case 2) between surface (2 m) and deep water (70 m). For case 3 and 4 the lake is considered to be stratified if a local consistent temperature gradient exist anywhere in the vertical water column greater than 0.5 °C m^{-1} (case 3) or 1.0 °C m^{-1} (case 4).

All four cases predict a decrease in the length of the stratified summer period as the MNPP heat is removed (Supporting Information Table 2.S3). The variability between the cases is due to difference in how stratification is defined in each case. We find that cases 1 (mean stratification length for all scenarios $MS = 235$ days) and 2 ($MS = 230$ days) are more suitable for our models. While cases 3 ($MS = 196$ days) and 4 ($MS = 115$ days) require a well-defined thermocline which is more complex to model correctly. Cases 3 and 4 are therefore more useful for evaluating real highly resolved vertical measurements of temperature.

M1 47° 7' 34"N / 7° 13' 23"E Station Depth: 20 m		M2 47° 7'14 "N / 7°13' 0"E Station Depth: 47 m		M3 47° 4' 58"N / 7°11' 8"E Station Depth: 28 m	
Instrument	*Depth (m)*	*Instrument*	*Depth (m)*	*Instrument*	*Depth (m)*
Minilog II-T	0.2	Minilog II-T	0.2	Minilog II-T	0.2
RBRduo	3.5	Minilog II-T	3.5	Minilog II-T	5
Minilog II-T	4.5	Minilog II-T	6.5	Minilog II-T	7
Minilog II-T	6.5	Minilog II-T	8.5	Minilog II-T	9
Minilog II-T	8.5	RBRconcerto	10	Minilog II-T	10.5
Minilog II-T	9.5	Minilog II-T	10.5	Minilog II-T	12
Minilog II-T	11.5	Minilog II-T	11.5	Minilog II-T	14.5
Minilog II-T	13	Minilog II-T	12.5	Minilog II-T	17
Minilog II-T	14.5	Minilog II-T	14.5	Minilog II-T	19.5
Minilog II-T	16.5	Minilog II-T	16.5	Minilog II-T	21
TR-1060	18	Minilog II-T	18.5	TR-1060	24
TR-1060	18.5	Minilog II-T	20.5	TR-1060	26.5
TR-1060	19	Minilog II-T	22.5	TR-1060	27
		Minilog II-T	24.5		
		Minilog II-T	27.5		
		Minilog II-T	32.5		
		Minilog II-T	37.5		
		Minilog II-T	43.5		
		TR-1060	45		
		TR-1060	45.5		
		TR-1060	46		
ADCP		ADCP		ADCP	
Frequency	*Resolution*	*Frequency*	*Resolution*	*Frequency*	*Resolution*
1200 kHz	0.25 m	600 kHz	1 m	300 kHz	1 m
	5 min		20 min		20 min

Table 2.S1. LB Field Campaign Instrumentation Setup

Depth	Horizontal Volume Mean ΔT (°C)[a]		Maximum ΔT (°C)[a]	
(m)	*Winter[b]*	*Summer[c]*	*Winter*	*Summer*
1	-0.32	-0.21	-2.89	-0.62
10	-0.31	-0.29	-1.02	-1.41
20	-0.34	-0.2	-1.26	-0.65
30	-0.26	-0.13	-0.95	-0.4
40	-0.25	-0.14	-0.92	-0.4
50	-0.26	-0.15	-0.85	-0.41
60	-0.28	-0.15	-1.26	-0.42
70	-0.33	-0.15	-1.98	-0.42

Table 2.S2. 1D Modelled Seasonal Change in Temperature ΔT

[a] April 1995 to March 2014.

[b] October to March.

[c] April to September.

Scenarios	*Case 1*	*Case 2*	*Case 3*	*Case 4*
1D-2010	-1	0	0	-1
3D-2010	-4	-2	-2	-19
1D-2013	-2	0	-6	-6
3D-2013	-1	-1	-2	-3

Table 2.S3. Change of Stratification Period Length (days)[a]

[a] Calculated according to the four case method described in Supporting Information Text 2.S2.

Flux Term	Mean Heat Flux Change (W m^{-2})							
	Cold Period[a]				Warm Period[b]			
	1D		3D		1D		3D	
	Winter[c]	*Summer*[d]	*Winter*	*Summer*	*Winter*	*Summer*	*Winter*	*Summer*
$|\Delta H_W|$	-1.5	-1.2	-1.5	-1.2	-1.6	-1.1	-1.3	-1
$|\Delta H_E|$	-2.6	-2.8	-2.4	-2.7	-2.2	-2.3	-2.1	-2.1
$|\Delta H_C|$	-2.1	-1.4	-2	-1.4	-2.2	-1.2	-1.7	-1.1
$|\Delta H_F|$	-11	-8.4	-10.8	-6.5	-10.5	-7.7	-8.5	-5.2
$|\Delta H_{Net}|$	-17.2	-13.8	-16.7	-11.8	-16.5	-12.3	-13.6	-9.4
	Heat Flux Percentage Change (%)[f]							
	Cold Period[a]				Warm Period[b]			
	1D		3D		1D		3D	
	Winter[c]	*Summer*[d]	*Winter*	*Summer*	*Winter*	*Summer*	*Winter*	*Summer*
$|\Delta H_W|/|H_W|$	< 1	< 1	< 1	< 1	< 1	< 1	< 1	< 1
$|\Delta H_E|/|H_E|$	10	6	11	6	5	8	5	6
$|\Delta H_C|/|H_C|$	3	3	2	3	9	1	7	1
$|\Delta H_F|/|H_F|$	48	9	35	11	54	14	26	10

Table 2.S4. Heat Flux Change

[a] April 2010 to March 2011.

[b] April 2013 to March 2014.

[c] October to March.

[e] April to September.

[f] Change in heat flux compared to heat flux for thermal pollution scenarios (X-X-In).

64

Chapter 3:

Tributaries affect the thermal response of lakes to climate change

Love Råman Vinnå[1], Alfred Wüest[1,2], Massimiliano Zappa[3], Gabriel Fink[4], Damien Bouffard[1,2]

[1]Aquatic Systems Laboratory, Margaretha Kamprad Chair, École Polytechnique Fédérale de Lausanne, Institute of Environmental Engineering, Lausanne CH-1015, Switzerland.

[2]Eawag, Swiss Federal Institute of Aquatic Science and Technology, Surface Waters - Research and Management, Kastanienbaum, Switzerland.

[3]Swiss Federal Institute for Forest, Snow and Landscape Research WSL, Birmensdorf, Switzerland.

[4]Center for Environmental Systems Research, CESR, University of Kassel, Kassel,

Abstract

Thermal responses of inland waters to climate change varies on global and regional scales. The extent of warming is determined by system-specific characteristics such as fluvial input. Here we examine the impact of ongoing climate change on two alpine tributaries, the Aare River and Rhône River, and their respective downstream, peri-alpine lakes: Lake Biel and Lake Geneva. We propagate regional atmospheric temperature effects into river discharge projections. These, together with anthropogenic heat sources, are in turn incorporated into simple and efficient deterministic models that predict future water temperatures, river-borne suspended sediment concentration (SSC), lake stratification and river intrusion depth/volume in the lakes. Climate-induced shifts in river discharge regimes, including seasonal flow variations, act as positive and negative feedbacks in influencing river water temperature and SSC. Differences in temperature and heating regimes between rivers and lakes in turn result in large seasonal shifts in warming of downstream lakes. The extent of this repressive effect on warming is controlled by the lakes hydraulic residence time. Previous studies suggest that climate change will diminish deep-water oxygen renewal in lakes. We find that climate-related seasonal variations in river temperatures and SSC shift deep penetrating river intrusions from summer towards winter. Thus potentially counteracting the otherwise negative effects associated with climate change on deep water oxygen content. Our findings provide a template for evaluating the response of similar hydrologic systems to on-going climate change.

3.1 Introduction

The thermal and hydrodynamic responses of lakes to climate change are considerably diverse. Observed responses vary on global, regional and even local scales [*O'Reilly et al.*, 2015]. Even neighbouring freshwater bodies can react differently to a given increase in air temperature. This indicates that lake-specific characteristics will determine the response to climate change (for clarity and brevity, we refer to anthropogenic climate change simply as 'climate change' or 'climate' from now on). Local factors which affect climate warming of lakes include, among others, morphology [*Toffolon et al.*, 2014], irradiance absorption [*Kirillin*, 2010; *Williamson et al.*, 2015], local weather conditions [*Zhong et al.*, 2016], stratification [*Piccolroaz et al.*, 2015], atmospheric brightening [*Fink et al.*, 2014a] and ice cover [*Austin and Colman*, 2007].

Throughflows affect epilimnion and hypolimnion temperatures of lakes. Studies of climate impact typically do not address these sorts of subtleties in lake dynamics due to lack of data or difficulties in predicting future temperature and discharge conditions [*Fenocchi et al.*, 2017]. Several studies of large lakes suggest that major tributaries play only a minor role in climate-induced warming and deep-water oxygen renewal [*Fink et al.*, 2014a; *Schwefel et al.*, 2016]. Medium- and smaller-scale lakes are, however, more abundant than large lakes [*Verpoorter et al.*, 2014] and exhibit a greater degree of sensitivity to point sources of anthropogenic thermal input which can affect temperature and stratification [*Kirillin et al.*, 2013; *Råman Vinnå et al.*, 2017a]. Medium- and small-sized lakes also make a more significant contribution to the temperature-dependent global greenhouse gas budget [*Holgerson and Raymond*, 2016]. Accurate prediction of climate change impact therefore requires a more detailed understanding of small- to medium-scale lake and tributary systems.

Climate change exerts dual influence on alpine rivers by introducing variation to both flow and temperatures. Discharge variation takes the form of less flow in summer and more flow in winter due to warmer high altitude snow and ice melt/runoff regimes [*Birsan et al.*, 2005; *Addor et al.*, 2014] which also influence river temperature [*Isaak et al.*, 2012; *Van Vliet et al.*, 2013]. Increased air temperature may also enhance erosion rates in river basins thereby supplementing river-borne suspended sediment loads [*Bennett et al.*, 2013b]. River temperature and suspended sediment content determine water density and by extension, the depth of river plume intrusions into downstream lakes or reservoirs. The depths and volumes of river intrusion plumes determine deep-water oxygen renewal, especially for deeper lakes where climate-related warming can reduce seasonal deep convective mixing and thereby deplete deep-water oxygen [*Schwefel et al.*, 2016]. Major (deep penetrating) river intrusion

events typically occur due to flooding, which flush large sediment loads into the river [*Fink et al.*, 2016]. The frequency and volume of floods in the Alps are notoriously hard to predict, although a decrease in floods has occurred in association with recent warmer summers observed in the Alps [*CH2011*, 2011; *Glur et al.*, 2013].

Recent model studies have identified inland waters as risk-hotspots under expected climate change scenarios [*Pachauri et al.*, 2015]. These systems require a more detailed analysis given their role in supporting fisheries, agriculture, drinking water supply, heat management and hydropower. This paper examines the complex interactions between tributaries and lakes in response to temperature increase and other modifications expected from climate change. Our objectives were to quantify the impact of specific climate change scenarios on (i) alpine tributaries and (ii) downstream peri-alpine lakes with a focus on river-borne suspended sediment concentration (SSC), water temperature, stratification and river intrusions.

We used coupled river-lake models to build on previous research by Fink et al. [2016]. These authors investigated the effect of flood frequencies on deep-water renewal under established climate change scenarios. Their work did not generate tightly constrained estimates for flooding events. Our analysis therefore provisionally assumed that flood frequency does not change in the future. In addition to these sources of natural variation, our models addressed variation in river discharge regimes (i.e. daily mean level shift) under the specified A1B climate change scenario. These in turn affect SSC and thermal regimes for rivers and their associated downstream lakes. Furthermore here we show that local point sources of anthropogenic thermal pollution can have major impact on the response of inland waters to climate change as previously suggested by Fink et al. [2014b].

3.2 Methods

3.2.1 Approach

The investigation of tributary influence on lake response to climate change followed these procedural steps:

(i)   Define river temperature and SSC models for two major alpine rivers and designate a one-dimensional lake model for a large- and a medium-sized peri-alpine lake.

(ii)   Integrate model (i) with a river intrusion scheme: Figure 3.1 shows the integration of the one-way component models.

(iii)   Obtain and apply estimates of future regional air temperature, tributary discharge and changes in local anthropogenic thermal emissions to both river and lake models.

(iv)   Identify patterns in model outputs of water temperature, SSC, lake stratification and river intrusion parameters (volume and depth).
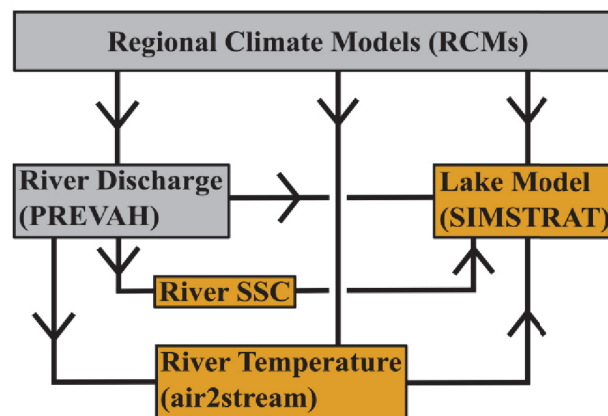

Figure 3.1. Schematic illustration of the one-way model chain of this study. Orange models represent modeling performed by this study while grey models represent simulated data inputs obtained from external sources.

3.2.2 Study area

This study examined two warm, monomictic, freshwater peri-alpine lakes in western Switzerland, Lake Biel (LB; 7°10' E, 47°5' N) and Lake Geneva (LG; 6°31' E, 46°27' N). Large tributaries originating in the Alps, the Aare River and Rhône River, feed into LB and LG, respectively (Fig. 3.2).
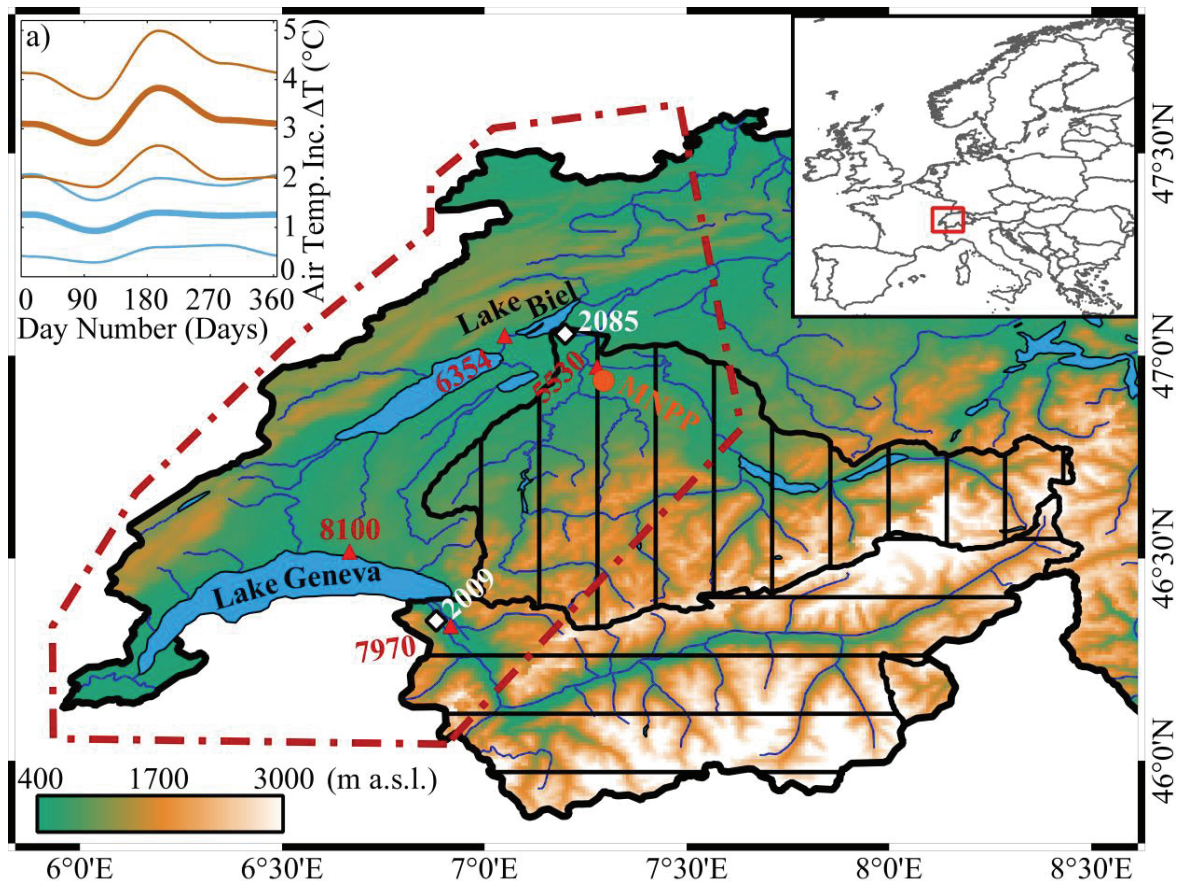
Figure 3.2. Study area and predicted regional air temperature increases. Elevation above sea level (green to white color ramp), locations and number of river stations (white diamonds) and atmospheric monitoring stations (red triangles), drainage area (Aare: vertical lines; Rhône: horizontal lines) and location of Mühleberg Nuclear Power Plant (MNPP, orange circle). Area covered by regional climate models (dark red dashed-dotted line) with a) predicted air temperature increase ΔT in the near-future (blue, 2030-2049) and far-future (orange, 2080-2099) for medium (thick lines) and upper/lower estimates (thin lines) under the A1B emission scenario [CH2011, 2011].

LG is a large, meso-eutrophic lake resting at 372 m elevation and covering an area of 580 km^2. It reaches a maximum depth of 309 m and holds a volume of 89 km^3 with an average hydraulic residence time of 11.5 years. Complete seasonal deep convective mixing occurs only on average every fifth winter but is predicted to become less frequent with on-going climate change [*Perroud and Goyette*, 2010; *Schwefel et al.*, 2016]. Whereas the average global surface lake water temperature has increased by ~0.34 °C decade^{-1} between 1985 and 2009 [*O'Reilly et al.*, 2015], the Rhône River supplying ~75% of LG's inflow has experienced a temperature increase of ~0.21 °C decade^{-1} from 1978 to 2002 [*Hari et al.*, 2006].

LB is a 74 m deep, meso-eutrophic, medium-sized lake resting at an elevation of 429 m. It covers a surface area of 39.3 km^2 and holds a volume of 1.18 km^3 with hydraulic residence

time of 58 days. Complete deep convective mixing occurs every winter and effectively replenishes the oxygen-depleted deep-water. The Aare River provides ~61% of LB's inflow and experienced a 0.34 °C decade^{-1} increase in temperature from 1978 to 2002 [*Hari et al.*, 2006]. Several dams/lakes trap sediment along the upstream Aare course and increase sediment settling and water temperature prior to entering LB. The Mühleberg Nuclear Power Plant (MNPP), situated ~19 km upstream from LB (7°16' E, 46°59' N; Fig. 3.2) represents a point-source of thermal pollution. Planned for decommission in 2019, the plant emits ~700 MW of heat into the Aare and substantially warms the river water [*Råman Vinnå et al.*, 2017a]. The ~8 km long Zihlkanal, LB's second largest tributary, supplies ~32% of the lake inflow and connects LB to Lake Neuchâtel (Fig. 3.2). This tributary is neglected here since it mainly transports lake surface water, which has approximately the same temperature as LB surface water and thus without net heat effects.

3.2.3 River models

3.2.3.1 Temperature

Uncertainties concerning river morphology, heat fluxes, shadowing and atmospheric conditions such as wind speed and cloudiness [*Caissie*, 2006] pose a significant challenge to accurately model future river temperatures. Deterministic models typically require detailed knowledge unavailable for future climate scenarios. Regressions and stochastic models rely heavily on observed natural variability of a given time frame and typically do not include inputs representing additional or interacting physical processes. On their own, these sorts of "black box" models cannot balance trade-offs between constraints available from empirical data and the complexity offered by theoretical frameworks.

To overcome these limitations, we used the hybrid model air2stream [*Toffolon and Piccolroaz*, 2015]. The model combines the simplicity of stochastic models with accurate representation of the relevant physical processes affecting temperature. Similar to the neural networks approach, the model calculates river water temperature (T_w) through a Monte Carlo-like calibration process, which identifies optimal parameters for weighting physically dependent variables. We used the eight-parameters (a_1 to a_8) version of the model which incorporates air temperature (T_a) and river discharge (Q) as a function of time (t).

$$\frac{\Delta T_{\mathrm{w}}}{\Delta t} = \frac{1}{\delta}\left\{ a_1 + a_2 T_{\mathrm{a}}(t) - a_3 T_{\mathrm{w}}(t) + \theta\left[a_5 + a_6 \cos\left(2\pi\left(\frac{t}{t_{\mathrm{y}}} - a_7 \right) \right) - a_8 T_{\mathrm{w}}(t) \right] \right\}, \qquad (3.1)$$

$$\delta = \theta^{a_4}; \theta = Q(t)\big/\overline{Q},$$

where t is expressed in years and t_{y} represents one year. Both Aare and Rhône (stations #2085 and #2009, respectively, Fig. 3.2) provided calibration (1990 – 1999) and validation data (2000 - 2009). Table 3.1 and Fig. 3.3 show best-fit parameters and model performance statistics. Model sensitivity to variation in T_{w} was assessed by removing MNPP thermal pollution as in Råman Vinnå et al. [2017a] and repeating the calibration/validation for station #2085 (Table 3.1).

Table 3.1. Air2stream river temperature model best-fit parameters and model performance statistics reported as coefficients of determination (R^2) and root mean square deviation (RMSD). Input parameters used in this study are shown in bold-faced type. The model was calibrated, validated and subjected to sensitivity tests using data from station #2085 (Aare River) representing past observed conditions and future predicted conditions assuming MNPP removal (No MNPP).

| Parameter (Unit)	Aare (#2085)		Rhône (#2009)
	Measurements	No MNPP	Measurements
a_1 (°C day^{-1})	**2.0316**	0.6434	**1.4927**
a_2 (day^{-1})	**0.2299**	0.3855	**0.2774**
a_3 (day^{-1})	**0.2267**	0.3177	**0.4133**
a_4 (-)	**0.0157**	0.5622	**0.6399**
a_5 (°C day^{-1})	**6.7022**	16.2387	**6.4792**
a_6 (°C day^{-1})	**4.4950**	9.9855	**2.3224**
a_7 (-)	**0.6066**	0.6066	**0.5244**
a_8 (day^{-1})	**0.7156**	1.5930	**1.0760**
	R^2 (-)		
Calibration [a]	0.97	0.96	0.94
Validation [b]	0.95	0.96	0.94
	RMSD (°C)		
Calibration [a]	0.83	0.95	0.52
Validation [b]	1.02	1.06	0.59

[a] 1990 - 1999

[b] 2000 – 2009
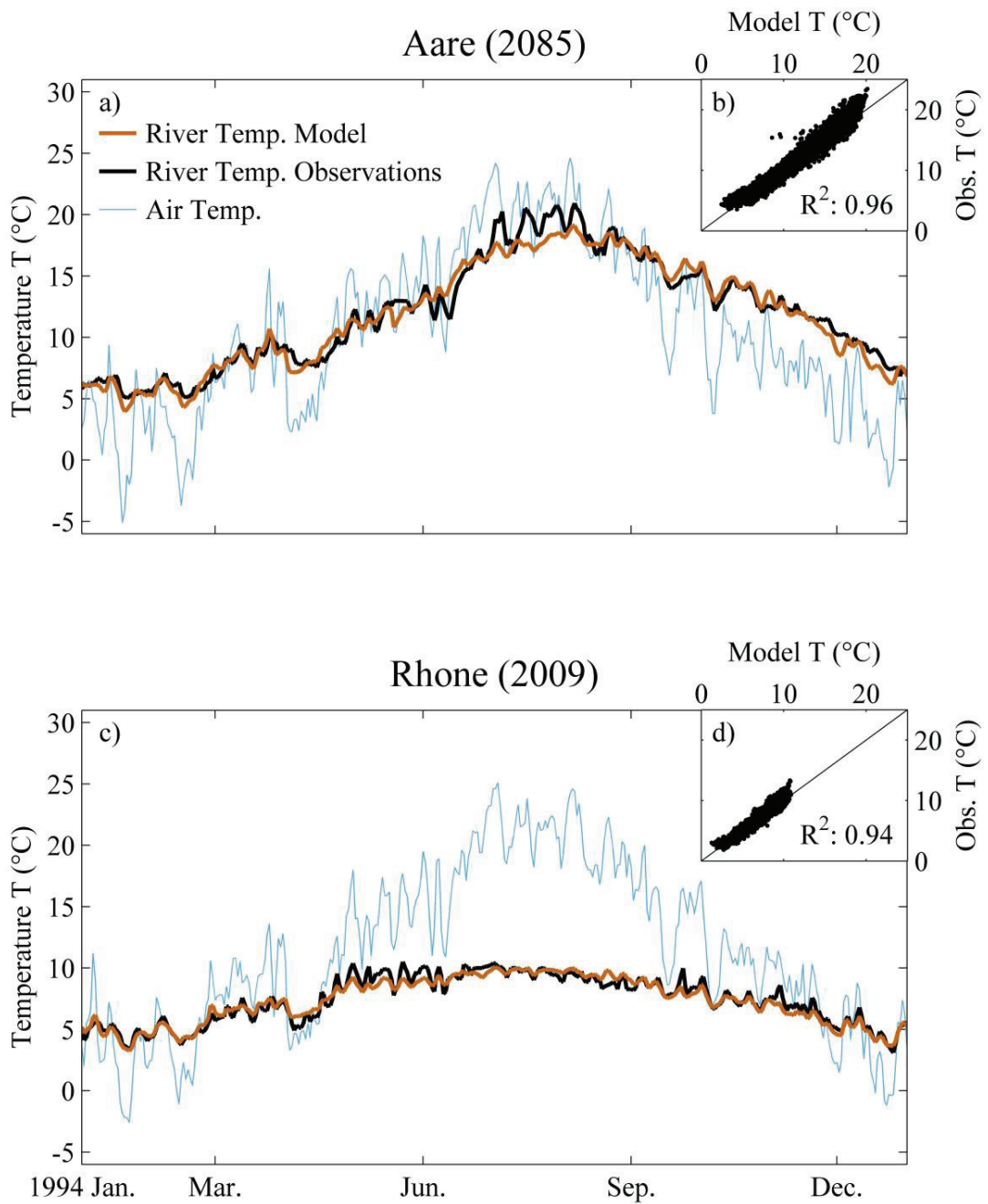
Figure 3.3. Air2stream modeled (orange) and measured (black) temperature (T) compared to air temperature (blue) for a) Aare River and c) Rhône River in 1994. The insets b) and d) show modeled versus observed temperature from 1990 to 2009 with coefficient of determination (R^2).

3.2.3.2 Suspended sediment concentration

Water density and intrusion depth of river water into downstream lakes is influenced by SSC. Intensive flow events create high levels of SSCs [*Rimmer and Hartmann*, 2014], as can exposure/erosion of sediment sources within the river basin through the so-called hysteresis effect, in which SSC varies for the same level of discharge [*Tananaev*, 2012]. River discharge regimes have been predicted to change in the future [*Birsan et al.*, 2005], suggesting that SSCs will also change. To simulate future SSCs, we used the supply-based rating model described in Doomen et al. [2008], which Fink et al. [2016] adapted to the River Rhine.

The model consists of a base level SSC (g m^{-3}) function expanded to express erosion of sediment at high discharge and sediment accumulation at low discharge. The model is expressed as

$$SSC(t) = m + b_1 Q(t)^{c_1} + d_1 d_2 b_2 \left(Q(t) - Q_{th}\right)^{c_2} - b_3 \left(1 - d_2\right), \tag{3.2}$$

where b_x, c_x and m are adjustable parameters in combination with the threshold discharge (Q_{th}), which determines whether erosion or deposition occurs within the river. The parameters d_1 and d_2 control the deposition/erosion of/from the river sediment storage (ψ (g))

$$d_1 = \begin{cases} 0 : \psi = 0 \\ 1 : \psi > 0 \end{cases} \tag{3.3}$$

$$d_2 = \begin{cases} 0 : Q \leq Q_{th} \\ 1 : Q > Q_{th} \end{cases} \tag{3.4}$$

Erosion occurs if Q exceeds Q_{th} and the river basin contains erodible sediment ($\psi > 0$). Sedimentation occurs if Q is smaller than Q_{th}. The change in ψ over time can be formulated as

$$\frac{\Delta \psi}{\Delta t} = \left(b_3 \left(1 - d_2\right) - d_1 d_2 b_2 \left(Q(t) - Q_{th}\right)^{c_2}\right) Q(t). \tag{3.5}$$

Parameters in equations (3.2) to (3.5) were calibrated (2013) and validated (2014) through an evolutionary algorithm [*Fink et al.*, 2016]. Table 3.2 and Fig. 3.4 give model performance statistics and best-fit parameter values.

Table 3.2. River suspended sediment concentration (SSC) model best-fit parameters and model performance statistics reported as coefficients of determination (R^2) and root mean square deviation (RMSD).

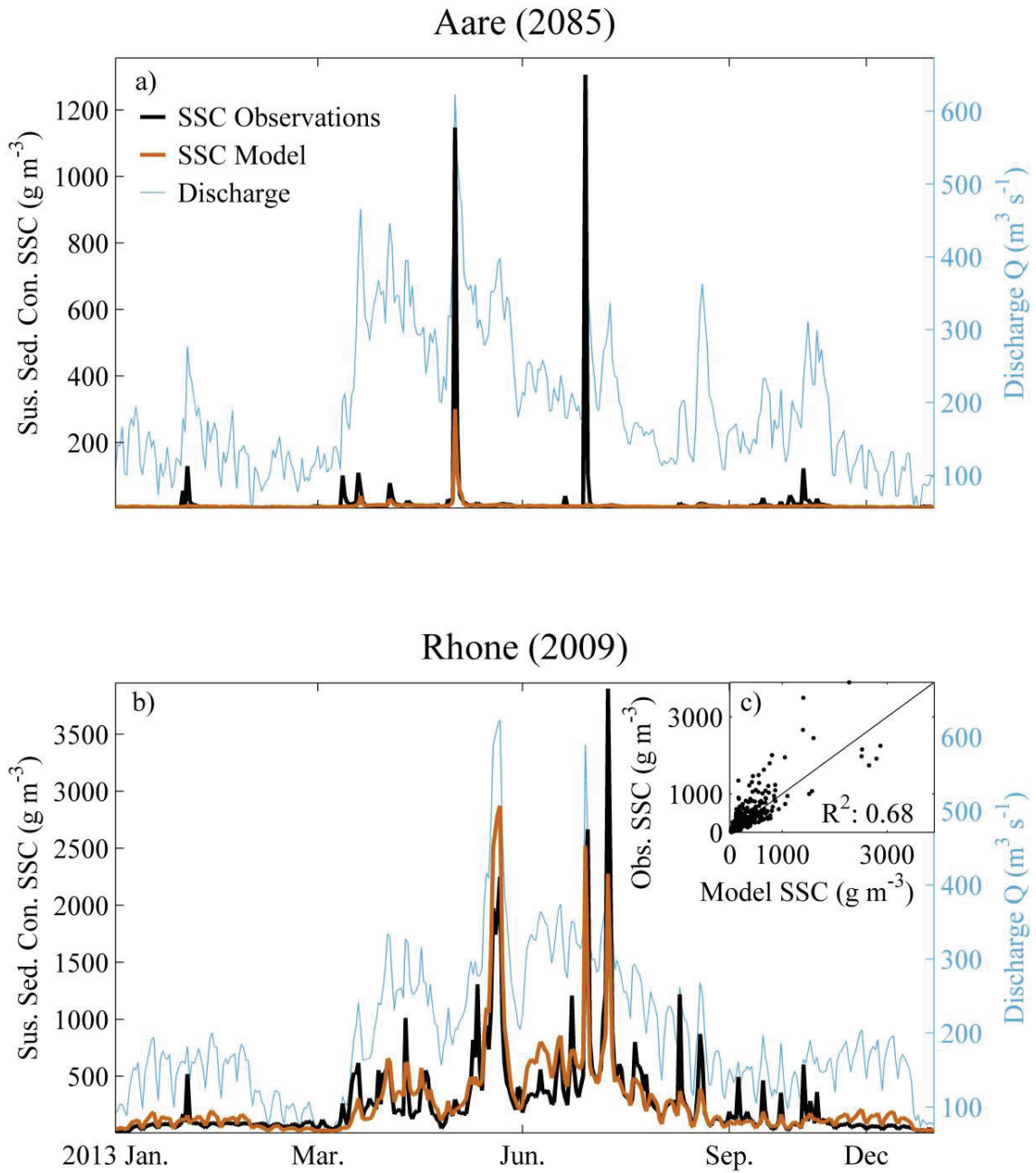| Parameter (Unit)	Aare (#2085)	Rhône (#2009)
m (g m^{-3})	8.8000	1.0000
b_1 (g day m^{-6})	0.2650	0.0006
c_1 (-)	0.6500	2.3200
b_2 (g day m^{-6})	0.0011	0.0010
c_2 (-)	2.3000	12.0000
b_3 (g m^{-3})	8.8000	2.0000
Q_{th} (m^3 day^{-1})	401	232
R^2 (-)		
Calibration [a]	0.20	0.74
Validation [b]	0.03	0.58
RMSD (g m^{-3})		
Calibration [a]	82	206
Validation [b]	217	222

[a] 2013

[b] 2014

Figure 3.4. Modeled (orange) and measured (black) suspended sediment concentration (SSC) compared to river discharge Q (blue) for a) Aare River and b) Rhône River in 2013. The insert c) shows modeled versus observed SSC for 2013 and 2014 in Rhône River with coefficient of determination (R^2).

3.2.4 Lake model

We used the one-dimensional model SIMSTRAT [*Goudsmit et al.*, 2002] to assess the impact of climate change on temperature and deep-water renewal in LB and LG. The model calculates heat fluxes and vertical mixing driven by wind and the internal wave field using a k-ε turbulence closure scheme. It has been adapted to and validated for multiple lakes including Lake Zürich [*Peeters et al.*, 2002], LG [*Perroud and Goyette*, 2010; *Schwefel et al.*, 2016], Lake Neuchâtel [*Gaudard et al.*, 2017], Lake Constance [*Fink et al.*, 2014b; *Wahl and Peeters*, 2014] and LB [*Råman Vinnå et al.*, 2017a].

The model contains seven tunable parameters, including p_1 (irradiance absorption), p_2 (sensible heat flux) and K (vertical light absorption) for heat flux adjustments from the atmosphere to the lake. Momentum and kinetic energy transfer from the wind to internal waves is tunable by C_{10} (wind drag). The internal seiche energy balance can be adjusted through α (production), C_{Deff} (loss by bottom friction) and q (vertical distribution of turbulent kinetic energy). To include the effect of seasonally varying stratification strength we followed Schwefel et al. [2016] and varied α: α_S for summer (April to September) and α_W for winter (October to March), where $\alpha_S > \alpha_W$. Here we used the best-fit parameter setup (Table 3.3) already established and validated for LG and LB by Schwefel et al. [2016] and Råman Vinnå et al. [2017a].

Building upon the model developed by Råman Vinnå et al. [2017a], we introduced an extended river intrusion scheme described in Appendix A1 (including sensitivity analysis). This scheme was chosen in order to include the effect of steep bathymetry on plume entrainment. Additionally, the robustness and simplicity of the intrusion scheme limits the uncertainty associated with more complex intrusion models including multiple parameters which can be hard to predict in the future. The entrainment of lake water into plunging underflows was modelled as proposed by Akiyama and Heinz [1984] with additional sedimentation of suspended load [*Syvitski and Lewis*, 1992; *Mulder et al.*, 1998]. The method addresses the transition of a homogenous open channel flow to a stratified underflow where entrainment and settling of sediment depend on bottom slope angle. The model scheme consists of (i) the homogenous region where river water extend from the surface to the lake bed, (ii) the plunging region where the plume separates from the lake surface and (iii) the underflow region where the plume descends downslope while entraining surrounding water until it separates from the bottom and intrudes into the lake interior [*Fink et al.*, 2016].

Table 3.3. One-dimensional lake model SIMSTRAT best-fit parameters and model performance statistics reported as vertical volume-weighted averaged root mean square deviation (RMSD-V).

Parameter (Unit)	Lake Biel	Lake Geneva
p_1 (-)	1.30	1.09
p_2 (-)	1.20	0.90
K (-)	0.70	1.40
q (-)	1.30	1.25
C_{Deff} (-)	0.0050	0.0020
C_{10} (-)	0.0016	0.0017
a_s (-)	0.0060	0.035
a_w (-)	0.0040	0.009
RMSD-V (°C)		
Calibration	0.73 [a]	0.66 [c]
Validation	0.68 [b]	

[a] 1995 - 2004

[b] 2005 - 2015

[c] 1981 – 2012

3.2.5 Data, hydrology and climate forcing

The models described above used hourly resolved data from 1989 to 2009 as inputs. For calibration/validation of river temperature, we used flow and temperature data from the Aare monitoring station #2085 (Fig. 3.2; 7°11' E, 47°03' N) and from the Rhône monitoring station #2009 (Fig. 3.2; 6°53' E, 46°21' N). The nearest meteorological stations, Mühleberg (#5530 in Fig. 3.2; 7°17' E, 46°58' N) for Aare and Aigle (#7970 in Fig. 3.2; 6°55' E, 46°20' N) for Rhône, provided air temperature data. Due to insufficient representation of high turbidity events, we calibrated/validated the SSC model with turbidity data converted to SSC with suspended sediment samples from 2013 and 2014.

The meteorological data used for SIMSTRAT included air temperature, vapour pressure, wind speed, solar radiation and cloud cover. These data were collected from the meteorological stations Cressier (#6354 in Fig. 3.2; 7°03' E, 47°03' N) for LB and Pully (#8100 in Fig. 3.2; 6°40' E, 46°31' N) for LG. Råman Vinnå et al. [2017a] and Schwefel et al. [2016] provide

additional information on climate data inputs to the one-dimensional model. The river intrusion scheme requires as input the slope angle travelled by the river underflow, which was obtained from a 25 m resolved digital height model (DHM25). Vertical temperature profiles, sampled at the deepest location of both lakes in January 1989, were used as initial conditions.

Van Vliet et al. [2013] suggested that river discharge and air temperature should be used while predicting future river temperatures. We incorporated recent findings of climate-induced changes in air temperature and river discharge regimes to model both future river temperature and SSC. Seasonal mean predictions for air temperature increase in western Switzerland (Fig. 3.2), were estimated from CH2011 [2011] for the A1B emission scenario (balanced use of renewable and fossil fuels) using results from twenty regional climate models. Flow projections were obtained from published results generated by the PREVAH (PREcipitation-Runoff-EVApotranspiration HRU Model) hydrological model [*Viviroli et al.*, 2009] using a gridded configuration as described in Speich et al. [2015] and Kobierska et al. [2011]. The model explicitly incorporates changes in glacial extent, snow melt, catchment runoff, floods and low water flows [FOEN, 2012; Bosshard et al., 2013; Speich et al., 2015]. The PREVAH outcomes for the 1981-2009 period have been validated with data from 65 river gauges [*Speich et al.*, 2015], including the two gauges upstream of LG (Rhône, #2009 in Fig. 3.2) and LB (Aare, #2085 in Fig. 3.2) used here.

3.2.6 Scenarios

Six different model scenarios were used to propagate climate change effects through the major tributaries and their associated downstream lakes. Model scenarios LG1 to LG3 represented LG while LB1 to LB3 represented LB (Table 3.4). Each scenario includes three time periods: a reference period (1990-2009), a near-future period (2030-2049) and a far-future period (2080-2099). The twenty-year intervals allowed us to resolve natural variations at seasonal and shorter time scales. We initialized the models one year prior to the investigated period for each time frame (1989, 2029 and 2079) in order to remove effects of initial conditions.

Scenarios LG1 and LB1 excluded river inflow in order to isolate lake response to climate change from potential tributary influence. Scenarios LG2, LG3, LB2 and LB3 were used to differentiate between the effects of tributary temperature and SSC, and to provide model sensitivity estimates. The LB3 scenario excluded MNPP thermal pollution from near-future and far-future time periods but not from the reference period. The LB2 scenario included

thermal pollution in modelling river water temperature. Scenarios LB2, LB3 and LG3 included SSC while LG2 did not. Low SSC values found in the Aare data resulted in negligible differences between models including and excluding SSC. Because they served primarily validation and sensitivity analysis purposes, the Aare/LB model results excluding particles and including/excluding MNPP thermal pollution (LB4 and LB5) are relegated to Appendix Figure 3.B1 and not discussed further. Scenarios LG3 and LB3 represent expected future developments.

Table 3.4. Model scenarios of climate change effects for near-future and far-future time periods, including (Inc.) and excluding (Exc.) the effects of rivers and suspended sediment. Thermal input from MNPP were also included/excluded. Most likely scenarios are shown in bold.

Lake	Exc. Rivers	Inc. Rivers	
		Exc. Suspended Sediment	Inc. Suspended Sediment
Geneva	LG1	LG2	**LG3**
		Inc. MNPP	Exc. MNPP
Biel	LB1	LB2	**LB3**

The unmodified air temperature and modelled river discharge/temperature/SSC were used as inputs for the reference periods. Near-future and far-future models incorporated predicted changes in air temperature and river discharge/temperature/SSC with maximum, medium/mean and minimum values serving as envelopes for each parameter (Figs. 3.2a and 3.5). This strategy gave nine simulations (three for scenario LG1 and LB1 which exclude rivers, i.e. no variation of discharge nor river temperature) for each near-future and far-future time period. Predicted results included a total of 87 model runs. Upper, mean and lower impact estimates (described and interpreted below) were derived from the nine basic model runs.

3.3 Results

3.3.1 Rivers

The seasonality of predicted river discharge (Q) from FOEN [2012] varies with respect to the reference period 1990-2009 (Figs. 3.5a and 3.5b). The PREVAH model show a future decrease of mean summer discharge (1st April to 30th September) for both the Aare (-3.7 m^3 s^{-1} decade^{-1}, #2085) and Rhône (-3.8 m^3 s^{-1} decade^{-1}, #2009). The decrease in summer will be compensated by an observed increase in winter flow (1st October to 31st March) of the Aare (+3.3 m^3 s^{-1} decade^{-1}) and Rhône (+3.7 m^3 s^{-1} decade^{-1}). These results confirm previous findings presented by Addor et al. [2014] and Bosshard et al. [2013].

Regional air temperatures from the A1B emission scenario (~+0.32 °C decade^{-1}; CH2011 [2011]; Fig. 3.2a) cause a predicted increase in mean annual water temperature (*T*) for both the Aare (~+0.10 °C decade^{-1}) and the Rhône (~+0.08 °C decade^{-1}). Both rivers experience seasonal variations in temperature increase similar to that predicted for air temperatures (Figs. 3.2a, 3.5e and 3.5f). The effect is strongest for Aare during summer with warming of up to +2.5 °C in water temperatures for the far-future time period relative to the reference period.

Thermal pollution from MNPP in the Aare during the reference period (blue-green line in Fig. 3.5e, Råman Vinnå et al. [2017a]) causes approximately twice as much heating in winter relative to warming from climate change in the far-future. In summer, the relationship reverses with minor MNPP warming relative to that induced by climate change. The net effect of climate warming and MNPP decommission (i.e. removal of MNPP heat from near-future and far-future time periods) on the Aare is cooling in winter and warming in summer relative to the reference period (Fig. 3.5c).

Like river temperatures, SSCs depend on river discharge. Our model therefore show SSC increasing in winter and decreasing in summer due to shifts in the discharge regime (Figs. 3.5g and 3.5h). The model results for the Rhône exhibit a mean seasonal increase of +14 g m^{-3} decade^{-1} in winter and a decrease of -11 g m^{-3} decade^{-1} in summer. For reasons explained above (section 3.2.2), results for the Aare show less variation, with a seasonal increase of +0.3 g m^{-3} decade^{-1} in winter and a decrease of -0.4 g m^{-3} decade^{-1} in summer. Altered temperature and SSC caused increases and decreases in water density for both rivers in winter and summer, respectively.
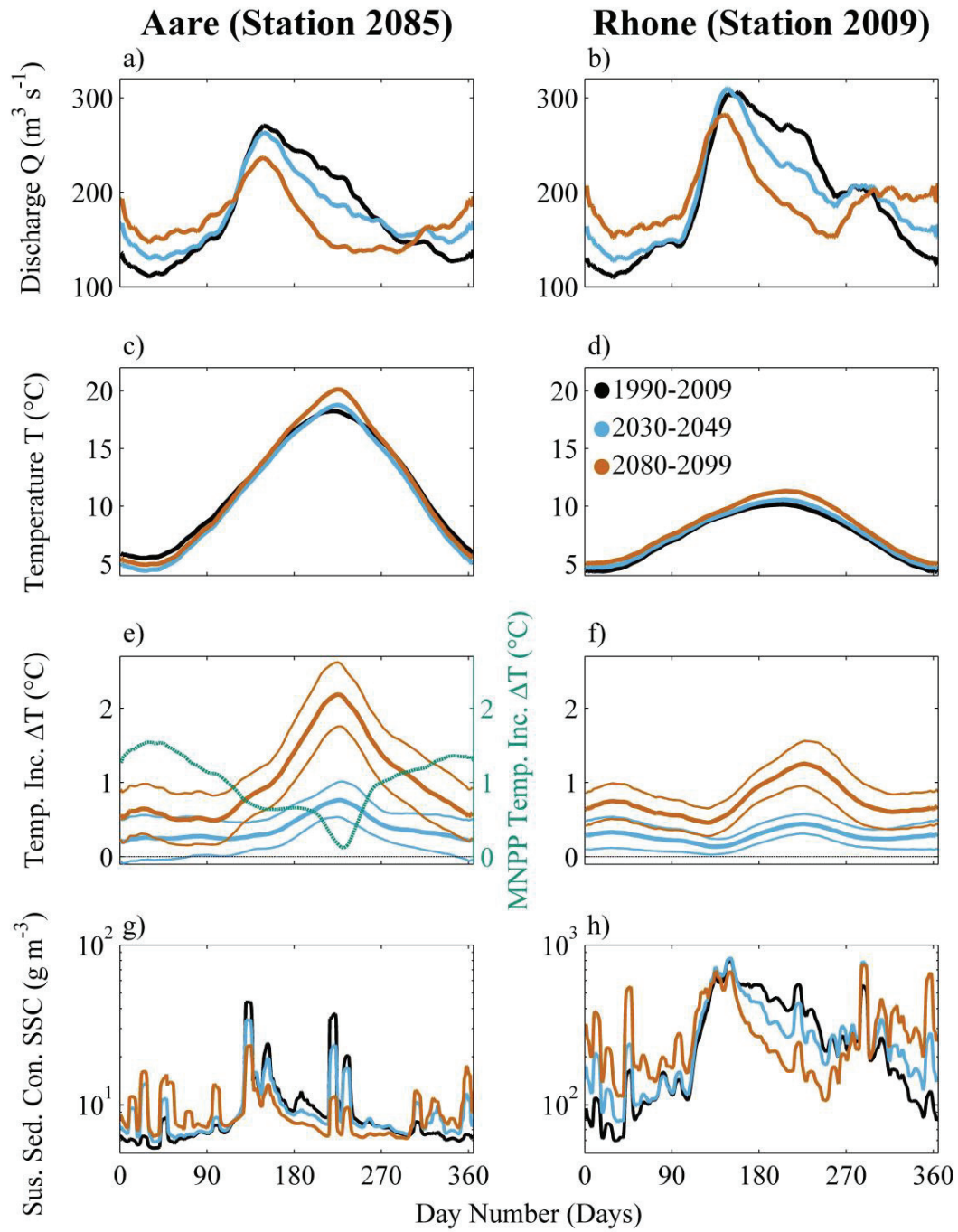
Figure 3.5. Modeled climate impact from scenarios LB3 (Aare River, left column) and LG3 (Rhône River, right column) displayed as daily average for reference (black, 1990-2009), near-future (blue, 2030-2049) and far-future (orange, 2080-2099) time periods. Discharge Q (a and b), net water temperature T (c and d) with anthropogenic heat from Mühleberg Nuclear Power Plant (MNPP) removed from near-future and far-future time periods, temperature increase ΔT (e and f) due to climate change (orange/blue) and MNPP (blue-green) as well as modeled SSC (g and h). Maximum and minimum modeled values are marked by fine lines (e and f) and or are omitted (c, d, g, and h) for clarity.

3.3.2 Lakes

Warmer air temperatures (Fig. 3.2a) predicted from climate change resulted in temperature increases in both LG and LB for all scenarios (Table 3.5). Models showed the highest warming rates in the epilimnion, intermediate values throughout the metalimnion and the lowest rates in the hypolimnion (Table 3.5). We defined the epilimnion, metalimnion and hypolimnion using the water column stability method described in Råman Vinnå et al. [2017a]. The predicted warming of LG varied only slightly among the three-different scenarios (Figs. 3.6a to 3.6c). Predicted warming of LB depends strongly on the scenario used (Figs. 3.6d to 3.6f).

Similar to the predicted warming patterns for rivers (section 3.3.1), both lakes showed seasonally varying warming patterns. Reduced warming corresponds with periods of high river discharge (Figs. 3.5a and 3.5b). This cooling effect occurs primarily in winter and mid-summer, and focussed in depth to the level of river intrusion (Figs. 3.D1b, 3.D1d and 3.7c to 3.7f). Model results showed a greater degree of fluctuations of the warming in LB than in LG. This probably results from the greater influence of the Aare on LB compared to that of the Rhône on LG, as LG has a longer hydraulic residence time. Scenario LB1, which excludes river intrusion, showed only limited seasonal variation in warming (Figs. 3.C1c and 3.C1e). According to these results, the closure of MNPP could offset climate-induced warming of LB by ~25%.

Model results show that enhanced warming of the epilimnion relative to the hypolimnion strengthens stratification (Figs. 3.7g and 3.7h). This enhances the duration of stratification (for both lakes ~+2 days decade^{-1}; Table 3.5) and slightly lifts the thermocline (in LB ~-0.1 m decade^{-1} and in LG ~-0.05 m decade^{-1}; Table 3.5).

Table 3.5. Change in temperature, length of the stratified period and depth of the thermocline (negative values correspond to a shallower thermocline) for each scenario listed in Table 3.4. Estimates given as mean of the daily difference between the reference period and the far-future time period. Temperature anomalies are volume-weighted and vertically averaged. Most likely scenarios shown in bold.

Scenario	Temperature ($°C$ decade^{-1})			Stratification (days decade^{-1})	Thermocline (m decade^{-1})
Lake Biel	Epilimnion	Metalimnion	Hypolimnion		
LB1	0.19	0.16	0.13	1.5	-0.02
LB2	0.15	0.13	0.06	2.0	-0.07
LB3	**0.13**	**0.11**	**0.05**	**2.2**	**-0.13**
Lake Geneva					
LG1	0.17	0.13	0.07	2.9	-0.07
LG2	0.17	0.12	0.07	2.8	-0.06
LG3	**0.18**	**0.16**	**0.08**	**2.2**	**-0.04**

Lake Geneva

River Excluded **SSC Excluded** **SSC Included**

Lake Biel

River Excluded **MNPP Included** **MNPP Excluded**
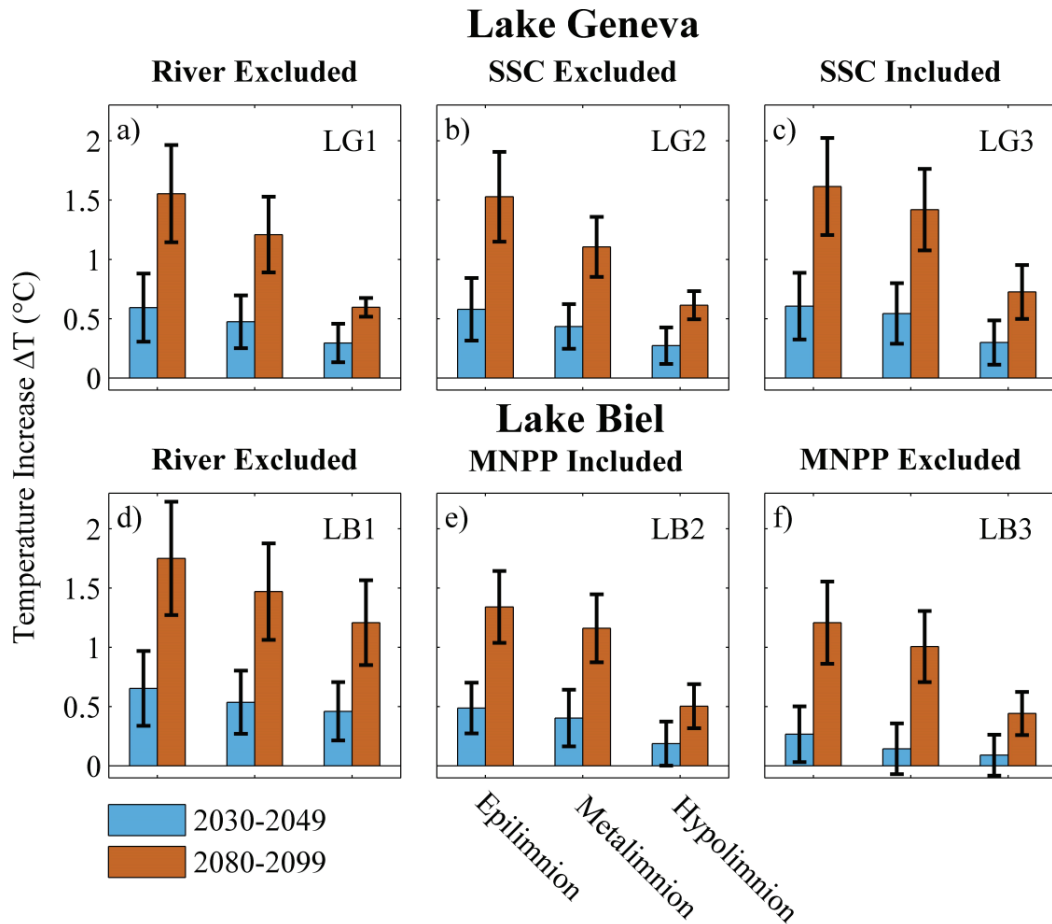
Figure 3.6. Temperature increase ΔT for near-future (blue) and far-future (orange) time periods relative to reference period temperatures, displayed as mean (columns) and standard deviation (black bars) calculated from the nine basic model runs in the near-future and far-future scenarios. Epilimnion (left pair of columns), metalimnion (middle pair) and hypolimnion (right pair) in LG (a to c) and LB (d to f). Graphs represent river intrusion excluded (a and d), river-borne SSC included (c, e and f) and excluded (b). Mühleberg Nuclear Power Plant (MNPP) heat release included in (e) and excluded (f) from near-future and far-future time periods but retained for the reference period.
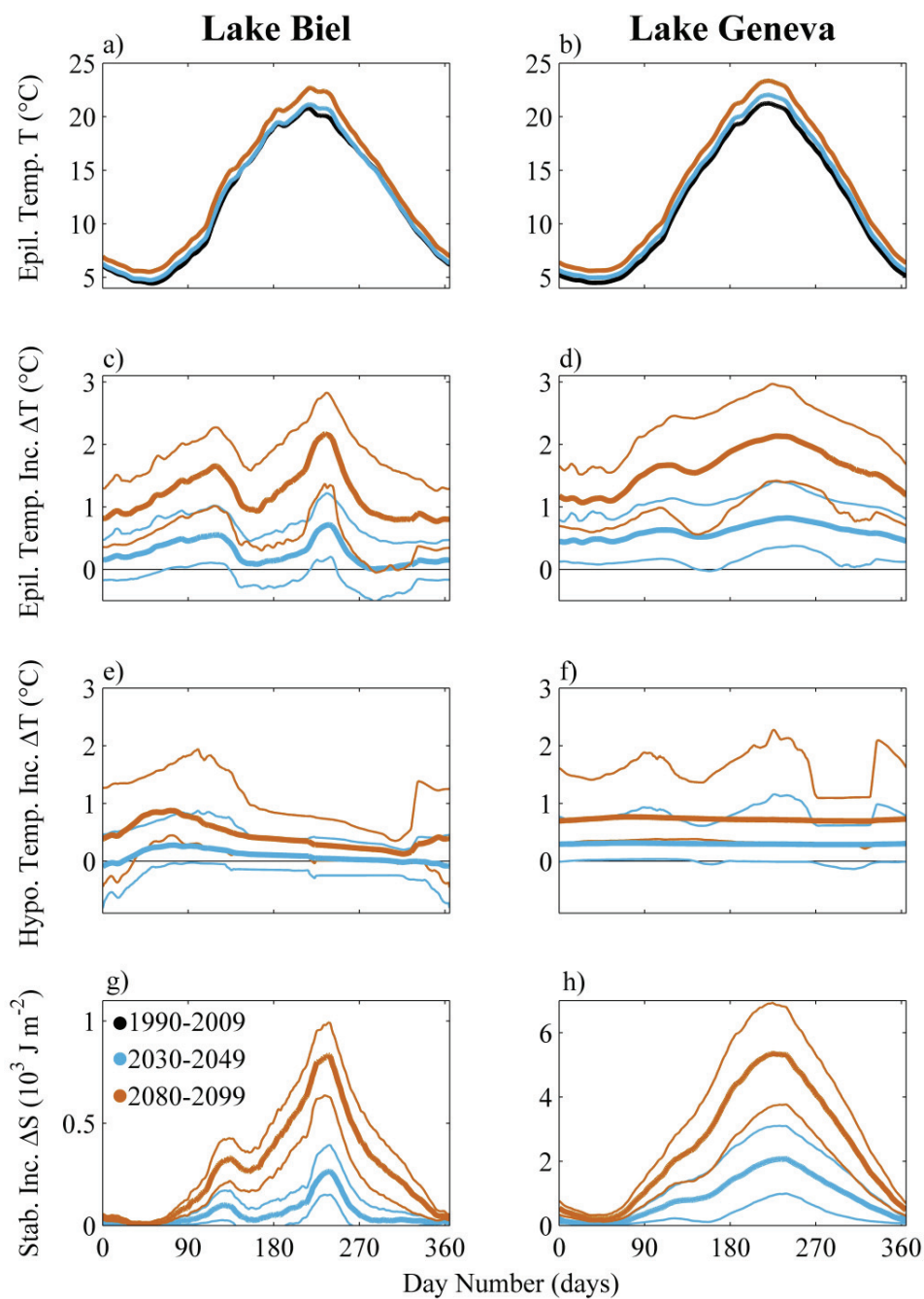
Figure 3.7. Modeled climate impact from scenarios LB3 (LB, left) and LG3 (LG, right) displayed as daily mean (thick lines) and maximum/minimum model values (thin lines) for near-future (blue, 2030-2049) and far-future (orange, 2080-2099) relative to the reference period (black, 1990-2009). Anthropogenic MNPP heat input entering LB has been excluded from near-future and far-future time periods but retained for the reference period. Temperature T (a and b), increase of temperature ΔT in epilimnion (c and d) and hypolimnion (e and f) as well as increase in stability ΔS (g and h).

We used the Schmidt [1928] stability (S) to estimate the strength of stratification (J m^{-2})

$$S = \frac{g}{A_0} \sum_{z=0}^{z_{max}} (z - z_m)(\rho(z) - \rho_m) A(z) \Delta z .$$ (3.6)

Eq. 3.6 incorporates gravity ($g = 9.81$ m s^{-2}), depth (z), lake surface area (A_0), horizontal cross section area ($A(z)$), lake density ($\rho(z)$), maximum depth (z_{max}), mean lake density (ρ_m), lake volume (V) and volumetric mean depth (z_m) defined as

$$z_m = \frac{1}{V} \sum_{z=0}^{z_{max}} z A(z) \Delta z .$$ (3.7)

The duration of stratification was determined by counting the days when temperature differed by more than 1 °C between surface (2 m depth) and deep-water (280 m for LG; 50 m for LB) [*Foley et al.*, 2012]. The maximum water column stability expression $N^2 = -(g/\rho) \Delta\rho(z)/ \Delta z$ (s^{-2}) was used to determine the thermocline depth.

The river intrusion depth is dependent on water density (temperature and SSC are dominant; dissolved solids are negligible). The Rhône is colder (Figs. 3.5c and 3.5d) and carries more suspended sediment (Figs. 3.5g and 3.5h) than Aare. Reference period results showed that the Rhône intruded in LG at greater depths relative to depths of the Aare intrusion into LB (Figs. 3.8 and 3.D1). Given the future change in river temperature and SSC, intrusion patterns will thus change as the densities of both Aare and Rhône increase and decrease during respective winter and summer seasons (section 3.3.1). This explains model results showing respective deeper and shallower intrusions during winter and summer for both rivers (Fig. 3.D1).

Model results show that warming of the Rhône generally diminishes the amount of river water penetrating beyond 200 m depth in LG (Fig. 3.8a). Enlarged river flow in winter enhances SSCs and counteracts heating, thereby increasing the amount of river water intruding beyond 200 m depth (near-future ~30%; far-future ~65%; Fig. 3.8b). The difference in winter heating for the Aare and LB epilimnion (Figs. 3.5c, 3.5e and 3.6c) generally increased the amount of water penetrating into the hypolimnion (Fig. 3.8c). Decommission of the MNPP enhances temperature differentials between LB and the Aare, thereby increasing the amount of water reaching past 30 m in LB (near-future +~80%; far-future +~120%; Fig. 3.8d). In summary, the change in river discharge regime for the Aare and Rhône results in respective increase and

decrease in winter and summer water density, resulting in a summer to winter shift of the amount of river water penetrating deeper than the metalimnion for both lakes.
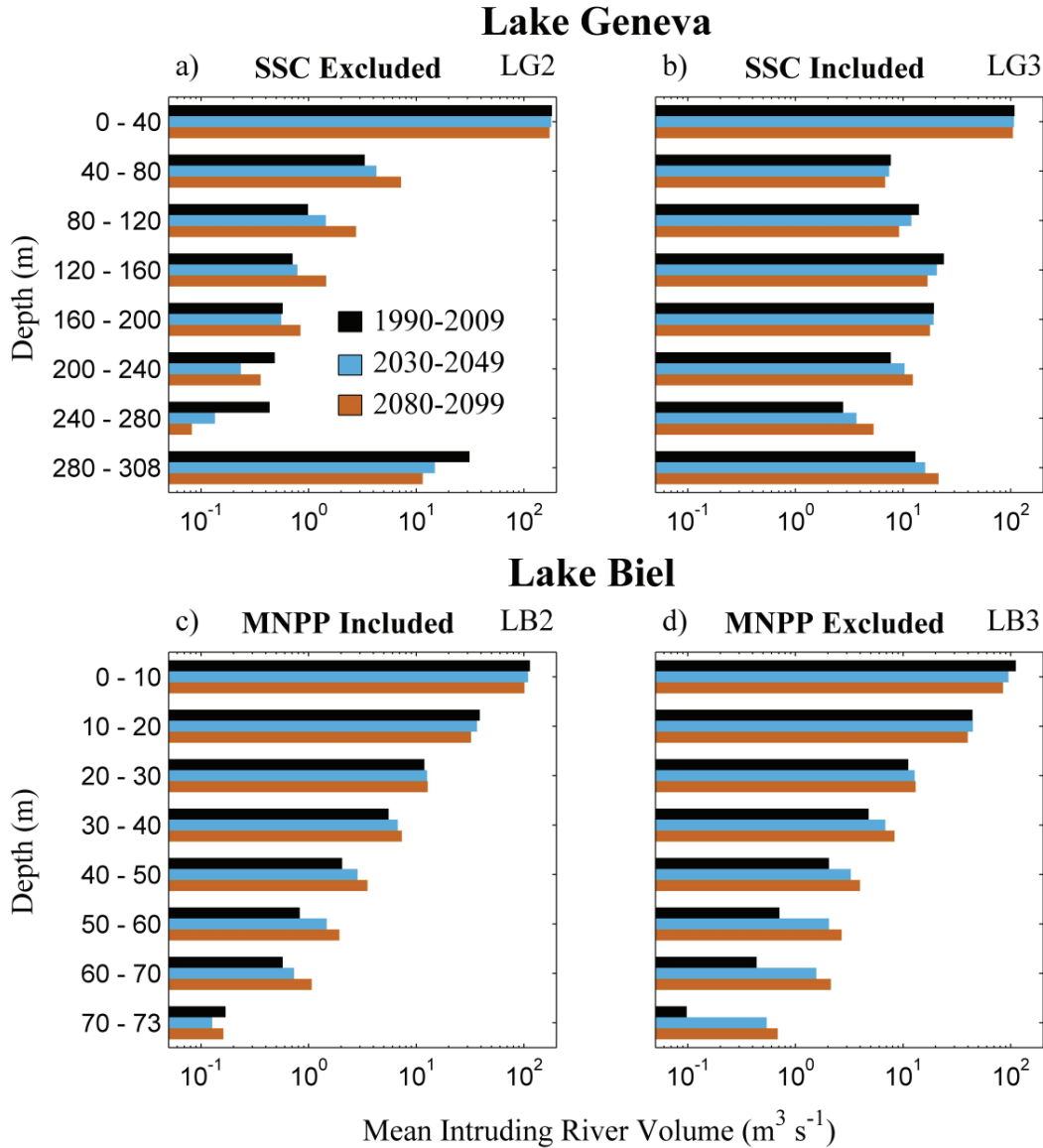

Figure 3.8. Modeled climate impact on intruding river volumes. Reference (black), near-future (blue) and far-future (orange) time periods for LG (a to b) and LB (c to d), including (b, c and d) and excluding (a) river- borne SSC and MNPP heat input included in (c) or excluded (d) from near- and far-future time periods but retained in the reference period.

3.4 Discussion

3.4.1 Rivers

Increases in air temperature expected from climate change modify tributary runoff. Less water is predicted to be bound in snow and ice at high elevation during winter and spring/summer floods will occur earlier [CH2011, 2011; FOEN, 2012]. The changed river discharge regime, appearing as increased flow in winter and decreased flow in summer (Figs. 3.5a and 3.5b), amplifies the increase and decrease in river temperature during respective summer and winter periods (Figs. 3.5e and 3.5f). Amplification results from (i) a smaller flow volume requiring less energy to heat and (ii) lower flow velocities which extend heat exposure. The PREVAH model predict that the future discharge of the Aare in summer will be ~20% smaller than summer discharge in the Rhône. These results therefore suggest that the Aare summer conditions will be more impacted by climate change than the Rhône summer conditions (Figs. 3.5e and 3.5f).

Model results concerning discharge-dependent responses to climate-induced warming were consistent with previous findings reported by Isaak et al. [2012] and van Vliet et al. [2013]. The river temperature increases predicted by this study (+0.10 °C decade^{-1} for the Aare and +0.07 °C decade^{-1} for the Rhône) were much smaller than past observed warming rates (0.34 °C decade^{-1} for the Aare and 0.21 °C decade^{-1} for the Rhône; Hari et al. [2006]). These differences may reflect contrasting reference periods with past observations conducted from 1971 to 2001 and modelled observations addressing 1990 to 2099. Past observations also incorporate effects of solar brightening during the 1980s [*Wild et al.*, 2007; *Sanchez-Lorenzo and Wild*, 2012; *Fink et al.*, 2014a], which led to additional warming of air and water.

Climate change effects aside, MNPP decommissioning in 2019 is predicted to decrease the temperature in the Aare by up to 4.5 °C at station #2085 [*Råman Vinnå et al.*, 2017a]. The cooling effect of this plant closure primarily affects winter conditions when climate change induced warming is weaker and river flow is lower (Fig. 3.5e). The heating of the Aare and LB by MNPP heat emissions equates to approximately one decade of climate-induced warming of lake surface waters [*O'Reilly et al.*, 2015; *Råman Vinnå et al.*, 2017a]. This result highlights the role of point source thermal contributions in local climate impact assessments.

The amount of suspended sediment carried by rivers depends on both discharge and the amount of erodible sediment in the watershed [*Fink et al.*, 2016]. We used a supply-based sediment rating model subjected to a changing discharge regime to examine seasonal changes in

suspended sediment for both Aare and Rhône (Figs. 3.5g and 3.5h). Consistent with previous findings reported by Pralong et al. [2015], we predict an increase in SSC during winter and decrease of SCC in summer. This is caused by two phenomena associated with increased river discharge; (i) amplified river bed erosion linked to increased intensity of high discharge events carrying enhanced volumes of SSC, and (ii) increase of the sediment available for erosion in the river catchment due to enhanced supply at low flow velocities.

Figure 3.4 and Table 3.2 show that the SSC model gives robust results for the Rhône (coefficient of determination $R^2 = 0.68$ from 2013 to 2014) but not for the Aare ($R^2 = 0.06$ from 2013 to 2014). The Aare includes several sediment-trapping reservoirs/lakes upstream of station #2085. Thus, peaks in SSC at station #2085 do not reflect watershed-scale discharge events (Fig. 3.4) but rather local precipitation and discharge events in the headwaters of a tributary (Saane River) to the Aare (Fig. 3.2). This tributary hosts few sediment traps and contributes ~34% of the downstream flow at station #2085. Given the limited impact of SSC on the Aare water density, models show only negligible impact on river intrusion depth and corresponding intruding volumes (Figs. 3.8c, 3.B1c, 3.B1e and 3.D1c). The lower reaches of the Rhône are not dammed, thus adhering more directly to model assumptions and giving clearer results (Fig. 3.4).

High SSC events are usually associated with extreme floods [*Fink et al.*, 2016], which are predicted to vary in alpine lake catchments with on-going climate change [*Glur et al.*, 2013]. The lack of constraints on extreme precipitation events introduces uncertainty into future flood frequency and magnitude predictions [*CH2011*, 2011]. Shifts in river discharge regimes also depend on the amount of water bound in snow and ice as well as on the timing of spring/summer melt. Future climate scenarios predict that ~30% of the glacier mass will remain in the Aare and the Rhône catchments by the end of the 21st century [FOEN, 2012]. Glacial meltwater is thus expected to continue to supply the Aare and Rhône throughout the time frames considered in this study. We thus assumed that the flood frequency remained unchanged, while the amplitude of the floods was adjusted in the future according to river discharge regime shifts predicted by FOEN [2012].

3.4.2 Lakes

All model scenarios showed that increased air temperature leads to warming of both lakes, especially of the epilimnion (Table 3.5, Fig. 3.6). Piccolroaz et al. [2015] showed that an increase of lake stability and earlier onset of stratification causes warming of surface waters due to the smaller volume undergoing warming and diminished heat transfer to the hypolimnion. The lake model used here showed an increase of stratification strength and a lengthening of the stratified period in both lakes (Table 3.5, Figs. 3.7g and 3.7h). Our results thus support consistently previous findings for LG reported by Foley et al. [2012], O'Reilly et al. [2015] and Schwefel et al. [2016].

Seasonal variations in warming of both epilimnion and hypolimnion (Figs. 3.7a to 3.7f) surpassed the seasonality of applied changes in air temperature (Fig. 3.2a). The model showed a decrease in warming during winter and mid-summer, which corresponds to time periods of high river discharge from the main tributaries (Figs. 3.5a and 3.5b). This cooling effect was more effective for LB than for LG (Fig. 3.7) and appeared in all scenarios except for LB1 and LG1 (Fig. 3.C1), both of which exclude coupled river effects. The extended seasonal variation in climate warming is thus driven by river discharge volume and temperature trends (Figs. 3.5 and 3.7). This response applies to aquatic systems in which a difference exist in temperature and heating regimes between rivers and lakes, but does not appear to affect water bodies with uniform temperature/heating regimes. Our results thus supports the hypothesis put forward by Zhang et al. [2014], stating that climate warming of lakes might be reduced and even reversed by addition of external water.

To investigate this effect, we varied the hydraulic residence time of LB and LG, while holding all other factors constant (Fig. 3.9). We implemented a stepwise reduction in LG size (to 1/80 of its original volume), simultaneously reducing hypsographic area but keeping maximum depth unchanged. Similar adjustments were made to LB to obtain corresponding hydraulic residence times. This stepwise approach required 972 additional model runs. These iterations showed that river water had to be cooler than lake water in order to generate a dampening effect for climate warming (Figs. 3.9a and 3.9d). Deep penetrations by large riverine volumes increase the cooling of the hypolimnion (Fig. 3.9b). The climate dampening effect is suppressed when river and epilimnion temperature are similar. MNPP thermal input creates such conditions in the Aare and therefore largely counteract the river cooling effect of the Aare on LB (Fig. 3.9c). For shorter residence times (< ~1000 days), rivers can exert influence if a

significant temperature difference exists between river and lake waters. For longer residence times (> ~1000 days), tributaries cannot significantly offset climate effects in downstream water bodies.

Climate-induced warming of lakes [*Schwefel et al.*, 2016], along with changing frequency or intensity of deep penetrating flood events [*Fink et al.*, 2016] may curtail oxygen supply to deep lakes. Recent flood analysis has also indicated that input of river-borne organic matter increases respiration, causing a paradoxical net oxygen reduction within the intruding layer [*Bouffard and Perga*, 2016]. Models showed respective winter increase and summer decrease in river water density relative to lake stability. This creates summer to winter seasonal shifts in deep intrusion dynamics for both lakes (Fig. 3.D1), causing a net annual increase of the river water penetrating into deeper parts of both lakes (Fig. 3.8). An increase of Rhône SCC in winter represented the primary driver in LG (Figs. 3.8a, 3.8b and 3.D1a, 3.D1b), while the dominant factor in LB was Aare river temperature, which cooled in winter by increased discharge and removal of MNPP heat (Figs. 3.8c, 3.8d and 3.D1c, 3.D1d).

Fink et al. [2016] also found evidence that climate change will cause diminished deep river intrusion events in summer and enhanced intrusion in winter. They predicted an annual decrease in the amount of river water reaching the deepest parts of Lake Constance. The tributaries considered here differ from the Rhine River investigated by Fink et al. [2016] primarily in terms of temperature. The Rhône catchment for example rests at a mean elevation of 2127 m and includes greater glacial coverage (11%), whereas the Rhine catchment has at mean elevation of 1771 m and only 1% glacial coverage (www.hydrodaten.admin.ch). The closure of the MNPP and associated temperature decrease contribute to increase the volume/frequency of deep intrusions (Fig. 3.5). While Fink et al. [2016] focused primarily on flood frequencies, our models emphasized river discharge regimes and interacting river and lake temperature regimes. The annual increase in river penetration to depth predicted by our models suggests future increase of deep-water oxygen supply in similar tributary-lake systems. This prediction applies mainly to meromictic lakes such as LG. Analogous effects in holomictic lakes such as LB, which mix completely each winter, are less significant. Similar to findings of Fink et al. [2016], our models indicate that deep-water oxygen conditions will worsen during strongly stratified conditions due to seasonal shifts in deep river intrusions from summer to winter. Concluding, as river water density increase in winter the volume of those intrusion events, which occurred in the reference period, will increase in the future. Likewise, high

discharge events which were previously unable to penetrate into the deep are likely to do so in the future.
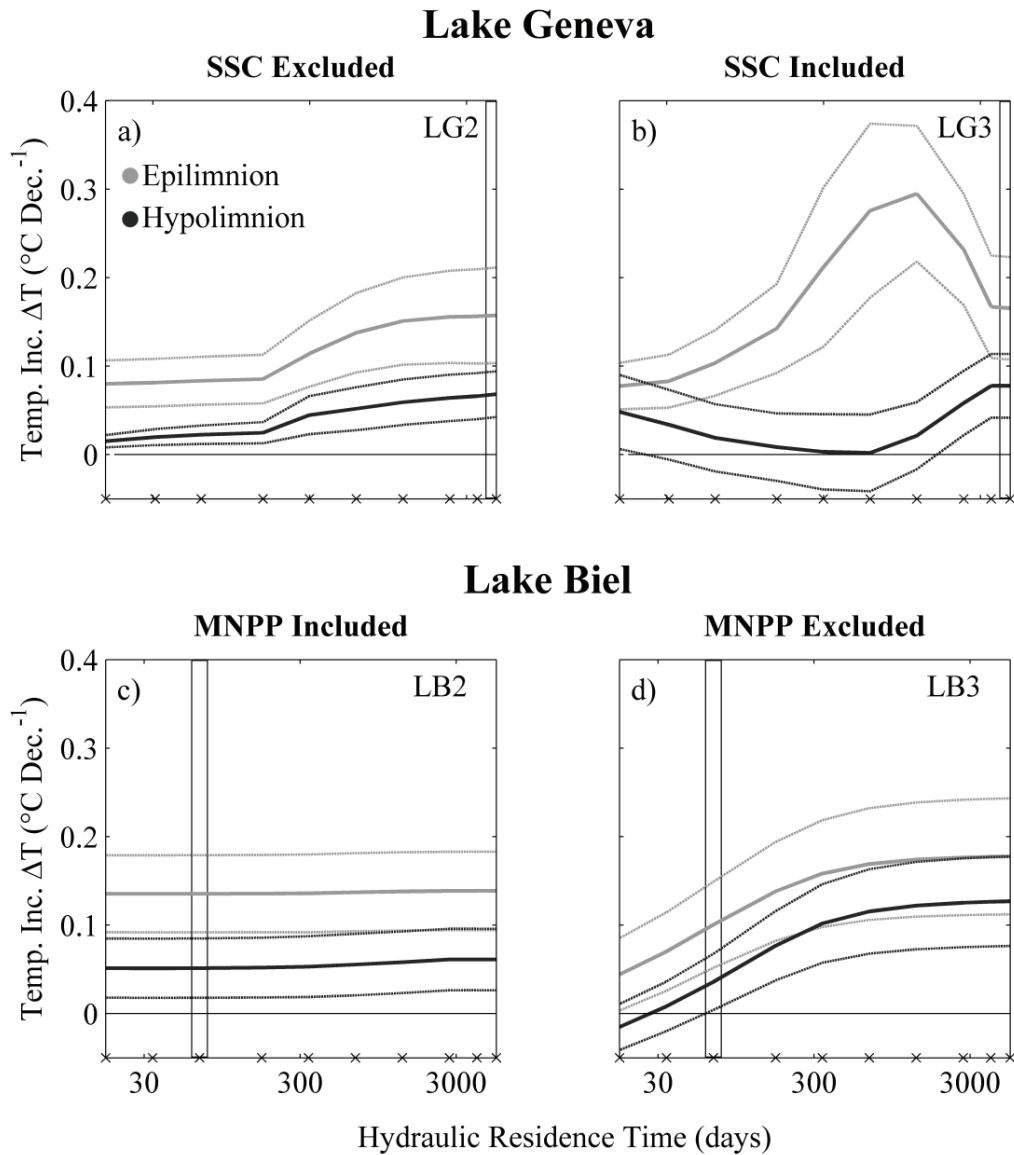

Figure 3.9. Variation in lake hydraulic residence times (changed lake volume) in response to modeled temperature increase (ΔT) in the epilimnion (grey) and hypolimnion (black) displayed as decadal mean (solid line) and standard deviation (dotted line) for LG (a and b) and LB (c to d). River-borne SSC included (b) and excluded (a, c and d), MNPP heat input included in (c) and excluded (d) from near-future and far-future time periods but retained for the reference period. Black x's mark modelled lake residence times while black rectangles mark the lakes present day residence times.

3.4.3 Model reliability

Predictions concerning the effect of climate change on rivers and lakes depend on (i) the choice of emission scenario, (ii) the accuracies of models linking climate to hydrology and climate to heat fluxes and (iii) natural variability of the system being investigated [*Raymond Pralong et al.*, 2015]. This section describes uncertainties and limitations of our approach.

Results of long-term forecasts (beyond 2050) depend strongly on representations of global greenhouse gas emission scenarios [FOEN, 2012]. Given the uncertainties in future global climate policy, we chose a median scenario, which falls between the best (ex. RCP3PD) and the worst case scenarios (e.g. A2) in terms of greenhouse gas emissions. A1B assumes a peak population at mid-century, balanced use of renewables and fossil fuels and rapid introduction of new technologies.

Estimates of future air temperatures and river discharge were obtained from a combination of regional climate models (RCMs; CH2011 [2011] and FOEN [2012]). Uncertainties associated with individual RCMs were offset by combined forecasts from multiple-model chains. Numerous studies have performed detailed evaluations of uncertainty in air temperature and river discharge under established emission scenarios (RCP3PD, A1B, A2) and accounting for global-regional climate model interactions [*Bosshard et al.*, 2011, 2013; *CH2011*, 2011; *Addor et al.*, 2014].

The degree of accuracy with which model input parameters represent future conditions determines the accuracy of model predictions. We therefore ran the river temperature model with varying parameters to evaluate model sensitivity (Table 3.1) for different yet similar datasets. The air2stream parameter a_1 showed the greatest degree of sensitivity, varying within three orders of magnitude. The a_1 parameter, however, does not respond to variations in river discharge or air temperature (Eq. 3.1), which limits its sensitivity to climatic input data. The other parameters (a_2 to a_8) varied only within one order of magnitude (Table 3.1). The SSC model gives better results for the Rhône (coefficient of determination $R^2 = 0.68$ from 2013 to 2014) than for the Aare ($R^2 = 0.06$ from 2013 to 2014). Dams and reservoirs infrastructure upstream of station #2085 along the Aare dampen sediment transport events and decouple them from regional discharge events (see above; Fig. 3.4). Given the relatively minor effect of SSC on the Aare water density, variation in the input parameter does not influence river intrusion depths (Figs. 3.B1e to 3.B1f and 3.D1c to 3.D1d). As with other vertical, one-dimensional models, SIMSTRAT cannot account for lateral heterogeneities in lakes. This inherent weakness

in model design however does not significantly diminish the accuracy of model predictions concerning LB and LG [*Schwefel et al.*, 2016; *Råman Vinnå et al.*, 2017a].

Of special importance for climate research in lakes is the sensitivity of models to shifts in the heat budget. Forcing parameters of importance, besides air temperature, include wind speed, solar irradiance, vapour pressure and light absorption. The sensitivity of SIMSTRAT to variable forcing has previously been established for lakes in Switzerland. Schmid and Köster [2016] demonstrated how solar brightening from 1981 to 2013 increased Lake Zürich surface warming comparable to heating by increased air temperature. Schwefel et al. [2016] revealed strengthening of the thermocline and decrease of the mean lake temperature by increased light absorption in LG, whereas a decrease in absorption had the reverse effect. As of yet, reliable predictions of wind speed, irradiance and vapour pressure under future climate conditions are not available for Switzerland [*CH2011*, 2011]. Therefore, we use long-term (1981 to 2013) data from station #8100 (Fig. 3.2) as guidance for potential annual atmospheric forcing trends (Fig. 3.A6; Table. 3.6).

The sensitivity of SIMSTRAT was tested in LG by applying these trends, individually and combined, to the reference period. The increasing trend in air temperature was included for comparison while no trend could be identified in cloud cover which was excluded. The decreasing trend in wind speed cooled the lake while the increasing trend in irradiance and vapour pressure heated the lake comparable to air temperature (Table 3.6). By combining all trends, we obtained similar warming of the LG epilimnion (~+0.38 °C decade^{-1}) as observed over land (+0.38 °C decade^{-1}; 1985-2002; Wild et al. [2007]) and globally in lakes (~0.34 °C decade^{-1}; 1985-2009; O'Reilly et al. [2015]) as well as monitored in LG surface waters (~+0.51 °C decade^{-1}, 1983-2000; Gillet and Quétin [2006]). The historical effect of increased air temperature caused ~40% to ~70% of the heating in the epilimnion/metalimnion and ~240% in the hypolimnion. Here we include predictions of future temperature and precipitation. The extrapolation of observed atmospheric trends into the future is outside the scope of the present study. Yet, we expect our lake water temperature predictions for the near-future and far-future scenarios to underestimate the total heating in shallow water and overestimate warming of deep water. Nonetheless, the solar brightening trend observed over Switzerland from 1980 to 2000, caused by a decrease in atmospheric aerosols, will not continue into the future [*Sanchez-Lorenzo and Wild*, 2012], thereby reducing the uncertainty of our predictions.

Table 3.6. Observed trends in atmospheric forcing (1981 to 2013) at station #8100 (Fig. 3.2) per decade (dec), and modelled temperature increase in Lake Geneva (LG) with forcing trends applied to the reference period (1990 to 2009).

Parameter	Observed Atmospheric Trend	Modelled LG Temperature Change ($°C\ dec^{-1}$)		
		Epilimnion	Metalimnion	Hypolimnion
Wind Speed	-0.097 ($m\ s^{-1}\ dec^{-1}$); -5.7 (% dec^{-1})	-0.022	-0.149	-0.089
Shortwave Irradiance	3.8 ($W\ m^{-2}\ dec^{-1}$); 2.6 (% dec^{-1})	0.134	0.131	0.027
Vapour Pressure	0.26 ($mbar\ dec^{-1}$); 2.6 (% dec^{-1})	0.122	0.085	0.05
Air Temperature	0.40 ($°C\ dec^{-1}$); 3.7 (% dec^{-1})	0.149	0.101	0.017
All Combined		0.379	0.147	0.007

In this study we assumed that glacial melt-water feeding both the Aare and Rhône in summer will not disappear within the time frames considered. Loss of glacial sources would modify the discharge regime, especially in summer, which would affect accuracy of temperature, SSC and intrusion depth estimates. However, as stated in section 3.4.1, FOEN [2012] predicts that the Aare and Rhône catchments will retain 30% of their glacial masses by the year 2100. These predictions support assumptions concerning the Aare and Rhône discharge regimes used here. Point sources/sinks of anthropogenic heat can affect inland water bodies response to climate change, as shown by the MNPP effects described here. Other changes in catchment management, such as hydropower damming would also alter river discharge regimes and by extension, temperatures, SSCs and deep-water renewal [*Fink et al.*, 2016]. Thus, the correctness of future climate change predictions depends on adequate accounting of regional anthropogenic factors affecting physical processes in the system under investigation.

3.5 Conclusion

Aquatic processes in lakes are the result of regional forcing and the upstream catchment environment. This study investigated the impact of climate change on inland waters by propagating climatic inputs through integrated fluvial-lacustrine systems. We fed predicted future climatic data into models for two connected river and lake systems in order to evaluate downstream thermal responses and how river discharge regime shifts might affect deep-water renewal in the lakes. Climate data propagated through discharge-dependent river temperature and suspended sediment concentration models, which were coupled to a one-dimensional lake model. We applied this approach for the two peri-alpine Lakes Biel and Geneva.

The models showed that climate warming of rivers is enhanced in summer and diminished in winter due to future river discharge regimes with decreased flow in summer and increased flow in winter. This climate-caused alteration of the flow regime likewise increase and decreases the river-borne suspended sediment load in winter and summer, respectively.

Both lakes showed large seasonal temperature increases that could not be solely explained by climate-related (predicted) increases in air temperature. Instead, the lakes experienced a cooling effect associated with upstream tributaries, which responses to increasing future air temperatures differed from that of the lakes. The smaller Lake Biel showed stronger response to this repressive effect of climate warming compared to the larger Lake Geneva. Predicted changes in Lake Biel strongly depend on the removal of upstream anthropogenic thermal emission into Aare River. Local anthropogenic point sources of heat can thus rival climate change in their influence on lakes. This damping of climate warming depends on the lakes hydraulic residence times and requires adequate river/lake temperature differences. Our models indicate that tributaries can exert system-wide influence on lakes with hydraulic residence times < ~1000 days. Lake systems with longer residence times are resistant to tributary effects but may respond on a local level.

The combination of changes in river SSC and differential lake/river temperature/warming result in a seasonal shift of deep-water penetration (by rivers) into lakes. The volume of river water penetrating to deeper parts of lakes specifically decreases in summer and increases in winter. Higher rates of deep-water renewal can in turn enhance reoxygenation of the deepest reaches of lakes, which may otherwise experience lower oxygen concentrations under climate change.

Appendices

Appendix 3.A1 River Intrusion Model

Figure 3.A1 summarizes the river intrusion model. The depth where the river plume separates from the surface, the so-called plunge depth (h_p), depends on the slope angle (σ), gravity (g), coefficients ($S_1 = 0.25$; $S_2 = 0.75$; Ellison and Turner [1959]), bed friction ($f_t = 0.02$; Akiyama and Heinz [1984]), initial flow per unit width (q_0) = V_r / W_r dependent on river discharge (V_r), river width ($W_r = 100$ m for Aare and $W_r = 120$ m for Rhône) and the relative density difference ($\rho' = (\rho_r - \rho_l(z_1)) / \rho_l(z_1)$) between the homogenous river (ρ_r) and lake (ρ_l) with z_1 = surface.

$$h_p = e_1 \left(\frac{f_t}{\sigma(z)S_2} \frac{q_0^2}{g\rho'} \right)^{1/3} + e_2 \left(\frac{q_0^2}{S_1 g\rho'} \right)^{1/3} \tag{3.A1}$$

The level of initial plume entrainment is treated differently on a gentle versus a steep slope. This is controlled by the two coefficients e_1 and e_2.

$$e_1 = \begin{cases} 1 : \sigma(z_1) < \sigma_c \\ 0 : \sigma(z_1) \geq \sigma_c \end{cases} \tag{3.A2}$$

$$e_2 = \begin{cases} 0 : \sigma(z_1) < \sigma_c \\ 1 : \sigma(z_1) \geq \sigma_c \end{cases} \tag{3.A3}$$

where the critical slope angle $\sigma_c = f_t S_1 / S_2$ distinguishes between gentle and steep slope designations. The initial height of the underflow (h_d) can then be written as

$$h_d(z_1) = h_p (1 + \gamma) \tag{3.A4}$$

where γ is the entrance mixing coefficient equal to ~0 for gentle slopes and increasing to larger values for steeper slopes. Here we find that a value of $\gamma = 0.1$ provides best results. The initial underflow temperature (T_u), velocity (U_u), particle content (P_u) and volume (V_u) is consequently expressed as a function of ambient lake water temperature (T_l), river temperature (T_r) and river particle content (P_r) in the homogenous region.

$$T_u(z_1) = T_l(z_1) \frac{(h_d(z_1) - h_p)}{h_d(z_1)} + T_r \frac{h_p}{h_d(z_1)} \tag{3.A5}$$

$$U_u(z_1) = (1 + \gamma) \frac{q_0}{h_d(z_1)} \tag{3.A6}$$

$$P_u(z_1) = P_r \frac{h_p}{h_d(z_1)} \tag{3.A7}$$

$$V_u(z_1) = V_r \frac{h_p}{h_d(z_1)} \tag{3.A8}$$

Once the plume has passed through the plunge region into the underflow region, we express h_d, U_u, T_u and V_u as

$$h_d(z+1) = h_d(z) + E(z)\Delta x \tag{3.A9}$$

$$U_u(z+1) = U_u(z) \frac{h_d(z)}{h_d(z+1)} \tag{3.A10}$$

$$T_u(z+1) = T_l(z) \frac{(h_d(z+1) - h_d(z))}{h_d(z+1)} + T_u(z) \frac{h_d(z)}{h_d(z+1)} \tag{3.A11}$$

$$V_u(z+1) = V_u(z) \frac{h_d(z)}{h_d(z+1)} \tag{3.A12}$$

where Δx is the horizontal distance between z and $z + 1$ and the entrainment factor (E) is expressed as a function of the entrainment constant ($\beta = 0.0015$; Ashida and Egashira [1975]) and the Richardson number (R_i).

$$E(z) = \frac{\beta}{R_i(z)} \tag{3.A13}$$

$$R_i(z) = \frac{f_t}{\sigma(z)S_2} \tag{3.A14}$$

For P_u, we include a sedimentation term as proposed by Syvitski and Lewis [1992], which depends on the removal rate (r) and $\Delta t = \Delta x / U_u(z)$.

$$P_u(z+1) = \frac{h_d(z)}{h_d(z+1)} \left(P_u(z) - re_3 P_u(z) e^{-r\Delta t} \Delta t \right) \tag{3.A15}$$

Sedimentation occurs only if the plume velocity drops below a critical settling velocity (U_c) subject to the parameter e_3:

$$e_3 = \begin{cases} 1 : U_u(z) < U_c \\ 0 : U_u(z) \geq U_c \end{cases} \qquad\qquad (3.A16)$$

We set U_c equal to 0.46 m s^{-1} and r equal to 4.7 day^{-1} to represent medium-sized silt following Mulder et al. [1998]. The plume travels downslope as long as the underflow plume density (ρ_u) exceeds $\rho_l(z)$. Once $\rho_u \leq \rho_l(z)$, the plume raises from the slope and intrudes into the lake proper. The terms T_u and V_u were thus added to the lake model at this depth. Calculations excluded expressions for the settling of accumulated particles following plume intrusion, assuming that these exert only minor impacts on lake temperature and density.

The sensitivity of the river intrusion depth to entrainment of ambient water into the plume was tested by propagating a range of β (Eq. 3.A13) values from 1 to 1×10^{-6} through model spaces composed of temperature, discharge and suspended sediment concentration data from the Aare (station #2085). Figures 3.A2 to 3.A4 compare modelled intrusion depths to empirical estimates based on vertical temperature and light transmission data at the centre of LB (7°11' E, 47°6' N) collected shortly after major river intrusion events. Additionally, acoustic Doppler current profiler (ADCP) measurements of river plume intrusions in LB (47°5'N 7°12'E, 2 km from Aare inlet) were used for a temporal sensitivity analysis of the intrusion model (Fig. 3.A5). Comparison of the modelled intrusion depth with light transmission depth (whose minimum value represents a proxy for actual river intrusion depth) suggests that $\beta = 0.0015$ offers an adequate representation of intrusion depth. Larger β values generate intrusion depths shallower than the empirical reference points whereas smaller β values exerted only minor impact on deepening the intrusion depth. The intrusion model used here was compared (Figs. 3.A2c to 3.A5c) to the intrusion scheme proposed by [*Cortés et al.*, 2014], which produced an inferior result for LB.
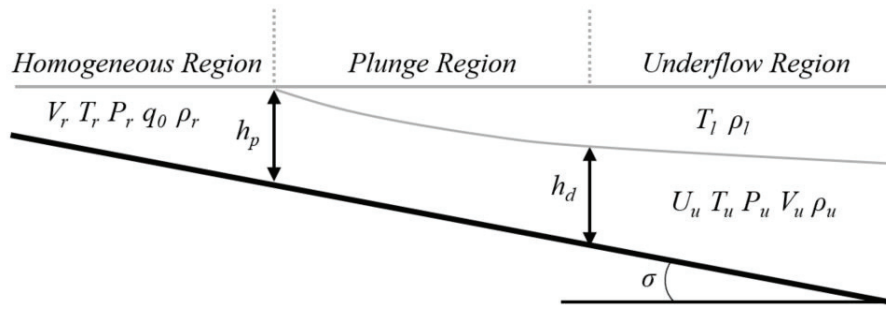
Appendix Figures

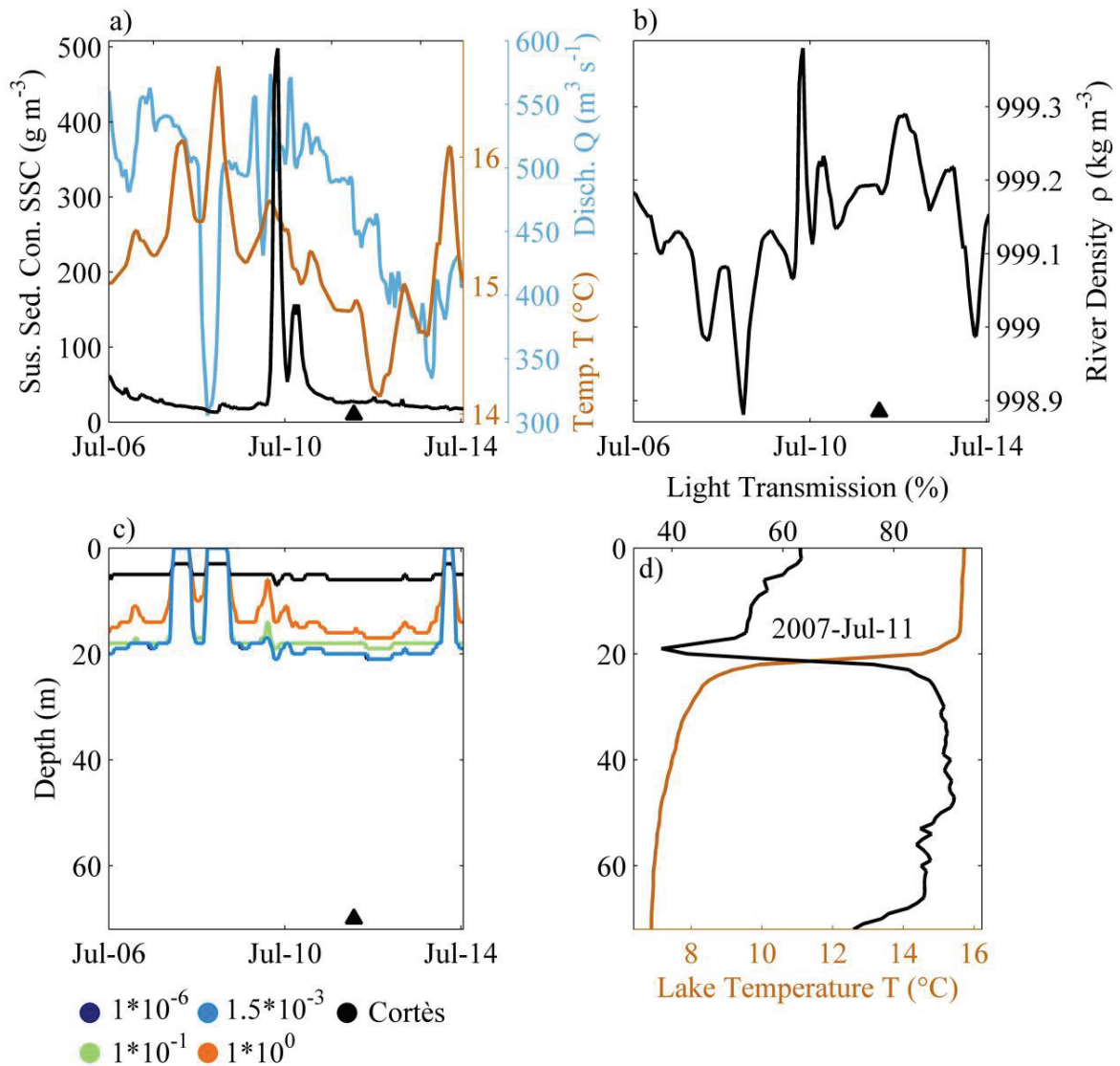**Figure 3.A1.** Illustration of river intrusion model.

Figure 3.A2. River intrusion entrainment sensitivity analysis for the LB/Aare system in July 2007. a) SSC (black), temperature (T; orange) and river discharge (Q; blue) from Aare station #2085. b) River density at station #2085 obtained from T and SSC in a). c) River intrusion depth calculated from supporting information (S1) with varying entrainment constant β (Eq. 3.18); light green denotes the value used in this study; black indicate intrusion depth modelled as in Cortés et al. [2014]. d) Vertical measurements of T and light transmission in LB for 11th July 2007. ▲ marks the time in a) to c) of the vertical profile in d).
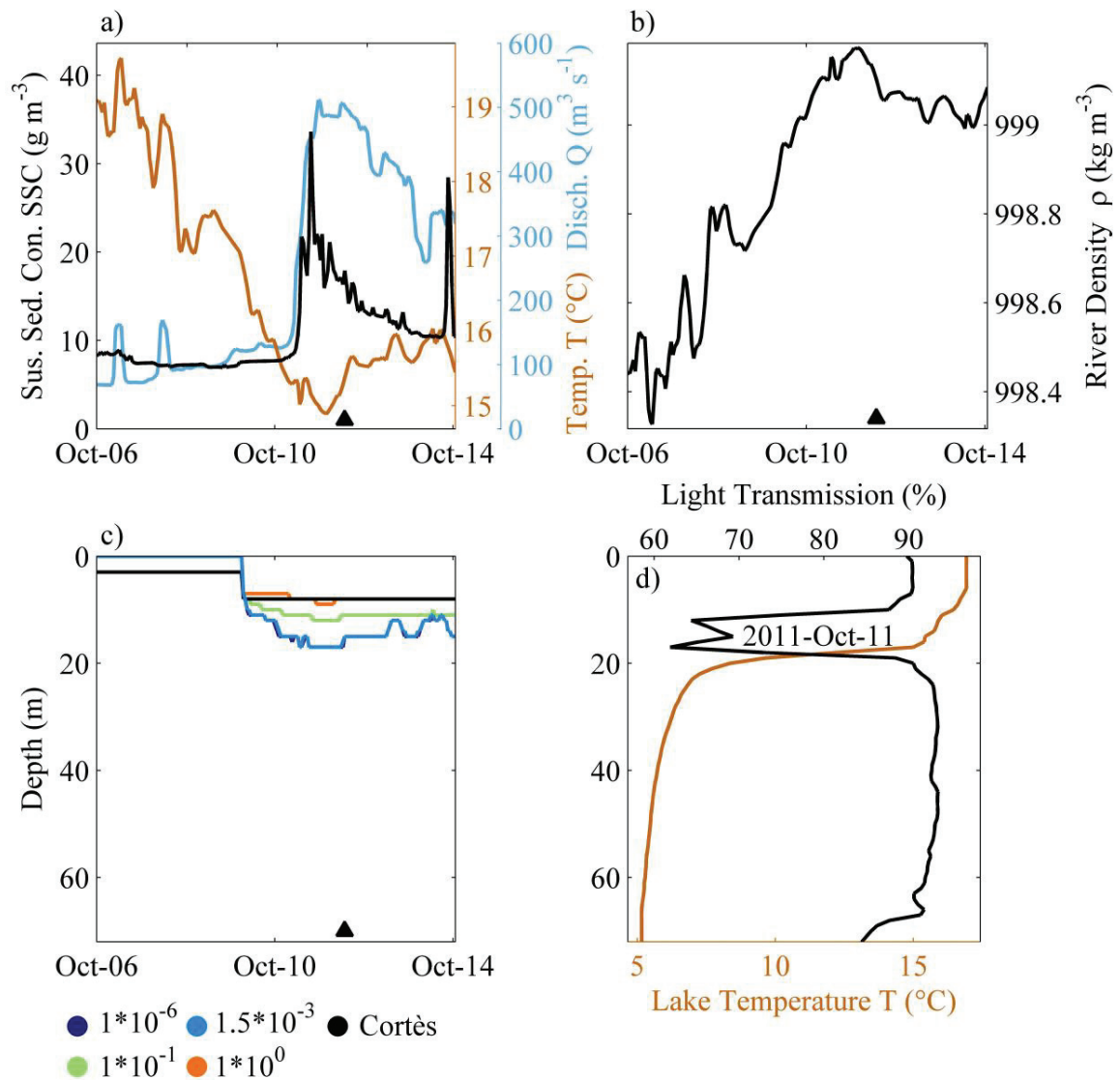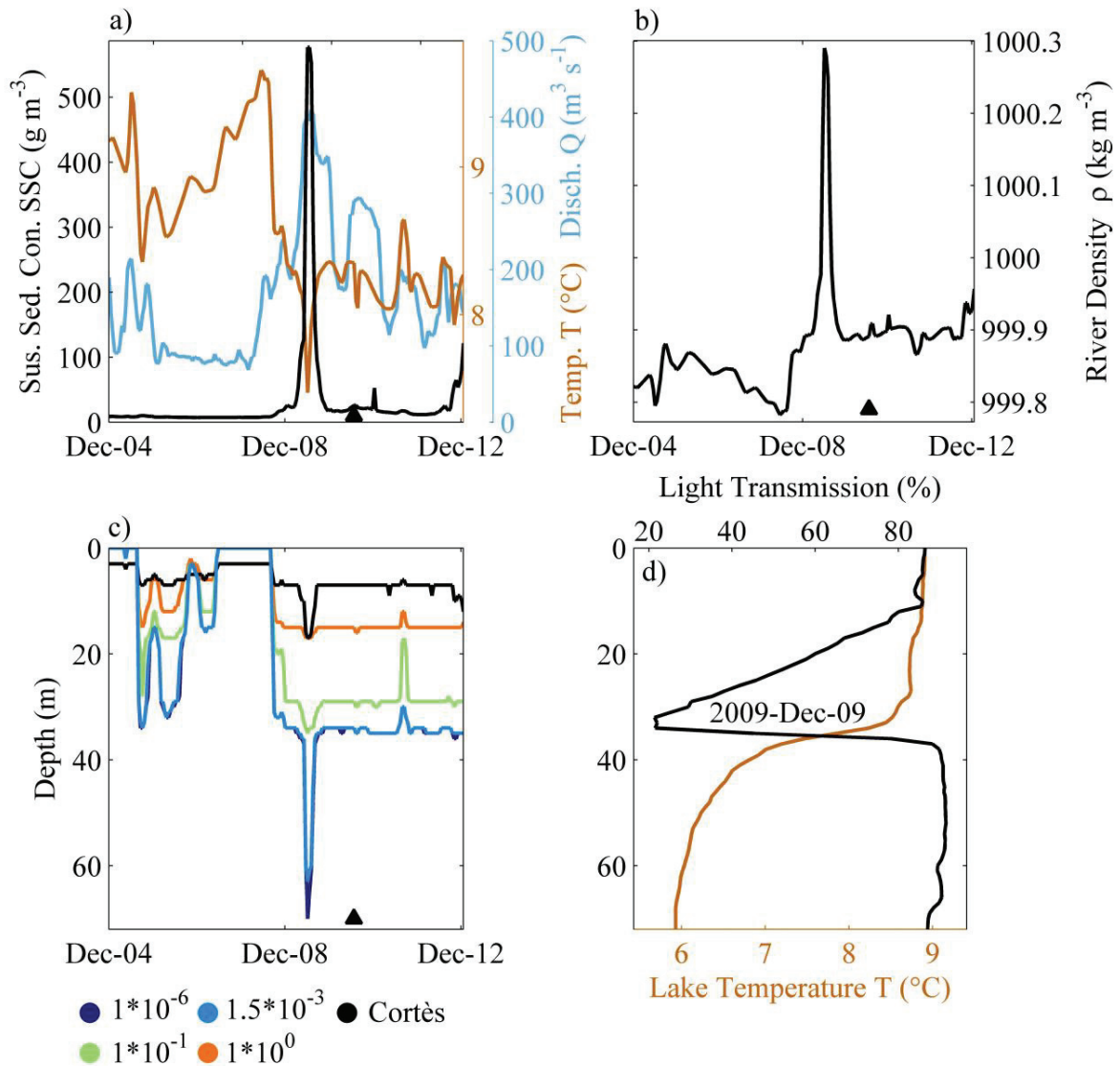
Figure 3.A3. River intrusion entrainment sensitivity analysis for the LB/Aare system in October 2011. a) SSC (black), temperature (T; orange) and river discharge (Q; blue) from Aare station #2085. b) River density at station #2085 obtained from T and SSC in a). c) River intrusion depth calculated from supporting information (S1) with varying entrainment constant β (Eq. 3.18); Light green denotes the value used in this study; black indicate intrusion depth modelled as in Cortés et al. [2014]. d) Vertical measurements of T and light transmission in LB for 11th October 2011. ▲ marks the time in a) to c) of vertical profile in d).

Figure 3.A4. River intrusion entrainment sensitivity analysis for the LB/Aare system in December 2009. a) SSC (black), temperature (T; orange) and river discharge (Q; blue) from Aare station #2085. b) River density at station #2085 obtained from T and SSC in a). c) River intrusion depth calculated from supporting information (S1) with varying entrainment constant β (Eq. 3.18); light green denotes the value used in this study; black indicate intrusion depth modelled as in Cortés et al. [2014]. d) Vertical measurements of T and light transmission in LB for 9th December 2009. ▲ marks the time in a) to c) of vertical profile in d).
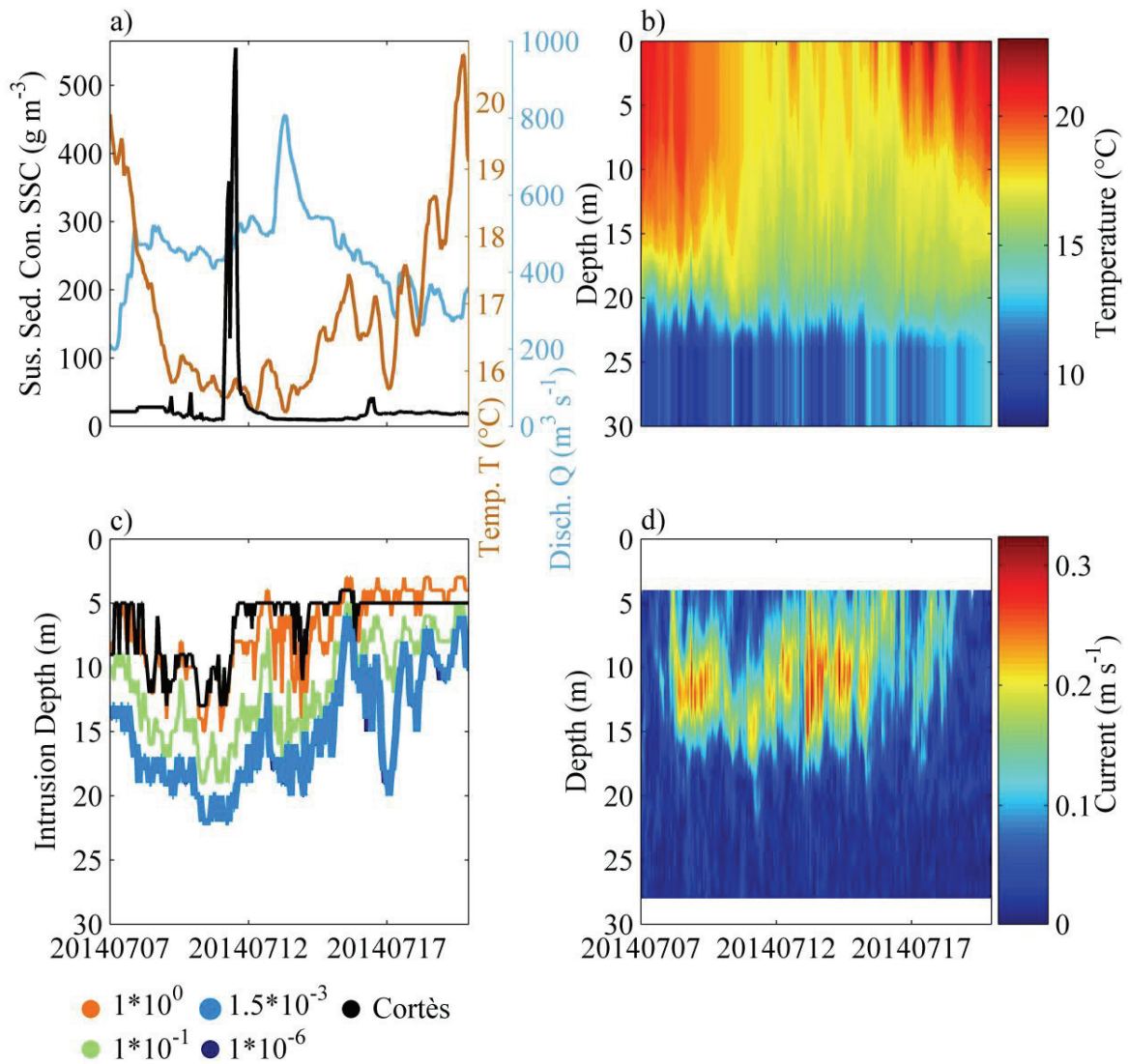
Figure 3.A5. River intrusion entrainment sensitivity analysis for the LB/Aare system in July 2014. a) SSC (black), temperature (T; orange) and river discharge (Q; blue) from Aare station #2085. b) Lake temperature at M3 station. c) River intrusion depth calculated as in supporting information (S1) using river/lake density obtained from a) and b) with varying entrainment constant β (coloured, Eq. 3.18); light blue denotes the value used in this study; intrusion depth (black) calculated with method described in Cortés et al. [2014]. d) Current speed obtained from ADCP at M3 station; velocities > 0.15 m s^{-1} are associated with the passing river plume.
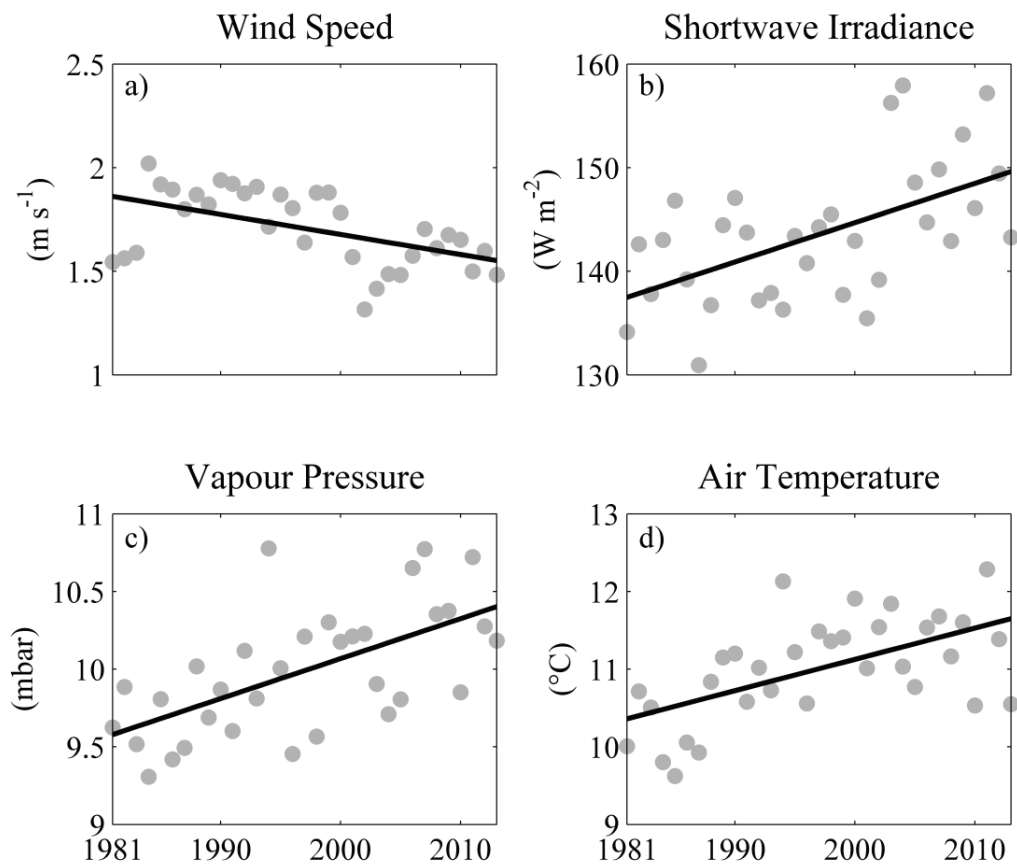
Figure 3.A6. Annual atmospheric forcing (grey dots) of wind speed a), shortwave radiation b), vapour Pressure c) and Air Temperature d) at station #8100 (Fig. 3.2). Black line shows trends (Table 3.6) with 95% confidence interval marked by black dots.
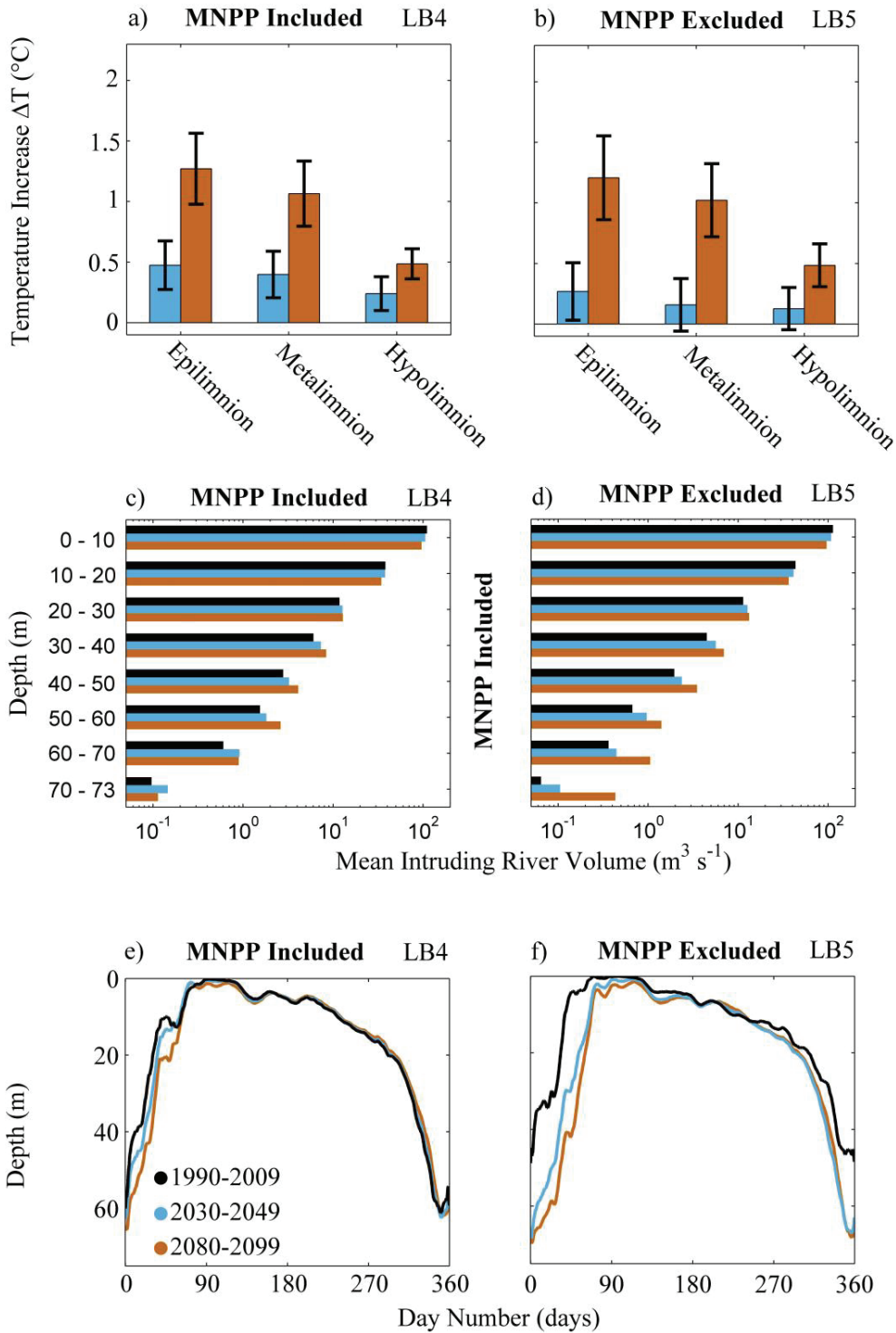
Figure 3.B1. Modeled climate impact on LB excluding river borne SSC. Temperature increase ΔT (a and b) displayed as means (bars) and standard deviations (black lines) in epilimnion (left bar group), metalimnion (middle bar group) and hypolimnion (right bar group); mean intruding river volume (c and d) and mean river intrusion depth (e and f). MNPP thermal input included (a, c and e) or excluded (b, d and f) in near-future (blue) and far-future (vermilion) time periods but retained in the reference period (black).
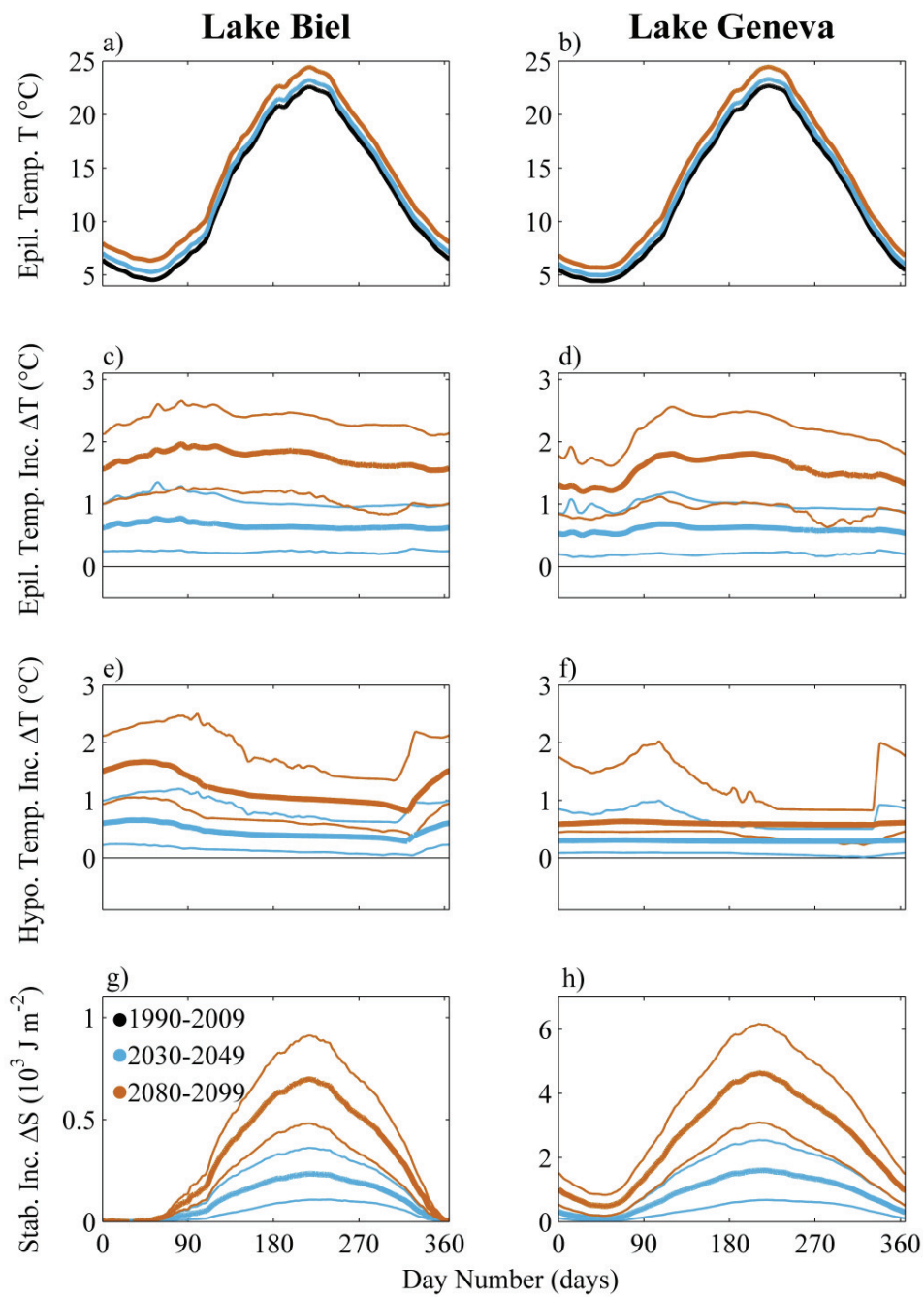
Figure 3.C1. Modeled climate impact (river intrusion excluded) on LB (left column, scenario LB1) and LG (right column, scenario LG1) shown as daily mean (thick lines) and maximum/minimum model values (thin lines) for near-future (blue, 2030-2049) and far-future (orange, 2080-2099) time periods relative to the reference period (black, 1990-2009). Temperature T (a and b), temperature increase (ΔT) in the epilimnion (c and d) and hypolimnion (e and f) as well as increase in stability (ΔS; g and h).
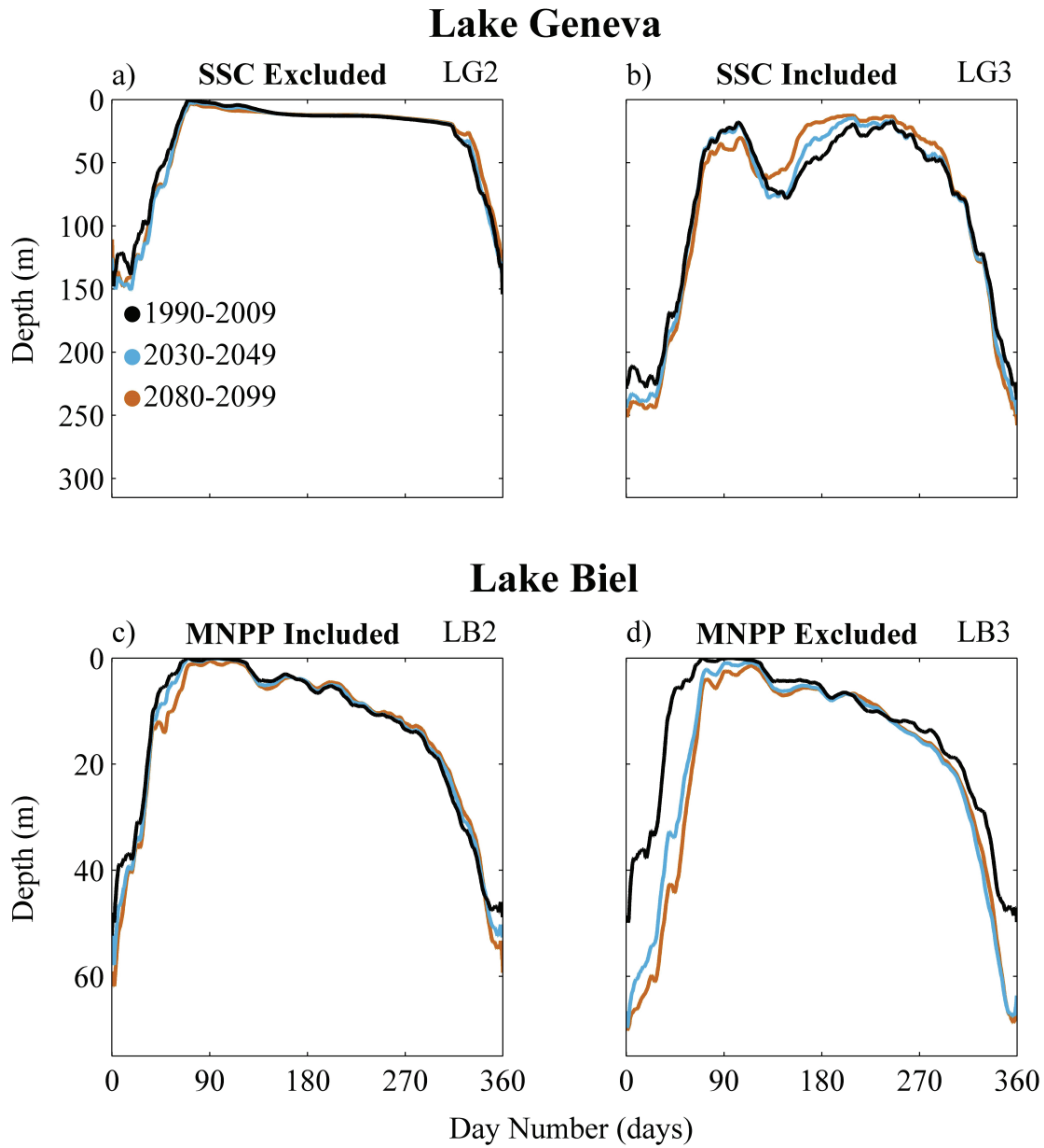
Figure 3.D1. Modeled climate impact on mean river intrusion depth. Reference period (black), near-future (blue) and far-future (orange) time periods for LG (a to b) and LB (c to d) with (b, c and d) and without (a) river borne SSC and MNPP thermal input included (c) or excluded (d) from near-future and far-future time periods relative to the reference period.

Chapter 4:

Wind driven circulation focusing lake sedimentation

Love Råman Vinnå[1], Damien Bouffard[1,2], Alfred Wüest[1,2], Stéphanie Girardclos[3], Nathalie Dubois[4,5]

[1]EPFL, Aquatic Physics Laboratory, ENAC-IEE, Lausanne

[2]Eawag, Abteilung Oberflächengewässer, Kastanienbaum.

[3]Section of Earth and Environmental Sciences, Université de Genève, Genève, Switzerland

[4]Department of Surface Waters - Research and Management, Eawag, Swiss Federal Institute of Aquatic Science and Technology, Dübendorf, Switzerland

[5]Department of Earth Sciences, ETHZ, Zürich, Switzerland

Abstract

Sedimentation patterns in aquatic systems affects the biosphere as well as utilitarian water resources management. Here we investigate sedimentation patterns in the perialpine Lake Biel which is greatly influenced by upstream diversion of the Aare River into the lake. The Aare, and the much smaller Schüss River, were tracked inside the lake during a field campaign in 2014 and 2015. In the lake we used Acoustic Current Doppler Profilers (ADCPs), temperature loggers, sediment traps as well as long and short gravity sediment cores in combination with turbidity and discharge measurements from the rivers. The majority of the river supplied sediment arrived to the lake in short term suspended sediment concentration (SSC) events. For the main river Aare these were linked to weather systems originating out over the Atlantic Ocean, resulting in seasonal varying sediment supply (mean for summer 42 and winter 6 $g\ m^{-2}\ day^{-1}$). The Atlantic weather systems, besides controlling the temporal frequency of the SSC events in the Aare, furthermore focused the sedimentation inside the lake along a shallow shelf north of the river delta. This led to large amounts of sediment being deposited on steep topography, resulting in series of subaqueous slides. Wind focused sedimentation patterns was thus attributed to increase the risk of subaqueous mass movements in the lake. The high flow speed in both river inlets and outlets caused selective sedimentation of particle sizes, with increased mass occurrence rate of sand (63 to 2000 μm) in high energetic environments, while smaller sized silt and clay ($< 63\ \mu m$) clearly dominated in the low energetic deeper parts of the lake.

4.1 Introduction

Lakes and rivers are since long affected by anthropogenic activities, both on a local and global scale. Nowadays the main focus is on the effect of global climate change and more specifically on temperature modifications, stratification and the subsequent effect on the biogenetical cycling and the biota [*Correll*, 1998; *Kirillin et al.*, 2013; *Van Vliet et al.*, 2013; *Schwefel et al.*, 2016]. Yet, there are equality strong influences by quantitative modifications of the hydrology, such as upstream damming [*Power et al.*, 1996; *Kunz and Wüst*, 2014], hydropower use of lakes with effects on ecosystem productivity [*Matzinger et al.*, 2007] and upstream water diversion [*Wirth et al.*, 2011; *Weber et al.*, 2017]. Those changes have not only physical and ecological effects on the rivers and the lakes but also influence the utilitarian water resources management by humans. Among those multiple anthropogenic interests, safe drinking water and safe infrastructure in- and around the lakes are fundamental for environmental management (and engineering). Here we show that upstream water diversion can strongly change the particle distribution and sedimentation pattern and thereby influence not only the water turbidity but also the safety of drinking water intakes.

Multiple negative effects have been linked to high levels of turbidity and sediment deposition. Problems include severely hampered productivity in aquatic food webs [*Henley et al.*, 2000; *Davies-Colley and Smith*, 2001], enhanced risk of subaqueous slides due to rapid sedimentation [*Lee et al.*, 2007] with risk for tsunami waves [*Kremer et al.*, 2012], and transport of pathogens attached to solids [*McDougall et al.*, 1991; *Davies-Colley and Smith*, 2001; *Schwarzenbach et al.*, 2010]. Lake Biel (LB) is a classic example of major anthropogenic modifications. Not only has the river inflow been extensively enhanced by an order of magnitude through upstream river diversion, but it has also been affected thermally by cooling water emission of an upstream nuclear power plant [*Råman Vinnå et al.*, 2017a].

Sediment deposition in lakes is a complicated problem including multi temporal scale processes. The net sedimentation is the outcome from river discharge. It is often related to large discharge events and decades are needed to extract statistically relevant patterns. Sedimentology is the ideal research field for such kind of long term study but lacks explanations regarding the processes involved. Hydrodynamic study are perfectly suited for studying the process involved on a particular event and explain the spatial distribution of a given sedimentation event, but lack of realistic statistics given the extremely long time scale investigated. Here we propose an interdisciplinary study combining the statistical benefit of

the sedimentology approach with the mechanistic benefit from the hydrodynamic approach. More specifically we focus on the following research questions:

(i)   What role do weather patterns play for extreme SSC events?

(ii)   What is the impact of the local wind field on sediment distribution?

(iii)   Can those sedimentation patterns explain the observed local occurrences of subaqueous mass movements in LB?

(iv)   How do the location of rivers influence sedimentation patterns?

This was accomplished through a field campaign where we observed the Aare River as well as the much smaller Schüss River. Water properties considered includes suspended sediment concentration (SSC), temperature, water velocity and sedimentation rate. Instrumentation used contained acoustics, optics, sedimentation traps, gravity corers and thermal sensors. Finally the observed sediment supply and sedimentation patterns were linked to the wind field using a high resolved metrological model.

4.2 Methods

4.2.1 Study area

The meso-eutrophic warm monomictic perialpine Lake Biel (LB; 7°10' E, 47°5' N) is located in western Switzerland on the Plateau between the Jura Mountains and the foothills of the Alps (Fig. 4.1a). The lake consist of three basins, Tüscherz basin which is the deepest at 74 m, Lüscherz basin and Neuenstadt basin (Fig. 4.1b). The lake holds a volume of 1.18 km^3 and has a total surface area of 39.3 km^2. Three tributaries supply the lake with water and sediment (Table 4.1), the Aare River with inflow at Hagneck (station 2085) is the main supplier of both water (~72%) and sediment from the Alps and Prealps, the Zihlkanal (station 2446) which connects LB to Lake Neuchâtel is the second largest (~23%), and Schüss (station 2029) which brings water from the upstream Jura mountains is the smallest (~2%). Several dams/lakes trap sediment along the upstream Aare originating in the Alps, thereby allowing sediment to settle and glacier water to warm [*Thevenon et al.*, 2013]. A sub tributary to the Aare, the Sarine River, provides the majority of sediment supplied during rain events since this rivers drainage area still remains largely unaffected by dams [*Råman Vinnå et al.*, 2017b]. The Aare continues out through the lakes main outflow at Aegerten (station 2029).

114

Table 4.1. Annually averaged rivers mass supply from 2013 to 2016, inflows are positive and outflow negative, *italic* column obtained from *Santschi and Schindler* [1977] for the period 1973 to 1974.

Station Name (ID number)	Position	Flow[a] (m³ s⁻¹)	SSC[b] (kg s⁻¹)	Sedimentation[c] (g m⁻² day⁻¹)	
				This study	Santschi
Hagneck (2085)	47°03'N 7°11'E	175	12.08	27.88	10.16
Zihlkanal (2446)	47°01'N 7°02'E	55			0.52
Schüss (2307)	47°11'N 7°10'E	5	0.10	0.23	0.25
Aegerten (2029)	47°07'N 7°17'E	-240			

[a]Mean 1985 to 2016

[b]Suspended Sediment Concentration

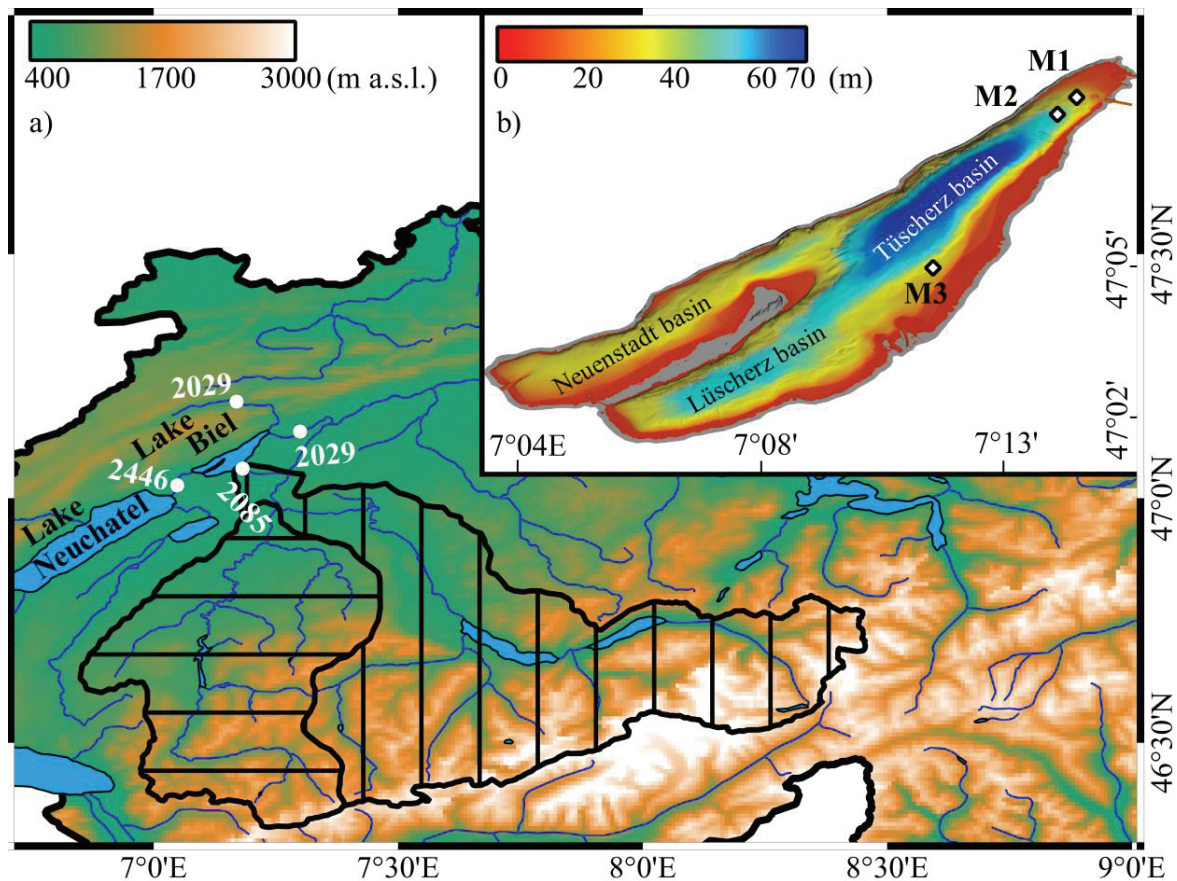[c]Calculated using LB surface area of 39.3 m²

Figure 4.1. Area of investigation a) with upper Aare River catchment marked with vertical lines and Sarine River catchment marked by horitontal lines, river station represented by white circles; b) Lake Biel bathymetry, basins and mooring locations marked by white dimonds.

During the first Jura Correction geoengineering project in 1878 the Aare River was redirected into LB, thereby drastically changing the annual sedimentation rate in the lake from 0.1 to 2.63 (later 1.1) cm year^{-1} [*Santschi and Schindler*, 1977; *Jeannet et al.*, 2013; *Thevenon et al.*, 2013] and reducing the average hydraulic residence time from 253 to 58 days [*Liechti*, 1994]. As the Aare River plume enter LB it sinks and gets trapped above the thermocline in summer, while in winter it is heavy enough to penetrate into the hypolimnion [*Albrecht*, 1999; *Råman Vinnå et al.*, 2017b]. While in the thermocline the plume can follow two main paths, either into the central parts of the lake [*Albrecht et al.*, 1999] or along the eastern shoreline towards the main outflow in the north [*Wright and Nydegger*, 1980]. The path taken by the plume depends mainly on the two dominant wind directions over the lake (Vent from South-East or Bise from North-West) [*Råman Vinnå et al.*, 2017a]. This temporally varying plume pathway affects sedimentation patterns with increased sedimentation along the eastern shoreline of LB [*Wright and Nydegger*, 1980].

4.2.2 Field Campaign Setup and Instrumentation

Hydrodynamics in LB were observed during a nearly 3-year long field campaign (May 2013 to September 2015) using three moorings M1, M2 and M3 (Fig. 4.1b). The instrumentation setup is summarized in Table 4.2. Here we focus on the summer of 2014 to autumn of 2015. Temperature was measured with two types of loggers, Vemco Minilog II-T and RBR TR-1060 deployed vertically on a straight line. The depth of the temperature loggers had to be adjusted due to the variable water level in LB. For this purpose we used highly resolved RBR temperature and pressure sensors. One RBRduo T.D (temperature and depth, accuracy 0.002 °C and 0.05% of pressure range) sensor at M1 and one RBRconcerto T.D.Fl.Tu (temperature, depth, fluorescence and turbidity, accuracy 0.002 °C and 0.05% of pressure range) at M2.

Currents intensity and direction over the water column were observed with three Teledyne RD Instruments Workhorse Sentinel Acoustic Doppler Current Profilers (ADCPs) in the 300, 600 and 1200 kHz frequency range (accuracy 0.3% to 0.5% of water velocity). The ADCPs were moored on the bottom facing upwards within a distance of 50 m from the temperature moorings. The echo amplitude backscatter signal, used for tracing progression of the intruding Aare plume, was compensated for signal loss as shown in Appendix 4.1.

Table 4.2. Field Campaign Instrumentation Setup

M1		M2		M3	
47° 7' 34"N / 7° 13' 23"E		47° 7'14 "N / 7°13' 0"E		47° 4' 58"N / 7°11' 8"E	
Station Depth: 20 m		Station Depth: 47 m		Station Depth: 28 m	
Instrument	*Depth (m)*	*Instrument*	*Depth (m)*	*Instrument*	*Depth (m)*
Minilog II-T	0.2	Minilog II-T	0.2	Minilog II-T	0.2
RBRduo	3.5	Minilog II-T	3.5	Minilog II-T	5
Minilog II-T	4.5	Minilog II-T	6.5	M3-Z1	7
Minilog II-T	6.5	M2-Z1	7	Minilog II-T	7
M1-Z1	7	Minilog II-T	8.5	Minilog II-T	9
Minilog II-T	8.5	RBRconcerto	10	Minilog II-T	10.5
Minilog II-T	9.5	Minilog II-T	10.5	M3-Z2	12
Minilog II-T	11.5	Minilog II-T	11.5	Minilog II-T	12
M1-Z2	12	M2-Z2	12	Minilog II-T	14.5
Minilog II-T	13	Minilog II-T	12.5	M3-Z3	17
Minilog II-T	14.5	Minilog II-T	14.5	Minilog II-T	17
Minilog II-T	16.5	Minilog II-T	16.5	Minilog II-T	19.5
M1-Z3	17	M2-Z3	17	Minilog II-T	21
TR-1060	18	Minilog II-T	18.5	TR-1060	24
TR-1060	18.5	Minilog II-T	20.5	TR-1060	26.5
TR-1060	19	Minilog II-T	22.5	M3-Z4	27
		Minilog II-T	24.5	TR-1060	27
		M2-Z4	27		
		Minilog II-T	27.5		
		Minilog II-T	32.5		
		M2-Z5	35		
		Minilog II-T	37.5		
		Minilog II-T	43.5		
		M2-Z6	45		
		TR-1060	45		
		TR-1060	45.5		
		TR-1060	46		
ADCP		ADCP		ADCP	
Frequency	*Resolution*	*Frequency*	*Resolution*	*Frequency*	*Resolution*
1200 kHz	0.25 m	600 kHz	1 m	300 kHz	1 m
	5 min		20 min		20 min

Sedimentation inside LB was monitored with sediment traps (two vertically placed PVC pipes, length 80 cm, area 65 cm^2) and both gravity cores (used for sedimentation rates) and core-top samples (surface samples used for sedimentation composition). Sediment core age models were developed using Caesium-137 radionuclide activity measured in 5 to 10 g freeze dried samples

(cores 14-52 and 14-61) in a high-purity Canberra Germanium Well Detector following the method used by *Thevenon et al.* [2013]. Water content (Table 4.3) was determined for cores 10-3, 10-8, 14-52 and 14-61 by the weight loss after freeze drying. The cores age models were used to determine sedimentation rate (SR; Table 4.3). Mass accumulation rate (MAR; Table 4.3) was calculated using the mean water content (WC; 63 %) of all cores (Table 4.3) and the sediment dry density (DD; 2650 kg m^{-3}) using *Steinsberger et al.* [2017]:

$$MAR = SR*DD*(1-WC)*1000/365 \quad (\text{g m}^{-2} \text{ day}^{-1}) \tag{4.1}$$
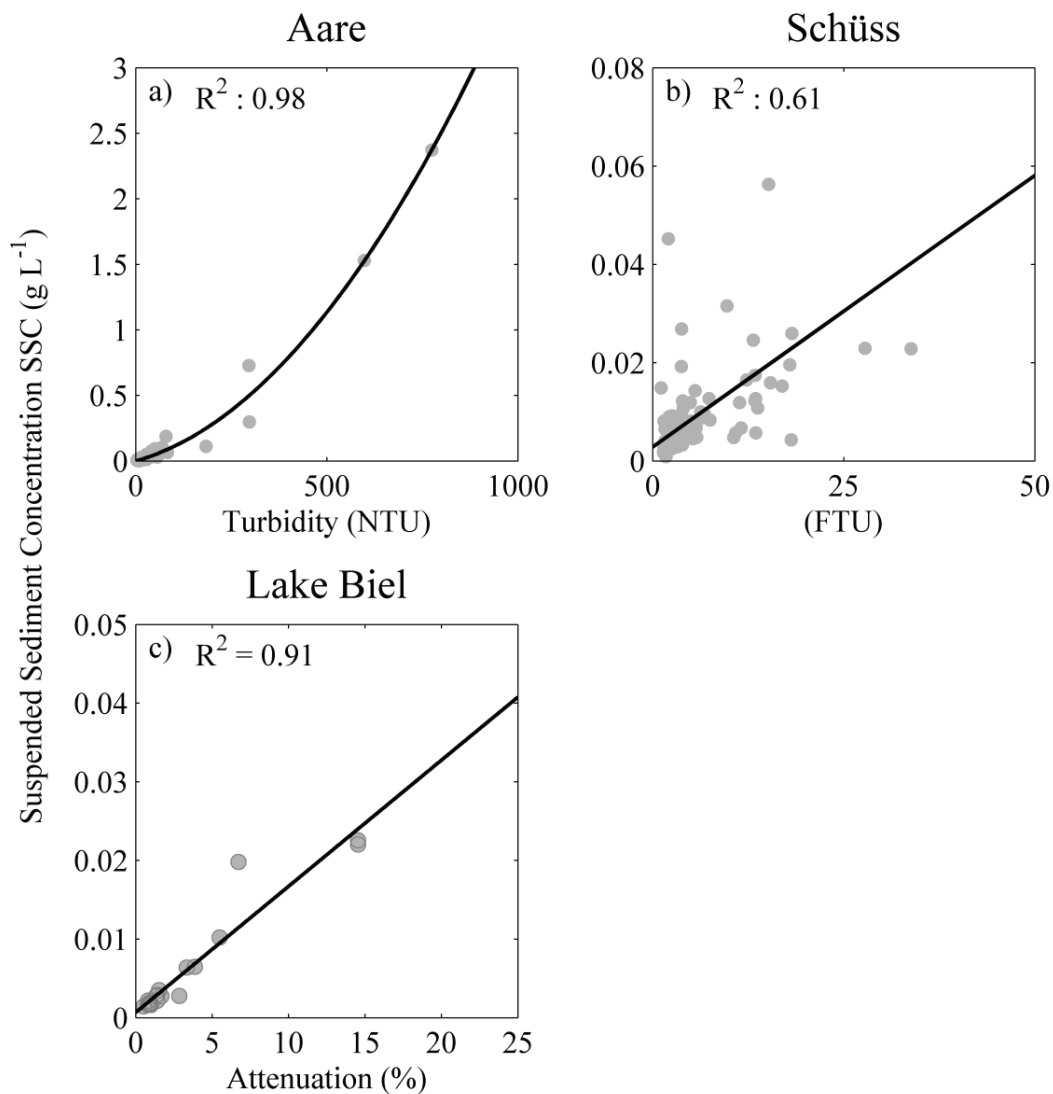

Figure 4.2. Sediment optical versus mass concentration measurements at Aare station Hagneck 2085 (a), Schüss (b) and Lake Biel stations M1, M2 and M3 (c) for sediment mass samples from 2013 to 2016. a) and b) Solitax TS-Line SC turbidity sensor and c) C-Star Wetlab 660 nm transmissometer (25 cm path length).

Grain size distribution in sediment traps and core top samples was measured with a Malvern Mastersizer 2000 (0.02 to 2000 μm) by laser diffraction technique. Samples were dispersed in NaPO$_4$ prior to analysis and disaggregated by brief ultrasonication. Each sample was measured at least three times. Total carbon (TC) was measured on freeze-dried and on homogenized ground samples from core 14-61 with an EURO EA 3000 Elemental Analyser. Total inorganic carbon (TIC) content was obtained from a Titration Coulometer (CM5015). Total organic carbon (TOC) was calculated as TOC = TC − TIC.
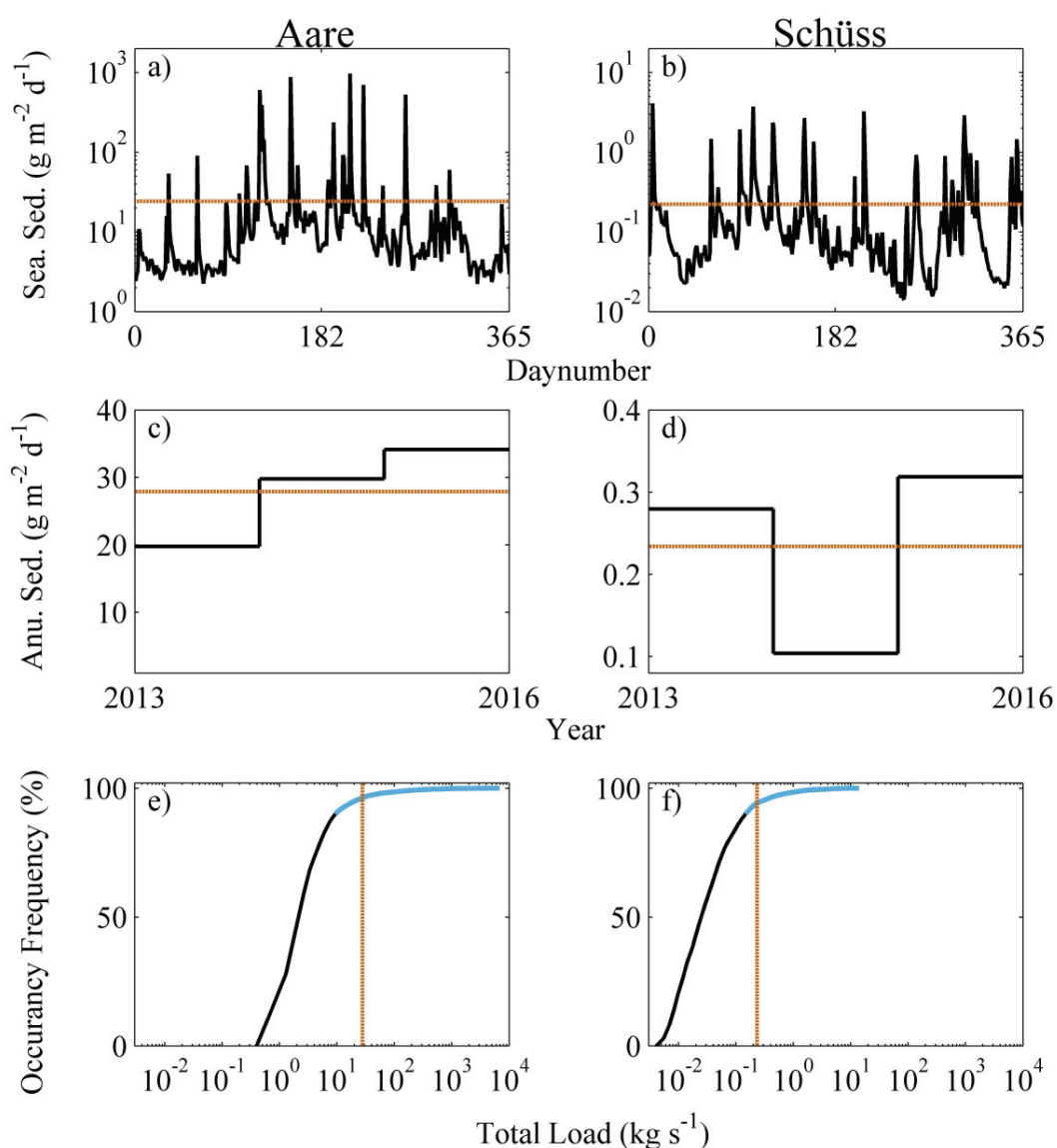

Figure 4.3. River sediment supply from Aare (left column) and Schüss (right column) from 2013 to 2016 with mean marked by orange dashed line. a) and b) seasonal sedimentation in Lake Biel (LB) displayed as daily mean between 2013 and 2016, and c) and d) annual sedimentation in LB, a) to d) calculated from the total load of each river with the LB area of 39,3 km^2; e) and f) temporal distribution of total load, the ninth decile (topmost 10 %) is marked in blue.

Turbidity in the inflowing Schüss and Aare (stations 2029 and 2085) was measured between 2013 and 2016 with Solitax TS-Line SC optical sensors (0.001 - 4000 NTU/FTU, accuracy < 1%). Turbidity vertical profiles in LB were measured with a 660 nm C-Star Wetlab Transmissometer (25 cm path length). Turbidity were fitted to suspended sediment concentrations (SSC; Fig. 4.2) and converted to SSC, using water samples (filter pore size < 1 μm) obtained in the rivers close to the probes as well as near the three moorings in LB every tenth meter from 5 m to 45 m depth. The total load (Fig. 4.3) for each river was obtained by multiplying river discharge with SSC.

SSC events in the Aare River were linked to rain patterns in the Sarine River catchment (6°54'E 46°35'N to 7°18'E 46°57'N) during 2014 and 2015, using hourly resolved wind and rain data from the highly resolved (2.2 x 2.2 km^2) meteorological COSMO-2 model (http://www.cosmo-model.org), which has been validated for the region surrounding LB [*Hug et al.*, 2010; *Weusthoff et al.*, 2010]. The model data was filtered by selecting model cells where rain occurred in the Sarine River catchment, the selected model values were saved and shown in Figs. 4.4 a,b for Sarine and Fig 4c) over LB (7°1'E, 47°0'N to 7°18'E, 47°10'N) at times of rain in the Sarine catchment, the unfiltered LB wind field is shown in Fig. 4.4d for comparison. Seasonal variations using the filter technique above are shown in Fig. 4.A3.

Table 4.3. Gravity core sedimentation rate (SR), mass accumulation rate (MAR) and water content (WC), *italic* rows were obtained from *Albrecht et al.* [1998].

Core name[a]	Position	(E N)	Sedimentation 1986-97/15		WC (%)
			SR (cm year^{-1})	MAR (g m^{-2} day^{-1})	min ; max ; mean
93_01	*7°11'*	*47°5'*	*1.4*	*20.5*	
94_07	*7°7'*	*47°3'*	*1.4*	*13.4*	
94_04	*7°8'*	*47°3'*	*1.5*	*12.9*	
94_01	*7°11'*	*47°6'*	*2.0*	*18.9*	
96_01	*7°11'*	*47°6'*	*1.7*	*15.9*	
96_02	*7°13'*	*47°7'*	*2.0*	*20.5*	
97_01	*7°10'*	*47°4'*	*3.5*	*65.8*	
			Mean		
			1.9	*24.0*	
10-3	7°8'	47°3'	0.9	24.2	44 ; 67 ; 55
10-8	7°10'	47°5'	1.3	33.6	44 ; 61 ; 57
10-9	7°11'	47°6'	1.4	36.3	
13-1C	7°11'	47°6'	1.1	29.5	
13-2C	7°11'	47°6'	1.1	30.6	
13-2E	7°7'	47°4'	0.9	24.2	
13-3E	7°8'	47°3'	0.6	16.1	
14-52	7°13'	47°7'	2.3	61.9	24 ; 66 ; 55
14-61	7°11'	47°6'	1.3	35.0	69 ; 90 ; 85
14-67	7°9'	47°5'	1.3	35.0	
15-05	7°12'	47°6'	1.1	30.1	
15-06	7°12'	47°6'	1.1	30.1	
			Mean		
			1.2	32.2	63

[a]First number from the left indicates year of sampling, ex. 93 = 1993 or 10 = 2010.
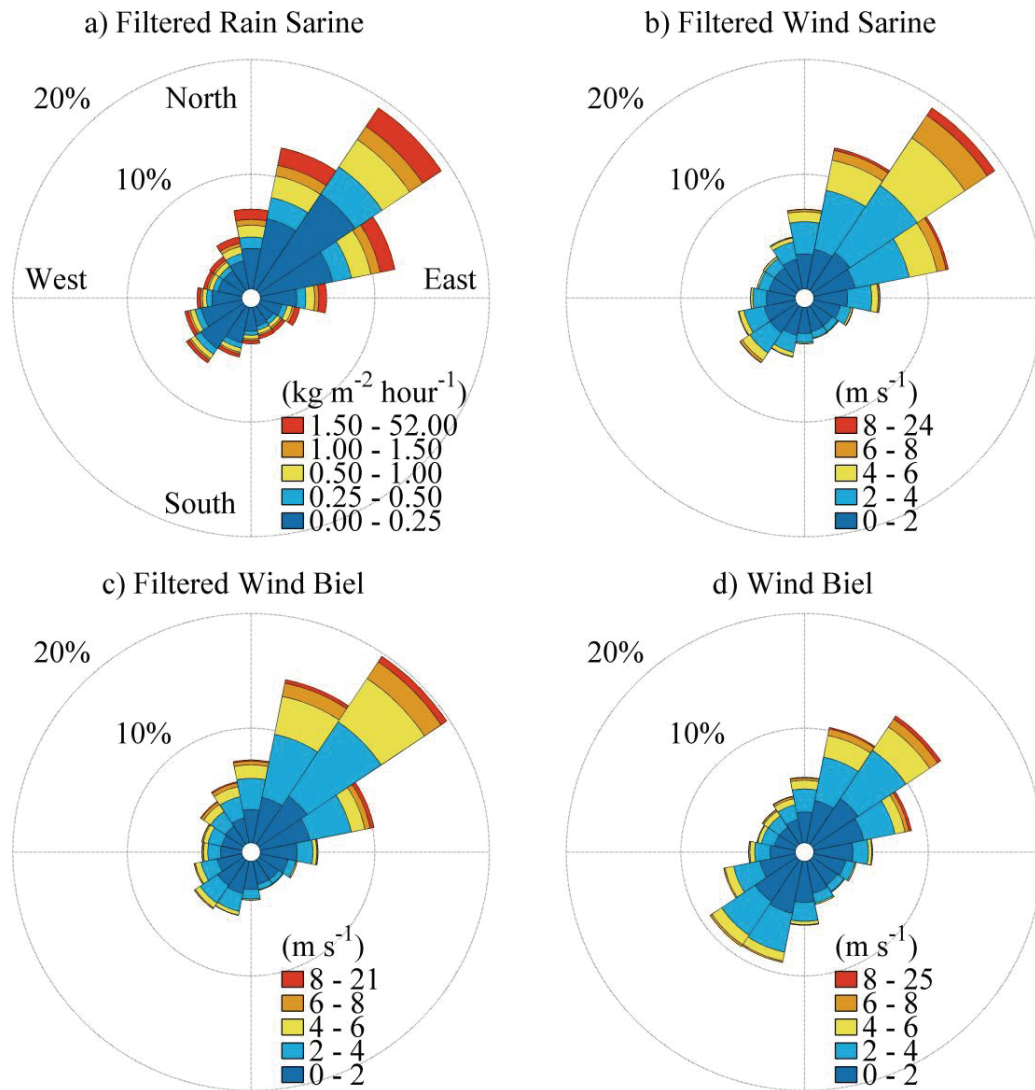
Figure 4.4. Temporal wind and rain patterns from COSMO-2 weather model during 2014. a) and b) the Sarine River catchment, c) and d) Lake Biel (LB). a) modelled wind direction of travel and amont of rain for cells in the Sarine catchment, filtered on a cell by cell basis to exclude times when no percipitation occurred; b) and c) temporal corresponding wind direction and magnitude as in a); d) unfiltered wind direction and magnitude over LB.
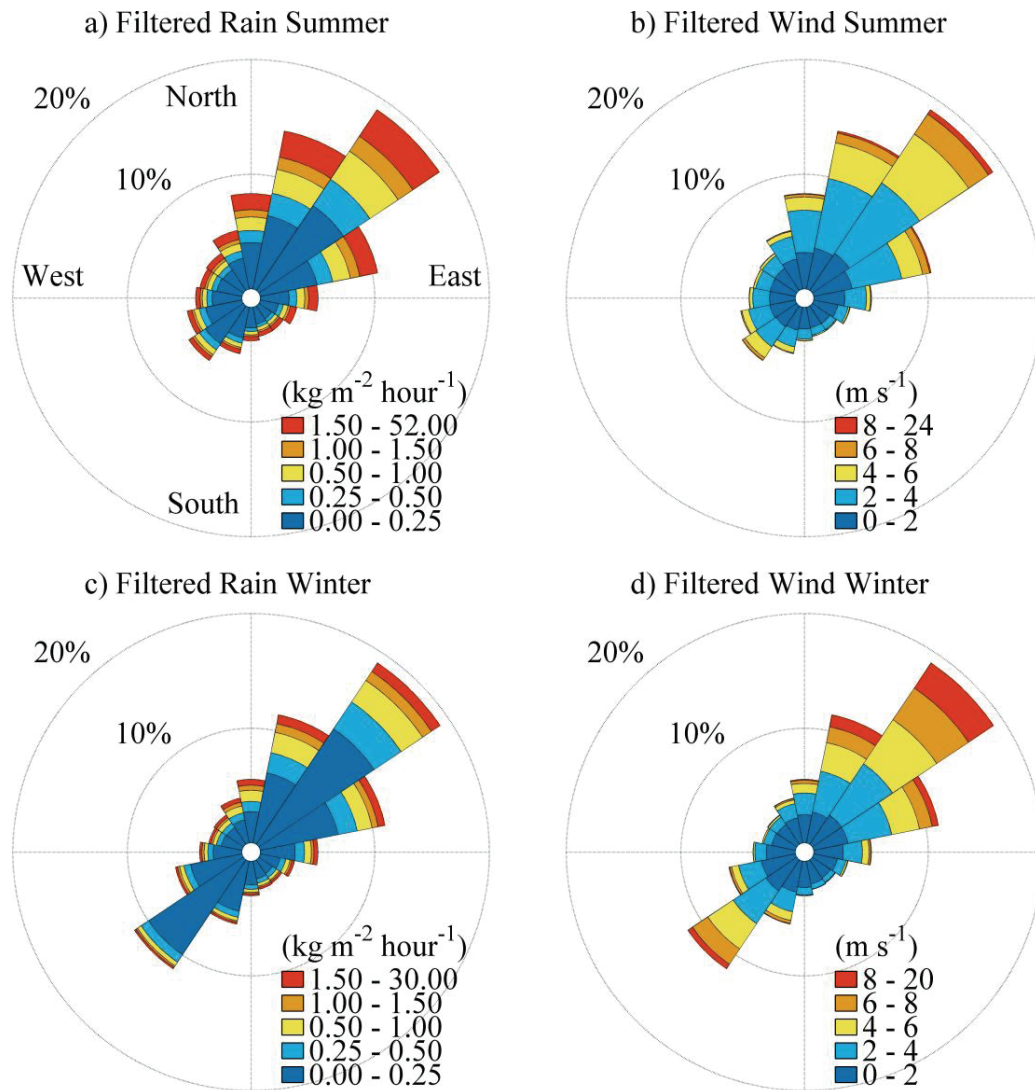
a) Filtered Rain Summer

b) Filtered Wind Summer

c) Filtered Rain Winter

d) Filtered Wind Winter

Figure 4.A3. Temporal wind and rain patterns from COSMO-2 2*2 km resolved weather model during April to September 2014 a) and b) and October 2014 to March 2015 c) and d) in the Sarine River catchment 6°54'E 46°35'N to 7°18'E 46°57'N. a) and b) modelled wind direction of travel and amount of rain for cells in the Sarine catchment, filtered on a cell by cell basis to exclude times when no percipitation occurred; b) and d) temporal corresponding wind direction and magnitude as in a) and c).

4.3 Results

4.3.1 Particle supply

We found that the Aare River was the dominant source of sediment into LB (Table 4.1). This tributary provided 97.4 % of the total riverine sediment supplied to LB. Corresponding contributions from the Schüss was 0.8 % and 1.8 % for the Zihlkanal for which values from *Santschi and Schindler* [1977] were used. A clear seasonal trend was observed in the Aare (Fig. 4.3a) with enhanced particle supply in summer (mean 42 g m^{-2} day^{-1}; standard deviation 127 g m^{-2} day^{-1}) and lower input in winter (mean 6 g m^{-2} day^{-1}; 9 g m^{-2} day^{-1}), while in the Schüss no seasonal trend was discernible (Fig. 4.3b).

The sediment supplies from both rivers is directly connected to high SSC events (Figs. 4.3a.b). For the Aare River, ~80 % of the supplied sediment entered LB during 10 % of the time (Fig. 4.3e, marked in blue. For the Schüss 70 % enter the lake during 10% of the time (Fig. 4.3f, marked in blue). Contrary to other rivers and with the exception of the large events, SSC in the Aare (station 2085) was hardly linked to discharge. This discrepancy results from upstream sediment trapping lakes/reservoirs along the Aare. Sediments supplied to station 2085 are mainly driven by rain events in the Sarine catchment, which lacks efficient sediment trapping features [*Råman Vinnå et al.*, 2017b]. In the Schüss, the events of high SSC were clearly linked to discharge. In conclusion, the main supplier of sediment to LB is the Aare, from which ~80 % is supplied in large SSC events correlated to Vent winds from Southwest. As the plume enters LB it is diverged as explained in the next section.

4.3.2 Plume Pathway

The path taken by the intruding Aare plume in LB was tracked during summer 2014 when the river discharge was high and the SSC occasionally increased (Fig. 4.5a). The riverine water was identified by the unusual observations of high currents (Fig. 4.5b), strong backscattering ADCP signals (i.e. turbidity; Fig. 4.5c and 4.6c) and weak negative temperature anomalies (Figs. 4.5d, 4.6d and 4.7d). The river intrusion induced signal is best resolved at M3 which is closest to the river delta, and becomes less clear as distance increase towards stations M2 and M1.
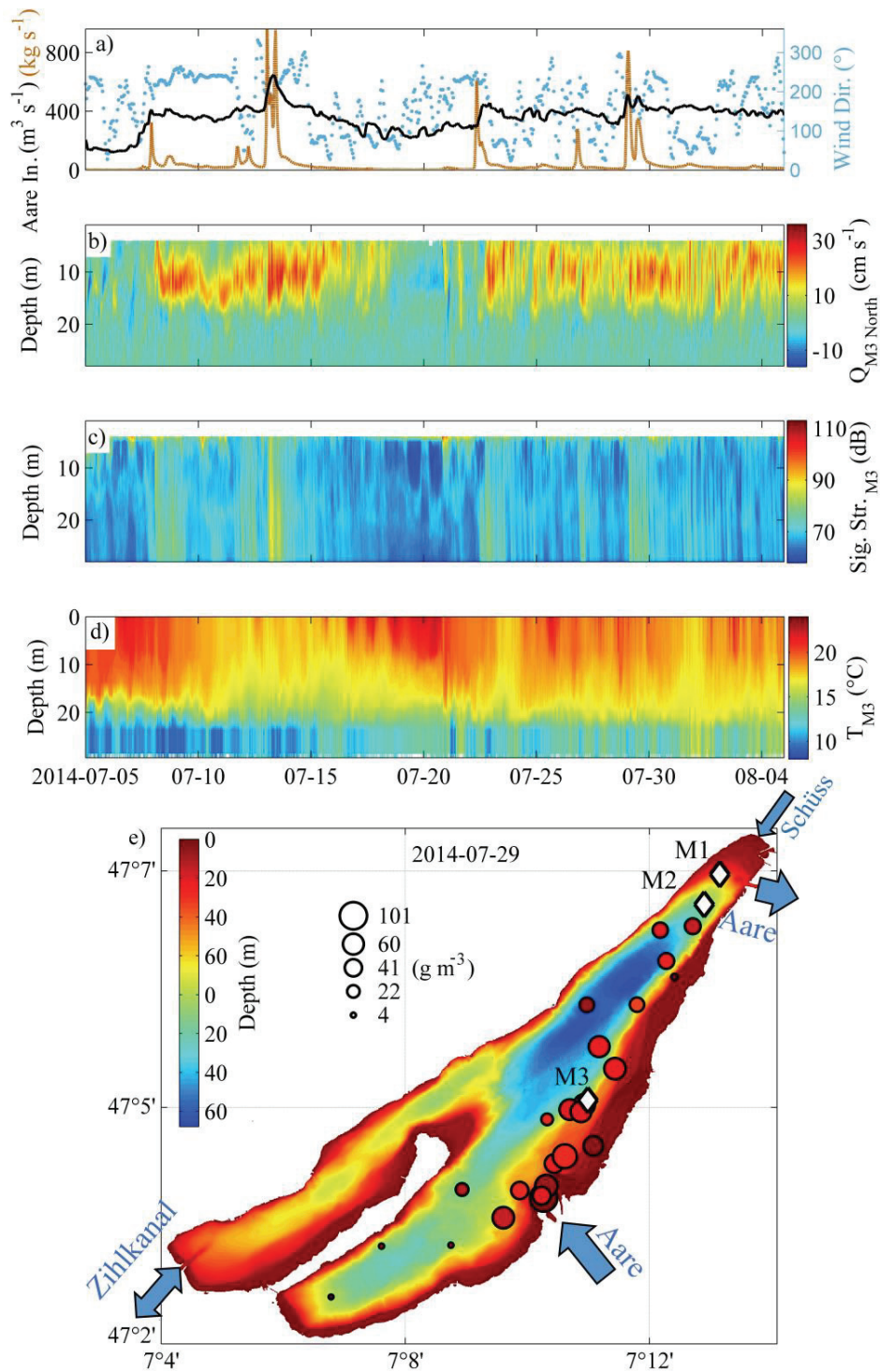
Figure 4.5. Spatial and temporal development of an intrusion event from the Aare River during July and August 2014 focused on station M3. a) Aare discharge at station 2085 (black) and Aare sediment load (orange), wind direction measured at Cressier station 6354 (blue); b) northern current speed measured at mooring station M3 ($Q_{M3\ North}$); c) backscatter signal strength at M3 (four beam mean); d) temperature at M3; e) LB bathymetry and river flow direction, measurement moorings locations (white diamonds), maximum sediment content (circle size) with corresponding depth (circle colour).
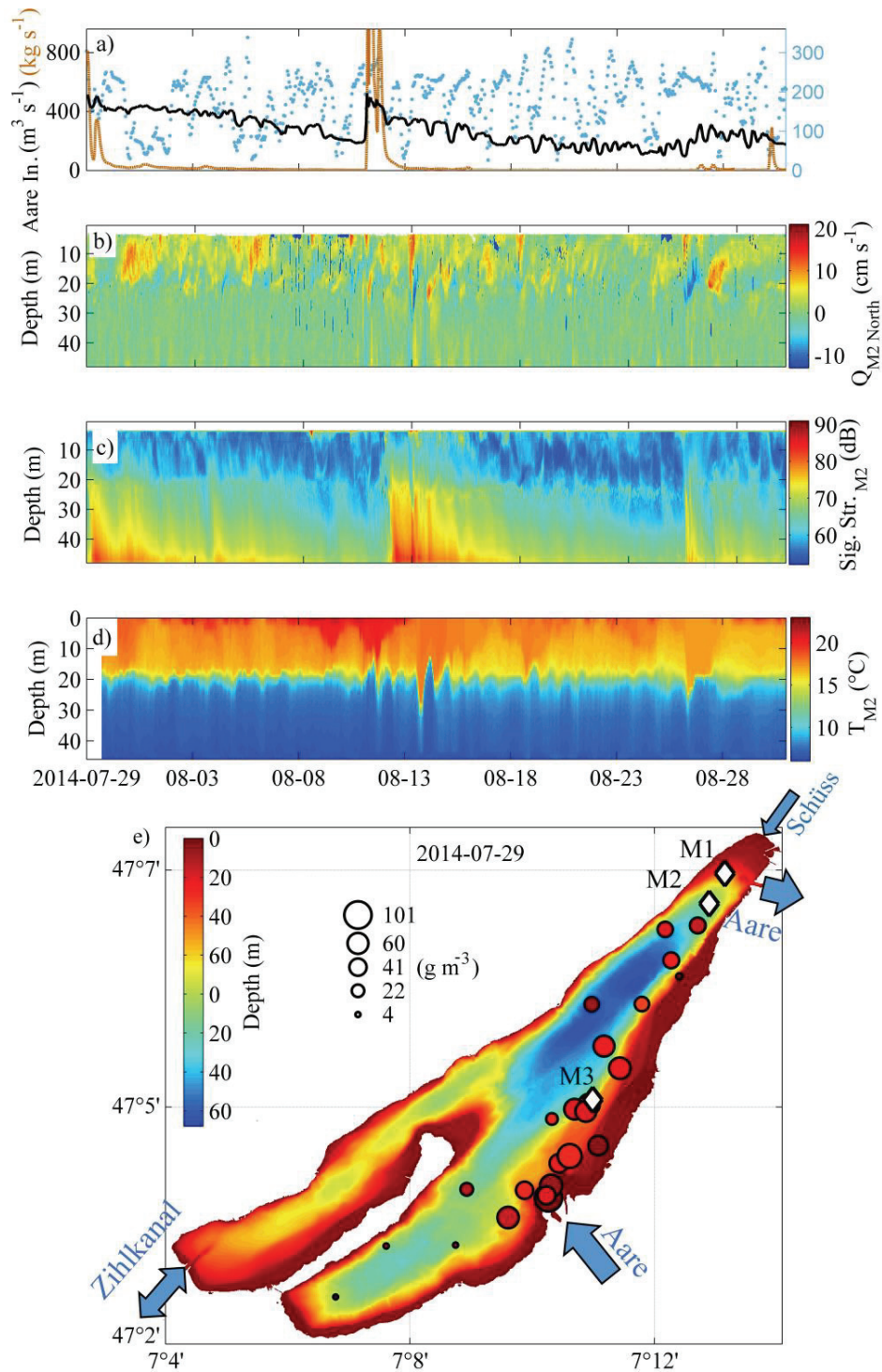
Figure 4.6. Spatial and temporal development of an intrusion event from the Aare River during July and August 2014 focused on station M2. a) Aare discharge at station 2085 (black) and Aare sediment load (orange), wind direction measured at Cressier station 6354 (blue); b) northern current speed measured at mooring station M2 ($Q_{M2\ North}$); c) backscatter signal strength at M2 (four beam mean); d) temperature at M2; e) LB bathymetry and river flow direction, measurement moorings locations (white diamond), maximum sediment content (circle size) with corresponding depth (circle colour).
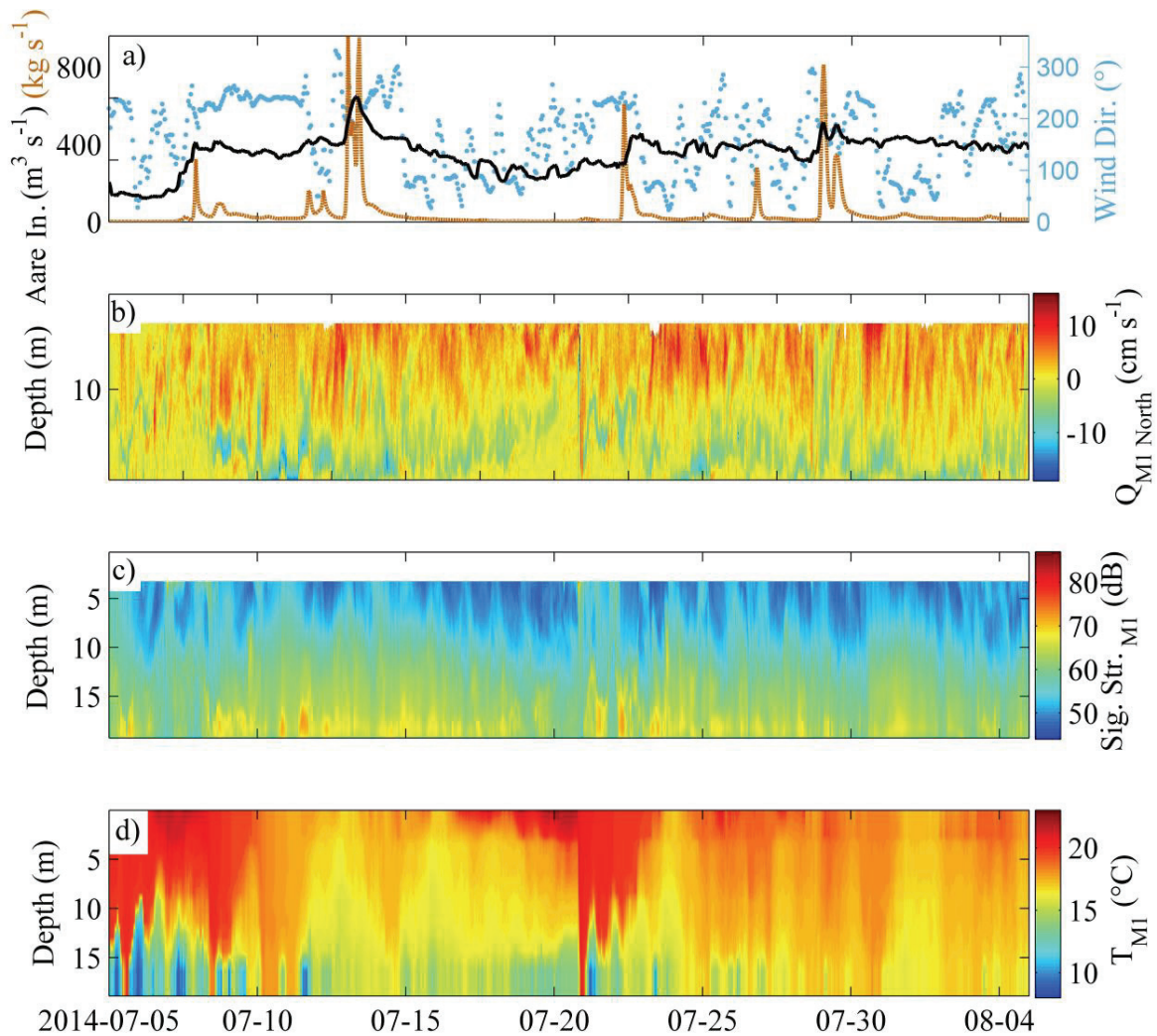
Figure 4.7. Spatial and temporal development of an intrusion event from the Aare River during July and August 2014 focused on station M1. a) Aare discharge at station 2085 (black) and Aare sediment load (orange), wind direction measured at Cressier station 6354 (blue); b) northern current speed measured at mooring station M1 ($Q_{M1 North}$); c) backscatter signal strength at M1 (four beam mean); d) temperature at M1.

As the plume enters LB in summer it intrudes above the thermocline (Figs. 4.5b and 4.5d). At M3 the plume velocity reached 30 cm s^{-1} and was easily identifiably from the ambient water velocity which is less than 10 cm s^{-1} (Fig. 4.5b).

The sediment loaded plume could be tracked at both M3 (three events; Fig. 4.5c) and M2 (two events; Fig. 4.6c) using the ADCP echo return signal, to infer both the time required by riverine particles to travel from the river delta to each station as well as their settling velocities. The signal was compensated for signal loss due to distance travelled through the water column but not due to particle scatter. Thus we can track the vertical location of river borne particles but

127

not their concentration (Appendix 4.1). As the plume arrived at the station a clear increase in the echo return signal was observed (Figs. 4.5c, 4.6c and 4.7c), this echo could then be tracked as it settled towards the bottom. At M3 we noticed a ~6 hours delay (mean from three events) in the occurrence of a high turbidity event in Hagneck and the appearance of a strong ADCP echo, i.e. arrival of the Aare plume at M3. At M2, the corresponding time was ~35 hours (mean from 2 events). The current direction justifies that the backscattering events observed at the two stations is the same event measured in the Aare River. The particle settling speed was calculated from the time of arrival at the station until the leading signal had settled by 10 m. At M3 the mean settling speed was ~2.4 mm s^{-1} and at M2 to ~1.8 mm s^{-1}. Using the formula of *Cheng* [1997] for settling velocity (w) of spherical particles

$$w = \upsilon \left(\sqrt{25 + 1.2 d_*^2} - 5 \right)^{1.5} \Big/ d \qquad (4.2)$$

$$d_* = d \left(\left[\rho_s - \rho \right] \rho g \Big/ \nu^2 \right)^{1/3} \qquad (4.3)$$

with particle size (d) = 65 μm, particle density (ρ_s) = 2650 kg m^{-3}, viscosity (ν) = 1.3*10^{-6} m^2 s^{-1} and water density (ρ) = 1000 kg m^{-3} we obtain a settling velocity of 2.1 mm s^{-1}. At both stations we could thus observe settling of sand-sized particles. Silt-sized particles were too small to be detected at M3 due to the low frequency of the ADCP (300 kHz), but could be resolved at M2 (600 kHz). The settling speed of silt was estimated to 0.09 mm s^{-1}. Using the equations (4.2, 4.3), we obtain for a particle size of 10 μm a settling velocity to 0.05 mm s^{-1}. We were unable to detect clay-sized particles (< 1 μm) with the ADCPs.

Cooling of the epilimnion temperature occurred shortly after events of high river discharge at all stations M3, M2 and M1 (Figs. 4.5d, 4.6d and 4.7d). However, the change was not as abrupt as for current speed or echo return signal. Temperature shifts at M1 could thus be caused by the river plume, but could also be associated with lifting of deeper water from below the thermocline caused by increased outflow.

A detailed survey of the northward propagating river plume was carried out on the 29th August 2014 between 1800 and 2200 hours, with vertical turbidity profiles (Fig. 4.5e). The maximum particle content stayed between 8 to 18 m depth as the plume travelled towards North-East, as it reached M2 the SSC had dropped by ~70 %. In conclusion, as the heavily SSC loaded plume enters LB it is diverged to the north carrying sediment on top of the eastern shallow shelf, the impacts on sedimentation are listed in the next section.

4.3.3 Sedimentation patterns

The seasonally varying supply of sediment from the Aare River (section 4.3.1) results in enhanced sedimentation in summer and lower sedimentation in winter as shown by the analysis of the sediment traps (Figs. 4.8b, 4.8e and 4.8g). Sedimentation was highest at M3, decreased towards M2 and increased again slightly at M1 (Table 4.4; Figs. 4.8b, 4.8e and 4.8g). Seasonal sedimentation at M1 was higher than at M2, but couldn't be directly linked to the discharge in the Schüss (Figs. 4.8a and 4.8b). The traps at M1 however had a higher mass fraction of sand compared to the traps at M2. The accumulated sediment mass increased with trap depth at all stations (Figs. 4.8b, 4.8e and 4.8g; Table 4.4) due to increased sedimentation of silt (2 to 63 µm) which dominated at all stations and depths. As silt increased with depth the mass of sand (63 to 2000 µm) decreased while the content of clay stayed mostly constant (0.01 to 2 µm; Table 4.4).

Sediment cores were in good agreement with trap measurements at M3 (Table 4.4), *Albrecht et al.* [1998] found high MAR close to the Aare inlet (65.8 g m^{-2} day^{-1}; Table 4.3). We obtained approximately two times larger MAR in the Tüscherz basin (~30 to ~35 g m^{-2} day^{-1}) compared to the Lüscherz and Neuenstadt basins (~15 to ~25 g m^{-2} day^{-1}; Fig. 4.9). Sedimentation increased in direction to the shore. We note one unusually high sedimentation rates in one core near M2, otherwise such high sedimentation rate were only found near to the Aare inlet (61.9 g m^{-2} day^{-1}; core 14-52; Table 4.3).

The mass quantity of sand found in the short cores was between ~5 and ~20 % of the total sediment mass (Fig. 4.10), with higher values close to the shoreline and lower ones towards deeper parts of the lake. Remarkably, on the shallow shelf North-East of the Aare inlet we found increased sand proportion up to ~60 %. Likewise close to the Aare outlet and the Zihlkanal the sand proportion increased with up to ~40 %. The quantity of silt in the deeper parts of LB was reversed to that of sand, with ~85 % silt mass in the sediment at deeper depths (Fig. 4.11). North-East of the Aare inlet, close to Zihlkanal and at the Aare outlet the silt content was between ~30 to ~60 %. The distribution of clay mimicked that of silt with ~7 to ~12 % in deeper parts of Tüscherz, Lüscherz and Neuenstadt basins (Fig. 4.12). In the areas of decreased silt mentioned above we found that the amount of clay dropped to less than 4 %. In conclusion, sedimentation of large particles (sand) was concentrated close to the rivers, smaller particles (clay and silt) mainly sediment in the deeper parts of the northern basin.
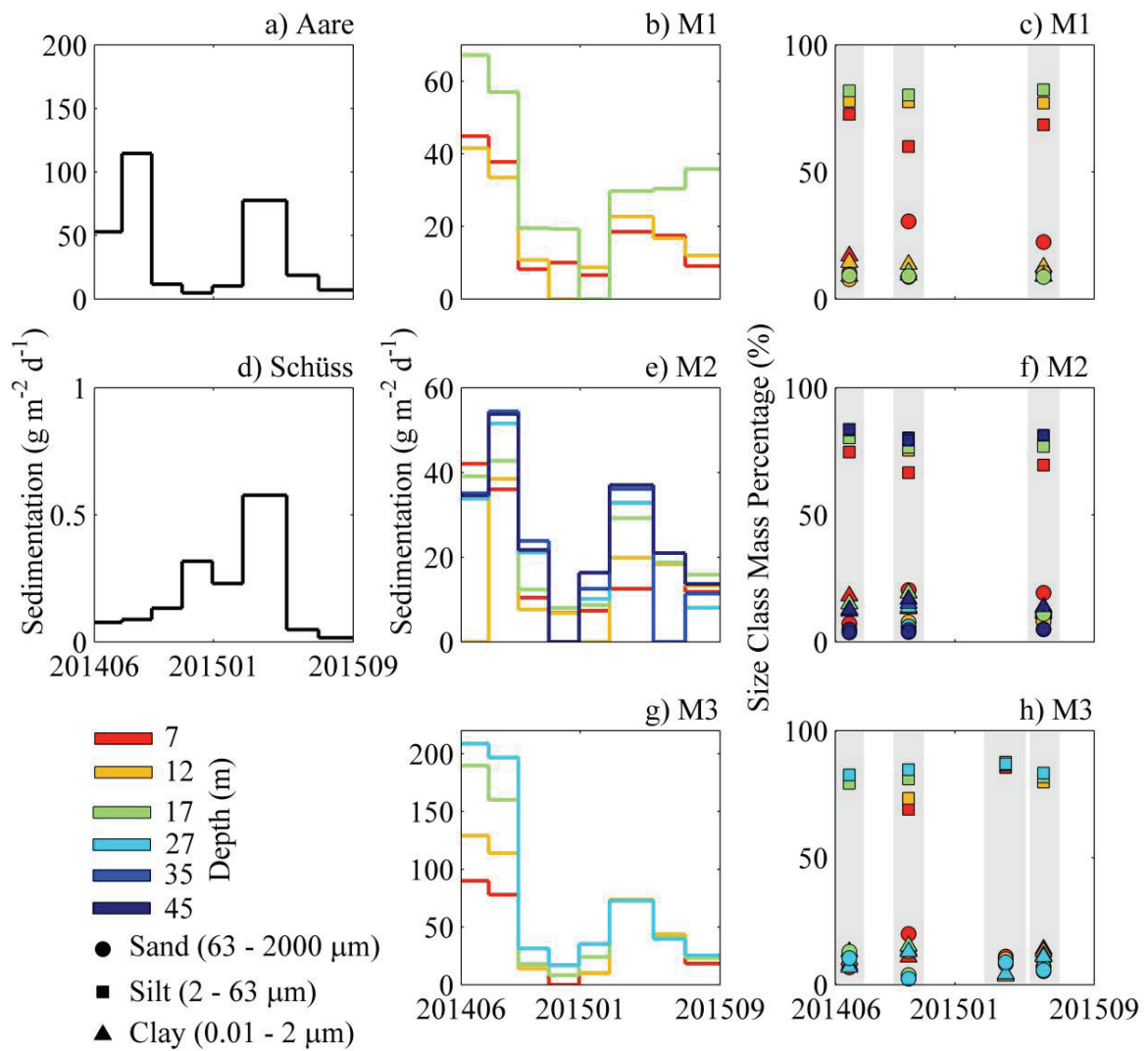
Figure 4.8. Sedimentation averaged across LB (39.3 km²) obtained using total load from the Aare (a) and the Schüss (d), as well as sediment trap mass samples at M1 (b), M2 (e) and M3 (g); (c, f and h) particle size distribution show as mass percentage for sand (circle, 63 to 2000 µm), silt (square; 2 to 63 µm) and clay (triangle; 0.01 to 2 µm). The horizontal extent of each graph as well as the grey areas denotes extent of each sample wet time.

Table 4.4. Sediment trap data for mass accumulation rate (MAR) and size range mass percentage (MP) for sand (63 to 2000 µm), silt (2 to 63 µm) and clay (0.01 to 2 µm), displayed as mean values.

Station-Trap	Depth (m)	MAR (g m^{-2} d^{-1})	Sand	Silt	Clay
			MP (%)		
M1-Z1	7	19	21	67	12
M1-Z2	12	21	9	78	14
M1-Z3	17	36	9	81	9
M2-Z1	7	18	16	70	14
M2-Z2	12	17	8	77	15
M2-Z3	17	22	7	78	15
M2-Z4	27	26	5	81	13
M2-Z5	35	29	5	82	14
M2-Z6	45	28	4	81	14
M3-Z1	7	47	11	79	10
M3-Z2	12	52	10	80	10
M3-Z3	17	67	8	82	10
M3-Z4	27	78	7	84	9

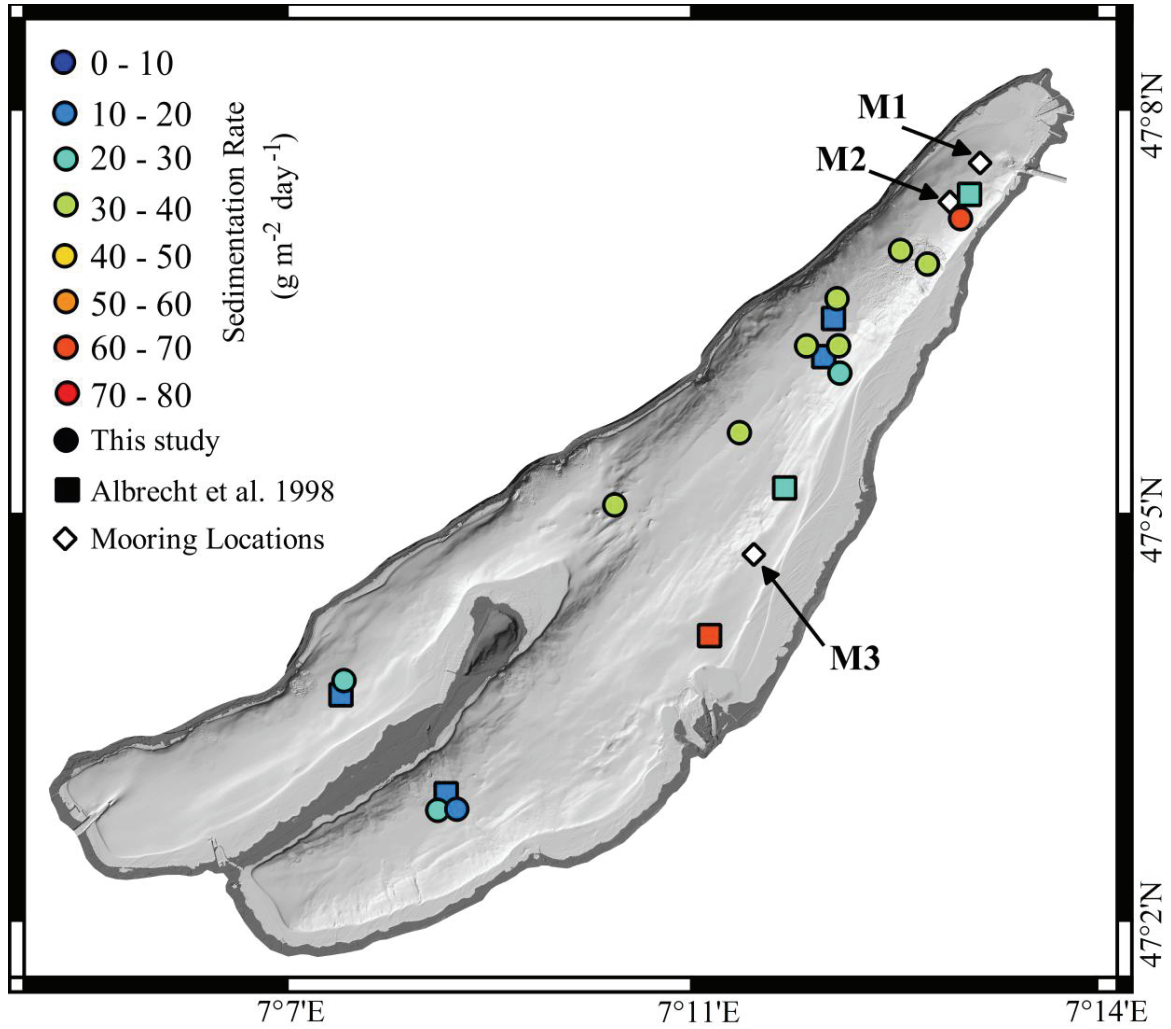**Figure 4.9.** Gravity core derived sedimentation rates in LB. Round symbols represent data from this study (mean 32.2 g m^2 day$^-$1; 1986 to 2010/2015) while squares denote sedimentation rates obtained from *Albrecht et al.* [1998] (mean 24.0 g m^2 day^{-1}; 1986 to 1993/97).
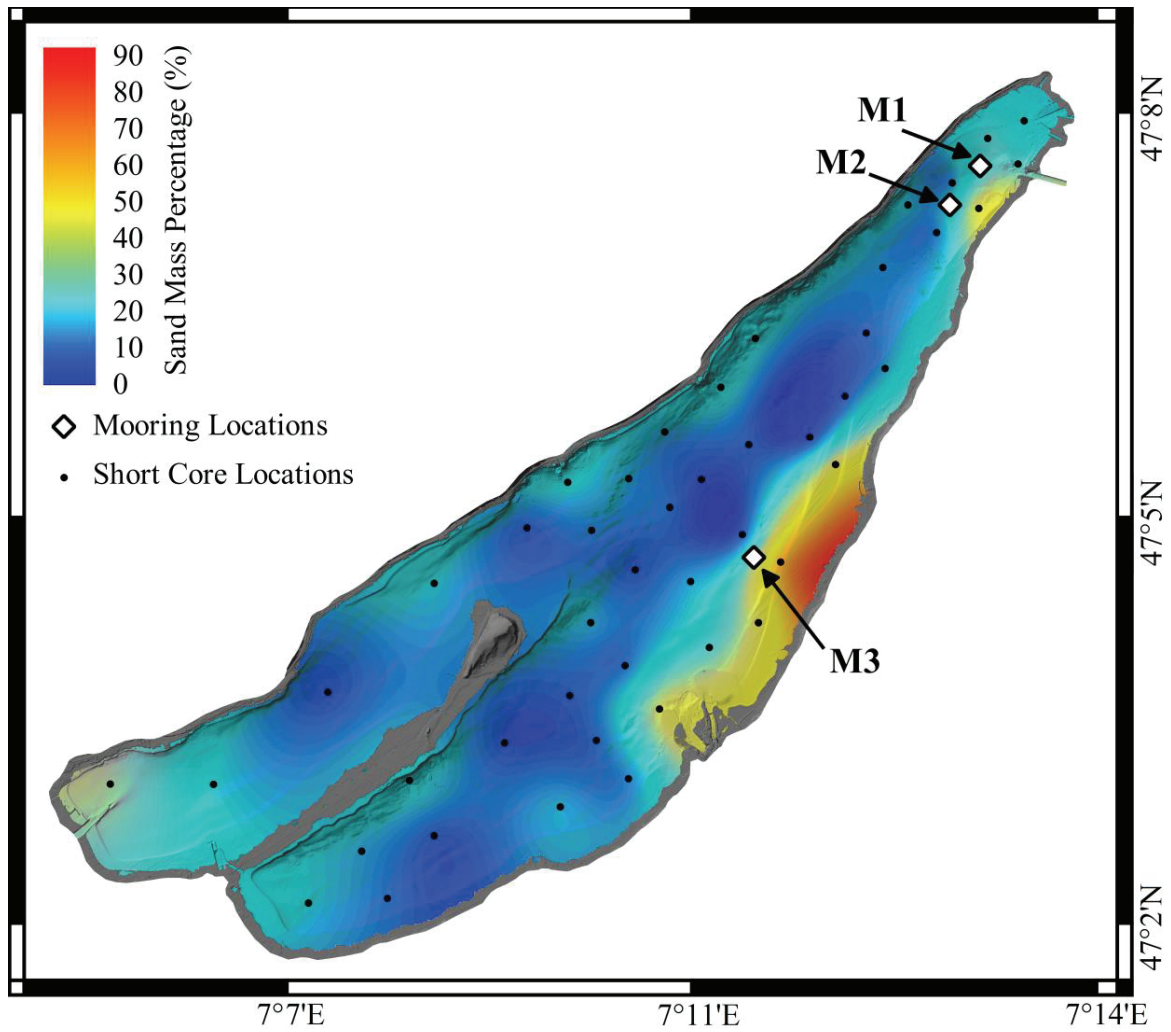
Figure 4.10. Spatially interpolated mass percentage of surface sediment consisting of sand (63 to 2000 µm). Core-top samples (sampled during 2014) locations marked by black dots, mooring locations marked by white diamonds.
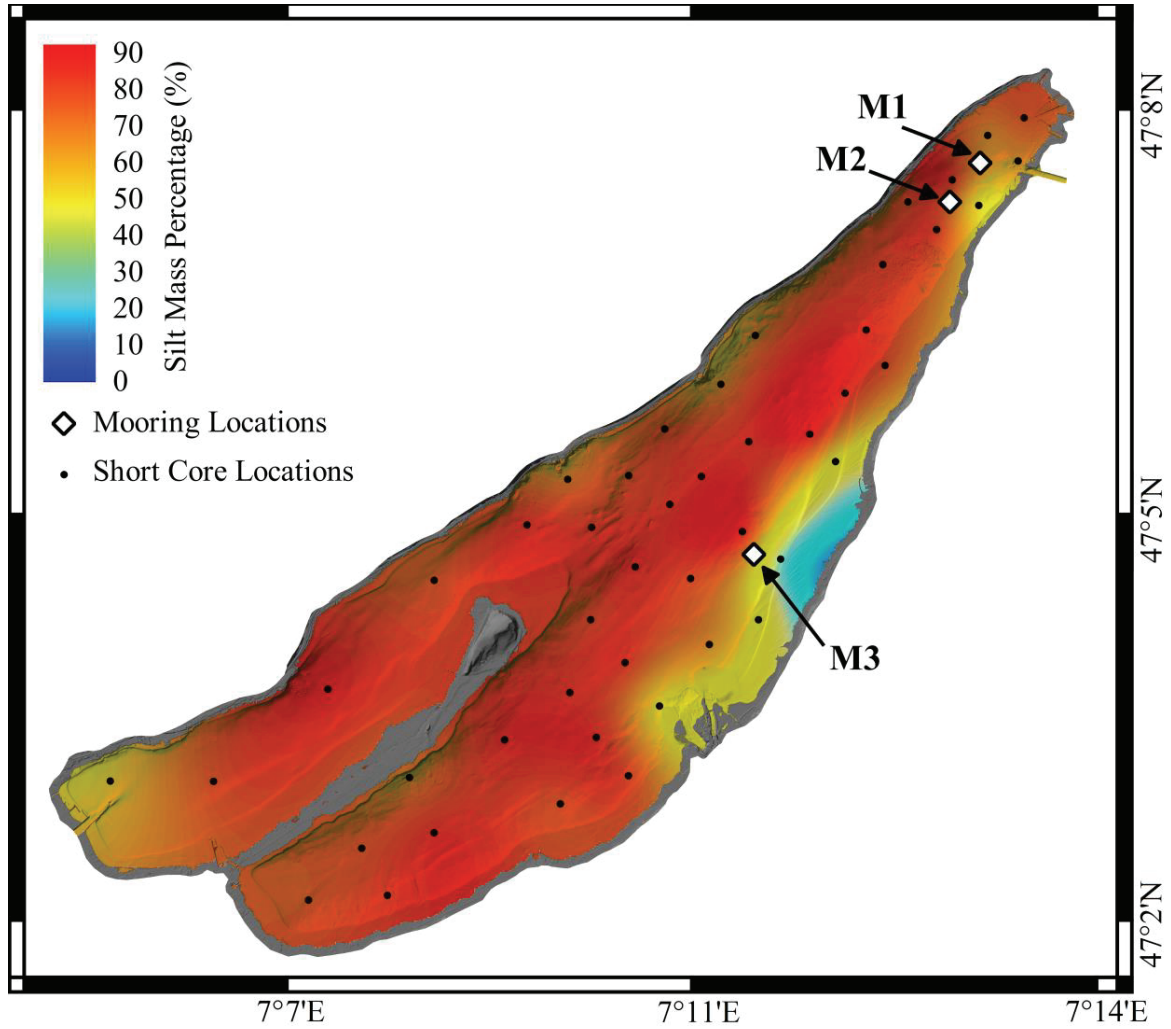
Figure 4.11. Spatially interpolated mass percentage of surface sediment consisting of silt (2 to 63 µm). Core-top samples (sampled during 2014) locations marked by black dots, mooring locations marked by white diamonds.
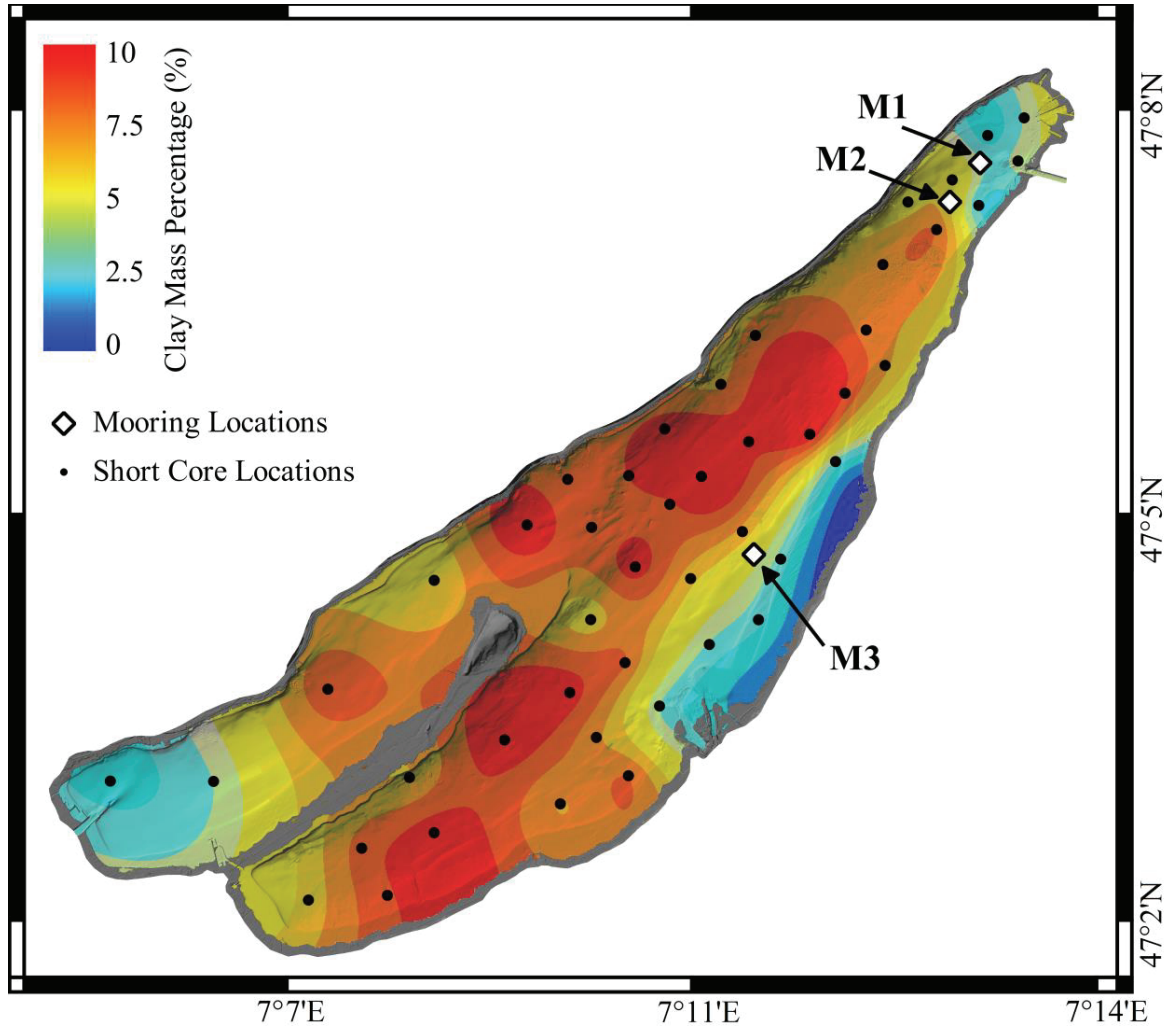
Figure 4.12. Spatially interpolated mass percentage of surface sediment consisting of clay (0.01 to 2 μm). Core-top samples (sampled during 2014) locations marked by black dots, mooring locations marked by white diamonds.

4.4 Discussion

Floods are usually associated with high catchment erosion, leading to large amounts of sediment being carried by the inflow far into the lake interior [*Fink et al.*, 2016]. Here we found that the majority (70 to 80 %) of the sediment supplied by both the Aare and the Schüss into LB arrived within less than 10 % of the time (Figs. 4.3e and 4.3f). High SSC events in the Aare are associated with rain events in the Sarine River catchment [*Råman Vinnå et al.*, 2017b]. These events mainly occur during Vent winds, which carries moist air up from the South-West (Figs. 4.4a and 4.4b). Rain patterns in the Sarine catchment are seasonally varying with increased precipitation in summer compared to winter (Figs. 4.A3a and 4.A3c). This affects the particle supply in the Aare, which varies according to the seasons with higher load in summer and lower load in winter (Fig. 4.3a). In the Schüss River catchment however, we could not find a seasonal variability of sediment load (Fig. 4.3b). These findings with a seasonal varying sediment supply from the Aare and non-seasonal supply from the Schüss follows results from *Santschi and Schindler* [1977], who furthermore showed a non-seasonal varying sediment supply from the Zihlkanal.

Compared to *Santschi and Schindler* [1977] we obtained a two orders of magnitude increase of the annual sediment supply from the Aare from 1973 to 2013 (Table 4.1). This is supported by results from *Albrecht et al.* [1998] who observed a ~40 % sedimentation increase in LB from 1963 to 1996 (7.7 to 16.4 g m^{-2} day^{-1} between 1963 and 1986; 13.4 to 20.6 g m^{-2} day^{-1} between 1986 and 1996, Table 4.3). For the Schüss, we could not find any significant change in the sediment supply between this study and *Santschi and Schindler* [1977] (Table 4.1).

With climate change, the amount of rain on the Swiss plateau is predicted to slightly increase in winter and decrease in summer [*CH2011*, 2011]. This might lessen the importance of the Sarine as a contributor of particles to LB in summer. As river discharge patterns in Switzerland shift from summer towards winter [*FOEN*, 2012; *Speich et al.*, 2015] sediment supply has been anticipated to increase in winter [*Råman Vinnå et al.*, 2017b]. Given the surge of sedimentation in LB since 1963 shown here and in *Albrecht et al.* [1998] a decrease in sediment supply to LB is considered unlikely.

4.4.1 Plume Pathway

Historical observations of the Aare plume pathway into LB suggest two drastically different patterns. *Wright and Nydegger* [1980] suggested a shore-following pathway with the plume being deviated towards the right while *Albrecht et al.* [1999] observed signature of the plume flowing into the center of the lake. *Råman Vinnå et al.* [2017a] used a hydrodynamic approach to explain the existence of these two characteristic patterns, which are driven by the wind-induced lake circulation. North-East wind and resulting lake circulation will move the plume towards the lake center while South-West winds will push the plume toward the South shore. Our analysis showed that most high SSC events are correlated to South-Western wind (Fig. 4.5 a and b), consequently we explain a higher sedimentation rate on the South shore as driven by the typical lake circulation during "extreme" rain events. Note that a clear difference exists to the normal (annual) wind field over the lake (Fig. 4.4d). During North-Eastern winds (origin 0 to 100°; Fig 4.5a) the northward current at M3, associated with the river plume was less consistent and fluctuated more. In summary, the plume was diverted towards M3 during South-Western winds and diverted away from this station during North-Eastern winds.

To investigate the effect of earth's rotation on the plume we use the Rossby radius (R) where $R = U/f = 1.6$, for velocity (U) = 0.3 m s^{-1} and the Coriolis parameter (f) at 47.5°N. This is on the same order as the distance from the river outflow to the lake center (1.8 km). The Coriolis effect on the river plume is thereby expected to be minor, the direct effect of the wind is considered to dominate the plume direction.

As the plume travels further north it loses momentum. Detection is usually possible either by the ADCPs echo return signals or as temperature anomaly (Figs. 4.6 and 4.7). Here we associate a temperature drop in the epilimnion to the passage of the plume, which is colder than LBs surface water. The authors acknowledge that the observed temperature drop in the epilimnion could also be due to other processes, such as atmospheric cooling due to the weather system coming in from the south west and causing high SSC from the Sarine. Of the three measurements used at the moorings for locating the plume, temperature was thus the least trustworthy. Turbidity-based measurements worked only during high SSC events and current measurements could only be used close to the river mouth.

4.4.2 Sedimentation patterns

Major SSC events in the Aare coincide with South-West winds (Figs. 4.4, 4.5a and 4.A3). This wind pattern affects the direction of the intruding plume and turns it northward alongside the eastern shoreline (Figs. 4.5, 4.6 and 4.7), with clear consequences for sedimentation patterns (Figs. 4.9 to 4.12).

As the plume travels northward, particles settles out resulting in increased sedimentation rates close to the Aare inlet (Fig. 4.9). Large quantities of sand settle on the shallow ~2 m deep shelf (Fig. 4.10), where turbulence and resuspension inhibit sedimentation of smaller sized particles (Figs. 4.11 and 4.12). These instead end up in the deeper parts of LB (Fig 4.8; Table 4.4). The net effect of both the northward plume direction as well as the resuspension/sedimentation of smaller sized particles towards the deeper parts of LB resulted in twice the amount of sedimentation in the Tüscherz basin compared to the Lüscherz and Neuenstadt basins (Fig 4.9).

Interestingly, we found less silt and clay within ~800 m of the Aare outflow as well as ~1500 m from the Zihlkanal (Figs 4.11 and 4.12). Both of these rivers have high discharge (Table 4.1), which resulted in that particles within this size range were likely to be carried away by the river current. The sand content observed close to the surface at M1 (Z1 at 7 m, Table 4.4) was thereby likely caused by a combination of supply from the Schüss and removal of the finer particles by the outflow.

In this study we obtained higher sedimentation rates (mean 32.2 g m^{-2} day^{-1}; Fig. 4.9; Table 4.3) compared to that obtained by *Albrecht et al.* [1998] (24.0 g m^{-2} day^{-1}; Table 4.3). The difference between both studies is probably due to a difference in the method used for estimating sediment density, but could point to an increased sedimentation trend due to the difference observed here and by *Santschi and Schindler* [1977] (Table 4.1). The sediment core MAR observed here fits well with MAR at the tributaries (Table 4.1). By using the Zihlkanal sediment supply from *Santschi and Schindler* [1977] (Table 4.1) we obtained a total mass supply from all three rivers of 29 g m^{-2} day^{-1}. This fits nicely with the mean sedimentation rate in LB observed here of 32 g m^{-2} day^{-1}.

Both the detailed survey conducted during the 29th July 2014 (Fig. 4.5e) and MAR difference near bottom between traps M3-Z3 and M2-Z6 (Table 4.4) indicate that ~70 % of the SSC gets lost through sedimentation and dispersion before reaching M2. Assuming that dispersion is much smaller than sedimentation we assume that ~70 % of the particles settle before reaching M2. This should be viewed as a maximum possible settling rate. The distance between the Aare

138

delta and M2 is ~7 km and between M2 and the Aare outlet ~1 km. Assuming settling and dispersion rate across the lake is linear, ~10 % of the SSC would be lost to settling out or dispersion before reaching the outflow. This does not include the silt and clay suppressive settling effect discussed above.

So by assuming that dispersion is much less effective at lowering SSC we conclude that up to ~80 % of the sediment supplied by the Aare during high turbidity events settle in the lake, while ~20 % may leave the lake through the outflow. This is valid for high SSC events triggered in Sarine catchment by storms coming from the South-West. During the other dominant wind regime, the Bise (Fig. 4.4d), the plume diverges into the center of the lake [*Albrecht et al.*, 1999; *Råman Vinnå et al.*, 2017a]. In this case ~80 to 100 % of the sediment entering into LB settles inside the lake. Thus, by combining both hydrodynamic and sedimentology measurements we can identify the cause behind the observed sediment pattern in LB.

4.4.3 Sediment instability by changed sedimentation regime

Rapid sedimentation as well as steep sloping bottoms are both associated with increased risks for subaqueous slides [*Lee et al.*, 2007]. These can damage water utility constructions, give rise to tsunamis and extremely high concentrations of resuspended particles. In the area South-East of M2, where the Aare plume leaves the shallow shelf, multiple subaqueous mass movements have occurred within the last fifty years [*Dubois et al.*, 2017].

The wind driven focusing of sedimentation observed here typically diverts the heavily SSC loaded Aare plume along the shallow northern shelf, thereby supplying large quantities of sediment to a limited geographical area. The historically active subaqueous mass movement region identified by *Dubois et al.* [2017] is located at the end of the shallow shelf north of the Aare inflow. As the Aare plume approaches this region, it is forced of the shallow shelf by the coast line towards the M2 station (Fig. 4.1b). As the plume exits the shelf area, it passes over the subaqueous mass movement region. In the free water bottom turbulence decrease and particles which were previously in suspension/advected close to the bottom can settle out. Even though SSC has dropped by ~70% before this happen, the plume still contains large quantities of sediment as shown by M2 sediment traps. Thus, large amounts of particles sediment on the steeper region just off the shelf. This hypothesis is strengthened by the measured settling velocity (sand size typical) of the detected echo signal at M2, which is attributed to the plume. This speed amounts to ~1.8 mm s^{-1} and was likewise measured at M3 (~2.4 mm s^{-1}). This sand

like settling velocity corresponds to a settling distance of ~300 m given the travel time to M2 (~35 hours). Thereby indicating that these particles would have settled long before reaching M2 if not kept in suspension by vertical turbulence. As rapid sedimentation and steep sloping bottoms are enhancing factors for subaqueous slides [*Lee et al.*, 2007], we claim that the wind caused selective focusing of sedimentation is likely to increasing the risk of subaqueous mass movements in LB.

4.4.4 Method comparison

When comparing MAR from the deepest sediment trap at each station with the closest sediment core we find that both methods fit nicely at M3 (Z4 trap mean: 78 g m^{-2} day^{-1}; 97_01 core: 66 g m^{-2} day^{-1}; Tables 4.3 and 4.4). The rates measured at M1 (Z6 trap 28 g m^{-2} day^{-1}) and M2 (Z3 trap 36 g m^{-2} day^{-1}) best follows core 96_02 (20.5 g m^{-2} day^{-1}), while the rate in core 14-52 was ~70 to 130 % higher (62 g m^{-2} day^{-1}). In this core earlier MAR has increased since 2000, which could not be picked up by core 96_02 due to the sampling date. Of note is that SR for 14-52 (2.3 cm year^{-1}) and 96_02 (2.0 cm year^{-1}; Table 4.3) is roughly similar. However, SR is affected by compression of the cores during transportation and MAR should therefore be used [*Albrecht et al.*, 1998]. Here we used the mean water content in combination with dry density while in *Albrecht et al.* [1998] the density of the core was measured directly. Unfortunately, the numbers of samples in the northern part of LB were too low to make clear statements regarding the increased MAR observed in 14-52. Possible explanations for this increased sedimentation in 14-52 could be increased supply from the Schüss, or creeping of sediment from the steep eastern slope (Fig. 4.9) sometimes between our measurement campaign and *Albrecht et al.* [1998]. This creeping would not be picked up by our traps (which recover sinking particles) or earlier cores.

4.5 Conclusions

Here we followed the intrusion of rivers into Lake Biel (LB) using multiple measurement techniques ranging from acoustic profiles across the water column to sediment. The main focus was on the major sediment supplier the Aare River. The discharge of this tributary is highly seasonal but lacks a clear link between discharge and suspended sediment concentration (SSC). High SSC events, responsible for ~80% of the supplied sediment mass, where instead linked to precipitation in the Sarine River catchment. Most rain events in Western Europe are related to weather fronts coming in from the Atlantic. This results in winds from South-West over LB, at the same time as the Sarine receive large amounts of precipitation, thereby eroding sediment from the catchment and increasing SSC in Aare. Extreme SSC events, caused by weather patterns, are consequently selectively deposited along the shallow Eastern shore of Lake Biel. This increases the local sediment load on the shallow shelf north of the Aare inflow. As the shelf ends, the plume still carrying large amount of sediment, passes over steep sloping topography. This area contains multiple documented major subaqueous mass movements. Therefore, wind focusing sedimentation patterns in LB are likely to increase the risk for subaqueous slides.

Furthermore, we found here that not only large tributary inflows but also outflows affect sedimentation. Through high discharge, and thereby increased flow in the lake, smaller sized particles (clay and silt) were kept in suspension with only larger particles (sand) settling. These small sized particles instead settled in the deeper parts of LB, or were transported out from the lake at the outflow. This increases the percentage of larger sized particles (sand) in the sediment close to the deltas and the main outflow. The spatial locations of inflows and outflows thus matter for sedimentation patterns.

To conclude, we showed here that both wind patterns, tributary inlets as well as outlets affect sedimentation patterns in LB. The wind has a focusing effect on sedimentation and concentrate the bulk of sediment supplied by the Aare River along a limited stretch of shallow shelf. This has potential harmful effects on shore facilities due to increased likelihood of subaqueous mass movements. Given the uncertainty associated with future rain events and the observed increase in sedimentation in LB over the last 40 years, our study highlights the importance to further investigations of the interactions between climate, rivers and lakes.

Appendices

Appendix 4.1. Particle tracking using ADCP echo intensity

To measure temporal and spatial development of the particle distribution in an aquatic system requires continuous sampling of the water column. While ADCP instruments can be used to obtain both the velocity and the particle concentration, the particle transport can then be estimated by combining these two. Here a detailed method for combing ADCP echo intensity with turbidity observations, laser diffraction size- / volume concentration measurements and water samples is presented. The purpose is to obtain a corrected backscatter signal in a system with inhomogeneous and changing suspended particle concentration and properties.

The method mostly follows the steps described by *Moore et al.* [2012]. However, their study was done with horizontal mounted ADCPs in a river. For such settings a uniform particle composition across the profiling range can be expected. This is not the case when the ADCP is deployed vertically in lakes, oceans or low turbulent rivers where the particle composition can change considerably across the measured water volume. Therefore the method is modified by using mass-, size- and composition measurements to adjust for the signal loss due to particle attenuation.

ADCP backscattering signal are delivered to the user in machine units (counts) which have to be converted into a system independent intensity unit, I_{dB} [dB], e.g. *Gostiaux and van Haren* [2010] and *Moore et al.* [2012],

$$I_{dB}=10\log_{10}\left(10^{KE/10}-10^{KE_{noise}/10}\right)$$

(4.A1)

here E is the ADCP received signal intensity in counts, E_{noise} is the machine noise in counts and K is the count to decibel conversion factor. This is valid while the signal to noise ratio $K(E-E_{noise})<10$ otherwise $I_{dB}=KE$. E_{noise} can be estimated if the signal traveling distance is long enough in regions with no expected backscatter or if the attenuation due to particles is significant. K is dependent on the electric component temperature, T_e [°C], and the following relationship is used by *Moore et al.* [2012].

$$K=\frac{127.3}{T_e+273}$$

(4.A2)

However, the conversion factor is also hardware dependent [*Lorke et al.*, 2004], and in this study we use:

$$K = \frac{k_i * 273}{T_e + 273}$$ (4.A3)

Where k_i is a scaling factor delivered by Teledyne RD Instruments for each beam, for T_e, the ADCP built-in temperature sensor is used. From the converted signal, Eq. 4.A1, the backscattering strength from particles, also called backscattering level BL [dB], is deduced by adjusting the signal received by the ADCP transducer for power lost due to signal spreading, attenuation and transmission weakening. To compensate for battery power deprivation [*Teledyne RDI*, 2014], i.e. signal source depletion, we add a fourth term to the equation given by *Moore* [2012]

$$BL = I_{dB} + 20\log_{10}(r) + 2\alpha r$$
$$- 20\log_{10}(B/Bfull)$$ (4.A4)

Here B is the decreasing ADCP battery power and Bfull is the battery power at deployment start. The second term compensates for signal power loss due to spherical spreading, r is the distance traveled. The third term handles the total attenuation, α, of the signal caused by the water and particles. Since the signal has to cross the water column twice the power loss has to be doubled, hence the numbers 20 and 2.

The total attenuation, α [m], can be divided into three parts as described by *Moore et al.* [2012]

$$\alpha = \alpha_w + \alpha_{p.s} + \alpha_{p.v}$$ (4.A5)

α_w represents attenuation caused by heating of the water, loss due to particle scattering is expressed in $\alpha_{p.s}$ and $\alpha_{p.v}$ is loss induced by viscous absorption of the signal in the boundary layer surrounding the particle. The water attenuation term, α_w [m], can be written as proposed by *Fisher and Simmons* [1977]

$$\alpha_w = (55.9 - 2.37T + 4.77*10^{-2} T^2$$
$$-3.48*10^{-4} T^3)*10^{-15} f^2$$ (4.A6)

here T is the water temperature in °C and f is the ADCP signal frequency in Hz. Since the temperature within the signal traversed volume have large seasonal and spatial variations we use vertical moored temperature loggers for T in Eq. 4.A6 as proposed by *Lorke et al.* [2004]. The particle caused scattering- and viscous attenuation coefficients can be written as

$$\alpha_{p.s} = M \langle \xi_s(a_s, f) \rangle$$ (4.A7)

144

$$\alpha_{p.v} = M \langle \xi_v(a_s, f) \rangle \qquad (4.A8)$$

where M is the mass concentration of particles, $\xi_s(a_s, f)$ and $\xi_v(a_s, f)$ is the particle diameter-, a_s, and frequency, f, dependent scattering- and viscous attenuation constants, angular brackets indicates average [*Hay*, 1983; *Moore*, 2012; *Moore et al.*, 2013]. ξ_v can be expressed as

$$\xi_v = \frac{ks(\sigma-1)^2}{2\rho_s(s^2+(\sigma-\delta)^2)}$$

$$s = \frac{9}{4\beta a_s}(1+1/(\beta a_s)) \qquad (4.A9)$$

$$\sigma = \frac{\rho_s}{\rho_0}, \qquad \delta = \frac{1}{2}(1+9/(2\beta a_s)), \qquad \beta = \sqrt{\frac{\omega}{\nu}}$$

here $k = 2\pi/\lambda$, λ is the signal wavelength, ρ_s and ρ_o are the particle- and water density, ν is the kinematic viscosity at 10 °C, $1.3 * 10^{-6}$ m^2 s^{-1}, and $\omega = 2\pi f$ [*Moore*, 2012]. ξ_s has its maximum value for particles with a diameter around 1 mm and can be assumed to be zero when the particle diameter drops below 100 μm, the maxima for ξ_v occurs for particle sizes around 1 μm [*Moore et al.*, 2013].
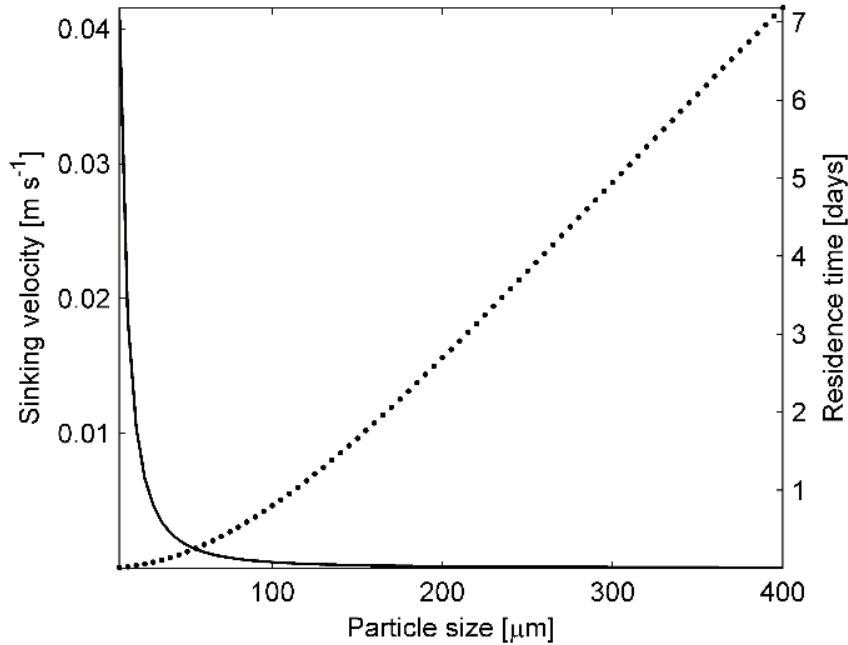

Figure 4.A1. Particle sinking velocity (dots) as in *Cheng* [1997b] for 10 °C and particle residence time (line) in Lake Biel calculated with a mean depth of 31 m.

145

Considering that the particles in a shallow lake have been in suspension for a long time it can be assumed that the majority of the particles with a size exceeding 100 µm have mostly fallen to the lake bottom, see Fig. 4.A1. This implies that the majority of the particles interacting with the ADCP signal will have a size smaller than 100 µm. Therefore $\alpha_{p.s}$ is neglected in Eq. 4.A5, subsequently Eq. 4.A4 can be written as

$$BL = I_{dB} + 20\log_{10}(r) + 2(\alpha_w + M\langle\xi_v\rangle)r$$
$$-20\log_{10}(B/Bfull)$$

(4.A10)

To solve this equation a laser diffraction instrument can be used to measure the particle size and volume concentration. To acquire the particle density the laser diffraction observations are combined with mass measurements from filtration of water samples. These mass samples are furthermore correlated to the corrected backscatter signal in order to obtain the particle concentration. The particle transport can then be attained by combining this backscattering derived concentration with ADCP current measurements.

To obtain satisfactorily correlation between samples and the ADCP echo it is important to catch the extreme conditions of both particle concentration and composition. If the echo is caused mainly by terrestrial or biological particles, it can be determined by comparing turbidity and chlorophyll observations for time periods with low respectively high chlorophyll content.

Chapter 5 Project synthesis:

Evaluation of ideal locations for a new drinking water intake in Lake Biel

5.1 Introduction

Today's Lake Biel (LB) Ipsach Drinking Water Plant (IDWP) and the corresponding lake water intake pipeline were built in 1974. At the end of the intake pipeline, the raw water is retrieved at 38 m depth and pumped to shore for processing. The capacity of IDWP is 900 m^3 h^{-1} and an average of 4.1 million m^3 year $^{-1}$ of water is distributed to the drinking water network in the City of Biel/Nidau. Due to ageing of the plant, Energy Service Biel (ESB) plans to replace it entirely. In this context, we examined here whether the position of the lake water intake has to be adapted due to changing environmental conditions.

The trigger of the present investigation was a strong turbidity event on December 31, 2009. Near the present lake water intake (M2, Fig. 5.1), a subaqueous mass movement occurred, suspended solids entered into IDWP and led to a four days operation closure. Since the reason for this extreme turbidity event was unclear before our project, ESB also raised questions on whether climatic changes and/or the decommissioning of the Mühleberg Nuclear Power Plant (MNPP) could alter the quality of the lake water. An agreement was reached to further analyse the current hydrodynamics and particle distribution as well as potential changes in LB by future climate change and MNPP closure.

On the basis of more than two years of fieldwork, the Aquatic Physics Laboratory, in collaboration with research groups at EPFL, Eawag and University of Bern, analysed the distribution of currents, as well as temperature, oxygen and turbidity in LB. In this chapter we summarise the answers to the five questions put forward in chapter 1.5.

148
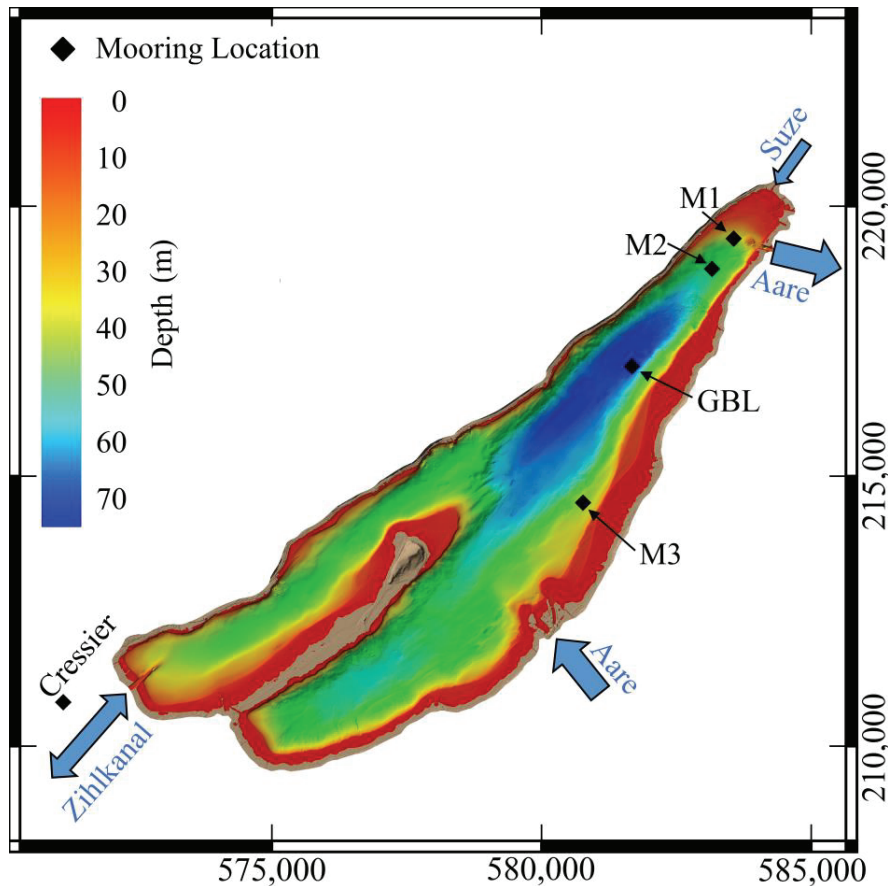
Figure 5.1. Bathymetry of Lake Biel (LB) from the lake surface (red) to the maximum depth of 74 m (dark blue) obtained from combined Lidar and multibeam surveys. Land is coloured in light brown. The four black diamonds indicate the position of field sampling sites (moorings M1, M2, M3, and monthly GBL monitoring). The current intake for the IDWP is located near M2 (anchored at 45 m depth, water intake depth at 38 m). Lake tributaries and flow directions are marked with blue arrows, arrow width indicate discharge size. For details of the bathymetric survey, see *Hilbe* [2015] for multibeam and *Baran* [2017] for LIDAR techniques.

Here we explain the arguments for the potentially ideal position of future raw water intake in LB. Other aspects, in particular the decommissioning of the MNPP [*Råman Vinnå et al.*, 2017a], climatic development [*Råman Vinnå et al.*, 2017b], the role of the Aare and the Schüss for turbidity and sedimentation [*Råman Vinnå et al.*, 2017c], as well as subaqueous mass movements [Thesis Appendix *Dubois et al.*, 2017], are presented in other publications. The bathymetry of LB, which was newly measured with a bathymetric Multibeam (water depths > 5 m [*Hilbe* 2015]) and a LIDAR (shallow water and shore zones [*Baran* 2017]), is available from the participating authorities. The focus of this synthesis is only on the future position of drinking water withdrawal.

149

5.2 Constraints on the vertical position of the lake water intake

5.2.1 Temperature

An important water quality criterion for selecting the intake depth of raw water is its temperature. Thanks to monthly monitoring at station GBL (Fig. 5.1) by the Office of Water Protection and Waste Management of Canton Bern (GBL / AWA), temperature profiles are available for the last 22 years (Fig. 5.2, 1994 to 2016). This allows for an ideal statistical foundation of expected temperature fluctuations as a function of depth.

The temperature in LB epilimnion (surface waters, 2.5 to 25 °C) is too warm and in the thermocline region too variable (seiching activity), which makes these regions unsuitable as raw water source (minima and maxima in Fig. 5.2). Production of drinking water requires cool water temperatures, ideally < 8 °C for IDWP. In Fig. 5.2 the upper limit of the depth at which the future lake water intake should be installed, was estimated from the probabilities of measured temperatures in LB during the last two decades. If, for example, a desirable maximum temperature of 8 °C should not be exceeded more than 2.5 % of the time (observed temperatures colder than 8 °C with a temporal occurrence of 97.5 %; arrows in Fig. 5.2), the lake water intake must be placed deeper than 42 m. Correspondingly, with reference to Fig. 5.2, with the occurrence probabilities for 2.5, 15, 50, 85 and 97.5%, it is possible for ESB to plan for any other desirable temperature range.

The water temperature in LB is likely to change during the lifetime of the future water intake due to both local and global anthropogenic influence. In the upcoming years, the entire water body of LB will be cooled down by ~0.3 °C [*Råman Vinnå et al.*, 2017a]. This will be caused by the planned decommission of the MNPP in 2019 and thereby the removal of ~700 MW of cooling water heat input from the upstream Aare River to LB. In the follow-on decades the climate-related warming of the atmosphere will lead, as in most lakes globally, to increased water temperature in LB [*Råman Vinnå et al.*, 2017b]. This corresponds to a heating of water at a depth of 42 m over 50 years by ~0.3 °C (0.06 °C decade^{-1}). This prediction should be viewed as the upper range of possible warming under the A1B emission scenario, since future heating will be affected by changes in atmospheric forcing parameters not considered in this dissertation (Table 3.6 and Fig. 3.A6 in *Råman Vinnå et al.* [2017b]). To compensate for this warming, the lake water intake would have to be shifted downward to greater depth by ~5 m (Fig. 5.2).
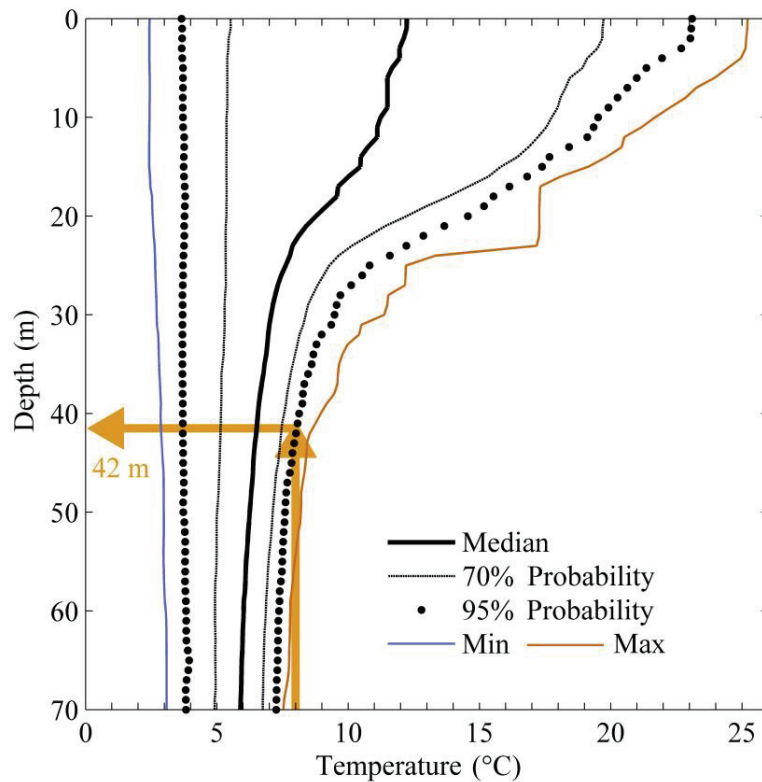
Figure. 5.2 Vertically resolved temperature distribution in LB based on profiles collected by AWA at station GBL (Fig. 5.1) from 1994 to 2016. Shown are the temperature median (bold line), maximum (thin vermilion), minimum (thin blue) and the 70% and 95% temporal occurrence range (i.e. within 95% of the measured time the temperature stayed within the dotted lines). This figure allows to select targeted water temperature for future water withdrawal. Arrows indicate the minimum depth required (42 m) to withdraw water colder than 8 °C during 97.5% of the time.

5.2.2 Oxygen

Another important water quality criterion for drinking water is the oxygen content. Anoxic waters can contain ammonium or dissolved iron and manganese, which are problematic in drinking water from the point of view of taste-and-odour as well as human health. In addition, oxygen is required when processing the raw water in order to remove the organic matter. A low concentration or lack of oxygen could thus interfere with subsequent processing in the plant. Organic material could enter into the distribution network, causing growth of undesirable microorganisms.

As for the temperature in section 5.2.1, the monthly profiling by AWA of vertically resolved oxygen concentration at station GBL (Fig. 5.1), is an ideal basis for the statistics of historical

dissolved oxygen in LB. Fig. 5.3a illustrates the minima, maxima and median oxygen concentrations from 2000 to 2015.

Annually, the oxygen concentration in LB drops to hypoxic levels in late autumn, to be replenished in the beginning of each year by complete deep convective mixing in winter. Accordingly, the oxygen content in the first half of the year is excellent (Fig. 5.3a, blue). With the decomposition of organic matter in the deep-water, the dissolved oxygen decreases during the stratified summer period (March to November) and reaches its lowest values in November (Fig. 5.3a). In the deepest parts of LB, hypoxic conditions usually occur at this time of the year (< 4 mg L^{-1}). In order to avoid such low oxygen levels all year round, the raw water intake should be shallower than 47 m depth (arrows in Fig. 5.3a).

Besides the absolute depth of the intake discussed above, the height above the sediment surface also plays an important role. As Fig. 5.3b shows for November samples, the oxygen content immediately above the sediment decreases significantly. This is particularly prominent in the deep central parts of the lake (Fig. 5.3b, orange lines) and is therefore undesirable as raw water source. In the area close to the current lake water intake mooring (at 45 m depth, close to M2 in Fig. 5.1) oxygen concentrations > 7 m above the lakebed were greater than 4 mg L^{-1} (arrows in Fig. 5.3b, green lines) and thereby acceptable as raw water source.

As future warming trends will weaken the deep mixing, especially in warm winters [*Schwefel et al.*, 2016], oxygen critical levels might be experienced higher up in the water column. Raw water withdrawal should thus not be deeper than indicated above. The decrease in nutrient load (and consequently reduced algae growth) experienced by LB since the early 1970s [*Liechti*, 1994], would have resulted in a decrease of oxygen consumption and improved deep water oxygen concentration. However, no such trend can be seen in existing oxygen measurements from LB. Reduction of nutrient loading to lakes occurs only slowly and the sediment oxygen demands can take decades to change [*Müller et al.*, 2012]. Therefore, we cannot assume that the oxygen content in the deepest parts of LB will significantly improve during the lifetime of future lake water intake installations. In summary, in regard to oxygen content, we conclude that lake water above ~50 m depth is suitable as raw water source for drinking water in the upcoming decades. As Fig. 5.3b shows, a distance of at least ~7 m from the local lakebed is necessary in order to avoid hypoxic conditions in late autumn.
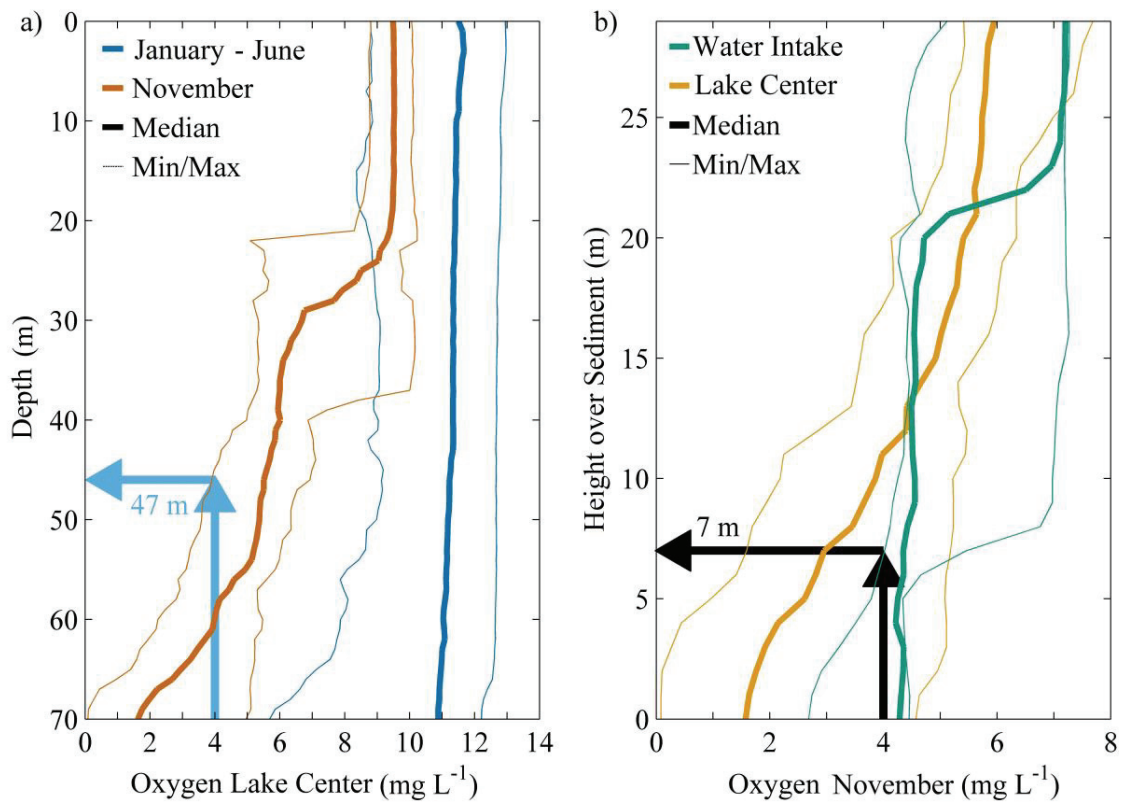
Figure 5.3. a) Vertically resolved oxygen concentration in LB based on profiles collected by AWA at station GBL (Fig. 5.1) from 2000 to 2016 for periods of high contents in winter/spring (dark blue) and at critical periods in November (red). b) Oxygen concentrations as a function of the height above the sediment in November in the area of the maximum depth (red, GBL station Fig. 1) and in the area of the current raw water intake (green, close to M2 Fig. 5.1). Above a depth of 47 m at station GBL and 7 m close to station M2, at any given time the oxygen content never dropped below 4 mg L^{-1} (arrows). Thick lines denote medians and fine lines the maxima and minima.

5.2.3 Particle content and turbidity

A third important water quality criterion for raw water intakes, which is less essential in LB, is the suspended sediment concentration (SSC), often referred to as turbidity. As the monthly monitoring of AWA shows for the period from 1997 to 2015 (station GBL in Fig 5.1), the turbidity in LB is generally low, and no pronounced zones of particularly turbid or particularly clear lake water are shown over the entire water column (bold line in Fig 5.4a,). The turbidity was determined by means of a transmissometer (WETLabs C-Star) over 10 cm at 600 to 650 nm and expressed as % of attenuation.

Close to the sediment surface, turbidity is enhanced and stable over time (Fig. 5.4b). The main cause is resuspension of organic flocks and hindered settling of particles close to the lake bottom [*Gloor et al.*, 1994], resulting in the most turbid (also called nepheloid) layer immediately above the sediment. Above 10 m from the sediment, turbidity was only ~20 to ~30% of the maximum turbidity immediately at the sediment (Fig. 5.4b). Therefore, it is clearly advantageous to maintain a distance between the water withdrawal nuzzle and the lakebed. In summary, the monitoring of the last two decades shows that the choice of the depth is uncritical as long as the intake is placed ~5 to 10 m above the local sediment.

The maximum turbidity event shown in Fig. 5.4a was measured on 9th December 2009 after a period of heavy precipitation. It was the largest turbidity event sampled by AWA inside LB within the 19 years of measurements. Heavy precipitation in the Sarine River catchment has been linked to high turbidity events in LB [*Råman Vinnå et al.*, 2017c]. The time required for the Aare plume to reach the existing lake water intake lasts ~40 hours (Fig. 5.5). At which point ~70 % of the river sediment has already settled out. Even though enhanced sediment concentration from both Aare and Schüss are evident even inside the plant (Fig. 5.5), no major production problems has ever been associated with these river-induced turbidity events. To conclude, the turbidity event on the 9th December caused by the Aare occurred 22 days earlier than the problematic event on 31st December 2009. It can thus not have caused the IDWP closure following 31st of December 2009.
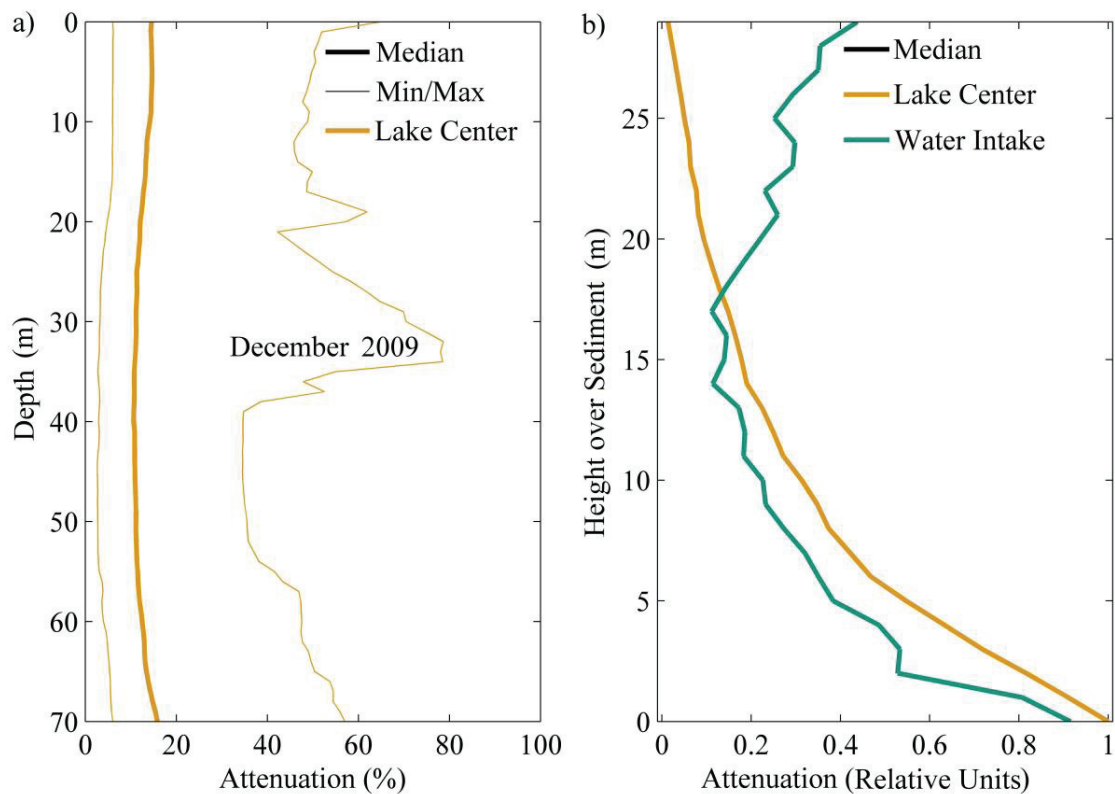
Figure 5.4. a) Vertically resolved turbidity in LB based on profiles collected by AWA at station GBL (Fig. 5.1) from 1997 to 2016. The median (bold line) and the minimum values are practically homogeneous and show no pronounced turbid or clear layers. The variation is larger for the maximum values with the highest turbidity peak measured on the 9th December 2009. b) Turbidity measured from the bottom, no apparent differences occur between station GBL (orange; 1997 to 2016) and M2 (green; 2014 to 2016). In general, directly above the sediment the water is more turbid than in the open water. In order to avoid this enhanced turbidity close to the sediment, the raw water intake should be placed ~5 to 10 m above the local sediment surface.

Figure 5.5. Pearson product-moment correlation between the turbidity signal measured in the Aare (red) and the Schüss (green) inflows towards turbidity measured in IDWP from 2013 to 2016. River turbidity signals have been shifted forward in time (hourly intervals). Peaks mark time required for the turbidity signal to cross the lake and enter into the plant. Water transfer time from the intake nuzzle to turbidity measurements inside IDWP equals 2 hours.

5.2.4 Subaqueous mass movements

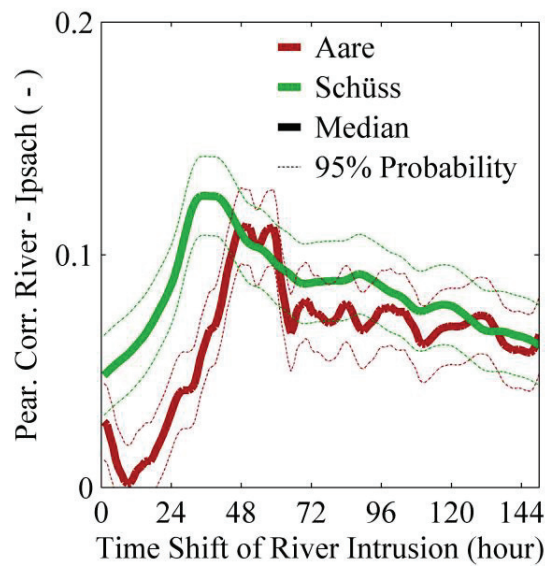The geological occurrence frequency of minor and major subaqueous mass movements (subaqueous slides) in LB is unusually high. During a subaqueous mass movement, massive amounts of sediment can be resuspended, aquatic infrastructure on the lakebed may be damaged and a resulting tsunami wave may damage infrastructure at the shore. The rate of occurrence of mass movements in LB has increased since the 1878 First Jura Waters Correction during which the Aare River was diverted into LB [Thesis Appendix *Dubois et al.*, 2017]. Diversion of rivers into lakes and the changes from previously low to high sedimentation load has been shown to increase the risk for subaqueous mass movements [*Wirth et al.*, 2011]. For LB the connection between high turbidity events and winds from the South-West concentrate sedimentation from the Aare tributary onto the shallow shelf slope of the eastern shore [*Råman Vinnå et al.*, 2017c]. This increases the likelihood of subaqueous mass movements to occur by overloading the sediment [Thesis Appendix *Dubois et al.*, 2017].

Major mass movements are usually occurring in areas with steep inclination of the sediment surface (> 10°) [*Schnellmann et al.*, 2006]. The slopes in LB exceed this limit for most parts of

the lake, including outside the shallow eastern shelf. Surprisingly, detailed bathymetry measurements show a concentration of recent larger mass movements ~500 to ~2000 m South-West of M2 (Fig. 5.6), and not as expected closer to the Aare inflow. The oldest slope failure in this area has been dated to 1964 and the most recent to ~2009/2010 (Fig. 5.6, [Thesis Appendix *Dubois et al.*, 2017]). This most recent aqueous slide is thus the most likely cause for the problematic turbidity event occurrence in IDWP on the 31st December 2009.
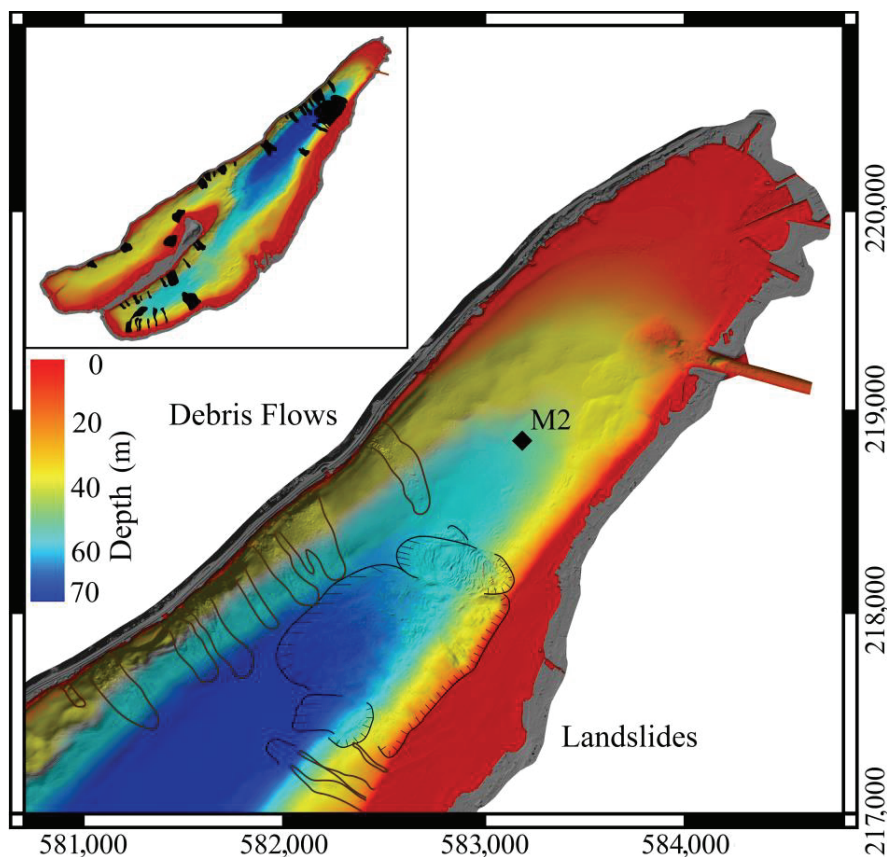
Figure 5.6. Documented subaqueous mass movements in LB (upper left: whole lake marked by black patches, lower right: zoom in on M2 station area). Major slides in the eastern parts of LB are outlined with black lines with markings of slide scar and slump extent, mud flows with brown lines. For further details see Thesis Appendix *Dubois et al.* [2017].

The highest sedimentation rate from the Aare plume occurs on the eastern shelf close to the delta [*Råman Vinnå et al.*, 2017c]. As the plume travels further northward, on top of the flat shallow shelf (~600 m wide), the transported particle masses decrease. The build-up of sediment mass thus decreases towards North-East. As the plume approaches the area with high

157

concentration of subaqueous mass movements South-West of M2, the width of the shallow shelf drastically drops down to ~5 m (Fig. 5.6). This forces the plume out over deeper waters where the slope angle is steep. Thus, even though the sediment load in the river plume has dropped down to ~40 to 30 %, sedimentation in this area occurs over a steeper slope causing an enhanced risk of subaqueous mass movements. Additionally, as the plumes leave the confinement of the shelf and enter into the open water, the levels of turbulence should decrease, resulting in a likely increase in the amount of particles which can settle.

The historical risks for major subaqueous mass movements has so far been elevated in this high risk area. Future risks are hard to determine, since most of the freshly settled sediment in the area already has been flushed down by slides and will now first be replenished (~50 years to reach previous levels). The risk closer to the Aare delta, with a higher degree of sedimentation but on a flatter slope, cannot be assessed here and would require a detailed geomorphological survey.

5.3 Summary

By combining the water quality selection criteria of temperature (max 8 °C for 97.5 % of the time; Fig. 5.2), oxygen (min 4 mg L^{-1}; Fig. 5.3) and turbidity (Fig. 5.4), the ideal depth for the raw water intake is between ~ 40 and ~ 50 m. The green coloured area in Fig. 5.7 indicates the lake bottom which fulfills all of the above mentioned water quality criteria, with the addition that the intake should be ~7 m above the bottom to counteract low oxygen levels close to the sediment, i.e. upper limit from Fig. 5.2: 42 m + 7 m = 49 m and lower limit from Fig. 5.3: 47 m + 7 m = 54 m. Shallower areas (marked in orange, Fig. 5.7) contain water layers which annually become too warm, deeper areas (marked in blue, Fig. 5.7) risk hypoxia during late autumn. As illustrated in Fig. 5.7, only a relatively modest area remains suitable for raw water intake. By relaxing the water quality criteria above, the suitable area in Fig. 5.7 can be increased.
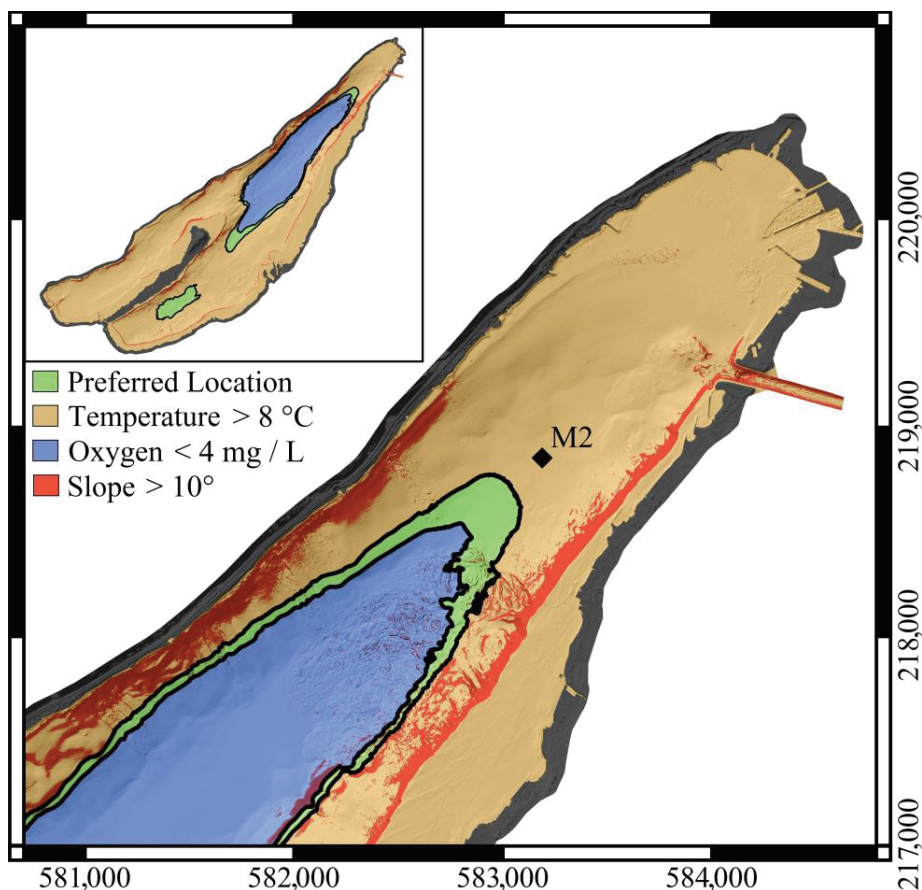
Figure 5.7. Suitable areas for raw water intakes combining water quality criteria for temperature (orange, depth < 42), open water oxygen (blue, depth > 47 m) and bottom oxygen (7 m distance from bottom, subtracted from previous depths; green marks lake bottom between 49 and 54 m depth), and topography (red, inclination > 10 °). Orange areas are too warm, blue areas become hypoxic in late autumn and red areas indicate a local inclination of > 10 ° and point to an increased risk of subaqueous landslides [*Schnellmann et al.*, 2006]. The green area indicates the water quality (with added 7 m distance to the sediment) suitable for raw water intake.

In general, pH, taste-and-odour are also considered as parameters of water quality, but they are to satisfaction in LB and not considered here. In Fig. 5.7, the 5 m depth reduction required to compensate for climate heating at 42 m depth is not considered. Since this prediction will likely be compensated by the decommission of the MNPP [*Råman Vinnå et al.*, 2017b].

Suspended sediments in the northern part of LB are caused by the distribution of particles supplied to LB by the two tributaries the Aare and the Schüss. The sediment trap measurements and the analyses of the sediment cores [Thesis Appendix *Dubois et al.*, 2017; *Råman Vinnå et al.*, 2017c], as well as hydrodynamic model calculations show that close to station M2, despite

159

the proximity to the Schüss (Fig. 5.1), the Aare largely determines the particle content in the water.

As pointed out by *Råman Vinnå et al.* [2017c], the sediment supply to LB by the Aare, the main particle source, has increased since the early 1970s. The base line sediment supply from the Aare is likely to increase in winter and decrease in summer [*Råman Vinnå et al.*, 2017b]. However this is of little concern for raw water withdrawal since ~80 % of the sediment arrives during high turbidity events [*Råman Vinnå et al.*, 2017c]. The uncertainty associated with predicting the extent of future high turbidity events, due to heavy precipitation in the Sarine catchment, is large [*CH2011*, 2011]. Caution is therefore required in selecting future potential lake water intakes closer to the Aare. The river-borne sediment content from this tributary increase by ~10 % km^{-1} from M2 towards the delta [*Råman Vinnå et al.*, 2017c]. Thus in order not to increase the Aare sediment load from present levels in the IDWP by more than ~50 %, the new raw water intake should not be more than 1000 m to the South-West of the present water intake.

The green area in Fig. 5.7, which is suitable for raw water withdrawal in regard to water quality, lies between steep slopes. Both slopes to the north and south have numerous slide scars, which extend far into the more central parts of LB (Fig. 5.6). To the North there are some individual slides with a limited spatial and volumetric extent, which have their incipient tear zones (width up to 100 m) often in close proximity to shore constructions [Thesis Appendix *Dubois et al.*, 2017]. To the North-East closer to the Aare outflow, less pronounced subaqueous slides/sediment markings point to artificial deposits of dredging waste and slow creeping of sediment [Thesis Appendix *Dubois et al.*, 2017]. The southern slope, on the other hand, has a large concentration of slides with a combined slide scar width of ~1 km (Fig. 5.6). The incipient tear is located on the step sloping bottom South-East from M2 and described further in section 5.2.4. The sediment cores collected here do not reach further back in time than ~1920. Previous subaqueous slides might thus be covered by sediment. However, given the large changes in sedimentation rate since the Jura Waters Corrections (from 0.1 to 1.1 cm year^{-1} [*Råman Vinnå et al.*, 2017c]), it is probable that the frequency of subaqueous mass movements in LB increased due to this geoengineering project.

In absence of more detailed studies of sediment stability in LB, slopes with an angle above ~10° are considered as potentially unstable. Steeper slopes coincide with the occurrence of subaqueous mass movements in LB and other lakes [*Schnellmann et al.*, 2006; Thesis

Appendix *Dubois et al.*, 2017]. Given additional loading (e.g., sedimentation, building activity, earthquakes, etc.), the occurrence of future mass movements on the slopes surrounding the green area in Fig. 5.7 cannot be ruled out, the steep slopes in the southwest being of particular concern. However, such subaqueous mass movements are very rare events. By considering both the water quality requirements and the risk for subaqueous mass movements as well as limiting construction costs of pipelines, it is obvious that the most suitable area for raw water withdrawal close to the IDWP is ~200 m to the South-West of station M2 (Fig. 5.7). A second favourable location (upper left Fig. 5.7), unsuitable for the IDWP due to required construction length of pipes, is located in the Lüscherz basin, south west of the Aare inlet. Here water quality requirements are fulfilled and sedimentation is low with decreased risk for subaqueous mass movements [*Råman Vinnå et al.*, 2017c].

5.4 Conclusion

The current lake water intake of the IDWP in LB (close to M2, Fig. 5.7) is already located close to the ideal position for a future intake. As Fig. 5.7 shows, the water quality criteria are fulfilled over a relatively small area to the South-West of M2. However, this area is surrounded by steep slopes and therefore subject to direct risk of subaqueous mass movements. Given this risk we propose to enlarge this suitable area by increasing the temperature tolerance levels past 8 °C. Thereby, a less risky area 100 m west of M2 could be used, with no recent evidence of major subaqueous mass movements (Fig. 5.6). Enhanced water temperature tolerance would furthermore limit the uncertainties associated with the expected climate warming, nonetheless a deeper depth than the current water intake located close to M2 would be preferable in order to limit the negative effect of water temperature increase. Given the risk of subaqueous mass movements in LB we recommend that damage control strategies should be prepared. Suitable strategies could include selective withdrawal of water from multiple different locations/depths or secondary water sources outside LB.

Acknowledgments

Chapter 6:

Conclusions and outlook

6.1 Summary

In this dissertation, the recent past, present and possible near future of Lake Biel water quality dynamics was investigated. A practical research outcome was the identification of suitable locations for a new forthcoming lake water intake for the Ipsach Drinking Water Plant (IDWP). Water quality criteria considered here included water temperature, oxygen, suspended sediment concentration (SSC) and the risk of subaqueous mass movements. These criteria where investigated in the field and by hydrodynamic models in one and three dimensions, resulting in the identification of optimal zones for the positioning of raw water withdrawal from the lake [Chapter 5; *Råman Vinnå et al.*, 2017d].

The results show an expected climate-caused increase of the Lake Biel volume-averaged water temperature by ~+0.1 °C per decade [Chapter 3; *Råman Vinnå et al.*, 2017b]. This warming will increase the stability of the lake stratification and prolong the stratified summer period by ~+2 days per decade, thereby potentially worsening the hypoxic conditions found in the hypolimnion between September and December. However, point-source anthropogenic thermal pollution was also found to play a major role. The upcoming closure of the Mühleberg Nuclear Power Plant (MNPP) in 2019, will temporarily counteract climate warming by lowering the lake temperature by ~-0.3 °C [Chapter 2; *Råman Vinnå et al.*, 2017a]. Furthermore, the climate-caused shift in river discharge counteracts warming in winter and at the same time increases SSC. This in combination with the MNPP closure increase the Aare River water density, thus intensifying hypolimnetic deep-water renewal, a phenomenon likewise predicted for Lake Geneva. Previous studies which did not include the combined effect of changed river discharge regime with corresponding effects on SSC as well as changed river temperature, usually found a decrease in annual deep-water renewal rate due to weakening of river intrusions [*Fink et al.*, 2016]. The results here suggest the opposite with increased annual river intrusion and faster deep-water renewal. This can have potential positive effects for hypoxia/anoxia in lakes, which are predicted to increase due to climate change [*Schwefel et al.*, 2016].

The direction taken by the intruding Aare plume within Lake Biel was shown to be dependent on the wind direction [*Råman Vinnå et al.*, 2017a]. This, in combination with weather system-dependent SSC supply, resulted in concentrated sedimentation on the shallow eastern shelf of Lake Biel [Chapter 4; *Råman Vinnå et al.*, 2017c]. General qualitative patterns in the pathway taken by the Aare River plume were previously suggested by *Wright and Nydegger* [1980] and

Albrecht et al. [1999]. In this work we provided a hydrodynamic explanation describing both the fate of the river water as well as the observed focused sedimentation pattern. The typical wind-driven circulation associated with strong synoptical south-west rain-wind events was found to preferentially distribute the sediment along the south shore of Lake Biel with potential consequences in term of lakebed slope stability.

Furthermore, multiple major and minor subaqueous sediment slides were found in Lake Biel. A steep sloping area with concentrated historic occurrences of major subaqueous mass movements (earliest dated to 1964/65 and latest to 2009/10), was identified south-west of the present day IDWP lake water intake [Thesis Appendix *Dubois et al.*, 2017]. The selective sedimentation pattern of suspended particles from the Aare River, forced by regional weather systems, was connected to this area. The latest (2009/10) occurring subaqueous slide in this area was attributed as the most likely reason behind the four days of production stop in IDWP. The Aare River redirection into Lake Biel, the key measure of the Jura Waters Corrections project, in combination with regional weather systems and steep local topography, are finally responsible for the occurrences of subaqueous mass movements, with severe implications for present and future aquatic infrastructure in this lake. In conclusion, each aquatic system is a different entity with local, regional and global processes collectively affecting water quality.

6.2 Outlook

The increased use of renewable energy as a consequence of the ongoing climate change debate opens up new, interesting and useful scientific topics regarding the physical and ecological climate impact on aquatic systems used as heat sources and/or sinks [*Fink et al.*, 2014b]. The immense variability observed in aquatic systems reaction to external thermal influence by e.g. *Kirillin et al.* [2013] and in this thesis, indicate the great potential benefit for society from extended knowledge of how aquatic systems interact with thermal infrastructure. For instance, due to the ongoing climate change aquatic systems can become more profitable for heat extraction purposes and/or less useful as heat sinks as water temperature increase [*Van Vliet et al.*, 2012]. Of special interest for water management planning is thus to evaluate how far downstream heat emissions/withdrawals have an impact.

Here I showed that for investigating climate effects the interaction between local weather, upstream catchment, rivers and lakes are important and should be combined in future

interdisciplinary research. Currently there is controversy regarding what climate-induced hydrological changes are going to do for hypolimnetic oxygen renewal [*Bouffard and Perga*, 2016; *Fink et al.*, 2016; *Råman Vinnå et al.*, 2017b]. Extended studies in this field are now possible given the recent advancement in regional climate model coupling with advanced hydrological models [*Bosshard et al.*, 2013].

Lake Biel, which is the focus of this dissertation, is a unique system due to the Jura Waters Corrections and the resulting short residence time and high sedimentation rate. Here it is shown how the coupling between weather systems, rivers and lakes can affect sedimentation and morphological stability. Future impact assessment studies of river redirection projects should thus analyse prevailing weather patterns, the resulting sedimentation load in the waterway, as well as downstream sedimentation patterns. Furthermore, the measured water balance in Lake Biel is not complete with ~2 % water missing. Given the newly observed pockmarks close to the central peninsula [Thesis Appendix *Dubois et al.*, 2017], sporadic intrusions of ground water from the karstic bedrock is likely occurring in this lake as well as in the neighbouring Lake Neuchâtel [*Reusch et al.*, 2015]. In summary, this dissertation puts the foundation for multiple interesting interdisciplinary research paths ranging from Meteorology/Climatology through Hydrology to Sedimentology. Promising future research questions are thus:

(i) In a global context: what is the effect of climate change in combination with major local point sources/sinks of heat in rivers and lakes? Can aquatic regions be identified where point sources are more/less important, and what are the implications for water management? What is the effect of atmospheric parameters such as humidity, typical excluded from Hydrological climate impact studies?

(ii) What is the effect of climate-induced shift in precipitation patterns and resulting change in snowmelt/river-discharge-regime on drainage area erosion? How are downstream sedimentation rates in lakes and reservoirs affected and do they change morphological stability? What are the implications for water quality, hazard mitigation and aquatic management?

(iii) How are temperature, stratification and deep water renewal as well as oxygen replenishing rates affected by a change of the future river discharge regimes? How is the local and system-wide effects of groundwater inflow into perialpine lakes affected by warmer temperatures at high altitudes?

166

References

Addor, N., O. Rössler, N. Köplin, M. Huss, R. Weingartner, and J. Seibert (2014), Robust changes and sources of uncertainty in the projected hydrological regimes of Swiss catchments, *Water Resour. Res.*, *50*(10), 7541–7562, doi:10.1002/2014WR015549.

Akiyama, J., and S. G. Heinz (1984), Plunging flow into a reservoir: theory, *J. Hydraul. Eng.*, *10*(110), 484–499.

Albrecht, A. (1999), Transport of radiocobalt discharged by the Muehleberg nuclear reactor in the aquatic systems of the Aare river and Lake Biel(Switzerland)., *Hydroecologie Appl.*, *11*(1), 1–28.

Albrecht, A., R. Reiser, A. Lück, J.-M. A. Stoll, and W. Giger (1998), Radiocesium dating of sediments from lakes and reservoirs of different hydrological regimes, *Environ. Sci. Technol.*, *32*(13), 1882–1887.

Albrecht, A., G. Goudsmit, and M. Zeh (1999), Importance of lacustrine physical factors for the distribution of anthropogenic 60Co in Lake Biel, *Limnol. Oceanogr.*, *44*, 196–206.

Ashida, K., and S. Egashira (1975), Basic study on turbidity currents, *Proc. Jpn. Soc. Civ. Eng.*, *1975*(237), 37–50.

Austin, J. A., and S. M. Colman (2007), Lake Superior summer water temperatures are increasing more rapidly than regional air temperatures: A positive ice-albedo feedback, *Geophys. Res. Lett.*, *34*(6), L06604, doi:10.1029/2006GL029021.

Baran, R. (2017), *Projektbericht: Bielersee – LiDAR-Daten und Digitales Geländemodell in Kombination mit Echolot-Daten, Alpine Airborne HydroMapping, Innsbruck, Österreich, 6 Februar 2017.*

Barnett, P. R. O. (1971), Some changes in intertidal sand communities due to thermal pollution, *Proc R Soc Lond. Ser B*, *177*(1048), 353–364, doi:10.1098/rspb.1971.0035.

Bennett, G. L., P. Molnar, B. W. McArdell, F. Schlunegger, and P. Burlando (2013a), Patterns and controls of sediment production, transfer and yield in the Illgraben, *Geomorphology*, *188*, 68–82, doi:10.1016/j.geomorph.2012.11.029.

Bennett, G. L., P. Molnar, B. W. McArdell, F. Schlunegger, and P. Burlando (2013b), Patterns and controls of sediment production, transfer and yield in the Illgraben, *Geomorphology*, *188*, 68–82, doi:10.1016/j.geomorph.2012.11.029.

Birsan, M.-V., P. Molnar, P. Burlando, and M. Pfaundler (2005), Streamflow trends in Switzerland, *J. Hydrol.*, *314*(1–4), 312–329, doi:10.1016/j.jhydrol.2005.06.008.

Bonvin, F., A. M. Razmi, D. A. Barry, and T. Kohn (2013), Micropollutant Dynamics in Vidy Bay—A Coupled Hydrodynamic-Photolysis Model to Assess the Spatial Extent of Ecotoxicological Risk, *Environ. Sci. Technol.*, *47*(16), 9207–9216, doi:10.1021/es401294c.

Bosshard, T., S. Kotlarski, T. Ewen, and C. Schär (2011), Spectral representation of the annual cycle in the climate change signal, *Hydrol. Earth Syst. Sci.*, *15*(9), 2777–2788, doi:10.5194/hess-15-2777-2011.

Bosshard, T., M. Carambia, K. Goergen, S. Kotlarski, P. Krahe, M. Zappa, and C. Schär (2013), Quantifying uncertainty sources in an ensemble of hydrological climate-impact projections, *Water Resour. Res.*, *49*(3), 1523–1536, doi:10.1029/2011WR011533.

Bouffard, D., and M.-E. Perga (2016), Are flood-driven turbidity currents hot-spots for priming effect in lakes?, *Biogeosciences*, *13*, 3573–3584, doi:10.5194/bg-13-3573-2016.

Bruno, M. C., A. Siviglia, M. Carolli, and B. Maiolini (2013), Multiple drift responses of benthic invertebrates to interacting hydropeaking and thermopeaking waves, *Ecohydrology*, *6*(4), 511–522, doi:10.1002/eco.1275.

Cairns, J. (1971), Thermal pollution: a cause for concern, *Water Pollut. Control Fed.*, *43*(1), 55–66.

Caissie, D. (2006), The thermal regime of rivers: a review, *Freshw. Biol.*, *51*(8), 1389–1406, doi:10.1111/j.1365-2427.2006.01597.x.

Cardoso-Mohedano, J. G., R. Bernardello, J. A. Sanchez-Cabeza, A. C. Ruiz-Fernández, R. Alonso-Rodriguez, and A. Cruzado (2015), Thermal impact from a thermoelectric power plant on a tropical coastal lagoon, *Water Air Soil Pollut*, *226*(1), 2202, doi:10.1007/s11270-014-2202-8.

CH2011 (2011), *Swiss climate change scenarios CH2011*, published by C2SM, MeteoSwiss, ETH, NCCR Climate, and OcCC, Zurich, Switzerland, 88 pp. ISBN: 978-3-033-03065-7.

Chen, C. W., L. H. Weintraub, J. Herr, and R. A. Goldstein (2000), Impacts of a thermal power plant on the phosphorus TMDL of a reservoir, *Environ. Sci. Policy*, *3*, 217–223, doi:10.1016/S1462-9011(00)00058-7.

Chen, C.-T. A., and F. J. Millero (1986), Thermodynamic properties for natural waters covering only the limnological range, *Limnol. Oceanogr.*, *31*(3), 657–662, doi:10.4319/lo.1986.31.3.0657.

Cheng, N.-S. (1997a), Simplified settling velocity formula for sediment particle, *J. Hydraul. Eng.*, *123*(2), 149–152.

Cheng, N.-S. (1997b), Simplified settling velocity formula for sediment particle, *J. Hydraul. Eng.*, *123*(2), 149–152.

Choi, B.-J., and J. L. Wilkin (2007), The effect of wind on the dispersal of the Hudson River plume, *J. Phys. Oceanogr.*, *37*(7), 1878–1897, doi:10.1175/JPO3081.1.

Coriolis, G. G. (1835), Sur les équations du mouvement relatif des systèmes de corps, *J Ecole R. Polytech.*, *15*, 144–154.

Correll, D. L. (1998), The Role of Phosphorus in the Eutrophication of Receiving Waters: A Review, *J. Environ. Qual.*, *27*(2), 261–266.

Cortés, A., W. E. Fleenor, M. G. Wells, I. de Vicente, and F. J. Rueda (2014), Pathways of river water to the surface layers of stratified reservoirs, *Limnol. Oceanogr.*, *59*(1), 233–250, doi:10.4319/lo.2014.59.1.0233.

Davidson, B., and R. W. Bradshaw (1967), Thermal pollution of water systems, *Environ. Sci. Technol.*, *1*(8), 618–630, doi:10.1021/es60008a606.

Davies-Colley, R. J., and D. G. Smith (2001), Turbidity, suspended sediment and water clarity: A Review, *JAWRA J. Am. Water Resour. Assoc.*, *37*(5), 1085–1101.

Dijkstra, J. A., E. L. Westerman, and L. G. Harris (2011), The effects of climate change on species composition, succession and phenology: a case study: CLIMATE CHANGE DESTABILIZES COMMUNITIES, *Glob. Change Biol.*, *17*(7), 2360–2369, doi:10.1111/j.1365-2486.2010.02371.x.

Dingman, S. L., W. F. Weeks, and Y. C. Yen (1968), The effects of thermal pollution on river ice conditions, *Water Resour. Res.*, *4*(2), 349–362, doi:10.1029/WR004i002p00349.

Doomen, A. M. C., E. Wijma, J. J. G. Zwolsman, and H. Middelkoop (2008), Predicting suspended sediment concentrations in the Meuse river using a supply-based rating curve, *Hydrol. Process.*, *22*(12), 1846–1856, doi:10.1002/hyp.6767.

Dracup, J. A., and T. J. Fogabty (1974), Optimal planning for a thermal discharge treatment system, *Water Resour. Res.*, *10*(1), 67–71, doi:10.1029/WR010i001p00067.

Dubois, N., L. Råman Vinnå, S. Girardclos, M. Hilbe, F. Anselmetti, M. Rabold, A. Wüest, L. Meuriot, and A. Jeannet (2017), Lake Biel's dumps and slumps: The aftermath of river engineering in the 19th and 20st centuries. In preparation,

Ellison, T. H., and J. S. Turner (1959), Turbulent entrainment in stratified flows, *J. Fluid Mech.*, *6*(03), 423–448, doi:10.1017/S0022112059000738.

Federal Office for the Environment FOEN (publ.) (2012), *Effects of climate change on water resources and waters, Synthesis report on "Climate Change and Hydrology in Switzerland" (CCHydro) project*, Federal Office for the Environment, Bern, Umwelt-Wissen No 1217: 74 S.

Fenocchi, A., M. Rogora, S. Sibilla, and C. Dresti (2017), Relevance of inflows on the thermodynamic structure and on the modeling of a deep subalpine lake (Lake Maggiore, Northern Italy/Southern Switzerland), *Limnol. - Ecol. Manag. Inland Waters*, *63*, 42–56, doi:10.1016/j.limno.2017.01.006.

Fink, G., M. Schmid, B. Wahl, T. Wolf, and A. Wüest (2014a), Heat flux modifications related to climate-induced warming of large European lakes, *Water Resour. Res.*, *50*(3), 2072–2085, doi:10.1002/2013WR014448.

Fink, G., M. Schmid, and A. Wüest (2014b), Large lakes as sources and sinks of anthropogenic heat: Capacities and limits, *Water Resour. Res.*, *50*(9), 7285–7301, doi:10.1002/2014WR015509.

168

Fink, G., M. Wessels, and A. Wüest (2016), Flood frequency matters: Why climate change degrades deep-water quality of peri-alpine lakes, *J. Hydrol.*, *540*, 457–468, doi:10.1016/j.jhydrol.2016.06.023.

Fisher, F. H., and V. P. Simmons (1977), Sound absorption in sea water, *J. Acoust. Soc. Am.*, *62*(3), 558–564.

Foley, B., I. D. Jones, S. C. Maberly, and B. Rippey (2012), Long-term changes in oxygen depletion in a small temperate lake: Effects of climate change and eutrophication: Oxygen depletion in a small lake, *Freshw. Biol*, *57*(2), 278–289, doi:10.1111/j.1365-2427.2011.02662.x.

Forel, F. A. (1892), *Le Léman: monographie limnologique*, F. Rouge.

García Berdeal, I. (2002), Influence of wind stress and ambient flow on a high discharge river plume, *J. Geophys. Res.*, *107*(C9), doi:10.1029/2001JC000932.

Gaudard, A., R. Schwefel, L. Råman Vinnå, M. Schmid, A. Wüest, and D. Bouffard (2017), Optimizing the parameterization of deep mixing and internal seiches in one-dimensional hydrodynamic models: a case study with Simstrat, *Geosci. Model Dev.*, *10*(9), 3411–3423, doi:10.5194/gmd-10-3411-2017.

Gill, A. E. (1982), *Atmosphere-Ocean Dynamics*, Academic Press, San Diego, California, USA.

Gillet, C., and P. Quétin (2006), Effect of temperature changes on the reproductive cycle of roach in Lake Geneva from 1983 to 2001, *J. Fish Biol.*, *69*(2), 518–534, doi:10.1111/j.1095-8649.2006.01123.x.

Girardclos, S., O. T. Schmidt, M. Sturm, D. Ariztegui, A. Pugin, and F. S. Anselmetti (2007), The 1996 AD delta collapse and large turbidite in Lake Brienz, *Mar. Geol.*, *241*(1–4), 137–154, doi:10.1016/j.margeo.2007.03.011.

Gleick, P. H. (1993), Water and Conflict: Fresh Water Resources and International Security, *Int. Secur.*, *18*(1), 79, doi:10.2307/2539033.

Gloor, M., A. Wüest, and M. Münnich (1994), Benthic boundary mixing and resuspension induced by internal seiches, *Hydrobiologia*, *284*(1), 59–68.

Glur, L., S. B. Wirth, U. Büntgen, A. Gilli, G. H. Haug, C. Schär, J. Beer, and F. S. Anselmetti (2013), Frequent floods in the European Alps coincide with cooler periods of the past 2500 years, *Sci. Rep.*, *3*, 2770, doi:10.1038/srep02770.

Golosov, S., O. A. Maher, E. Schipunova, A. Terzhevik, G. Zdorovennova, and G. Kirillin (2007), Physical background of the development of oxygen depletion in ice-covered lakes, *Oecologia*, *151*(2), 331–340, doi:10.1007/s00442-006-0543-8.

Golosov, S., A. Terzhevik, I. Zverev, G. Kirillin, and C. Engelhardt (2012), Climate change impact on thermal and oxygen regime of shallow lakes, *Tellus Ser A*, *64*, 17264, doi:10.3402/tellusa.v64i0.17264.

Gostiaux, L., and H. van Haren (2010), Extracting meaningful information from uncalibrated backscattered echo intensity data, *J. Atmospheric Ocean. Technol.*, *27*(5), 943–949, doi:10.1175/2009JTECHO704.1.

Goudsmit, G.-H., H. Burchard, F. Peeters, and A. Wüest (2002), Application of k-ε turbulence models to enclosed basins: The role of internal seiches, *J. Geophys. Res.*, *107*(C12), 3230, doi:10.1029/2001JC000954.

Hampton, M., and L. Homa (1996), Submarine landslides, *Rewiews Gheophysics*, *34*(1), 33–59.

Hanafiah, M. M. (2013), Quantifying effects of physical, chemical and biological stressors in life cycle assessment, Ph.D., thesis, Radboud Uni. Nijmegen, Netherlands.

Hari, R. E., D. M. Livingstone, R. Siber, P. Burkhardt-Holm, and H. Guettinger (2006), Consequences of climatic change for water temperature and brown trout populations in Alpine rivers and streams, *Glob. Change Biol.*, *12*, 10–26, doi:10.1111/j.1365-2486.2005.01051.x.

Hay, A. E. (1983), On the remote acoustic detection of suspended sediment at long wavelengths, *J. Geophys. Res. Oceans*, *88*(C12), 7525–7542.

He, C., Y. R. Rao, M. G. Skafel, and T. Howell (2006), Numerical modelling of the Grand River plume in Lake Erie during unstratified period, *Water Qual. Res. J. Can.*, *41*(1), 16–23.

Henley, W. F., M. A. Patterson, R. J. Neves, and A. D. Lemly (2000), Effects of sedimentation and turbidity on lotic food webs: a concise review for natural resource managers, *Rev. Fish. Sci.*, *8*(2), 125–139.

Hilbe, M. (2015), *Bathymetriedaten Bielersee 2015 (Version 1.0.1)*, University of Bern, Bern.

Hitzfeld, B. C., S. J. Höger, and D. R. Dietrich (2000), Cyanobacterial toxins: removal during water treatment, and human risk assessment, *Env. Health Perspect*, *108*, 113–122.

Hoerger, C. C., Y. Akhtman, L. Martelletti, R. Rutler, F. Bonvin, A. Grange, J. S. Arey, and T. Kohn (2013), Spatial extent and ecotoxicological risk assessment of a micropollutant-contaminated wastewater plume in Lake Geneva, *Aquat. Sci.*, doi:10.1007/s00027-013-0315-6.

Holgerson, M. A., and P. A. Raymond (2016), Large contribution to inland water CO_2 and CH_4 emissions from very small ponds, *Nat. Geosci.*, *9*(3), 222–226, doi:10.1038/ngeo2654.

Hoyer, A. B., S. G. Schladow, and F. J. Rueda (2015), Local dispersion of nonmotile invasive bivalve species by wind-driven lake currents: Species dispersion by lake currents, *Limnol. Oceanogr.*, *60*(2), 446–462, doi:10.1002/lno.10046.

Hug, C., P. Kaufmann, and D. Ruffieux (2010), Verification of COSMO-2 with independent data from a wind profiler, *COSMO Newsl. No*, *10*(6), 64–69.

Irwin, A. J., and M. J. Oliver (2009), Are ocean deserts getting larger?, *Geophys. Res. Lett.*, *36*(18), doi:10.1029/2009GL039883.

Isaak, D. J., S. Wollrab, D. Horan, and G. Chandler (2012), Climate change effects on stream and river temperatures across the northwest U.S. from 1980–2009 and implications for salmonid fishes, *Clim. Change*, *113*(2), 499–524, doi:10.1007/s10584-011-0326-z.

Jeannet, A., J. P. Corella, A. Reusch, K. Kremer, and S. Girardclos (2013), Lake Biel sediment record during the last 7500 years and impact of the Aare river deviation in 1878 AD., vol. 15, p. 4027.

Jones, I., and Y. Toba (2008), *Wind Stress Over the Ocean*, Cambridge Univ. Press, Cambridge, UK.

Kirillin, G. (2010), Modeling the impact of global warming on water temperature and seasonal mixing regimes in small temperate lakes, *Boreal Env. Res*, *15*, 279–293.

Kirillin, G., T. Shatwell, and P. Kasprzak (2013), Consequences of thermal pollution from a nuclear plant on lake temperature and mixing regime, *J. Hydrol.*, *496*, 47–56, doi:10.1016/j.jhydrol.2013.05.023.

Kobierska, F., T. Jonas, J. Magnusson, M. Zappa, M. Bavay, T. Bosshard, F. Paul, and S. M. Bernasconi (2011), Climate change effects on snow melt and discharge of a partly glacierized watershed in Central Switzerland (SoilTrec Critical Zone Observatory), *Appl. Geochem.*, *26*, S60–S62, doi:10.1016/j.apgeochem.2011.03.029.

Koschel, R. H., T. Gonsiorczyk, L. Krienitz, J. Padisák, and W. Scheffler (2002), Primary production of phytoplankton and nutrient metabolism during and after thermal pollution in a deep, oligotrophic lowland lake (Lake Stechlin, Germany), *Ver Int Ver Limnol*, *28*, 569–575.

Kremer, K., G. Simpson, and S. Girardclos (2012), Giant Lake Geneva tsunami in AD 563, *Nat. Geosci.*, *5*(11), 756–757, doi:10.1038/ngeo1618.

Kremer, K. et al. (2014), Lake dwellers occupation gap in Lake Geneva (France–Switzerland) possibly explained by an earthquake–mass movement–tsunami event during early bronze age, *Earth Planet. Sci. Lett.*, *385*, 28–39, doi:10.1016/j.epsl.2013.09.017.

Kuhn, W. (1977), *Berechnung der Temperatur und Verdunstung alpiner Seen auf klimatologish-thermodynamischer Grundlage*, Report, MeteoSwiss, Zürich; Switzerland.

Kunz, M. J., and A. Wüst (2014), Impacts by dams: From water quality modelling to management optimization, pp. 2357–2362, Taylor & Francis Group, London, Lausanne.

Laborde, S., J. P. Antenucci, D. Copetti, and J. Imberger (2010), Inflow intrusions at multiple scales in a large temperate lake, *Limnol. Oceanogr.*, *55*(3), 1301–1312.

Lane, A. (1989), *The heat balance of the North Sea*, Proudman Oceanogr. Lab., Merseyside, UK.

LeChevallier, M. W., N. J. Welch, and D. B. Smith (1996), Full-scale studies of factors related to coliform regrowth in drinking water., *Appl. Environ. Microbiol.*, *62*(7), 2201–2211.

Lee, H. J., J. Locat, P. Desgagnes, J. Parsons, and B. McAddoo (2007), *Submarine Mass Movements on Continental Margins, in Continental Margin Sedimentation: From Sediment Transport to Sequence Stratigraphy (eds C. A. Nittrouer, J. A. Austin, M. E. Field, J. H. Kravitz, J. P. M. Syvitski and P. L. Wiberg)*, Blackwell Publishing Ltd., Oxford, UK.

Liechti, P. (1994), *L'état des lacs en Suisse. Cahier de l'Environnement, 237, Office Federal de l'Environnement, des Forêts et du Paysage (OFEFP), Berne, Suisse, p. 159*.

Livingstone, D. M., and D. M. Imboden (1989), Annual heat balance and equilibrium temperature of Lake Aegeri, Switzerland, *Aquat. Sci.*, *51*(4), 351–369, doi:10.1007/BF00877177.

Loizeau, J.-L., and J. Dominik (2000), Evolution of the Upper Rhone River discharge and suspended sediment load during the last 80 years and some implications for Lake Geneva, *Aquat. Sci.*, *62*(1), 54–67.

Lorke, A., D. F. McGinnis, P. Spaak, and A. Wuest (2004), Acoustic observations of zooplankton in lakes using a Doppler current profiler, *Freshw. Biol.*, *49*(10), 1280–1292, doi:10.1111/j.1365-2427.2004.01267.x.

Luksiene, D., O. Sandström, L. Lounasheimo, and J. Andrersson (2000), The effects of thermal effluent exposure on the gametogenesis of female fish, *J. Fish Biol.*, *56*, 37–50, doi:10.1111/j.1095-8649.2000.tb02085.x.

Matzinger, A., R. Pieters, K. I. Ashley, G. A. Lawrence, and A. Wüest (2007), Effects of impoundment on nutrient availability and productivity in lakes, *Limnol. Oceanogr.*, *52*(6), 2629–2640.

McDougall, S., J. Hilton, and A. Jenkins (1991), A dynamic model of caesium transport in lakes and their catchments, *Water Res.*, *25*(4), 437–445.

Meier, W., P. Reichert, A. Wüest, and H. R. Wasmer (1997), *Auswirkungen des Kernkraftwerkes Mühleberg auf den Wärmehaushalt der Aare*, Rep., CH-8600, Eawag, Dübendorf, Switzerland.

Moore, S. A. (2012), Monitoring flow and fluxes of suspended sediment in rivers using side-looking acoustic doppler current profilers, University of Grenoble, Grenoble.

Moore, S. A., J. Le Coz, D. Hurther, and A. Paquier (2012), On the application of horizontal ADCPs to suspended sediment transport surveys in rivers, *Cont. Shelf Res.*, *46*, 50–63, doi:10.1016/j.csr.2011.10.013.

Moore, S. A., J. Le Coz, D. Hurther, and A. Paquier (2013), Using multi-frequency acoustic attenuation to monitor grain size and concentration of suspended sediment in rivers, *J. Acoust. Soc. Am.*, *133*, 1959.

Mulder, T., J. P. M. Syvitski, and K. I. Skene (1998), Modeling of erosion and deposition by turbidity currents generated at river mouths, *J. Sediment. Res.*, *68*(1), 124–137, doi:10.2110/jsr.68.124.

Mulhollem, J. J., R. E. Colombo, and D. H. Wahl (2016), Effects of heated effluent on Midwestern US lakes: Implications for future climate change, *Aquat. Sci.*, *78*(4), 743–753, doi:10.1007/s00027-016-0466-3.

Müller, B., L. D. Bryant, A. Matzinger, and A. Wüest (2012), Hypolimnetic oxygen depletion in eutrophic lakes, *Env. Sci Technol*, *46*(18), 9964–9971, doi:10.1021/es301422r.

Nast, M. (2006), *Terre du lac, l'histoire de la correction des eaux du Jura. Verein Schlossmuseum Nidau*.

O'Reilly, C. M. et al. (2015), Rapid and highly variable warming of lake surface waters around the globe, *Geophys Res Lett*, *42*(24), 10,773–10,781, doi:10.1002/2015GL066235.

Pachauri, R. K., L. Mayer, and Intergovernmental Panel on Climate Change (Eds.) (2015), *Climate change 2014: synthesis report*, Intergovernmental Panel on Climate Change, Geneva, Switzerland.

Paturi, S., L. Boegman, D. Bouffard, and Y. R. Rao (2015), Three-dimensional simulation of Lake Ontario north-shore hydrodynamics and contaminant transport, *J. Hydraul. Eng.*, *141*(3), 04014082, doi:10.1061/(ASCE)HY.1943-7900.0000963.

Peeters, F., D. M. Livingstone, G.-H. Goudsmit, R. Kipfer, and R. Forster (2002), Modeling 50 years of historical temperature profiles in a large central European lake, *Limnol. Oceanogr.*, *47*(1), 186–197, doi:10.4319/lo.2002.47.1.0186.

Perroud, M., and S. Goyette (2010), Impact of warmer climate on Lake Geneva water-temperature profiles, *Boreal Environ. Res.*, *15*, 255–278.

Piccolroaz, S., M. Toffolon, and B. Majone (2015), The role of stratification on lakes' thermal response: The case of Lake Superior, *Water Resour. Res.*, *51*, 7878–7894, doi:10.1002/2014WR016555.

Power, M. E., W. E. Dietrich, and J. C. Finlay (1996), Dams and downstream aquatic biodiversity: potential food web consequences of hydrologic and geomorphic change, *Environ. Manage.*, *20*(6), 887–895.

Prats, J., R. Val, J. Dolz, and J. Armengol (2012), Water temperature modeling in the Lower Ebro River (Spain): Heat fluxes, equilibrium temperature, and magnitude of alteration caused by reservoirs and thermal effluent, *Water Resour. Res.*, *48*(5), W05523, doi:10.1029/2011WR010379.

Quijano, J. C., P. R. Jackson, S. Santacruz, V. M. Morales, and M. H. García (2016), Implications of climate change on the heat budget of lentic systems used for power station cooling: Case study Clinton Lake, Illinois, *Environ. Sci. Technol.*, *50*(1), 478–488, doi:10.1021/acs.est.5b04094.

Raithby, G. D., R. V. Elliott, and B. R. Hutchinson (1988), Prediction of three-dimensional thermal discharge flows, *J. Hydraul. Eng.*, *114*(7), 720–737, doi:10.1061/(ASCE)0733-9429(1988)114:7(720).

Råman Vinnå, L., A. Wüest, and D. Bouffard (2017a), Physical effects of thermal pollution in lakes, *Water Resour. Res.*, *53*(5), 3968–3987, doi:10.1002/2016WR019686.

Råman Vinnå, L., A. Wüest, M. Zappa, G. Fink, and D. Bouffard (2017b), Tributaries affect the thermal response of lakes to climate change, *Hydrol. Earth Syst. Sci. Discuss.*, 1–40, doi:10.5194/hess-2017-337. In review.

Råman Vinnå, L., D. Bouffard, A. Wüest, S. Girardclos, and N. Dubois (2017c), Wind driven circulation focusing lake sedimentation. In preparation,

Råman Vinnå, L., D. Bouffard, N. Dubois, M. Hilbe, R. Käser, and A. Wüest (2017d), Seewasserentnahme im Bielersee - Gibt es eine ideale Position?, *Aqua Gas - Fachz. Für Gas Wasser Abwasser*, *97*(9), 14–20.

Raymond Pralong, M., J. M. Turowski, D. Rickenmann, and M. Zappa (2015), Climate change impacts on bedload transport in alpine drainage basins with hydropower exploitation, *Earth Surf. Process. Landf.*, *40*(12), 1587–1599, doi:10.1002/esp.3737.

Razmi, A. M., D. A. Barry, R. Bakhtyar, N. Le Dantec, A. Dastgheib, U. Lemmin, and A. Wüest (2013), Current variability in a wide and open lacustrine embayment in Lake Geneva (Switzerland), *J Gt. Lakes Res*, *39*(3), 455–465, doi:10.1016/j.jglr.2013.06.011.

Reusch, A. et al. (2015), Giant lacustrine pockmarks with subaqueous groundwater discharge and subsurface sediment mobilization, *Geophys. Res. Lett.*, *42*(9), 3465–3473, doi:10.1002/2015GL064179.

Reutter, J. M., and C. E. Herdendorf (1976), Thermal discharge from a nuclear power plant: Predicted effects on Lake Erie fish, *Ohio J. Sci.*, *76*(1), 39–45.

Riccioli, G. B. (1651), *Almagestum Novum vol. 2, Bologna, Italy*.

Righetti, M., M. Toffolon, C. Lucarelli, and M. Serafini (2011), Sediments as tracers for transport and deposition processes in peri-alpine lakes: A case study, *J. Hydrol.*, *411*(1–2), 1–11, doi:10.1016/j.jhydrol.2011.08.018.

Rimmer, A., and A. Hartmann (2014), Optimal hydrograph separation filter to evaluate transport routines of hydrological models, *J. Hydrol.*, *514*, 249–257, doi:10.1016/j.jhydrol.2014.04.033.

Rueda, F., and G. Schladow (2009), Mixing and stratification in lakes of varying horizontal length scales: Scaling arguments and energy partitioning, *Limnol. Oceanogr.*, *54*(6), 2041.

Rueda, F. J., W. E. Fleenor, and I. de Vicente (2007), Pathways of river nutrients towards the euphotic zone in a deep-reservoir of small size: Uncertainty analysis, *Ecol. Model.*, *202*(3–4), 345–361, doi:10.1016/j.ecolmodel.2006.11.006.

Salgueiro, D. V., H. de Pablo, R. Neves, and M. Mateus (2015), Modelling the thermal effluent of a near coast power plant (Sines, Portugal), *Rev. Gest. Costeira Integrada*, *15*(4), 533–544, doi:10.5894/rgci577.

Sanchez-Lorenzo, A., and M. Wild (2012), Decadal variations in estimated surface solar radiation over Switzerland since the late 19th century, *Atmospheric Chem. Phys.*, *12*(18), 8635–8644, doi:10.5194/acp-12-8635-2012.

Santschi, P. W., and P. W. Schindler (1977), Chemical and geochemical studies of Lake Biel I. A mass balance for Lake Biel and its implications for the rates of erosion of the drainage area, *Aquat. Sci.-Res. Boundaries*, *39*(2), 182–200.

Scherer, C. R. (1975), On the efficient allocation of environmental assimilative capacity: The case of thermal emissions to a large body of water, *Water Resour. Res.*, *11*(1), 180–181, doi:10.1029/WR011i001p00180.

Schimmelpfennig, S., G. Kirillin, C. Engelhardt, and G. Nützmann (2012), Effects of wind-driven circulation on river intrusion in Lake Tegel: Modeling study with projection on transport of pollutants, *Environ. Fluid Mech.*, *12*(4), 321–339, doi:10.1007/s10652-012-9236-5.

172

Schmid, M., and O. Köster (2016), Excess warming of a Central European lake driven by solar brightening, *Water Resour. Res.*, *52*(10), 8103–8116, doi:10.1002/2016WR018651.

Schmidt, W. (1928), Über die Temperatur- und Stabilitätsverhältnisse von Seen, *Geogr. Ann.*, *10*, 145–177, doi:10.2307/519789.

Schnellmann, M., F. S. Anselmetti, D. Giardini, and J. A. Mckenzie (2006), 15,000 Years of mass-movement history in Lake Lucerne: Implications for seismic and tsunami hazards, *Eclogae Geol. Helvetiae*, *99*(3), 409–428, doi:10.1007/s00015-006-1196-7.

Schwarzenbach, R. P., T. Egli, T. B. Hofstetter, U. von Gunten, and B. Wehrli (2010), Global Water Pollution and Human Health, *Annu. Rev. Environ. Resour.*, *35*(1), 109–136, doi:10.1146/annurev-environ-100809-125342.

Schwefel, R., A. Gaudard, A. Wüest, and D. Bouffard (2016), Effects of climate change on deepwater oxygen and winter mixing in a deep lake (Lake Geneva): Comparing observational findings and modeling, *Water Resour. Res.*, *52*(11), 8811–8826, doi:10.1002/2016WR019194.

Speich, M. J. R., L. Bernhard, A. J. Teuling, and M. Zappa (2015), Application of bivariate mapping for hydrological classification and analysis of temporal change and scale effects in Switzerland, *J. Hydrol.*, *523*, 804–821, doi:10.1016/j.jhydrol.2015.01.086.

Steinsberger, T., M. Schmid, A. Wüest, R. Schwefel, B. Wehrli, and B. Müller (2017), Organic carbon mass accumulation rate regulates the flux of reduced substances from the sediments of deep lakes, *Biogeosciences Discuss.*, 1–17, doi:10.5194/bg-2017-26.

Stelling, G. S., and J. A. T. M. Van Kester (1994), On the approximation of horizontal gradients in sigma co-ordinates for bathymetry with steep bottom slopes, *Int. J. Numer. Methods Fluids*, *18*(10), 915–935, doi:10.1002/fld.1650181003.

Sylvester, J. R. (1972), Possible effects of thermal effluents on fish: A review, *Environ. Pollut.*, *3*, 205–215, doi:10.1016/0013-9327(72)90004-3.

Syvitski, J. P. M., and A. G. Lewis (1992), The seasonal distribution of suspended particles and their iron and manganese loading in a glacial runoff fiord, *Geosci. Can.*, *19*(1), 13–20.

Tananaev, N. I. (2012), Hysteresis effect in the seasonal variations in the relationship between water discharge and suspended load in rivers of permafrost zone in Siberia and Far East, *Water Resour.*, *39*(6), 648–656, doi:10.1134/S0097807812060073.

Taylor, K. E. (2001), Summarizing multiple aspects of model performance in a single diagram, *Geophys. Res.*, *106*(D6), 7183–7192, doi:10.1029/2000JD900719.

Teledyne RDI (2014), Personal communication,

Thevenon, F., N. D. Graham, M. Chiaradia, P. Arpagaus, W. Wildi, and J. Poté (2011), Local to regional scale industrial heavy metal pollution recorded in sediments of large freshwater lakes in central Europe (lakes Geneva and Lucerne) over the last centuries, *Sci. Total Environ.*, *412–413*, 239–247, doi:10.1016/j.scitotenv.2011.09.025.

Thevenon, F., S. B. Wirth, M. Fujak, J. Poté, and S. Girardclos (2013), Human impact on the transport of terrigenous and anthropogenic elements to peri-alpine lakes (Switzerland) over the last decades, *Aquat. Sci.*, *75*(3), 413–424, doi:10.1007/s00027-013-0287-6.

Toffolon, M., and S. Piccolroaz (2015), A hybrid model for river water temperature as a function of air temperature and discharge, *Environ. Res. Lett.*, *10*(11), 114011, doi:10.1088/1748-9326/10/11/114011.

Toffolon, M., S. Piccolroaz, B. Majone, A.-M. Soja, F. Peeters, M. Schmid, and A. Wüest (2014), Prediction of surface temperature in lakes with different morphology using air temperature, *Limnol. Oceanogr.*, *59*(6), 2185–2202, doi:10.4319/lo.2014.59.6.2185.

Van Vliet, M. T. H., J. R. Yearsley, F. Ludwig, S. Vögele, D. P. Lettenmaier, and P. Kabat (2012), Vulnerability of US and European electricity supply to climate change, *Nat. Clim. Change*, *2*(9), 676–681, doi:10.1038/nclimate1546.

Van Vliet, M. T. H., W. H. P. Franssen, J. R. Yearsley, F. Ludwig, I. Haddeland, D. P. Lettenmaier, and P. Kabat (2013), Global river discharge and water temperature under climate change, *Glob. Environ. Change*, *23*(2), 450–464, doi:10.1016/j.gloenvcha.2012.11.002.

Vandysh, O. I. (2009), The effect of thermal flow of large power facilities on zooplankton community under subarctic conditions, *Water Resour.*, *36*(3), 310–318, doi:10.1134/S0097807809030063.

Verpoorter, C., T. Kutser, D. A. Seekell, and L. J. Tranvik (2014), A global inventory of lakes based on high-resolution satellite imagery, *Geophys. Res. Lett.*, *41*(18), 6396–6402, doi:10.1002/2014GL060641.

Vidal, J., R. Marcé, T. Serra, J. Colomer, F. Rueda, and X. Casamitjana (2012), Localized algal blooms induced by river inflows in a canyon type reservoir, *Aquat. Sci.*, *74*(2), 315–327, doi:10.1007/s00027-011-0223-6.

Vitruvius, M. (10AD), *De architectura; in two volumes; translated into English by Frank Granger, The Loebv Classical Library.*

Viviroli, D., M. Zappa, J. Gurtz, and R. Weingartner (2009), An introduction to the hydrological modelling system PREVAH and its pre- and post-processing-tools, *Environ. Model. Softw.*, *24*(10), 1209–1222, doi:10.1016/j.envsoft.2009.04.001.

Vuorinen, H. S., P. S. Juuti, and T. S. Katko (2007), History of water and health from ancient civilizations to modern times, *Water Sci. Technol. Water Supply*, *7*(1), 49, doi:10.2166/ws.2007.006.

Wahl, B., and F. Peeters (2014), Effect of climatic changes on stratification and deep-water renewal in Lake Constance assessed by sensitivity studies with a 3D hydrodynamic model, *Limnol. Oceanogr.*, *59*(3), 1035–1052, doi:10.4319/lo.2014.59.3.1035.

Weber, M., K. Rinke, M. R. Hipsey, and B. Boehrer (2017), Optimizing withdrawal from drinking water reservoirs to reduce downstream temperature pollution and reservoir hypoxia, *J. Environ. Manage.*, *197*, 96–105, doi:10.1016/j.jenvman.2017.03.020.

Weusthoff, T., F. Ament, M. Arpagaus, and M. W. Rotach (2010), Assessing the benefits of convection-permitting models by neighborhood verification: Examples from MAP D-PHASE, *Mon. Weather Rev.*, *138*(9), 3418–3433, doi:10.1175/2010MWR3380.1.

Wild, M., A. Ohmura, and K. Makowski (2007), Impact of global dimming and brightening on global warming, *Geophys. Res. Lett.*, *34*, L04702, doi:10.1029/2006GL028031.

Williamson, C. E., E. P. Overholt, R. M. Pilla, T. H. Leach, J. A. Brentrup, L. B. Knoll, E. M. Mette, and R. E. Moeller (2015), Ecological consequences of long-term browning in lakes, *Sci. Rep.*, *5*, 18666, doi:10.1038/srep18666.

Wirth, S. B., S. Girardclos, C. Rellstab, and F. S. Anselmetti (2011), The sedimentary response to a pioneer geo-engineering project: Tracking the Kander River deviation in the sediments of Lake Thun (Switzerland), *Sedimentology*, *58*(7), 1737–1761, doi:10.1111/j.1365-3091.2011.01237.x.

WMO (2008), *Guide to meteorological instruments and methods of observation*, 7th ed., World Meteorological Organization, Geneva, Switzerland, 681 pp.

World Health Organization (2017), *Guidelines for drinking-water quality.*

Wright, R. F., and P. Nydegger (1980), Sedimentation of detrital particulate matter in lakes: Influence of currents produced by inflowing rivers, *Water Resour. Res.*, *16*(3), 597–601, doi:10.1029/WR016i003p00597.

Wüest, A., and A. Lorke (2003), Small-scale hydrodynamics in lakes, *Annu. Rev. Fluid Mech.*, *35*(1), 373–412, doi:10.1146/annurev.fluid.35.101101.161220.

Yelland, M., and P. K. Taylor (1996), Wind stress measurements from the open ocean, *Phys. Oceanogr.*, *26*(4), 541–558, doi:10.1175/1520-0485(1996)026<0541:WSMFTO>2.0.CO;2.

Zhang, G., T. Yao, H. Xie, J. Qin, Q. Ye, Y. Dai, and R. Guo (2014), Estimating surface temperature changes of lakes in the Tibetan Plateau using MODIS LST data, *J. Geophys. Res. Atmospheres*, *119*(14), 8552–8567, doi:10.1002/2014JD021615.

Zhong, Y., M. Notaro, S. J. Vavrus, and M. J. Foster (2016), Recent accelerated warming of the Laurentian Great Lakes: Physical drivers, *Limnol. Oceanogr.*, *61*, 1762–1786, doi:10.1002/lno.10331.

Zhu, Y., J. Yang, J. Hao, and H. Shen (2009), Numerical simulation of hydrodynamic characteristics and water quality in Yangchenghu Lake, in *Advances in Water Resources and Hydraulic Engineering*, pp. 710–715, Springer, Berlin, Heidelberg.

Appendix:

Lake Biel's dumps and slumps: The aftermath of river engineering in the 19th and 20st centuries

Nathalie Dubois[1,2], Love Råman Vinnå[3], Stéphanie Girardclos[4], Michael Hilbe[5], Flavio Anselmetti[5], Marvin Rabold[1], Alfred Wüest[3,6], Laetitia Meuriot[1], Alice Jeannet[4]

[1] Department of Surface Waters - Research and Management, Eawag, Swiss Federal Institute of Aquatic Science and Technology, Dübendorf, Switzerland

[2] Department of Earth Sciences, ETHZ, Zürich, Switzerland

[3] Physics of Aquatic Systems Laboratory, Margaretha Kamprad Chair, Ecole Polytechnique Fédérale de Lausanne, Institute of Environmental Engineering, Lausanne, Switzerland

[4] Section of Earth and Environmental Sciences, Université de Genève, Genève, Switzerland

[5] Institute of Geology, UniversityBern, Bern, Switzerland

[6] Department of Surface Waters - Research and Management, Eawag, Swiss Federal Institute of Aquatic Science and Technology, Kastanienbaum, Switzerland

Abstract

The Jura Water Corrections – the largest river engineering works ever undertaken in Switzerland – dramatically modified the hydrological system of Lake Biel and the surrounding Seeland region in the 19th and 20th century. Decades later, new high-resolution bathymetric and seismic reflection datasets acquired in Lake Biel document the consequences of the deviation of the Aare River into the lake in 1878. A 1.2 km wide slump complex was detected in the high-resolution bathymetry, in front of Sutz-Lattrigen along the eastern shore. Different levels of surface roughness of individual events in the slide complex can be observed in the hillshade map and on the seismic lines crossing them, which suggest that slope failures occurred at different times in the last ca. 50 years. Sediment cores retrieved in and outside of the mass transport deposits support this interpretation. The large amount of sediment delivered by the Aare River since its deviation into Lake Biel undoubtedly resulted in sediment overloading, which caused large mass movements on the eastern shore along the flow path of the Aare in the lake. Additional smaller-scale mass movements and mudflows can be observed across the entire lake, but are more prominent in the southwestern basin and along the northern shore. Some of these small-scale slumps can clearly be attributed to constructions on shore.

The new high-resolution bathymetric dataset documents additional previously unknown morphological features such as subaquatic dunes and craters, while seismic profiles along the lake reveal a peculiar shallow seismic unit attributed to the dumping of material excavated during the second phase of river engineering, in the1960s-1970s, when the channels flowing into and out of Lake Biel were widened and deepened. The dumping of excavated material in a subaquatic landfill might have been the trigger of the largest and oldest slump, although two nearby earthquakes in 1964 and 1965 cannot be dismissed. Three additional medium-scale mass movements followed in 1970s-1990s (uncertain dating), 2000 and 2010, and form – together with the oldest mass transport deposit – the large Sutz-Latttrigen slump complex.

1. Introduction

River engineering, dam construction and other human activities have drastically modified watercourses and sediment transfer across the globe, with numerous additional constructions underway or planned. As a result, a large proportion of sediment is now retained within reservoirs and does not reach the oceans [Syvitski et al., 2005]. In Switzerland, several large-scale engineering projects modified watercourses already two centuries ago, allowing us now to study the longer-term effects of such man-made modifications [e.g. Wirth et al., 2011].
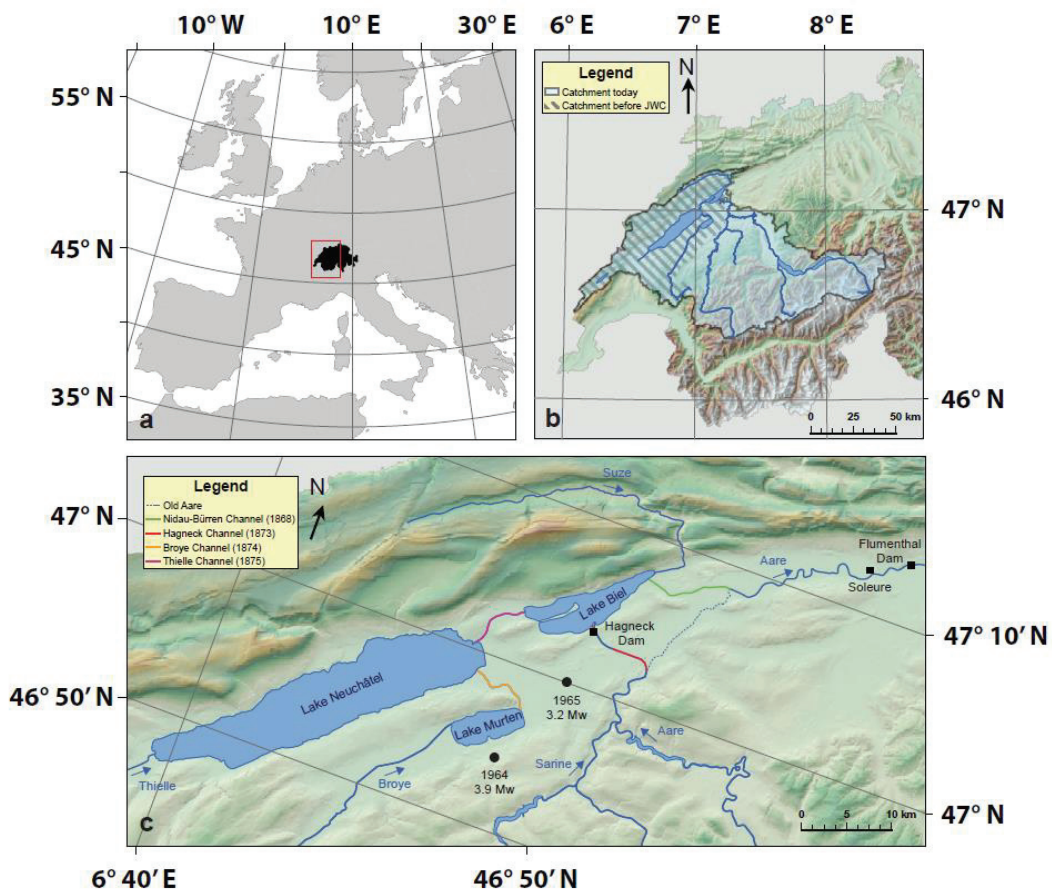

Figure 1. Location map of Lake Biel. (a) Location of Switzerland in Central Europe (b) Catchment of Lake Biel, before (hatched) and after (plain and hatched) the First Jura Water Correction [Swisstopo, 2014] (c) Map of the Seeland showing Lake Biel, Lake Neuchâtel and Lake Murten, the various engineering work of the first and second Jura Water Corrections, as well as the locations of the 1964 and 1965 earthquakes [Swisstopo, 2014].

Lake Biel, a Swiss Plateau lake on the foothills of the Jura Mountains (Fig. 1), is an ideal site to study the effects of river engineering on lake sedimentation. The Aare River was rerouted into Lake Biel at the end of the 19th century as part of the large-scale "Jura Waters Corrections" (hereafter JWC). The first JWC engineered from 1868 to 1891, were the greatest river management works ever undertaken in Switzerland. The Aare River deviation increased the catchment area of Lake Biel by a factor of four (Fig. 1), leading to a significant increase in sediment delivery from the catchment. This rerouting also increased the average water input from 55 to 240 m^3/s, which in turn reduced the mean residence time from 253 down to 58 days [Liechti, 1994].

Here we present the results of a recent geophysical and sedimentological survey of Lake Biel. Seismic profiles, sediment cores and multibeam bathymetry data were recovered to study the large anthropic modification of Lake Biel's depositional system.

2. Study Area

Lake Biel (German: Bielersee, 47°5'N, 7°10'E, 429 m a.s.l.) is a 39.3 km^2 alpine lowland lake located between the Alps and the Jura Mountains in North Western Switzerland (Fig. 1), in a region commonly called Seeland (literally "Lake Country") due to numerous historically recorded floods. As part of the Swiss Plateau (relatively flat lowlands between the Jura Mountains and the Alps), the Seeland was formed through former glaciations, depositing extensive moraine beds. The southern shore of Lake Biel is on the edge of the Swiss Plateau and has relatively flat banks [Brombacher, 1997]. The north shore of the Lake has relatively steep banks, part of the southern edge of the Jura Mountain, which climbs to 1600 m a.s.l. in only 8 km distance. Due to its topography, this northern bank is only covered in certain places by a narrow alluvial zone.

Lake Biel is relatively shallow with an average depth is of 31 m and a volume of 1.24 km^3 (Fig. 2). It comprises three major basins, the Tüscherz basin (74 m depth) in the northeast, the Lüscherz basin (55 m depth) to the south of the St Petersinsel, and the Neuenstadt basin (35 m depth) to the north of the peninsula (Fig. 2). Lake Biel is holomictic and has changed from mesotrophic in the 1950s to eutrophic in the 1990s, with a hyper-eutrophic peak in the 1970s, and is now meso-eutrophic again [Wright et al., 1980; Liechti, 1994]. Physical characteristics are similar to those of other Swiss Plateau lakes. During the warm period (mid-April to mid-

October), temperature increases in the upper layers and a stable density stratification develops. At the end of the winter deep mixing period (November-March) the lake is nearly homogenous and O_2 saturation is almost complete [Santschi and Schindler, 1977].
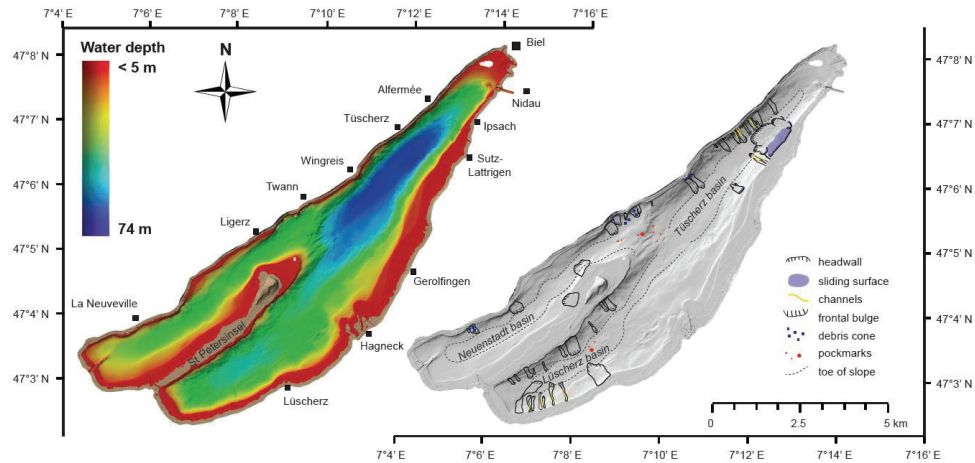

Figure 2. Sublacustrine bathymetric map (shaded relief, color indicating depth) of Lake Biel (left) with a hillshade map and interpretation of observed morphology (right).

The main tributaries include the Thielle River (Zihl in German), which forms the outlet from the nearby Lake Neuchâtel to the southwest, the Suze River (Schüss in German), which enters at Biel City, and the Aare River, the only tributary for the southern basin and the main water supplier of Lake Biel (Fig. 1). The Aare River, which is the main water supplier of the High Rhine River, has only been flowing into Lake Biel since 1878 when the river was deviated through the Hagneck Channel into the lake in order to control devastating floods in the surrounding downstream Seeland area. It now supplies about 80-90% of the water, suspended particulate matter and dissolved substances to Lake Biel [Santschi and Schindler, 1977]. The sediment load carried by the Aare at Hagneck largely derives from the Sarine River (Saane in German), a major tributary that joins the Aare River 30 km upstream of Hagneck. Since the Aare River flows through Lake Brienz, Lake Thun and Wohlensee Reservoir before reaching Lake Biel, these upstream lakes act as large decantation basins and efficiently trap most of Aare's sediment [Wright et al., 1980].

Lake Biel has a rapid water renewal time (58 days) due to its very large catchment area relative

to the lake volume. Its drainage basin encompasses 8305 km^2 (about 20 % of Switzerland), including large sections of the northern Swiss Alps, which creates an hydrologic regime dominated by late spring snowmelt. The present day hydrology of the lake differs greatly from that prior to 1878. Current measurements suggest that the water circulation patterns in Lake Biel are strongly dominated by inflow-induced currents [Nydegger, 1967; 1976]. These set up a general counterclockwise water circulation at all depths, induced by the deflection of the inflowing Aare to the right by the wind [*Råman Vinnå et al.*, 2017]. The composition of the surface sediment reflects this circulation pattern, with terrigenous Aare River material predominantly deposited along the southeast shore and in the Tüscherz basin, to the right of the river mouth [Weiss, 1977; Wright and Nydegger, 1980]. Sedimentation in the Neuenstadt basin is influenced by particulate matter inputs from the Thielle Channel, which may explain the higher sedimentation rate relative to that in the Lüscherz basin [Wright et al., 1980].

Finally, hydroelectric constructions have also altered the flow of water and particles in the Aare system. Upstream of Lake Brienz, the flow of the Aare River is affected by seven reservoirs associated with six hydropower units. These hydropower dams constructed in the high alpine Grimsel area (in the 1930's – 1950's) have altered the seasonality of the Aare River flow (shift of the particle input from summer to winter) and reduced by two-third the particle input from upstream glaciers to Lake Brienz [Wüest et al. 2007; Anselmetti et al., 2007]. The most important hydrological change in the Sarine River system was the construction of the Rossens dam in 1948. Since then, the Sarine River discharge pattern has been heavily influenced by the hydroelectricity production, which maintains the downstream water discharge almost constant, excluding times of strong flood events [Thevenon et al., 2013]. The construction of the Hagneck hydroelectric dam facilities on the mouth of the Hagneck Channel in 1900 [Nast, 2006] undoubtedly reduced the energy level and, therefore, the sediment transport capacity of the Aare River.

3. The Jura Waters Corrections

Starting from the Middle Age, numerous historic records describe terrible flood events in the Seeland region surrounding the lakes of Neuchâtel, Murten and Biel. First mention of these events is made with reference to a "millennial flood" in 1342, which was followed by several other important floods [Nast, 2006]. Every single flood event was certainly not reported, but based on written testimony, Nast [2006] inferred that flooding occurred in the Seeland region at least every 9.5 years between 1500 and 1882. As a result of these floods, the Seeland was a poverty stricken marshy zone in which epidemic risk was very high and agriculture difficult.

The first documented flood mitigation measures were taken in the second half of the 16th century: fish traps were banned from the Thielle River (flowing out of Lake Biel) in Nidau, to ensure that the Lake Biel water level does not increase [Vischer, 2003]. However, flooding remained recurrent. The worst historic flood was recorded in 1651, when the overflowing Aare River merged with Lake Biel to form one large "Lake of Soleure", spreading from the lake to the city of Soleure (Solothurn in German; see location on Fig. 1; Schneider [1881]; Vischer [2003]). Additional measures were then implemented to prevent such catastrophic floods, and several regional projects were initiated, marking the beginning of the "Jura Waters Corrections".

In 1868, after multiple debates about the planning and the realization of the river engineering, the cantons of Bern, Fribourg, Vaud, Neuchâtel and Soleure finally launched the first modification of the Jura hydrological system: The first JWC. One of the major achievements of this project was the construction of a deviation channel of 8 km in length: the Hagneck Channel, in order to modify the path of the Aare River from Aarberg directly into Lake Biel as a flood control scheme (Fig. 1; Nast [2006]. The construction of the Hagneck Channel implied the excavation of millions cubic meters of mollassic grounds, composed of hard sandstone and alterable shale [Vischer, 2003]. Before the opening of the Hagneck Channel in 1878, the Thielle River (i.e. the lake outlet) had to be widened. The JWC thus started in 1868 with the construction of the Nidau-Büren Channel, which allowed the lake level to drop rapidly by 2 m. The construction of the Hagneck Channel then started in 1873, and was opened in 1878, but the river continued to intensely erode the river-bed and new stabilization constructions were built between 1887 and 1900 [Thevenon et al., 2013]. With the completion of these additional constructions, the Hagneck hydroelectric dam was finally inaugurated in 1900 (Nast 2006). In addition to this major deviation, the regional river management program also included the

channelization of the naturally inflowing small rivers (Broye and Thielle, which started in 1874 and 1875, respectively).

The JWC, especially the lowering of Lake Biel mean level by 2 m, allowed the draining of the surrounding wetland areas. The former swampy Seeland became a vast fertile agricultural area. Changes in the soil and surface properties following this major landscape and river managing work even affected the local and regional climate on the Swiss Plateau [Schneider et al., 2004].

A second phase of river engineering took place between 1962 and 1973: The second JWC. The need for this second phase had already been anticipated at the time of the first JWC. It consisted essentially of the construction of the Flumenthal Dam in 1970, ca. 20km downstream of Lake Biel (Fig. 1) to regulate the outflow of the three-lake hydrologic system and the confluence with the Emme River. In addition, the Broye (1962-1970), Thielle (1965-1970) and Nidau-Büren (1963-1973) Channels were widened and deepened by 2.3, 5 and 2.3 m, respectively (Fig. 1). 2.5 million cubic meters were excavated from the Nidau-Büren Channel and dumped into an subaquatic disposal site in Lake Biel. Since the second JWC, only two major flooding occurred in the Seeland, in 2007 and 2015.

4. Previous investigations

Jeannet [2012] investigated a 10 m long composite UWITEC core recovered close to the Aare River mouth, in the Lüscherz basin, in an effort to detect changes in sediment composition following the first JWC. The main findings are summarized hereafter. The deviation of the Aare River is evidenced by changes in the grain size distribution, in the sedimentation rate and in the elemental composition. Major/Minor element distributions from XRF core scanning reveal an abrupt increase in elements of allochtonous origin (Ti, Si, K, Fe, and Mn) in response to the Aare River deviation, while Ca decreases. Higher Fe/Mn ratios suggest an increase in oxygenation of the hypolimnion subsequent to the new permanent inflow of large water masses.

The year following the end of the Hagneck Channel excavation (i.e. 1879) displays extremely high sediment rate (> 10 cm/yr, more than 10 times its previous rate at any time in the past 7500 years) attributed to strong erosion in the channel, which induced very high sediment input. The sediment record is also marked by a layer with significantly coarser material at 147.5 cm

182

depth (> 60 vol-% of sand-size particles), which clearly reveals an event of strong water discharge flowing into the lake, intense enough to erode and transport coarse grains. The sedimentation rates subsequently stabilized at significantly lower levels in two steps. A first decrease was observed in the years following the opening of the channel (2.63 cm/yr), with a second marked step around 1900 AD (1 cm/yr). The first decrease is attributed to the decline of the erosion in the Hagneck channel and further upstream along the Aare River bed, whereas the second drop is caused by the construction of the Hagneck dam facilities in 1900 [Nast, 2006], which regulate the discharge of the inflowing Aare River. The construction of the dam resulted in a general reduction of sediment input.

5. Methods

5.1 Seismic

Almost 50 km of reflection seismic profiles were acquired on April 26th 2010 using a 3.5 kHz pinger source fixed on an inflatable cataraft that was pushed in front of the R/V ArETHuse (Fig. 3). The seismic profiles were recorded digitally in SEG-Y format using a global positioning system (GPS; error ± 5 m) for navigation. Seismic data were processed using band-pass filtering (2.2 to 6.3 kHz). The time-depth conversion in water and sediment is based on a p-wave velocity of 1450 m/s. Interpretation of seismic data was accomplished with the KingdomSuite^{TM} 8.1 software (Seismic Micro-Technology, Houston, TX, USA).
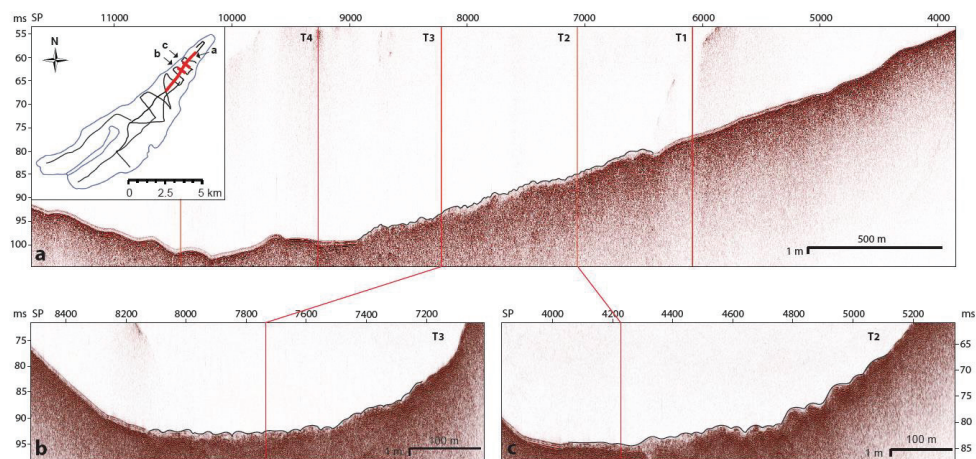
Figure 3. (a) Longitudinal seismic profile and (b, c) transverse seismic profiles (SP = shot points, ms = milliseconds in two way travel time). The insert on the top left shows the location of the acquired the 3.5 kHz seismic lines. The location of the longitudinal line (a) and transvere lines (b) and (c) are highlighted in thick red lines. The sediment surface in (b - transverse line T3) is less rough than in (c – transverse line T2).

5.2 Multibeam bathymetry

In March 2015, high-resolution bathymetric data was acquired with a multibeam echosounder (Kongsberg EM2040; 1° × 1° beam width; operating at 300 kHz), installed on the R/V ArETHuse. A detailed description of the method has been published by Wessels et al. [2015], thus only a brief summary is provided hereafter. The track of the vessel was determined with a Trimble SPS361 GPS compass. Positioning of the data was done with a GNSS (Global Navigation Satellite System)-Receiver (Leica GX1230+ GNSS) in combination with the real-time positioning service data swiposGIS/GEO streamed from a mobile communications network. The orientation-parameters 'roll', 'pitch', and 'heave' of the boat were corrected by an inertial navigation system Kongsberg Seatex MRU5+. Data were recorded with the Kongsberg SIS software. Sound velocity profiles in the water column were acquired at least once per day with a Valeport miniSVP probe in order to calculate the water depth considering refraction. The raw depth information was processed with CARIS HIPS/SIPS 8.1. From the manually cleaned point cloud, a DDM was interpolated with the 'swath angle' algorithm. The elevation data was corrected to a mean lake level of 429 m (National height network 95; LHN95) during the data acquisition period.

The shallow (<5 m water depth) nearshore zone cannot be measured efficiently with the multibeam technology and was instead measured using airborne topobathymetric laserscanning

184

(LiDAR). Again, please refer to Wessels et al. [2015] for more details on the LiDAR methodology. Combining both methods (i.e. multibeam and LiDAR surveys) enables the generation of a seamless digital terrain models of the entire Lake Biel as shown on Fig. 2.

5.3 Sediment coring and analyses

Forty-eight short cores of 1-2 m in length and 63 mm in diameter were retrieved with a gravity corer (Eawag-63/S corer). Campaigns took place in 2010, 2013, 2014, and again in 2015, following the multibeam campaign. 16 cores were logged using a GEOTEK multisensor core logger at the Limnogeology Laboratory of ETH Zürich. Gamma density, P-wave velocity, and magnetic susceptibility were measured at intervals of 0.5 cm. All 48 cores were then split for further description and analyses. Open cores were photographed using a line scan.

Elemental analysis of 5 sediment cores was performed with an Avaatech X-Ray Fluorescence (XRF) Core-Scanner at the Limnogeology Laboratory of ETH Zürich with resolutions of 1 cm for four cores (BIE 14-54, 58, 59 and 60) and a resolution of 2 mm for one core (BIE 14-52). Grain size was measured for 7 cores using laser diffraction technique (Malvern Mastersizer 2000) which covers a range of 0.02 to 2000 um, at the limnogeology laboratory of ETH Zürich. Samples were dispersed in $NaPO_4$ prior to analysis and disaggregated by ultrasonication. Each sample was measured at least three times. Samples were analyzed for grain size distribution at 1 cm resolution in cores BIE-14-52 (from 0 to 88cm) and BIE-14-61 (from 0 to 111cm), whereas 10 discrete samples were analyzed in cores BIE-14-54, BIE-14-57, BIE-14-58, BIE-14-59, and BIE-14-60.

Aliquots of the same sediment samples analyzed for grain size were freeze-dried and ground to quantify their the total carbon (TC) content using an Elemental Analyzer EURO EA 3000 and their total inorganic carbon (TIC) content using an UIC Inc. CM5015 Total Inorganic Carbon Analyzer. Both measurements were conducted in the sedimentology laboratory at Eawag.

The Caesium-137 activity in the samples of cores BIE-14-61 and BL13-1C was determined on high-purity Germanium Well detectors (Canberra) in the Gamma laboratory at Eawag. A total of 5–10 g of freeze-dried and ground sediment samples were weighted into sample tubes.

5.4 Results

5.4.1 Seismic

Due to high methane content in the lake's sediments (gas blanking), the seismic profiles are not distinct enough to interpret deep sedimentary units. However, the structure of the sediment surface (i.e. the lake floor) as well as shallow units down to almost 1.5 m (i.e. 2 ms in Two-Way Travel Time – TWTT) can be distinguished (Fig. 3). On the seismic profile along the lake (later described as longitudinal line) and on several transverse lines, the lake floor appears disturbed (rough) over a large area (ca 0.5 km^2). There, the uppermost sediments reveal acoustically semi transparent to chaotic deposits, later clearly identified as mass movements on the multibeam bathymetry. Interestingly, on transverse line T2 (Fig. 3c), the surface appears rougher (i.e. more strongly disturbed) than on transverse line T3 (Fig. 3b), pointing to a more recent underwater mass movement. The "freshness" of the surface suggests that this mass movement has not yet been strongly overprinted by sediment cover. The multibeam indeed supports the presence of several mass movements of different ages (see Fig. 2 and section 5.4.2).

On the longitudinal line, a thin peculiar seismic unit of low amplitude (almost transparent) can be traced across the entire Tüscherz basin, with increasing thickness towards the center of the basin (Fig. 4). This seismic unit reaches 35 cm thickness (0.5 ms), thus is above the limit of vertical seismic resolution (ca. 10 cm; vertical seismic reflection is defined as ¼ of the wave length of the seismic signal, i.e. ~ 100 mm for the 3.5 kHz source). It is located in-between seismic units of higher amplitudes showing undisturbed layered sediments.
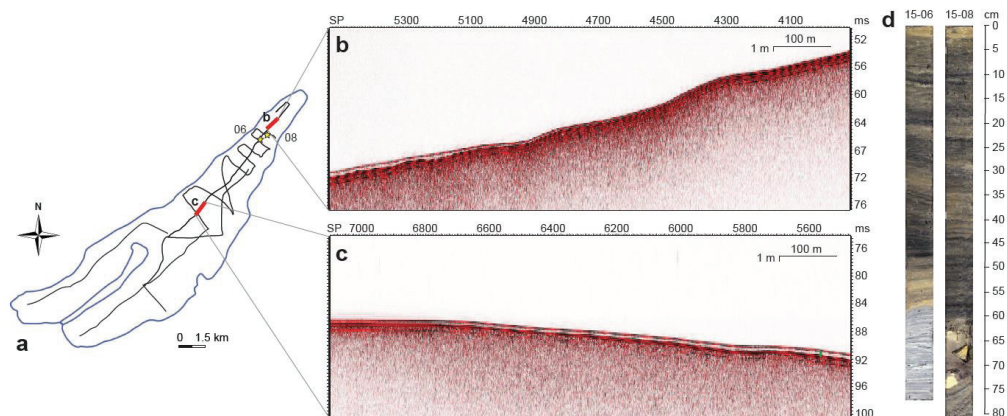
186

Figure 4. Seismic lines along the longitudinal section (a) revealing the "dump" unit across the entire Tüscherz basin (b, c). The locations of the seismic lines (b) and (c) are highlighted in red in (a). The dump is thinning up towards the shallower regions (b, c). Sediment cores that reach this dump (at ca. 60 cm depth) reveal heterogeneous sediments, some of grayish colors or containing sharp stones (d). Locations of cores BIE-15-06 and BIE-15-08 are shown by yellow stars in (a).

5.4.2 Multibeam

Analyses of the bathymetry dataset were performed in standard GIS software. Descriptions and interpretations are based mainly on a shaded relief version of the bathymetric map (Fig. 2). The layout and general topography of the basins have been known since the first bathymetric surveys (see section 2), therefore, we will focus here on the distinct geomorphological features newly revealed by the high-resolution bathymetric survey.

The new bathymetry data document several features characteristic of subaqueous slides/mass flows affecting soft lacustrine sediments. Interpretation and mapping of these signatures rely on descriptions of the morphology (elements such as escarpments, bulges or ridges), but also on the identification of surface textures, i.e. small-scale relief resulting in a distinct appearance of the lake floor in hillshade images (Fig. 2). Numerous underwater mass movements are clearly distinguishable, both on the northwestern shore characterized by steep slopes (up to ~30°) and the more gently dipping southeastern slopes.

The mass movements are rather small-scale on the northern shore (Fig. 5a). In the region Ligerz-Twann, four such mass movements can be observed, while the southern flank of the St Petersinsel seem to be affected more strongly. The region Tüscherz-Alfermée on the other hand

187

is home to numerous mudflows, some of them with erosional channels incising the northern slope (Fig. 5b).

The mass movements on the southeastern slopes are less numerous, but a very large slump complex is visible between Sutz-Lattrigen and Ipsach, which represents the amalgamation of several distinct events (Fig. 2, 6). The main slide scar extends laterally over 1 km, in ca. 5m water depth, at the upper slope break. The headwalls, i.e. the source and transit areas of the mass movements, appear as very sharp escarpments with rough and variable textures on the upper slope break, bordering the shore platform. The presence of a ridge in the 1 km long headwall, as well as the different freshness of the sediment surface observed in seismic lines T2 and T3 (Fig. 3 and 6), suggests that there were at least two distinct mass movements.
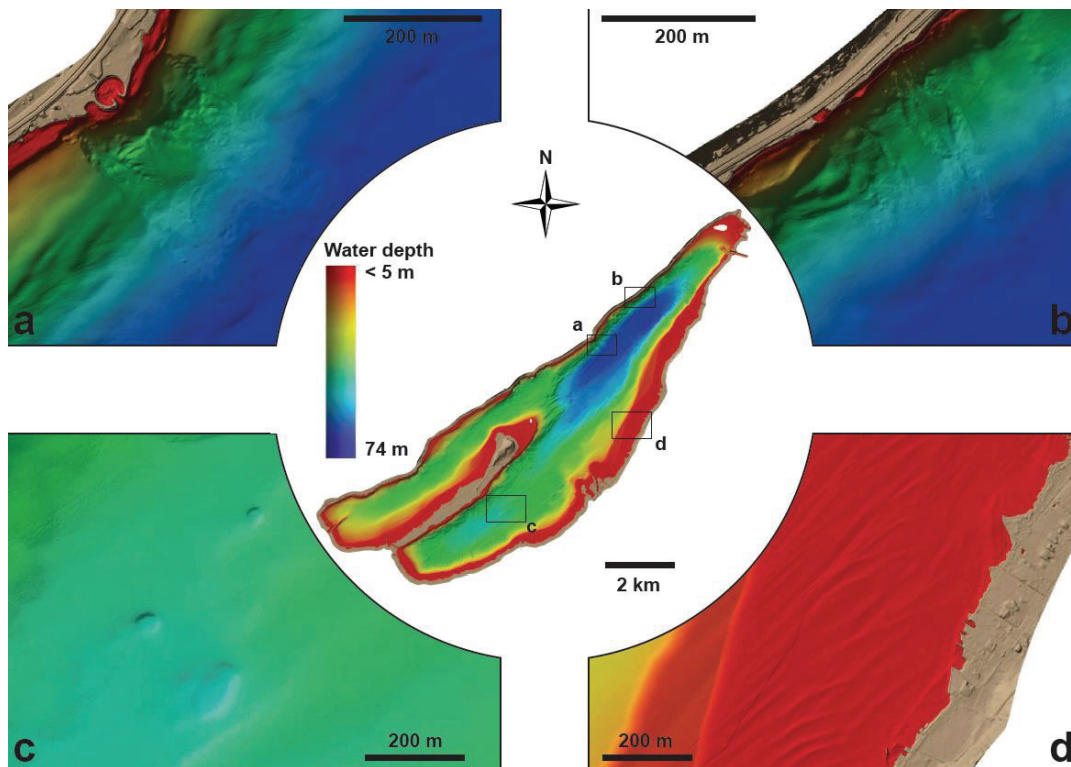

Figure 5. Selection of distinct geomorphologic features observed in the high-resolution bathymetric data of Lake Biel: (a) small-scale mass transport deposit resulting from construction work on shore (b) channel incisions on the slope and mudflows (c) pockmarks (d) subaquatic sand dunes.

Two additional slide scars with their headwalls can be distinguished on both sides of the two larger mass movements, overprinting or even cutting across the sliding surface of the larger older mass flows, indicating thus that the large slump complex results from at least four failures

188

(Fig. 6). The surface sediment structure of the mass flow deposits at the toe of the slope, in particular their prominent relief, suggests that large portions moved as coherent packages. These mass flow deposits in Lake Biel do not form semi-circular lobes characteristic for instance of Lake Lucern mass movements [Hilbe et al., 2011]. It is estimated that about 1 m of sediment went in motion. The total volume of the mass transport deposits (MTD) in the Sutz-Lattrigen slump complex is thus on the order of 1 million cubic meter.
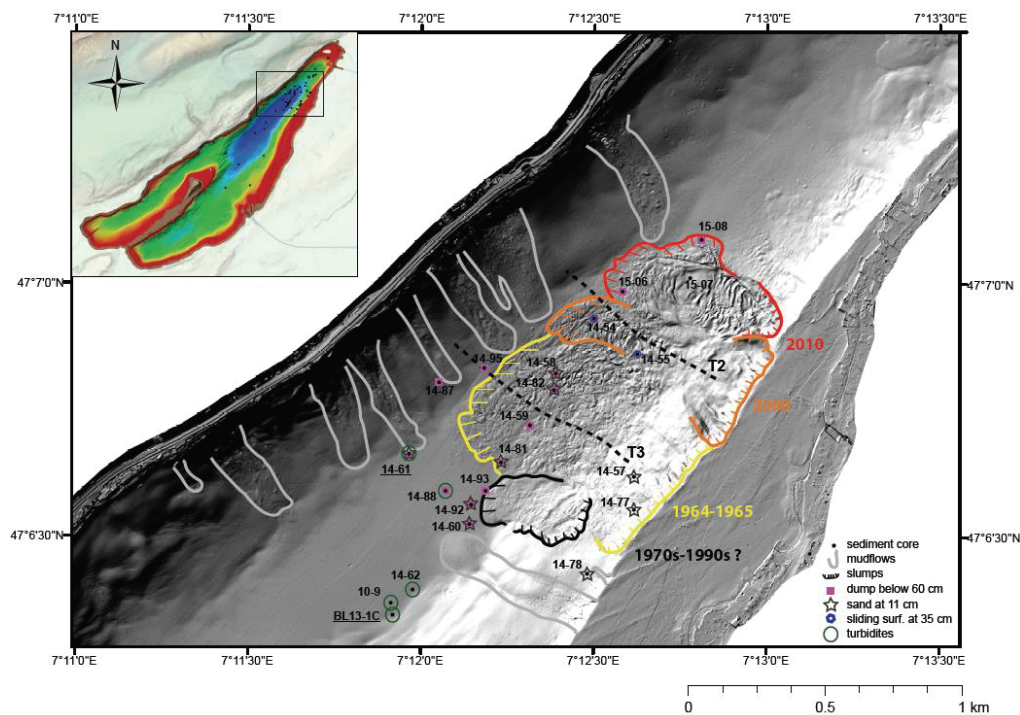

Figure 6. Interpretation of the Sutz-Lattrigen slump complex on a hillshade map. The locations of all the sediment cores retrieved are given in the small insert on the top left. Core analyzed in further detail are indicated with small black dots and their core names on the black and white hillshape map. The transverse seismic profiles T2 and T3 (see Fig. 2) are shown by dotted lines. Outline of mudflows (grey) and mass transport deposits (colors by age as indicated on the figure) are provided. Location where excavated material was retrieved (at depth below 60cm) are shown by pink squares. Green circles indicate cores in which turbidites were observed. Blue pentagons show the two cores revealing a sliding surface at 35 cm depth. Black stars represent cores in which a sand layer is present at 11 cm depth.

The lakefloor morphology is further characterized by 10 pockmarks of varying sizes: most are 20-30 m in diameter, while the two larger ones are 60 and 70 m in diameter (Fig. 5c). Seven pockmarks are located on the toe of the slopes along the northwestern shore close to the Jura Mountain front, between Ligerz and Twann, in a similar position as the giant pockmarks discovered in Lake Neuchâtel (Fig. 2; Reusch et al. [2015]). However, the last three are located at the toe of the southern slope of the St Petersinsel, almost in the central part of the Lüscherz basin, in front of the village of the same name (Fig. 2). In both locations some of the pockmarks reveal a succession of pockmarks of different sizes and ages, the older stages appearing less sharply (Fig. 5c).

Finally, the relatively wide southeastern shore platform hosts several subaquatic sediment dunes, especially in front of Gerolfingen (Fig. 5d, 2).

5.4.3 Sediment cores

In the following, only a selection of the sediment cores most useful for the interpretation of the mass movements and of the sedimentary units visible on the seismic lines will be presented.

Dating of the various mass movements in the Stutz-Lattrigen complex has revealed difficult. Generally, mass movements can be best dated based on the accompanying turbidites deposited in the basin, where sedimentation is continuous and undisturbed. Unfortunately, cores BIE10-9 and BIE-14-62 (located in the deepest part of the Tüscherz basin) only reveal 2 larger turbidites (Fig. 7).
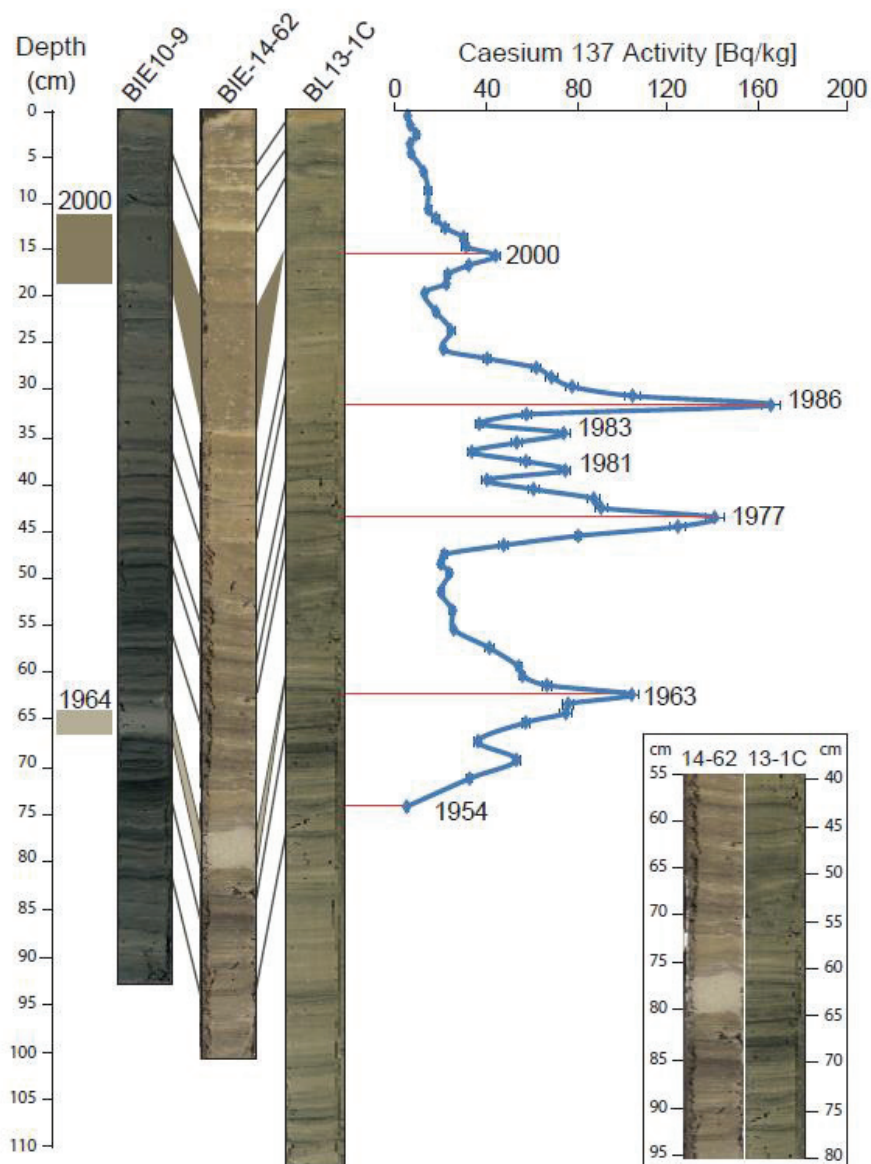
Figure 7. (a) Cross core correlation of cores BIE10-9, BIE-14-62, and BL13-1C (b) Dating of core BL13-1C based on its ^{137}Cs activity profile.

Several hypotheses can be put forward to explain the lack of a turbidite corresponding to each of the four larger MTDs. First, the westernmost slump is of a relatively smaller size, thus it may well be that we cannot clearly distinguish its correspondingly small turbidite amongst the succession of heterogenous diffuse laminations in the sediments within the basin. Second, the strong flow caused by the Aare might also contribute to the missing turbidites in the deep Tüscherz basin, as suspended sediments tend to be entrained eastwards towards the outflow of the lake. Third, some of the slumps moved as coherent packages, which does not result in the

large-scale resuspension of finer particles leading to a turbidite: Cores BIE-15-06, BIE-15-07, and BIE-15-08 (located in the easternmost and youngest slump) can thus be precisely correlated with each other (Fig. 8). In addition, if a small turbidite had been generated from this very recent mass transport, its deposit might be difficult to distinguish, as it would still be located in the oxygenated upper layers. As a result, we ascribed the two turbidites to the two larger mass movements located in the center of the Stutz-Lattrigen slump complex. Through correlations with nearby core BL13-1C dated by gamma spectrometry (^{137}Cs), the age of these two turbidites have been set as 1964 and 2000 (Fig. 7). The larger and oldest mass transport (yellow on Fig. 6) would thus have occurred in the mid 1960s, whereas the medium-scale (orange on Fig. 6) slump would be dated to the year 2000. Sediment core BIE-14-54 retrieved from this MTD reveal two possible sliding surfaces: one at 64 cm, which would correspond to the older yellow slump, and a second one at 36 cm, which would correspond to the sliding surface of the year 2000 slump (orange; Fig. 9). Core BIE-14-55, which was also recovered in the orange MTD, only reaches down to 34 cm (Fig. 9). It thus supports the presence of a sliding (i.e. harder) surface around 35 cm depth.

A thick dark sandy layer in core BIE-14-60 (from 32 to 11 cm depth), at the base of the slope, might reflect a small local slope failure consisting of sand (Fig. 10). Cores BIE-14-78 and BIE-14-77 upslope reveal a sharp transition at 8 cm depth, from well-oxygenated beige silts to a base composed mostly of darker sand (Fig. 10). This sharp transition most likely represents the failure scar where some of the sand moved downslope. In addition to the thick deposit in BIE-14-60, several cores reveal a small 0.5-1 cm layer of dark sand around 11 cm sediment depth (core BIE-14-57 located in the slope, and cores BIE-14-58, BIE-14-61, BIE-14-81, BIE-14-82 and BIE-14-92 located in the basin; Fig. 10).

Last but not least, most cores located in the central part of the Tüscherz basin reveal the presence of excavated material dumped into the lake during the second JWC (Fig. 6, pink squares). These materials can be clearly distinguished by their distinct colors and composition (Fig. 4). In some of the cores, angular stones were even discovered (see BIE-15-08 in Fig. 4).
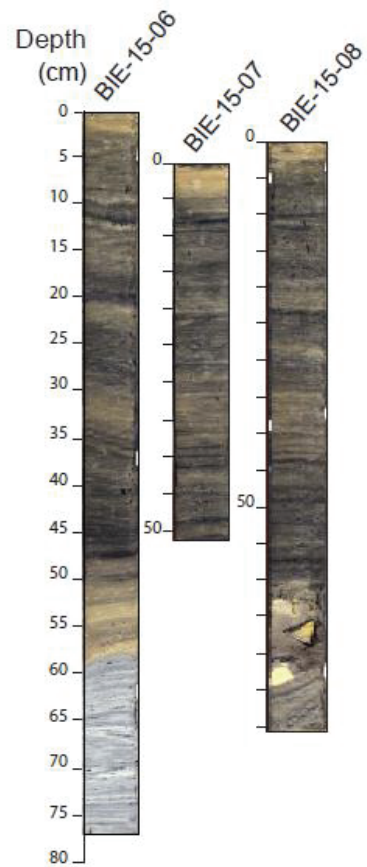
192

Figure 8. Cross core correlation of cores BIE-15-06, BIE-15-07 and BIE-15-08 located in the youngest mass transport deposit (red, see Fig. 6 for locations). The very good correspondence indicates that the slump moved as coherent packages. Note that cores BIE-15-07 and BIE-15-08 have been slightly compressed to better highlight the similitudes.
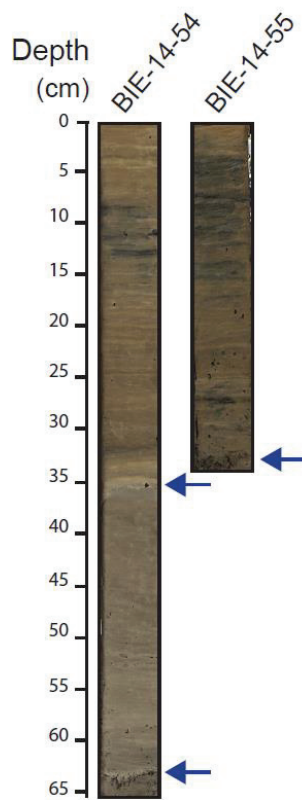
Figure 9. Cores BIE-14-54 and BIE-14-55 revealing a common sliding surface (blue arrow) at 36 and 34 cm depth, respectively, attributed to the orange mass transport deposit (see Fig. 6, also for the locations of the two cores). Core BIE-14-54 reveals a second older sliding surface at 64 cm depth potentially attributed to the yellow slump.
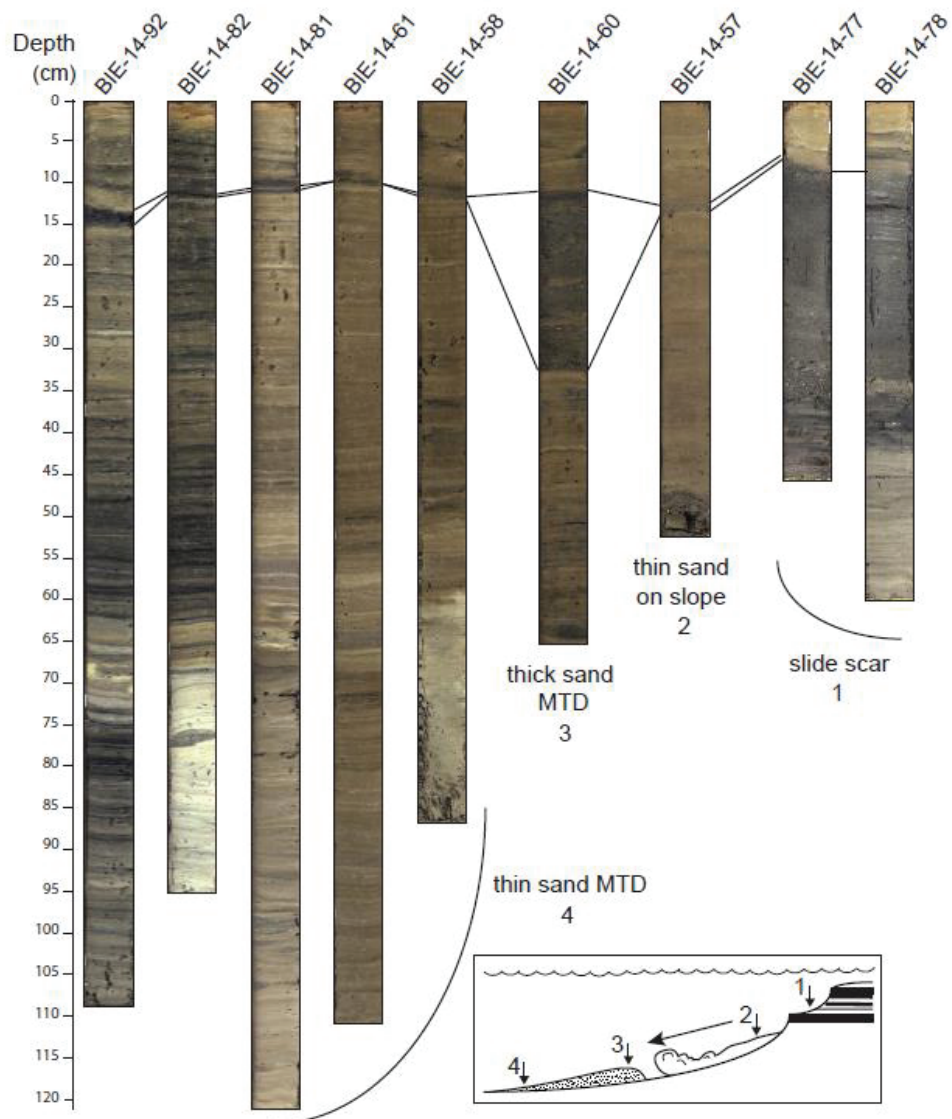
Figure 10. Cross cores correlation of the dark sandy layer. A thick deposit can be observed from 11 to 32 cm depth in core BIE-14-60, located at the bottom of the slope (See Fig. 6 for location and small schema on the bottom right). Cores BIE-14-77 and BIE-14-78 (upslope) reveal the potential source of the sand, with sand at the base of the core up to 8cm, with light silty mud on top. Cores BIE-14-57, BIE-14-58, BIE-14-61, BIE-14-81, BIE-14-82 and BIE-14-92, located in the slope (BIE-14-57 only) or in the basin reveal a thin sandy layer at 11 cm depth.

6. Discussion and conclusion

In recent years, many lakes in Switzerland and around the world have been surveyed with multi-beam bathymetry [e.g. Hilbe et al., 2011; Miller et al., 2013; Kremer et al. 2015; Reusch et al., 2015; Wessels et al., 2015]. These high-resolution bathymetric measurements allow the underwater-morphology to be visualized, revealing often the presence of various geological or hydrodynamic processes such as subaqueous mass movements, currents or pockmarks. Such morphologically complex observations are almost impossible using only reflection seismic profiles, even with a dense gridline.

The subaqueous landscape of Lake Biel revealed numerous mass movements, even on relatively gentle slopes. Various anthropogenic (e.g. construction works on shore) and natural factors (e.g. earthquakes, sediment accumulation) can trigger subaqueous mass movements [e.g. Locat and Lee 2002]. For instance, the small-scale MTD located in front of Wingreis and Twann were most likely caused by construction works on shore (Fig. 5a).

In the case of Lake Biel, the deviation of the Aare River into the lake – in particular the concomitant five-fold increase in sediment delivery – probably plays a large role in creating the instability of the eastern shore, where most of the sediment is deposited. Wirth et al. [2011] already demonstrated such increase in mass movement numbers following the deviation of the Kander River into Lake Thun in 1714. However, both sedimentation rates and mass movements frequency in Lake Thun decreased after 1840, as the Kander River adjusted to its new base level. As a measure of comparison, the deviation of the Kander increased the inflow in Lake Thun by 60% whereas the deviation of the Aare into Lake Biel increased the inflow by 290%.

In Lake Biel, the largest slump can be dated to the mid 1960's (Yellow MTD in Fig. 6), based on a turbidite found in the Tüscherz basin (Fig. 7). This slide has a smoother appearance both on the multibeam and on the seismic line (T3) that crosses it (Fig. 2 and 3), as it already starts to be covered by a sediment drape. Possible triggers include two earthquake of a magnitude of 3.9 and 3.2, in 1964 and 1965, respectively [Fäh et al., 2011]. The 1964 one was located between Courgevaux and Coussiberlé at 46.9°N, 7.117°E (ca. 23 km away from the slide), whereas the 1965 earthquake occurred at 47.0°N, 7.2°E by Fräschels (ca. 11 km away from the slide, see Fig. 1 for location of the epicenters). An alternative trigger could be the dumping of materials excavated during the second JWC, which started in 1963. Many cores retrieved from the central part of the Tüscherz basin, thus within or close to the MTD, reveal the presence of

dumped material below 60 cm depth (Fig. 4 and 6). The longitudinal seismic line shows a peculiar seismic unit of low amplitude in the Tüscherz basin, whose thickness is increasing towards the deeper basin, which we attribute to the subaquatic landfill of the 2nd JWC.

The youngest turbidite deposited in the basin, which was dated to the year 2000, was attributed to the second largest slump (orange MTD in Fig. 6). This MTD reveals a rougher surface in the seismic line T2 (Fig. 3) than the 1964 MTD seen on T3. Cores BIE-14-54 and BIE-14-55, both located within the year 2000 slump (orange MTD), reveal the presence of the sliding surface at around 35 cm depth.

The two smaller MTD (black and red), located at each extremities of the Sutz-Lattrigen slump complex, did not produce any recognizable turbidites in the basin. We attribute this lack of turbidite mainly to their smaller size (for the black MTD), and to the fact that it moved as coherent packages (for the red MTD). Additionally, depending on the season in which the mass movements occurred, the suspended particles could have been entrained by the Aare towards the outflow. Based on the fact that the black MTD (which started mid-slope) overprints the yellow MTD, but also that its surface is relatively smooth, we suggest a date of occurrence between the 1970's and the 1990's (Fig. 6). The red slump to the northeastern part of the Sutz-Lattrigen slide complex has the roughest morphology (visible on the multibeam, Fig. 6), pointing to a very recent event. Interestingly, the intake pipe for the drinking water supply of the city of Biel, which is located in the vicinity of Ipsach, reported a large turbidity event on New Year eve 2009-2010 (Energy Service Biel, personal communication). We thus assume that this recent close-by mass movement (red MTD) occurred at the turn of the year 2010.

The subaqueous mass movements described here can pose a risk for communities and infrastructures: the tsunamis they can potentially trigger can have catastrophic impacts on the shorelines, whereas slides can directly damage subaquatic infrastructures. An integrated approach, combining subaqueous geomorphological mapping with interpretation of reflection seismic profiles and dating of sediment cores, allows an estimation of spatial distribution, magnitudes and recurrence times for such disasters. Unfortunately, in Lake Biel, only recent events can be traced as the seismic lines suffer from gas blanking.

In conclusion, large-scale river-managing works such as the Jura Water Corrections need to take into account possible short-term consequences of subaquatic landfills as well as longer-term effects, including the effects of higher sediment load on slope stability.

Acknowledgments

References

Anselmetti FS, Bühler R, Finger D, Girardclos S, Lancini A, Rellstab C, Sturm M (2007) Effects of Alpine hydropower dams on particle transport and lacustrine sedimentation. Aquat Sci 69:179–198

Brombacher C (1997) Archaeobotanical investigations of Late Neolithic lakeshore settlements (Lake Biel, Switzerland) *Vegetation History and Archaeobotany* 6(3): 167-186

Fäh D, Giardini D, Kästli P, Deichmann N, Gisler M, Schwarz-Zanetti G, Alvarez-Rubio S, Sellami S, Edwards B, Allmann B, Bethmann F, Wössner J, Gassner-Stamm G, Fritsche S, Eberhard D (2011) ECOS-09 Earthquake Catalogue of Switzerland Release 2011 Report and Database. Public catalogue, 17. 4. 2011. Swiss Seismological Service ETH Zurich, Report SED/RISK/R/001/20110417

Hilbe M, Anselmetti FS, Eilertsen RS, Hansen L and Wildi W (2011) Subaqueous morphology of Lake Lucerne (Central Switzerland): Implications for mass movements and glacial history. Swiss Journal of Geosciences 104:425–443. doi: 10.1007/s00015-011-0083-z

Jeannet A (2012), Lake Biel sediment record during the last 7500 years and impact of the Aare River deviation in 1878 AD, 82p. Maîtrise universitaire en sciences de l'environnement, Mémoire # 91, University of Geneva.

Kremer K, Hilbe M, Simpson G, Decrouy L, Wildi W and Girardclos S (2015) Reconstructing 4000 years of mass movement and tsunami history in a deep peri-Alpine lake (Lake Geneva, France-Switzerland). Sedimentology 1305–1327. doi: 10.1111/sed.12190

Liechti P (1994) L'état des lacs en Suisse. Cahier de l'Environnement, 237. Office Fédéral de l'Environnement, des Forêts et du Paysage (OFEFP), Berne , Switzerland, p 159

Locat J and Lee HJ (2002) Submarine landslides: advances and challenges. Canadian Geotechnical Journal 39:193–212. doi: 10.1139/t01-089

Miller H, Bull JM, Cotterill CJ, Dix JK, Winfield IJ, Kemp AES and Pearce RB (2013) Lake bed geomorphology and sedimentary processes in glacial lake Windermere, UK. Journal of Maps 9:299–312. doi: 10.1080/17445647.2013.780986

Nast M (2006) Terre du lac, l'histoire de la correction des eaux du Jura. Verein Schlossmuseum Nidau. 200 pp.

Nydegger P (1967) Untesuchungen über Feinstoftransport in Flüssen und Seen, über Entstehung von Trübungshorizonten und zuflussbedingten Strömungen im Brienzersee und einige Vergleichseen, Beitr. Geol. Schwiez Hydrol. Ser., 16, 92 pp.

Nydegger P (1976) Strömungen in Seen: Untersuchungen in situ und an nachgebileten Modellseen, Beitr. Geol. Schweiz. Kl. Mitt., 66, 141-177.

Reusch A, Loher M, Bouffard D, Moernaut J, Hellmich F, Anselmetti FS, Bernasconi SM, Hilbe M, Kopf A, Lilley MD, Meinecke G, and Strasser M (2015) Giant lacustrine pockmarks with subaqueous groundwater discharge and subsurface sediment mobilization: *Geophysical Research Letters*, 42, doi:10.1002/2015GL064179

Råman Vinnå, L., D. Bouffard, A. Wüest, S. Girardclos, and N. Dubois (2017), Wind driven circulation focusing lake sedimentation. In preparation,

Santschi PW, and PW Schindler (1977) Chemical and geochemical studies of Lake Biel I. A mass balance for Lake Biel and its implications for the rates of erosion of the drainage area, Schweiz. Z. Hydrol. 39, 182-200.

Schneider JR (1881) Das Seeland der Westschweiz und die Korrektion seiner Gewässer. – Krebs, Bern.

Schneider N, Eugster W, and Schichler B (2004) The Impact of Historical Land-Use Changes on the Near-Surface Atmospheric Conditions on the Swiss Plateau. Earth Interactions 8 (12): 1-27.

Swisstopo (2014) Das hoch aufgelöste Terrainmodell der Schweiz. Detaillierte Produktinformation. Bundesamt

für Landestopografie swisstopo, Wabern.

Syvitski JPM, Vörösmarty CJ, Kettner AJ, Green P (2005) Impact of Humans on the Flux of Terrestrial Sediment to the Global Coastal Ocean. Science 308(5720): 376-380

Thevenon F, Wirth SB, Fujak M, Poté J, Girardclos S (2013) Human impact on the transport of terrigenous and anthropogenic elements to peri-alpine lakes (Switzerland) over the last decades. Aquat Sci 75: 413–424

Vischer, DL (2003) Histoire de la protection contre les crues en Suisse: Des origines jusqu'au 19e siècle. Rapports de l'OFEG, Série Eaux. No 5. Bienne. 208 p.

Weiss, HP (1977) Sedimentologische und isotopengeochemische Untersuchung der Lockersedimente im Bielersee, 106p. Thesis, University of Bern.

Wessels M, Anselmetti F, Artuso R, Baran R, Daut G, Gaide S, Geiger A, Groeneveld JD, Hilbe M, Möst K, Klauser B, Niemann S, Roschlaub R, Steinbacher F, Wintersteller P and Zahn E (2015) Bathymetry of Lake Constance - A high-resolution survey in a large, deep lake. ZFV - Zeitschrift fur Geodasie, Geoinformation und Landmanagement 140:203–210. doi: 10.12902/zfv-0079-2015

Wirth SB, Girardclos S, Rellstab C, Anselmetti F. (2011) The sedimentary response to a pioneer geo-engineering project: Tracking the Kander River deviation in the sediments of Lake Thun (Switzerland), Sedimentology, 58, 1737–1761.

Wright RF, Matter A, Schweingruber M, Siegenthaler U (1980), Sedimentation in Lake Biel, an eutrophic, hard-water lake in northwestern Switzerland. Schweiz. Z. Hydrol. 42(2): 101–126

Wright, R.F. and P. Nydegger (1980), Sedimentation of Detrital Particulate Matter in Lakes: Influence of Currents Produced by Inflowing Rivers, Water Resources Research, 16, 597-601.

Wüest A, Zeh M, Ackermann JD (2007) Lake Brienz project: an interdisciplinary catchment-to-lake study. Aquat Sci 69:173–178

Personal information: 2017-10-15
Name: *Carl* Love *Mikael* Råman Vinnå
Address: Rue de Crause 7D
Zip code, City: 1373 Chavornay
Country: Switzerland
Mobile: +41 787 966 454
Mail: love.ramanvinna@epfl.ch
Date of birth, Place: 1985-10-08, Stockholm, Sweden

CV

Professional profile:

I enjoy working in and leading projects which are beneficial for the development of society and strives to improve water management and sustainable usage of aquatic systems. I have great knowledge in the physical, chemical and biological processes that occur in oceans and inland waters. I like programing, usage of hydrodynamic models and to take initiative.

Work experience:

2017 and ongoing **Postdoc at Department of Environmental Hydraulics and Water Resources, HKUST, Hong Kong, China**.

The project goal is to investigated entrainment into and propagation of the Rhône River plume as it enters Lake Geneva. Special emphasis is put on initial plunging mixing and underflow entrainment. This is obtained from optical, in situ and acoustic measurements and implemented into hydrodynamic models.

2013 to 2017 **Ph.D. at Physics of Aquatic Systems Laboratory, EPFL, Lausanne, Switzerland**

Thesis title: *Global and local anthropogenic effects on hydrodynamics of lakes - Applications to Lake Biel drinking water management.* The aim of this project was to find optimal locations for drinking water withdrawal in a perialpine lake. Methods included numerical modelling in one to three dimensions which was validated by a long term field campaign. The position contained project management, scientific publication, student supervision and teaching.

2012 to 2013 **Research assistant at GU, Gothenburg, Sweden.**

Development of a numerical box model replicating the Baltic Sea in the interdisciplinary geoengineering project Box-Win. Project aim was to improve oxygen condition in the Baltic Sea through artificial mixing.

2008 to 2013 **Security guard at Securitas, Gothenburg, Sweden.**

Customer contact; conflict management; technical support; administrative responsibilities.

2010 to 2011 **Scientific teaching assistant at GU, Gothenburg, Sweden.**

Supervision of chemical and physical offshore sampling onboard Research Vessel Skagerak.

2005 to 2006 **Salesman at Åhléns, Stockholm, Sweden.**

Customer contact; display arrangement.

2004 to 2005 **Military service: Radio squad leader at Air Combat School, Uppsala, Sweden.**

Independent leadership responsibilities; advanced radio technology and communication methods.

Education:
2006 to 2012 **M.Sc and B.Sc in Physical Oceanography, GU, Gothenburg, Sweden.**
Thesis titles; M.Sc.: *Comparing satellite and FerryBox measurements of sea surface temperature in Skagerrak and Kattegat*. B.Sc.: *Geothermal heating of Canada basin deep water*. This education has given me knowledge in the following fields:

Physical Oceanography	Programing	Marine Chemistry
Fluid mechanics	Numerical modeling	Marine Biology
Turbulence	Data assimilation	Marine Environmental Monitoring
Physics	Remote Sensing	Climate Change
Wave motions	Scientific Computing	Pollution of marine environments
Mathematics	Statistics	Chemistry

2001 to 2004, **Upper secondary school, Nacka Gymnasium, Stockholm, Sweden.**
Main field of study: mathematics, physics, chemistry and biology.

Language skills:
Swedish (native), English (scientific level), German (basic).

Mastered numerical models:
Delft3D (3D hydrodynamic model)
Simstrat (1D hydrodynamic model)
Air2stream and Air2water (River/Lake surface temperature model).

Computer program skills:
MATLAB, FORTRAN, C++, Ocean Data View, Arc/Q GIS, R, Linux, Windows, Microsoft Office.

Scientific instrumentation and sampling techniques:
CTD, ADCP, Aquadopp, Multibeam sonar, Vemco Temperature logger, RBR duo/concerto/solo loggers, LISST-100X, SOLITAX turbidity, Winkler titration, photometric analysis, particle and chlorophyll filtration.

Additional qualifications:
Swiss car (B) and boat (motor) driver's license, advanced open water diver certificate, certified self-defense instructor.